

**A Numerical Study of the Far Field Effects of Wave Energy Converters
in Short and Long-Crested Waves Utilizing a Coupled Model Suite**

Een numerieke studie van de far-fieldeffecten van golfenergieconvertoren
in kort- en langkruinige golven met behulp van een gekoppeld model

Gael Verao Fernandez

Promotoren: prof. dr. ir. P. Troch, dr. ir. V. Stratigaki
Proefschrift ingediend tot het behalen van de graad van
Doctor in de ingenieurswetenschappen: bouwkunde



**UNIVERSITEIT
GENT**

Vakgroep Civiele Techniek
Voorzitter: prof. dr. ir. P. Troch
Faculteit Ingenieurswetenschappen en Architectuur
Academiejaar 2018 - 2019

ISBN 978-94-6355-259-2

NUR 956

Wettelijk depot: D/2019/10.500/67

Examination board

Supervisors:

prof. Peter Troch
dr. Vasiliki Stratigaki
Coastal Engineering Research Group
Department of Civil Engineering
Faculty of Engineering and Architecture
Ghent University
Technologiepark 60
B-9052 Ghent, Belgium

Voting members:

ereprof. Ronny Verhoeven	Ghent University, Belgium	chairman
prof. Tom de Mulder	Ghent University, Belgium	secretary
prof. Eva Loukogeorgaki	Aristotle University, Greece	
em. prof. Marc Vantorre	Ghent University, Belgium	
prof. Eugen Rusu	University Dunarea de Jos Galati, Romania	
prof. Lieven Vandevelde	Ghent University, Belgium	

Internal defence (Ghent University): 27/05/2019

Public defence (Ghent University): 08/07/2019

*'As you set out for Ithaka hope your road is a long one, full of
adventure, full of discovery [...]*

-Constantino Cavafis -

Á Pilar, por ensinarme ca súa intelixencia o lugar ao que pertenzo.

Acknowledgements

When I look back over the past four years I just can see how similar this journey has been for me as setting for Ithaka. Pursuing a PhD is not just adding a dr. in front of my name but getting up every morning arriving to a new port. Sometimes there were dark gray ports of frustration and dead ends. Other times there were wise ports of outbreaks in the research and moving forward. Most of the times there were ports of joy with nice talks with colleagues about research or anything related to Galicia, boiling water for tea and enjoying birthday treats. But what has made me rich is not setting for Ithaka. It is all the people I have met along the way and everything that I have learned from them.

First, I would like to thank my supervisors Peter Troch and Vicky Stratigaki for giving me the opportunity to embark in this journey and staying by my side. Thank you Peter, for all the nice discussions about cycling and coastal engineering, nice presentation tips and support during hard writing times. Thank you Vicky for all the effort you have put in improving my scientific writing style and keeping me focused on my research and objectives, specially the last difficult year of these journey.

Like Odysseus in his journey I have travelled in lots of different boats, all of them with magnificent crews. I cannot express in words all my gratitude to the AWW crew members for surviving my endless talks these four years. Thank you Sam and Dave for helping me with my dutch and showing me how to do a proper master thesis bbq. Thank you Herman for sparkle my desire to travel on the road, even though it is going to be on a bike. Not to mention all the rabbits Tom has pulled out of his hat to help me. Thank you Andreas for your coastal engineering discussions. Thanks Lien for all the nice chats and patience with me, and Ellen for more conversations and even more patience. Thank you Vincent for teaching me how to be meticulous with my work, Minghao for your exotic chinese snacks, Carlos for opening my eyes with the truth of South America and Timothy and Nicolas for teaching my father: "when you hike we drink". I cannot forget my small cabin, thank you Panagiotis for your friendship and knowledge. A special thank you to Philip for all we have gone through together. I would also like to mention those who left with Calypso. Thanks Ine for the secret cookies recipe, Brecht for your eternal intelligent smile and support and Tim for his unconditional help.

Thanks to my Carnales crew Max, David, Almudena and Luis for their warming

welcome to Belgium, and all the time we have spent together while I was fighting against the syrens. Thank you Corrado and Maria for discovering me Gent, I cannot wait to meet Maia. Thanks to the Nomadés for all the cycling adventures. A special thanks goes to Olalla and Cesar for keeping Galiza close to me all the time. Not to forget all the people that passed the Voskenslaan 280. Specially Karsten, two people on a strange land who now find themselves at home. I cannot forget Chika, off all the beings I have met these 4 years she is the only one who never knows what is going on but always gives me the most warming cuddles. Also a big hug to Josué for discovering me the classical guitar world. I am sure I forgot somebody, so to all of them a big thank you.

Hearing from me far in the distance, not knowing exactly what is going on with me or what I am doing but always supporting I would like to give a special thanks to all my friends and family. Grazas Branca e Suso por todo o que aprendo de vós, polo voso apoio incondicional e por facer todo o posible para que puidese chegar ao final deste longo camiño. Grazas ao Xacobe por verme sempre cos pés na terra e recordarme que a viaxe rematará algun día en Galiza. And finally a warm thank you to Angie, for taking care of me during this hard process. Coidote !!!

Gael Verao Fernández
July 2019

Contents

1	Introduction	1
1.1	Background	1
1.2	Numerical modelling of WECs	4
1.2.1	Wave structure interaction solvers	4
1.2.2	Wave propagation models	6
1.2.3	Coupling methodologies for array modelling	7
1.3	Knowledge gaps	8
1.4	Objectives and outline	9
2	Theoretical Background	11
2.1	Linear wave theory	11
2.1.1	Fundamentals	11
2.1.2	Wave energy	16
2.1.3	Wave power	17
2.2	Analysis of irregular waves	17
2.2.1	Time-domain analysis of irregular waves	18
2.2.2	Frequency-domain analysis of irregular waves	19
2.2.3	Construction of irregular waves from variance density spectrum	22
2.2.4	Conversion of irregular surface elevation into variance spec- trum	23
2.3	Hydrodynamics of a floating body	24
2.3.1	Problem decomposition	24
2.3.2	Equation of motion: single degree of freedom WEC	26
2.3.3	Forces	28
2.3.4	Complex amplitude of the body motion	29
2.3.5	Power absorption	30
2.4	The wave propagation model MILDwave	30
2.4.1	Governing equations	30
2.4.2	Periodic lateral boundaries	32
2.5	The wave-structure Interaction solver NEMOH	33
2.5.1	Potential Flow Theory	33
2.5.2	Solution of the boundary value problem	34
3	MILDwave - NEMOH Coupled Model	37

3.1	Introduction	37
3.2	Generic Coupling Methodology	38
3.3	MILDwave-NEMOH coupled model	40
3.3.1	Basis of the MILDwave-NEMOH coupled model	40
3.3.2	MILDwave-NEMOH coupled model implementation	45
3.3.3	MILDwave-NEMOH coupled model algorithm	46
3.4	Numerical validation of the MILDwave-NEMOH coupled model	53
3.4.1	Test Cases	53
3.4.2	Numerical set-up in MILDwave	57
3.4.3	Numerical set-up in NEMOH	58
3.4.4	Criteria Used for the numerical validation	59
3.5	Sensitivity analysis	60
3.5.1	Internal wave generation boundary	61
3.5.2	Dimensions of the internal wave generation boundary	64
3.5.3	Grid cell size	65
3.5.4	Number of regular wave components	71
3.5.5	Directional spreading function	72
3.6	Numerical validation results	74
3.6.1	Test Case 13	74
3.6.2	Test Case 31	79
3.6.3	Test Case 16	82
3.6.4	Comparison Summary	87
3.6.5	Computational Time	87
3.7	Discussion	89
3.8	Conclusions	91
4	Experimental validation of the MILDwave-NEMOH coupled model	93
4.1	Introduction	93
4.2	WECwakes experimental data-set	93
4.3	Experimental validation strategy	96
4.3.1	Validation Test Cases	96
4.3.2	Criteria used for the experimental validation	96
4.3.3	Numerical set-up in MILDwave	97
4.3.4	Numerical set-up in NEMOH	97
4.4	Experimental validation results	99
4.4.1	Regular waves results	99
4.4.2	Irregular waves results	101
4.5	Conclusions	107
5	Numerical Applications of the MILDwave-NEMOH Coupled Model	109
5.1	"Far field" effects of WEC arrays over varying bathymetry	109
5.2	"Far field" effects of WEC arrays in irregular long-crested and short-crested waves	114
5.2.1	Disturbance coefficient calculation for long and short-crested irregular waves	115
5.2.2	Comparison between long and short-crested irregular waves	121

5.3	"Far field" effects of WEC arrays over a real bathymetry	123
6	Conclusions and Further Work	127
6.1	Summary of the key findings	127
6.2	Recommendations for future research	128
A	MILDwave-NEMOH original source code	131
B	Numerical validation results	141
C	Experimental validation results	179
	References	186

Nomenclature

Most used symbols (I)

a	wave amplitude	m
B_{hyd}	hydrodynamic damping coefficient	kg/s
B_{PTO}	power take off damping coefficient	kg/s
B_p	length of the sponge layer for the peak period	m
B_S	length of the sponge layer	m
B_{max}	length of the sponge layer for the maximum period	m
C	wave celerity	m/s
C_g	group celerity	m/s
d	water depth	m
D	spreading function	m
E	energy	J
E_k	kinetic energy	J
E_p	potential energy	J
f	wave frequency	Hz
f_p	peak wave frequency	Hz
F	force	N
F_{dif}	diffraction force	N
F_e	excitation force	N
F_{FK}	Froude-Krylov force	N
F_{hyd}	hydrodynamic force	N
F_{hys}	hydrostatic restoring force	N
F_m	mooring force	N
F_{pe}	body external pressure force	N
F_{PTO}	power take off reaction force	N
F_{rad}	radiation force	N
F_{re}	reaction force	N
g	acceleration of gravity	m/s^2
H	wave height	m
H_s	significant wave height	m
i	imaginary number part	—
J	total number of wave energy converters	—
k	wave number	—

Most used symbols (II)

K	spring stiffness	N/m
K_d	disturbance coefficient	—
K_m	mooring spring stiffness	N/m
K_H	hydrostatic spring coefficient	N/m
K_{PTO}	power take off spring coefficient	N/m
L	wave length	m
m	mass	kg
M_A	added mass	kg
n	unit vector normal to the body surface	—
N	number of regular wave components	—
N_f	number of frequency components	—
P	energy flux	W
p	pressure	N/m^2
R_c	coupling radius	m
s_1	directional spreading parameter	—
S_b	body free surface	—
S_b	mean wetted body surface	—
S	variance density spectrum	m^2
t	time	s
t_{sim}	simulation time	s
T	wave period	s
T_p	peak period	s
T_r	resonance period	s
T_s	mean wave period	s
u	horizontal particle velocity	m/s
w	vertical particle velocity	m/s
x	first horizontal space coordinate	—
\tilde{X}	Response Amplitude Operator	—
y	second horizontal space coordinate	—
z	vertical space coordinate	—
\dot{z}	vertical velocity	m/s
\ddot{z}	vertical acceleration	m/s^2
ϵ	wave steepness	—
η	surface elevation	m
$\hat{\eta}$	complex amplitude	m
$ \eta $	absolute complex amplitude	m
ϕ	velocity potential	—
ϕ_R	radiation potential	—
ϕ_D	diffraction potential	—
ϕ_I	incident potential	—
Δ	difference	—
Δt	time step	s

Most used symbols (III)

Δx	grid cell size in X -direction	m
Δy	grid cell size in Y -direction	m
Σ	sum	—
σ	standard deviation	—
σ_θ	standard deviation of the directional spreading	—
α	slope angle	—
θ	wave direction	—
θ_{mean}	mean wave direction	—
ρ	density	kg/m^3
φ	wave phase	—
ω	wave angular frequency	rad/s
Γ	Gamma function	—

Symbols

$^\circ$	angle	$^\circ$
∂	partial derivative	—
$\hat{}$	complex number	—
\varnothing	diameter	m

Subscripts

b	wave generation boundary
c	center of the internal wave generation boundary
dif	diffracted
$freq$	frequency domain
I	incident
irr	irregular
i	cartesian index
j	cartesian index
k	cartesian index
m	cartesian index
max	upper limit
min	lower limit
n	cartesian index
MN	MILDwave-NEMOH coupled model
NM	NEMOH
$pert$	perturbed
rad	radiated
$rand$	random
reg	regular
tot	total
WG	wave gauge
WW	WECwakes

Abbreviations

BEM	Boundary Element Method
BVP	Boundary Value Problem
CFD	Computational Fluid Dynamics
CLI	Command-line interface
CPU	Central Processing Unit
DHI	Danish Hydraulic Institute
EMEC	European Marine Energy Centre
GEC	Golfenergieconvertor
HCWEC	Heaving Cylindrical Wave Energy Converter
IRREG	Irregular waves
NS	Navier-Stokes
OSWEC	Oscillating Wave Surge Wave Energy Converter
PTO	Power take off
PTFE	Polytetrafluoroethylene
RAO	Response Amplitude Operator
REG	Regular waves
RMSE	Root Mean Square Error
SPH	Smoothed Particle Hydrodynamics
SWL	Still Water Level
WEC	Wave Energy Converter
WG	Wave Gauge

Samenvatting

Dutch summary

Oceaangolven zijn een enorme bron van mariene hernieuwbare energie met het potentieel om bij te dragen tot een afhankelijkheidsvermindering van fossiele brandstoffen in de wereld. Golfenergie kan worden omgezet in bruikbare elektriciteit met behulp van golfenergieconvertoren (GECs). GECs vangen de kinetische en potentiële energie van de golven, die vervolgens wordt overgebracht naar een PTO-systeem (power take-off) die ze omzet in elektriciteit. Tot op heden is een groot aantal GECs in ontwikkeling, echter weinige bereiken een pre-commerciële fase. Om golfenergieprojecten economisch rendabel te maken, zou er een groot aantal GECs ingezet moeten worden in golfenergieconvertoorparken (GEC-parken) voor de productie van elektriciteit. De inzet van veel GECs in de oceaan brengt een ander aantal uitdagingen met zich mee. Ten eerste vergt het een hoge economische investering, zowel tijdens de installatie, de levensduur als het onderhoud van het project. Ten tweede worden GECs blootgesteld aan zware stormen. Daarom moeten ze zo worden ontworpen dat ze een groot aantal stormen kunnen overleven, waardoor de onderhoudskosten en de vervanging van eenheden worden beperkt. Ten slotte brengen GEC-park projecten een reeks milieueffecten met zich mee die niet over het hoofd mogen gezien worden. Een bijzondere zorg voor de mariene hernieuwbare energie sector is het mogelijke effect van de energieabsorptie van het GEC-park bij de herverdeling van de golfenergie in de luwte van het GEC-park.

De totale golfvermogenabsorptie van een GEC-park zal het omringende golfveld beïnvloeden, waardoor gebieden met verminderde golfenergie (gebieden met verminderde golfhoogte) ontstaan in de luwte van een GEC-park. Het hydrodynamische probleem van absorptie tussen de GECs binnen een GEC-park en tussen de GECs en het invallende golfveld wordt gekenmerkt door drie verschillende fenomenen, namelijk: golfreflectie, diffractie en radiatie. De superpositie van de gereflecteerde, gediffracteerd en geradieerde golfvelden resulteert in een verstoord golfveld. Het verstoord golfveld dicht bij de GECs van het park, veroorzaakt door zowel de GEC-GEC en golf-GEC interactie wordt in de literatuur vaak de "near-field" effecten genoemd. De propagatie van dit verstoord golfveld dat plaatsvindt op grotere afstand van de GEC-parken, bijv. in de kustzone, wordt "far field"-effecten genoemd.

Het modelleren van het verstoord golfveld rond een GEC-park is een complex proces. Meestal worden "near-field" en "far-field" effecten afzonderlijk benaderd. Dit is te wijten aan de moeilijkheden die ontstaan bij het gebruik van een enkel

numeriek model om een snelle en accurate oplossing voor beide effecten te verkrijgen. Om deze beperkingen te verhelpen, is er de afgelopen jaren een generieke koppelingsmethodologie ontwikkeld voor het koppelen van de golfstructuur interactie solvers met golfpropagatie solvers. Koppelingsmethodes met verschillende resoluties laten een hogere precisie toe bij het schatten van "far-field" effecten. Een golfstructuur interactie-solver wordt gebruikt om een accurate oplossing van het golfveld in een beperkt gebied rond het GEC van het park te verkrijgen en het resulterende golfveld wordt verder gepropageerd met behulp van een golfpropagatie model.

Het doel van dit doctoraatsonderzoek is om deze generieke koppelingsmethode toe te passen tussen het lineaire golfvoortplantingsmodel MILDwave en het lineair golfstructuur interactiemodel NEMOH. De resulterende koppelingsmethode is in staat tot kostefficiënte computersimulaties die kunnen bijdragen aan het bestuderen van de effecten van GEC-parken op de kust. Het model kan gebruikt worden om de reductie van golfenergie die de kustlijn bereikt en de co-locatie van golfenergieparken als bescherming voor offshore windprojecten te onderzoeken. Evenals kan het model, gecombineerd met bestaande morfodynamische modellen, gebruikt worden om de effecten op het sedimenttransport aan de kust te onderzoeken.

De MILDwave-NEMOH-koppelingsmethode is ontwikkeld door de stapsgewijze procedure voor generieke koppelingsmethoden toe te passen. De berekening van het totale golfveld rond de GECs gebeurt in vier stappen. Ten eerste wordt het invallende golfveld verkregen in MILDwave zonder enige GECs. Ten tweede wordt het verstoorde golfveld dicht bij de WECs berekend in NEMOH in een beperkt NEMOH numeriek domein. Ten derde wordt het verstoorde golfveld van NEMOH geïntroduceerd in MILDwave via een koppelingsinterface en gepropageerd in het "far field". Uiteindelijk wordt het totale golfveld verkregen als een superpositie van de invallende en verstoorde golfvelden in het MILDwave-numerieke domein.

De efficiëntie van het gekoppelde model om de informatie van de golfstructuur interactie solver over te brengen naar de golfpropagatie solver wordt gevalideerd voor verschillende golfcondities en GEC types. De validatie wordt uitgevoerd door de MILDwave-NEMOH gekoppelde modelresultaten te vergelijken met NEMOH-resultaten. Daarnaast wordt de accuraatheid van de koppelingsmethode beoordeeld door een experimentele validatie met de GEC park experimentele data van het WECwakes-project.

De numerieke en experimentele validatie van het gekoppeld model bewijst dat dit model in staat is om de informatie van NEMOH correct over te brengen naar het MILDwave numerieke domein, zowel voor langkruinige als kortkruinige onregelmatige golven. Kleine verschillen worden gevonden in de koppelingsinterface wanneer een groot aantal GECs worden gemodelleerd. Desalniettemin, het effect van deze verschillen in het "far field" is minimaal.

Aangezien MILDwave correct kusttransformaties modelleert, is het mogelijk om de "near-field" effecten, verkregen met NEMOH, in het "far-field" te propageren, over grote kustgebieden met variërende bathymetrie. Om de mogelijkheden van het gekoppeld model te tonen, is het toegepast op drie verschillende scenario's: twee met variërende bathymetrie onder onregelmatige langkruinige golven en één onder onregelmatige kortkruinige golven. De eerste twee toepassingen tonen het belang

van verondieping en refractie bij het bestuderen van “far field” effecten van GEC-parken. De derde toepassing geeft een verschil aan in het gedrag van de grootte van de “far-field” effecten tussen langkruinige en kortkruinige onregelmatige golven. Dit wijst op een lagere impact op de kustlijn in de luwte van WEC-parken onder de invloed van kortkruinige onregelmatige golven. Desalniettemin heeft het gekoppeld model beperkingen. De toepasbaarheid ervan is beperkt tot lineaire en zwak niet-lineaire golfomstandigheden. Het model is niet in staat om GECs onder extreme golfcondities te modelleren. Bovendien kan de computationele kost aanzienlijk toenemen bij het modelleren van lang- en kortkruinige onregelmatige golven over realistische bathymetriën. Verder neemt de numerieke performantie van het model af wanneer het aantal gemodelleerde GECs wordt verhoogd. Om de computationele kost te verminderen werd het gekoppeld model geparalleliseerd met een Pythongebaseerde code. De parallelisering van de code heeft bewezen de simulatietijd aanzienlijk te kunnen verminderen.

Summary

Ocean waves are an enormous marine renewable energy source with the potential to contribute to a reduction in the world's fossil fuel dependency. Wave energy can be converted into usable electricity using wave energy converters (WECs). WECs capture the kinetic and potential energy of the waves, transferring it to a power take-off (PTO) system that converts it to electricity. To date a large number of WECs are under development, with only a few of them reaching pre-commercial stage. Additionally, for wave energy projects to be economically viable a large number of WECs will have to be deployed and arranged in WEC farms to produce large amounts of electricity.

The deployment of a lot of WECs in the ocean brings a different number of challenges. Firstly, it requires a high economical investment both during installation, operation and maintenance of the project. Secondly, WECs are exposed to heavy storms. Therefore they need to be designed to survive subjected to heavy wave impacts that can damage them, reducing maintenance cost and the replacement of units. Finally, WEC farm projects entail a series of environmental effects that cannot be overlooked. A particular concern for the marine renewable energy sector is the potential impact of the WEC farm power absorption in the redistribution of the wave energy in the lee of the WEC farm.

The overall wave power absorption of a WEC farm will affect the surrounding wave field creating areas of increased and reduced wave energy (areas of increased and decreased wave height) in the lee of the WEC farm. The hydrodynamic problem of wave power absorption between the WECs within a farm, and between the WECs and the incident wave field is characterized by three different problems namely: wave reflection, diffraction and radiation. The superposition of the reflected, diffracted and radiated wave fields results in a perturbed wave field. The perturbed wave field close to the WECs of the farm caused both by WEC–WEC and wave–WEC interactions is often referred to in literature as the "near field" effects while the propagation of this perturbed wave field at a larger distance from the WEC farm e.g., in the coastal zone, is referred to as the "far field" effects.

Modelling the perturbed wave field around a farm of WECs is a complex process. Usually "near field" and "far field" effects are approached separately due to the difficulties in using a single numerical model to obtain a fast and accurate solution for both effects. To rectify these limitations, a generic coupling methodology for coupling wave-structure interaction solvers and wave propagation models has been developed in the recent years. Coupling models with different resolutions allows

higher precision in the estimation of "far field" effects. A wave-structure interaction solver is used to obtain an accurate solution of the wave field in a limited area around the WECs of a farm and resulting wave field is propagated further away using a wave propagation model.

The aim of this doctoral research is to apply this generic coupling methodology between the linear wave propagation model MILDwave and the linear wave-structure interaction solver NEMOH. The resulting coupled model is capable of cost-efficient computational time simulations that can contribute to studying the coastal impacts of WEC farms. It can be used to investigate the reduction of wave energy reaching the coastlines, the co-location of wave energy farms as protection for off-shore wind projects and the effects on coastal sediment transport combining the developed numerical tool with existing morphodynamic models.

The MILDwave-NEMOH coupled model has been developed by applying an existing generic coupling methodology step-by-step procedure. The calculation of the total wave field around the WECs is performed in four steps. Firstly, the incident wave field is obtained in MILDwave without any WECs. Secondly, the perturbed wave field close to the WECs is calculated in NEMOH in a restricted NEMOH numerical domain. Thirdly, the perturbed wave field from NEMOH is introduced in MILDwave through a coupling interface and propagated in the "far field". Finally the total wave field is obtained as a superposition of the incident and perturbed wave fields in the MILDwave numerical domain.

The efficiency of the coupled model to transfer the information from the wave-structure interaction solver into the wave propagation model is validated for different wave conditions and WEC types. The validation is performed comparing the MILDwave-NEMOH coupled model results to NEMOH results. Additionally, the accuracy of the coupled model is assessed by performing an experimental validation with the WEC array experimental data obtained from the WECWakes project.

The numerical and experimental validation of the coupled model proves that it is capable of correctly transferring the information from NEMOH into the MILDwave numerical domain for regular waves, and long-crested, and short-crested irregular waves. Small discrepancies are found close to the coupling interface when a large number of WECs are modelled. Nevertheless, the effect of this discrepancies in the "far field" is minimal.

As MILDwave correctly models coastal transformations, it is possible to propagate the "near field" effects obtained with NEMOH in the "far field" over large coastal areas with varying bathymetries. To show the capabilities of the coupled model, it has been applied in three different case scenarios: two with varying bathymetries under irregular long-crested waves, and one under the action of irregular short-crested waves. The first two applications show the importance of shoaling and refraction when studying "far field" effects of WEC farms. The third application indicates a difference in the behaviour in the "far field" effects magnitude between long-crested and short-crested irregular waves. This points out to a lower impact in the coastline of WEC farms under the effect of short-crested irregular waves.

Nevertheless, the coupled model has limitations. Its applicability is limited to linear and weakly non-linear wave conditions. It is not capable of model WECs

subjected to extreme wave conditions. The computational time can increase considerably when modelling long-crested and short-crested irregular waves over realistic bathymetries. Additionally, the model numerical performance is reduced when the number of WECs modelled is increased. To reduce the computational time effort, the coupled model has been parallelized using a Python based code. The code parallelization has proven to significantly decrease the simulation time.

List of relevant publications

Part of the research used in this PhD has been published in journals and conference proceedings. A list of the relevant publications is given below:

A1 Journal papers:

Verao Fernandez, G., Stratigaki, V., Vasarmidis, P., Balitsky, P., and Troch, P. (2019). "Wake Effect Assessment in Long- and Short-crested Seas of Heaving-point Absorber and Oscillating Wave Surge WEC Arrays." *Water* 11 (6): 1–25. doi: 10.3390/w11061126.

Balitsky, P., Quartier, N., Stratigaki, V., Verao Fernandez, G., Vasarmidis, P., and Troch, P. (2019). "Analysing the Near-field Effects and the Power Production of Near-shore WEC Array Using a New Wave-to-wire Model." *Water*. 11 (6), 1–30, doi: 10.3390/w11061137.

Verao Fernandez, G., Stratigaki, V., and Troch, P. (2019). "Irregular Wave Validation of a Coupling Methodology for Numerical Modelling of Near and Far Field Effects of Wave Energy Converter Arrays." *Energies* 12 (3). doi: 10.3390/en12030538.

Balitsky, P., Quartier, N., Verao Fernandez, G., Stratigaki, V., and Troch, P. (2018). "Analyzing the Near-field Effects and the Power Production of an Array of Heaving Cylindrical WECs and OSWECs Using a Coupled hydrodynamic-PTO Model." *Energies* 11 (12). doi: 10.3390/en11123489.

Verao Fernandez, G., Balitsky P., Stratigaki, V., and Troch, P. (2018). "Coupling Methodology for Studying the Far Field Effects of Wave Energy Converter Arrays over a Varying Bathymetry." *Energies* 11 (11). doi: 10.3390/en11112899.

Balitsky, P., Verao Fernandez, G., Stratigaki, V., and Troch, P. (2018). "Assessment of the Power Output of a Two-array Clustered WEC Farm Using a BEM Solver Coupling and a Wave-propagation Model." *Energies* 11 (11): 1–23. doi: 10.3390/en11112907.

Conference proceedings:

Verao Fernandez, G., Balitsky, P., Vasarmidis, P., Quartier, N., Stratigaki, V., and Troch, P. (2019). ““Far Field” effects of arrays of wave energy converters in Irregular Long –Crested and Short-Crested Waves: a Comparative Study.” In *Proceedings of the 13th Wave and Tidal Energy Conference*. In Press.

Verao Fernandez, G., Balitsky P., Tomey Bozo, N., Stratigaki, V., and Troch, P. (2017). “Far-field Effects by Arrays of Oscillating Wave Surge Converters and Heaving Point Absorbers : a Comparative Study.” In *Proceedings of the 12th Wave and Tidal Energy Conference*, 1030–1039. ISSN: 2309-1983.

Balitsky, P., Verao Fernandez, G., Stratigaki, V., and Troch, P. (2017). “Assessing the Impact on Power Production of WEC Array Separation Distance in a Wave Farm Using One-way Coupling of a BEM Solver and a Wave Propagation Model.” In *Proceedings of the 12th Wave and Tidal Energy Conference*, 1176–1186. ISSN: 2309-1983.

Balitsky, P., Verao Fernandez, G., Stratigaki, V., and Troch, P. (2017). “Coupling Methodology for Modelling the Near-field and Far-field Effects of a Wave Energy Converter.” In *Proceedings of the ASME 36th International Conference on Ocean, Offshore and Arctic Engineering*, 1–10. ISBN: 978-0-7918-5772-6, doi: 10.1115/OMAE2017-61892.

Verao Fernandez, G., Balitsky, P., Stratigaki, V., and Troch, P. (2017). “Coupling Methodology for Modelling the Near Field and Far Field Effects of an Array of Wave Energy Converters.” In *VLIZ Special Publication 97*. ISSN: 1377-0950.

Verao Fernandez, G., Balitsky, P., Stratigaki, V., and Troch, P. (2018). “Validation of a Coupling Methodology for Numerical Modelling of Near and Far Field Effects of Wave Energy Converter Arrays Using the MILDwave and NEMOH Models, Based on the WECwakes Experimental Database.” In *VLIZ Special Publication 80*, 124–125. ISSN: 1377-0950

Chapter 1

Introduction

1.1 Background

In the past decades, the world has seen a major increase in the global energy demand, mainly driven by population rise and the economic growth of developing countries. Nowadays, more than 83 % of the world energy supply is still based on fossil fuels, which high CO_2 emissions are significantly contributing to the unequivocal warming of the world's climate. Climate change and the eventual shortage of fossil fuels have become a major concern for most of the world's governments as it shows the sign of the Kyoto protocol, the 2020 targets of the European Union or the recent Paris Summit. All these agreements show that there is a global consensus on the need to switch to more sustainable energy sources in order to lessen global warming and prevent a shortage in the energy supply.

In this context, renewable energy sources appear as the alternative to fossil fuels and nuclear power, which has also a finite life and rises numerous safety concerns among the population. Typically, the main renewable energy sources studied have been hydro-power, onshore wind, solar power and biomass (Leijon et al. (2003)). Nevertheless, the oceans are a vast energy resource powered by the sun and in the past decades an increased attention has been drawn towards them. Renewable energy from the ocean, commonly know as Marine Renewable Energy, is meant to play a major role in reducing the world's fossil fuels dependency (Greaves and Iglesias (2018)). Among the different types of Marine Renewable Energy such as offshore wind, tidal, and thermal energy; ocean waves appear as an enormous energy source.

Ocean waves are generated by the wind blowing over the sea. When the wind blows for a certain period of time over the water surface, there is a transmission of mechanical energy between the wind and the water creating waves. These waves then travel in the wind blowing direction over long distances with a minimal energy loss reaching the coast. This means that ocean waves are virtually an unlimited energy resource that has been estimated by Mørk et al. (2010) in 32000 TWh per year.

It is clear that wave energy has a huge potential to contribute to the renewable

energy mix. It is a practically endless and predictable energy source, it has reduced environmental impacts, and almost 40 % of the world's population lives in 100 km from the coast. Despite its potential, the exploitation of wave energy is a complex and expensive process that takes place in a rough environment. There are or have been at least 157 Wave Energy Converters (WECs) technologies under development (European Marine Energy Centre (2019)), with none of them yet reaching commercial stage. Therefore, wave energy has been considered not economically viable due to the lack of maturity of the sector. According to Greaves and Iglesias (2018) the present status of wave energy resembles that of wind energy in the 1980s.

Nevertheless, if a breakthrough would happen in the wave energy industry with any of the aforementioned WECs converging to one or a few feasible designs, analogously to the wind energy sector, wave energy will play a key role in contributing to the world's electrical grid. Yet, to have economically viable wave energy projects many WECs will have to be deployed in clusters, also named as WEC arrays, and arranged in so called wave farms to produce large amounts of electricity. In this research, the term WEC farm refers to a scale comparable to a wind farm, while a WEC array is a small group of WECs closely spaced within the farm. The overall wave power absorption of a WEC farm will affect the surrounding wave field creating areas of increased and reduced wave energy (areas of increased and decreased wave height) around the WEC farm. These areas can have a positive or negative impact on the bathymetry and other sea users. For example, they can act as coastal protection reducing the amount of wave energy reaching the shoreline.

The hydrodynamic problem of wave power absorption between the WECs within a farm, and between the WECs and the incident wave field is characterized by two different problems, namely: wave diffraction and radiation. The diffraction problem studies the change in direction of the incident wave field due to the presence of the WECs. The radiation problem refers to the generation of a radiated wave field around the WECs due to their oscillations caused by the incident wave field.

The superposition of the diffracted and radiated wave fields results in the perturbed wave field. The perturbed wave field close to the WECs of the farm caused both by WEC-WEC and wave-WEC interactions is often referred in literature as the "near field" effects, illustrated in Figure 1.1. The propagation of this perturbed wave field at a larger distance from the WEC farm e.g. in the coastal zone, is referred as the "far field" effects, (Stratigaki (2014); Troch and Stratigaki (2016)).

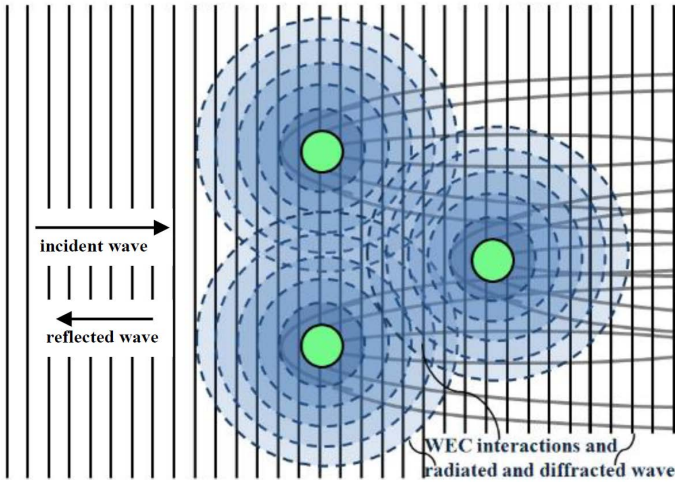


Figure 1.1: Visual representation of the "near field" effects between neighbouring oscillating WECs (represented by solid circles) in a WEC array under incident waves. Figure adopted from Stratigaki (2014).

Substantial numerical research has been carried out to study the "near field" effects in WEC farms, focusing on optimizing the WEC farm lay-out and maximizing the power output by employing wave-structure numerical models. On the other hand, "far field" effects are traditionally studied in a computationally cost-efficient way using wave propagation models. Nevertheless, it is clear that modelling the perturbed wave field around a farm of WECs is a complex process. Usually "near field" and "far field" effects are approached separately due to the difficulties in using a single numerical model to obtain a fast and accurate solution for both of them.

To rectify these limitations, different coupling methodologies between wave-structure interaction solvers and wave propagation models have been developed in the recent years Stratigaki (2014); Verbrugghe et al. (2017, 2018); Tomey-Bozo et al. (2018); Rijnsdorp et al. (2018). This allows higher precision in the estimation of "far field" effects, by using a wave-structure interaction solver to obtain an accurate solution of the wave field in a limited area around the WECs of a farm and propagating this resulting wave field further away using a wave propagation model over a coastal zone.

Within this research, a one-way coupled model between the wave propagation model MILDwave (Troch and Stratigaki (2016); Troch (1998)) and the wave-structure interaction solver NEMOH (Babarit and Delhommeau (2015)) has been developed. This coupled model is based on the work of Stratigaki (2014), who first presented a coupling between a wave propagation model (MILDwave) and a wave-structure interaction solver (WAMIT (2006)), as well as the principles of the generic coupling methodology between any wave-structure interaction solver and any wave propagation model.

1.2 Numerical modelling of WECs

This section provides an overview of the state-of-the-art of WEC(s) (array) numerical modelling. An extensive review of existing numerical models is included in the book: "Numerical modelling of wave energy converters: state-of-the-art techniques for single devices and arrays" edited by Folley (2016a).

Nowadays, there is a wide range of numerical modelling techniques that can be used to study a WEC. Nonetheless, the key challenge is to identify which is the most suitable model for a particular case study or modelling objective. Typically, a model is chosen as a trade-off between the accuracy of the results and the computational time. For example, linear models can be suitable for studying operational conditions of WEC arrays, as it is possible to obtain fast and efficient solutions in trade of accuracy. While nonlinear models, which are much more computationally demanding, are more suitable for survivability studies where a higher accuracy is needed.

Another important aspect when identifying a suitable model is the model experimental validation. It is not possible to assess the accuracy and suitability of a model if it is not validated. To date, there are only a few WEC devices that have been deployed at full-scale for testing. Nonetheless, the data obtained within this studies are very limited and in most of the cases are not accessible to other researchers. An alternative to real data is the use of experimental tank testing, taking into account that the scale and laboratory effects will induce some differences between the experimental data-set and the full-scale model.

Within this research, WEC numerical models are identified based on the modelling objectives in models either used to simulate "near field" or "far field" effects of WEC(s) (arrays). The first are classified as wave-structure interaction solvers, while the latter as wave propagations models.

1.2.1 Wave structure interaction solvers

1.2.1.1 Semi-analytical array models

Semi-analytical techniques were the first approaches used to solve array interactions of simple WEC geometries including pioneering work from Budal (1977) and Falnes (1980) in the study of point absorbers. Starting from linear wave theory it is possible to explicitly obtain the mathematical formulation of the hydrodynamic interactions in a WEC array. Afterwards it is required to truncate an infinite series to allow computation in practice. Nevertheless, such is the convergence of these series that semi-analytical methods can allow efficient calculation of array interactions. Even though the computational power has increased significantly since semi-analytical methods were first used, these are still very efficient models that can be applied to perform preliminary simulations of WEC array modelling or to optimize WEC array layout configurations (Child and Venugopal (2010); Garcia Rosa et al. (2015); Götteman et al. (2018)).

1.2.1.2 Boundary elements methods

Boundary elements methods (BEMs) (also referred as panel methods) are numerical models based on potential flow theory that are used to estimate the hydrodynamic coefficients of added mass and hydrodynamic damping and the diffraction and excitation forces per unit of incident wave amplitude. BEM models can be solved in the frequency or the time-domain. Examples of frequency-domain BEM models can be found in Aquaplan (Delhommeau (1987)), WAMIT (WAMIT (2006)) and NEMOH (Babarit and Delhommeau (2015)). These models have been used to study layout optimization (Borgarino et al. (2012); Balitsky et al. (2017)) and "wake effects" of WEC arrays (Babarit (2013); Sismani et al. (2017)). The aforementioned numerical models, are suited to resolve more accurately the details of WEC (array) "near field" effects. However, they are not able to account for the physical processes that influence the "far field" effects such as wave propagation over a varying bathymetry and wave breaking. Furthermore, the numerical simulation time can increase considerably when increasing the number of WECs modelled and the size of the numerical domain.

As an alternative to frequency-domain models, time-domain BEM solvers offer a more realistic solution of the underlying working principles of a WEC. As presented in Ricci (2016) time-domain refers to the possibility of deterministically computing the dynamics of floating bodies directly in time, with no reference to the properties of the process. They offer the opportunity to implement realistic power take-off configurations, WEC control strategies and moorings, which typically have a nonlinear behaviour. On the other hand, they are much more computationally demanding than a frequency-domain approach.

1.2.1.3 Nonlinear models

In recent years, the use of nonlinear numerical models based on Computational Fluid Dynamics (CFD) and Smoothed Particle Hydrodynamics (SPH) for WEC modelling has increased as the available computational power has incremented significantly. CFD numerical models solve the fully nonlinear Navier-Stokes equations in three dimensions with the inclusion of appropriate turbulence closure models. CFD models can represent the hydrodynamics of a WEC at high accuracy. They are suitable to study highly nonlinear problems such as wave breaking over a WEC (Devolder et al. (2018)), WEC subjected to extreme wave conditions (Ransley et al. (2017)) or wave-to-wire modelling (Penalba et al. (2017)), where nonlinearities, viscosity and turbulence effects play a major role. SPH models, also known as Lagrangian mesh-less methods, have been applied successfully in WEC array modelling (e.g. by Verbrugge et al. (2018); Crespo et al. (2015, 2017)). SPH uses particles moving inside the computational domain instead of grid cells. The physical properties of the particles are calculated as a weighted average of the neighbouring particles. SPH is suitable for solving problems with large deformations and distorted free surfaces. Nonetheless, the use of these models is restricted to a small spatial and temporal scale and to an even more limited number of WECs, which makes them not suitable to study WEC (array) "far field" effects in a large numerical domain due to the high computational cost.

1.2.2 Wave propagation models

1.2.2.1 Phase-averaging wave propagation models in array modelling

Phase-averaging wave propagation models, also called wave propagation spectral models, have been used extensively to model wave propagation and to study the wave energy resource (Iglesias and Carballo (2010); Rusu (2018)) at large scales. Spectral models consider the waves as an energy spectrum and their mathematical formulation is based on the conservation of energy. The generation/dissipation of wave energy is defined by a source term, included in the wave action equation used to solve wave propagation (a more detailed description of the underlying theory can be found in Folley (2016b)). Therefore, a WEC can be represented by modifying the initial source term. However, it is not possible for the phase-averaged wave propagation model to determine how the WEC changes the wave action, but it can be used to estimate which impact the WEC has on the surrounding wave conditions.

In Millar et al. (2007); Carballo and Iglesias (2013); Iglesias and Carballo (2014); Abanades et al. (2014); Venugopal and Smith (2007); Chang et al. (2016); Stokes and Conley (2018) the wave field in the lee of a WEC array is studied by considering the WECs of the array as "obstacles" with a fixed transmission (and thus wave power absorption) coefficient. Using the same methodology, Rusu and Guedes Soares (2013); Rusu and Diaconu (2014); Bento et al. (2014); Onea and Rusu (2016); Rusu and Onea (2016) studied the coastal impacts of WEC arrays operating in the near shore. In all this studies, the fixed transmission coefficient has to be calculated either using a different numerical model like in Millar et al. (2007) or by wave tank testing as in Iglesias and Carballo (2014). In spite of that, without experimental validation it is difficult to assess the accuracy of these models. As pointed out in Folley (2016b) these transmission coefficients depend on the wave frequency, wave direction, and amplitude. To overcome this limitation Smith et al. (2012) improved the fixed transmission coefficient source term introducing a frequency and direction dependency. Nevertheless, the simplified parametrization of the wave power absorbed by WECs does not take into account the wave-structure interactions of diffraction and radiation of the different WECs modelled as indicated by Tuba Özkan-Haller et al. (2017). This inaccuracy may lead to an overestimation or underestimation of the WEC farm power absorption and consequently an unrealistic estimation of the "far field" effects in the coastal zone.

Phase-averaging wave propagation models have two limitations when modelling "near field" effects of WEC arrays. The first one, is intrinsic to the model itself where all the array interactions are modelled based on a phase-averaged assumption. Phase relationship between the WECs in an array has an impact on the array interactions, therefore it is not possible to accurately model the near field, especially for closely spaced WEC arrays. The second limitation, is that the calculation of the transmission coefficient requires the use of another model. Therefore the phase-averaging wave propagation model relays not only on its own accuracy but on the accuracy of a second model when solving the hydrodynamic interactions of WECs.

1.2.2.2 Phase-resolving wave propagation models in array modelling

In a similar way to phase-averaging wave propagation models, Beels et al. (2010a) and Stratigaki et al. (2011) used the time-dependent mild slope equation model, MILDwave, to study "far field" effects of WEC arrays simplifying each WEC as a wave power absorbing obstacle. The WEC is implemented in the model using the sponge layer technique (Troch and Stratigaki (2016)) assigning to an array of cells a given degree of reflection, absorption and transmission. By changing the numerical value of this coefficients in each cell or the extent of the grid cells it is possible to replicate the "far field" impact that the WEC(s) (array) will have on the surrounding wave conditions. The sponge layer technique allows for a frequency-dependent coefficient implementation. Notwithstanding, in order to achieve a realistic solution of the "far field" impacts, the used coefficients need to be validated against numerical or experimental data. This induces the same limitations mentioned for phase-averaging propagation models: a simplified parametrization of the WECs can lead to an unrealistic estimation of the "far field" effects in the coastal zone, and the model is dependant on the accuracy of the experimental or numerical test used to tune the internal MILDwave grid cell coefficients.

1.2.3 Coupling methodologies for array modelling

Based on the different numerical modelling techniques illustrated in Sections 1.2.1 and 1.2.2 it is clear that WEC numerical modelling either focuses on the modelling of the "near field" effects at high fidelity but with high computational cost, or on the modelling of the "far field" effects with lower fidelity but low computational cost, in part due to the limitation of modelling both effects simultaneously using a single solver. On the one hand, wave-structure interaction solvers require a long computational time, which increases exponentially with the number of bodies of the WEC array and the size of the domain. Additionally, some BEM based solvers (WAMIT (2006); Babarit and Delhommeau (2015)) are limited to a constant bathymetry, other solvers like CFD or SPH will increase the computational time even more when considering irregular bathymetry. On the other hand, wave propagation models offer a lower computational time for modelling large domains to study the WEC array impact at a regional scale. Nonetheless the simplification in modelling the WEC hydrodynamic problem can lead to erroneous model conclusions.

Lately, to overcome these limitations wave-structure interaction solvers and wave propagation models have been combined to perform accurate simulations of both "near" and "far" field effects of WEC arrays. These coupled models combine the strength of each numerical model to perform simulations in an accurate and cost-efficient manner. The wave-structure interaction solver is used to calculate the hydrodynamic interactions in a small domain nested in the wave propagation model, achieving an accurate solution of the "near field" effects at a reasonable computational time. Afterwards, the "near field" information is transferred to the wave propagation model that calculates the wave propagation over a large domain with minimal computational effort.

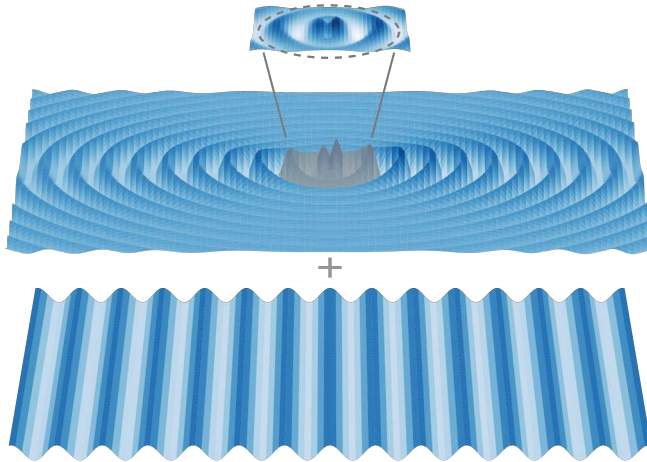


Figure 1.2: Visualization of the generic coupling methodology first introduced by Stratigaki et al. (2014). Figure adopted from Verbrugghe et al. (2018).

The first generic coupling methodology for modelling WEC arrays was introduced by Stratigaki et al. (2014). This methodology has been then adapted and applied to obtain different coupled models using one-way and two-way couplings, respectively. In one-way coupled models there is information transfer in one direction only, where each numerical model is run independently. Examples of such studies, which present linear simulation of "far field" effects of WEC farms by coupling a wave propagation model and a BEM solver, are carried out by Stratigaki (2014); Troch and Stratigaki (2016); Charrayre et al. (2014); Balitsky et al. (2017); Verbrugghe et al. (2017); Bozo et al. (2017). Alternatively, in two-way coupled models both numerical models are run at the same time with a two-way transfer of information between them. Examples of two-wave coupled models are provided by Verbrugghe et al. (2018) who demonstrated the coupling of a nonlinear wave propagation model with an SPH wave-structure interaction solver, or by Rijnsdorp et al. (2018) who simulated a submerged buoy using a non-hydrostatic wave-flow model implemented in the wave propagation model SWASH (Zijlema et al. (2011)).

1.3 Knowledge gaps

Based on the state of the art of WEC array modelling the following knowledge gaps have been identified:

1. There is a lack of numerical tools to model "far field" effects of WEC arrays over realistic bathymetry
2. No coupling has been performed yet to model WEC array "far field" effects under the action of short-crested waves

3. No experimental validation has been performed to date to determine the accuracy of a one way linear coupled model in modelling "near field" and "far field" effects of WEC arrays under irregular waves
4. There is a lack of studies estimating the "far field" effects of WEC arrays with a direct calculation of the WEC hydrodynamics

1.4 Objectives and outline

Based on the literature review included in Section 1.2 and the knowledge gaps identified in Section 1.3, the aim of this research is to:

Develop and validate a numerical tool that can provide an understanding of WEC array "far field" effects over realistic bathymetries under regular, long-crested and short-crested wave conditions.

The underlying objectives within this research are to:

1. Develop a coupled model between the wave propagation model MILDwave and the wave-structure interaction solver NEMOH.
2. Validate the developed coupled model using numerical and experimental data
3. Simulate WEC array "far field" effects under irregular short-crested wave conditions
4. Simulate WEC array "far field" effects over a varying realistic bathymetry

In order to achieve these goals an extensive research has been performed and documented in this manuscript. Chapter 1 provides a short overview of the state-of-the-art and problem statement, knowledge gaps are identified and the research aim and objectives are presented. In Chapter 2, an overview of the theoretical background required to fully understand the numerical models employed is given. Chapter 3 presents the linear coupled model between the mild-slope wave propagation model MILDwave and the BEM solver NEMOH. The generic coupling methodology used is explained in detail, including a complete description of the coupling methodology implementation and a numerical validation of the transfer of information between the two models. Next, the MILDwave NEMOH coupled model is validated against existing WEC array experimental data in Chapter 4. Chapter 5 includes the application of the developed MILDwave-NEMOH coupled model to study WEC array "far field" effects over a varying bathymetry, for a realistic bathymetry and under short-crested irregular waves. Finally, the findings of this research are summarized in Chapter 6.

Additionally, Appendix A presents the source code of the MILDwave-NEMOH coupled mode developed by the author of this manuscript. Appendix B includes the full numerical validation fo the MILDwave-NEMOH coupled model against NEMOH, while Appendix C provides the full MILDwave-NEMOH experimental validation.

Chapter 2

Theoretical Background

2.1 Linear wave theory

2.1.1 Fundamentals

Linear wave theory, also known as Airy wave theory, is the core element to describe ocean waves. In this section, linear wave theory will be discussed step by step using (Sorensen (1978)). It provides a mathematical description of the flow corresponding to the propagation of a wave as a sinusoidal variation of the water surface elevation. Even though there are limitations to its applicability, linear wave theory is useful when the following assumptions are met :

1. The flow is irrotational.
2. The water is homogeneous and incompressible, and surface tension is neglected.
3. The sea bed is stationary, impermeable and horizontal.
4. The pressure along the air-sea interface is constant.
5. The wave height is small compared to the wavelength and the water depth.

A simple, periodic wave over a horizontal sea bed, as seen in Figure 2.1 is represented by its x (spatial) and t (temporal) variables, which combined, correspond to the wave phase, $\varphi = kx - \omega t$. The highest point of a wave is known as the wave crest while the lowest point is known as the trough. A wave can be completely characterized by its wave height, H , wave period, T , wavelength, L and water depth, d . H is the distance between the crest and the trough, T is the time corresponding to the passing of two consecutive wave crests or wave troughs at a given location, and L corresponds to the distance between two consecutive wave crests or wave troughs.

Other important parameters can be derived from H , L , and T : the wave amplitude, a ; the wave celerity, C ; the wave number, k ; the wave angular frequency,

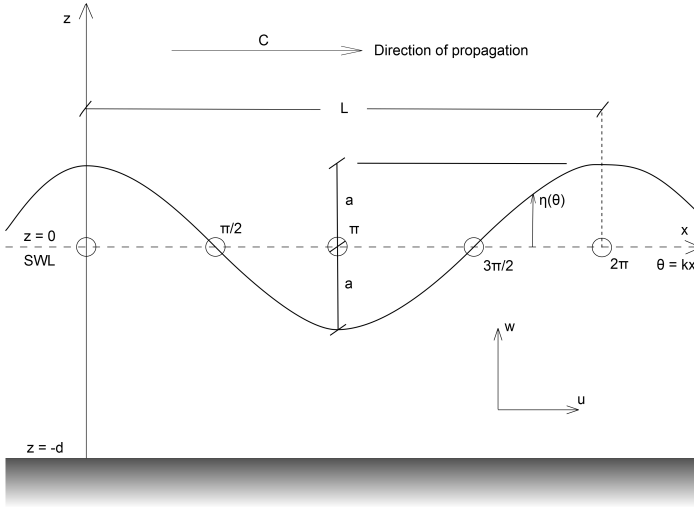


Figure 2.1: Definition of wave parameters over a sinusoidal wave (Figure adopted from Verbrugge (2018)).

ω ; and the wave steepness, ϵ . $a = \frac{H}{2}$ corresponds to the distance between the wave crest and the still water level (SWL), $C = \frac{L}{T}$ is the velocity at which the wave travels and $k = \frac{2\pi}{L}$, $\omega = \frac{2\pi}{T}$ and $\epsilon = \frac{H}{L}$ are dimensionless parameters, often used to describe the wave behaviour.

Following the aforementioned assumptions in the domain shown in Figure 2.1 it is possible to develop the linear wave theory. The assumption of irrotational flow allows to characterize the wave propagation flow in terms of the velocity potential $\phi(x, z, t)$, a scalar function whose partial derivatives in x and z correspond to the horizontal, u , and vertical, w , particle velocities:

$$u = \frac{\partial \phi}{\partial x}, \quad (2.1)$$

$$w = \frac{\partial \phi}{\partial z}. \quad (2.2)$$

Under the assumption of incompressible flow the continuity equation then becomes:

$$\frac{\partial u}{\partial x} + \frac{\partial w}{\partial z} = 0. \quad (2.3)$$

It follows that in the fluid domain the velocity potential must satisfy the second-order partial differential equation, known as the Laplace equation:

$$\frac{\partial^2 \phi}{\partial x^2} + \frac{\partial^2 \phi}{\partial z^2} = 0. \quad (2.4)$$

To solve the partial differential equation in the fluid domain, boundary conditions need to be defined at the sea bed and the free surface. Firstly, at the sea bed there is no flow perpendicular to it, thus the vertical velocity has to be zero at all time instants giving the sea bed boundary condition (BBC):

$$w(x, z = -d, t) = \frac{\partial \phi}{\partial z}(x, z = -d, t) = 0. \quad (2.5)$$

Secondly, at the free surface there is a kinematic boundary condition (KSBC) that forces a fluid particle at the free surface to remain at the free surface at all time instants:

$$w = \frac{\partial \eta}{\partial t} + u \frac{\partial \eta}{\partial x}, \quad (2.6)$$

where η is the surface elevation. And thirdly, the pressure along the air-sea interface has to be constant yielding the dynamic boundary condition (DSBC). At the surface where the atmospheric pressure is assumed to be constant and equal to zero the DSBC can be derived from the Bernoulli equation and becomes:

$$\frac{1}{2}(u^2 + w^2) + g\eta + \frac{\partial \phi}{\partial t} = 0. \quad (2.7)$$

There is no complete solution for Equation 2.4 applying these boundary conditions. However, assuming that the SWL line is close to the wave surface elevation and linearising the KSBC and the DSBC by applying them at the SWL ($\eta = 0$) instead of applying them at the surface elevation. Then Equation 2.6 yields:

$$w = \frac{\partial \eta}{\partial t}, \quad (2.8)$$

and Equation 2.7:

$$g\eta + \frac{\partial \phi}{\partial t} = 0. \quad (2.9)$$

Employing the Laplace equation, the BBC, and the linearised DSBC it is possible to derive the velocity potential for linear wave theory:

$$\phi(x, z, t) = \frac{ag \cosh(k(z+d))}{\omega \cosh(kd)} \cos(\omega t - kx), \quad (2.10)$$

where x and z are the horizontal and vertical particle co-ordinates, t is the time and g is the acceleration of gravity. Introducing the velocity potential into

the linearised DSBC with $z = 0$ the equation of the water surface profile can be determined as:

$$\eta(x, t) = \frac{H}{2} \cdot \cos\left(\frac{2\pi}{L}x - \frac{2\pi}{T}t\right). \quad (2.11)$$

Introducing Equation 2.10 in Equations 2.1 and 2.2 it is possible to obtain the horizontal, u , and vertical, w , wave particle velocities:

$$u(x, z, t) = \frac{H}{2}\omega \frac{\cosh(k(d+z))}{\sinh(kd)} \cos(kx - \omega t), \quad (2.12)$$

$$w(x, z, t) = \frac{H}{2}\omega \frac{\sinh(k(d+z))}{\sinh(kd)} \sin(kx - \omega t). \quad (2.13)$$

Note that each velocity component consists of three parts: the surface deep water particle $\frac{\pi H}{T}$, an hyperbolic variation of the water velocity decreasing with depth and a phase term dependent on the horizontal and vertical position and time. The horizontal and vertical components of the wave velocity are in 90° out of phase.

The horizontal component of a particle acceleration a_x may be written as:

$$a_x = u \frac{\partial u}{\partial x} + w \frac{\partial u}{\partial z} + \frac{\partial u}{\partial t}, \quad (2.14)$$

where the first two terms are the convective acceleration and the third term is the local acceleration. For small amplitude waves the convective acceleration is of the order of the wave steepness and therefore it can be neglected when determining the particle acceleration. This yields the vertical, a_x and horizontal, a_z components of the acceleration:

$$a_x(x, z, t) = \frac{H}{2}\omega^2 \frac{\cosh(k(d+z))}{\sinh(kd)} \sin(kx - \omega t), \quad (2.15)$$

$$a_z(x, z, t) = \frac{H}{2}\omega^2 \frac{\sinh(k(d+z))}{\sinh(kd)} \cos(kx - \omega t). \quad (2.16)$$

It can be seen that the wave acceleration also has the same hyperbolic decrease with water depth as the wave velocity and it has a phase shift of 90° with respect to it.

By integrating u and w in Equations 2.12 and 2.13 with respect to time, it is possible to obtain the particle positions in the horizontal, ζ and vertical, ϵ coordinates:

$$\zeta = -\frac{H}{2} \frac{\cosh(k(d+z))}{\sinh(kd)} \sin(kx - \omega t), \quad (2.17)$$

$$\epsilon = \frac{H}{2} \frac{\sinh(k(d+z))}{\sinh(kd)} \cos(kx - \omega t). \quad (2.18)$$

These equations indicate that the particles are moving in circular orbits with the radius of the orbit decreasing exponentially with the water depth. The pressure beneath the regular surface wave is given by :

$$p = -\rho g z + \frac{\rho g H}{2} \frac{\cosh k(d+z)}{\cosh(kd)} \cos(kx - \omega t), \quad (2.19)$$

where ρ is the water density. If now, Equation 2.11 is rewritten as:

$$\eta(x, t) = a \cdot \cos(kx - \omega t). \quad (2.20)$$

And combined with the DBSC and the KSBC conditions the well know dispersion equation can be obtained:

$$\omega^2 = gk \tanh(kd). \quad (2.21)$$

The dispersion equation can be rearranged to provide C and L in terms of T :

$$C = \frac{gT}{2\pi} \tanh\left(\frac{2\pi d}{L}\right), \quad (2.22)$$

$$L = \frac{gT^2}{2\pi} \tanh\left(\frac{2\pi d}{L}\right). \quad (2.23)$$

Equations 2.21 and 2.23 combined are known as the dispersion relationship. It can be seen that for a given T there is a unique L that satisfies the dispersion relationship. Thus for a spectrum of waves travelling in the same direction, waves having a longer T will travel faster than waves with lower T that will lag behind. This will generate an envelope of waves travelling at a different velocity than the individual wave components, known as the group velocity, C_g . The group velocity indicates the speed at which the wave energy propagates and it is given by equation:

$$C_g = \frac{C}{2} \left(1 + \frac{2kd}{\sinh 2kd}\right). \quad (2.24)$$

It can be demonstrated that when a wave propagates from the ocean to shore the wave period remains constant. On the contrary, other wave characteristics that include H , L , C , C_g , u , w , a_x , a_z , ζ and ϵ will change when travelling from deep water to the near shore area. Based on this variation it is possible to classify surface waves based on the dimensionless relative depth ratio, $\frac{d}{L}$, in deep, transitional and shallow water waves, respectively:

1. Deep water surface waves are propagating at a $\frac{d}{L} > 0.5$. Here, particle velocities and orbit dimensions are close to zero. Consequently, the waves do not interact with the sea bed, and the wave characteristics are independent from the water depth.
2. Transitional water surface waves are propagating between the range of $0.5 < \frac{d}{L} < 0.05$. Waves start interacting with the sea bed and wave characteristics depend both in the water depth and the wave period.
3. Shallow water surface waves are propagating at a range of $\frac{d}{L} < 0.05$. At these water depth conditions, the small amplitude theory yields that the wave parameters are independent on the wave period and they depend only on the water depth.

2.1.2 Wave energy

The total mechanical energy in a surface wave can be obtained as the sum of the kinetic and potential energies:

$$E = E_k + E_p, \quad (2.25)$$

where the kinetic energy, E_k , is the energy carried by the moving water particles, and the potential energy, E_p , originates from the water mass that is above the SWL (Figure 2.1).

E_k for a unit width of wave crest and for one wavelength is equal to:

$$E_k = \int_0^L \int_{-d}^0 \frac{1}{2} \rho dx dz (u^2 + w^2) = \frac{1}{16} \rho g H^2 L, \quad (2.26)$$

E_p is obtained by subtracting the potential energy of a mass of still water (with respect to the sea bed) from the potential energy of the wave form. As such, the potential energy solely due to the wave form is:

$$E_p = \int_0^L \rho g (d + \eta) \left(\frac{d + \eta}{2} \right) dx - \rho g L d \left(\frac{d}{2} \right) = \frac{1}{16} \rho g H^2 L. \quad (2.27)$$

Introducing Equations 2.26 and 2.27 in Equation 2.28 it is possible to obtain the total energy in a wave per unit crest width, E :

$$E = \frac{1}{8} \rho g H^2 L. \quad (2.28)$$

Both the kinetic and the potential wave energies are available from point to point along a wavelength. Nevertheless, a useful concept is the average energy per unit surface area or energy density given by:

$$\bar{E} = \frac{E}{L} = \frac{1}{8} \rho g H^2. \quad (2.29)$$

2.1.3 Wave power

The wave power P_{wave} is the wave energy per unit time transmitted in the direction of wave propagation. Wave power can be written as the product of the force acting on a vertical plane normal to the direction of the wave propagation times the particle flow velocity acting in this plane, integrated over the entire water depth, d :

$$P_{wave} = \int_0^T \int_{-d}^0 (p + \rho g z) u dz dt. \quad (2.30)$$

By inserting the dynamic pressure (Equation 2.19) and horizontal velocity (Equation 2.12) in Equation 2.30 and by rearranging, P_{wave} expressed per unit length of wave crest can be obtained as:

$$P = EC_g = \frac{1}{8} \rho g H^2 C_g. \quad (2.31)$$

2.2 Analysis of irregular waves

The analysis of irregular waves is important, as regular waves are hardly found in nature. Irregular waves can be studied as a superposition of a finite number of regular waves with different wave heights and periods. Two types of irregular waves can be found: long-crested and short-crested waves. In long-crested waves, the direction of each individual regular wave component is the same, and they are also referred as uni-directional waves. For short-crested waves, the wave components are typically multi-directional. The irregular wave analysis included in this Section has been performed based on the procedures outlined in Sabatier (2006).

Considering a time record, t_r , of the surface elevation of an irregular wave train (Figure 2.2) it is possible to define a single wave as the profile of the surface elevation between two consecutive zero-down crossings of the mean SWL. Therefore, a large number of waves with different wave heights and periods are identified on a time record. This short-term variations can be described statistically averaging all the individual wave heights and wave periods in the time record. In order for the averages to be representative of the wave train, the time record requires to be short enough to be statistically stationary but long enough to be representative of its characteristics. The commonly used compromise at the sea is to take recordings between 15 to 30 minutes.

There are two ways for describing irregular waves:

1. Through a time-domain analysis considering the wave train as a sequence of individual waves with different wave heights and periods.
2. Through a frequency-domain analysis considering the wave train as a sum of a large number of statistically independent, harmonic waves, with different wave heights and wave periods.

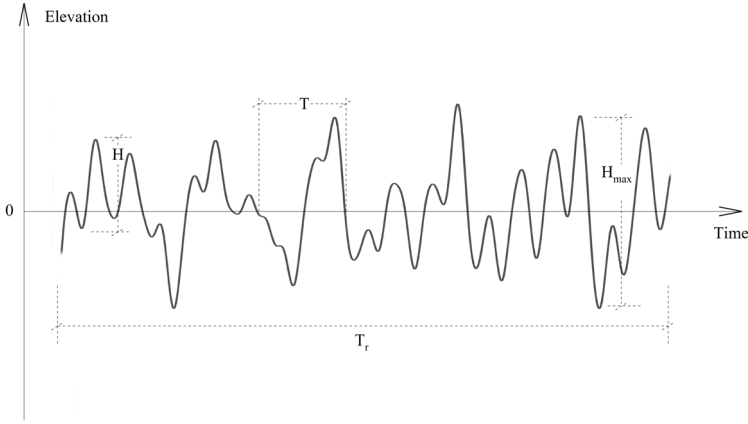


Figure 2.2: Irregular wave time record (Figure adapted from Verbrugge (2018)).

2.2.1 Time-domain analysis of irregular waves

The wave height of a wave is defined as the vertical distance between the highest and the lowest surface elevation of a wave. Considering a time record with N waves, it is possible to define the significant wave height, H_s , as the mean of the highest one-third of the waves in the time record:

$$H_s = \frac{1}{N/3} \sum_{l=1}^{N/3} H_l, \quad (2.32)$$

where, N is the total number of waves and H_l is the wave height of the l -th wave based on the wave heights. Another useful parameter for energy related calculations is the root-mean-square wave height, H_{rms} :

$$H_{rms} = \left(\frac{1}{N} \sum_{j=1}^N H_j^2 \right)^{1/2}, \quad (2.33)$$

where j is the sequence number of the waves in the record. The wave periods are characterized by their mean, also defined as the zero-crossing period:

$$T_0 = \frac{1}{N} \sum_{j=1}^N T_j^2, \quad (2.34)$$

where j is the sequence number of the waves in the record. In analogy with the significant wave height, the significant wave period, T_s , is defined as the mean

period of the highest one-third of the waves:

$$T_s = \frac{1}{N/3} \sum_{l=1}^{N/3} T_l. \quad (2.35)$$

2.2.2 Frequency-domain analysis of irregular waves

Frequency-domain analysis aims to describe ocean waves with a wave energy spectrum, decomposing the physical phenomena in individual frequency components. As it has already been mentioned in Section 2.2, irregular waves at a certain location can be constructed as a superposition of N regular waves with different wave amplitudes and wave frequencies (as shown in Figure 2.3):

$$\eta(t) = \sum_{j=1}^N a_j \cdot \cos(\varphi_j), \quad (2.36)$$

where a_j is the wave amplitude and φ_j is the wave phase of the j -th regular wave component.

By applying a Fourier analysis (Tucker and Pitt (2001)) it is possible to determine the amplitude and phases in Equation 2.36. If the problem is described in terms of the amplitude variance of each regular harmonic component, $a_j^2/2$, the amplitude variance can be converted into a spectral density variance by distributing $a_j^2/2$ over the wave frequency interval Δf_j at frequency, f_j . This has been

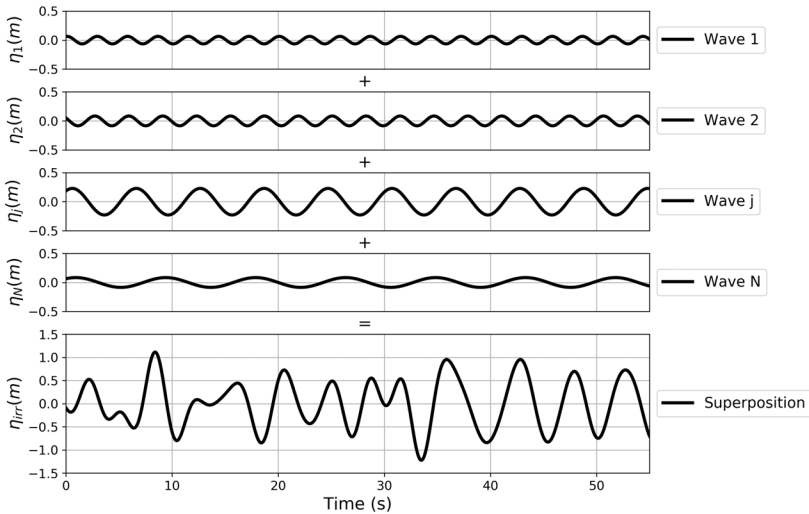


Figure 2.3: Irregular wave, η_{irr} as a superposition of N regular waves. η_1 is the surface elevation of the first regular wave component, η_j is the surface elevation of the j -th regular wave component and η_N is the surface elevation of the N -th regular wave component.

illustrated using Figures 2.4 and 2.5, respectively. Then, the total discrete variance density spectrum can be obtained as a summation of the variance density of each wave frequency component:

$$S^*(f_j) = \sum_{j=1}^N \frac{1}{\Delta f_j} \frac{a_j^2}{2}, \quad (2.37)$$

where $S^*(f_j)$ denotes the discrete variance density spectrum. In reality irregular waves are composed of infinity regular waves components. Thus, the continuous variance density spectrum, illustrated in Figure 2.6, is given when the frequency interval tends to 0:

$$S(f_j) = \lim_{\Delta f \rightarrow 0} \sum_{j=1}^N \frac{1}{\Delta f_j} \frac{a_j^2}{2}. \quad (2.38)$$

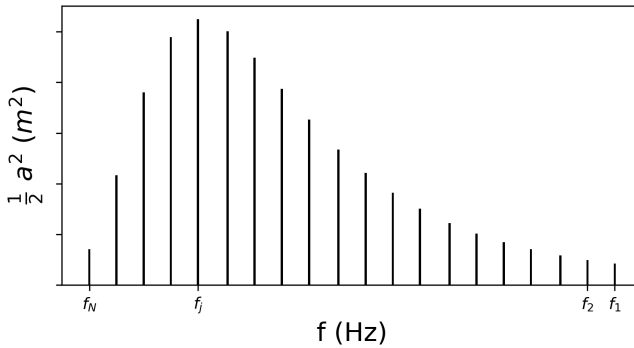


Figure 2.4: Illustration of the amplitude variance decomposition.

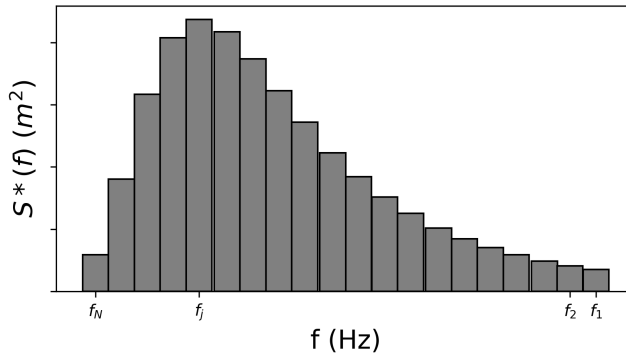


Figure 2.5: Illustration of the discrete variance density spectrum.

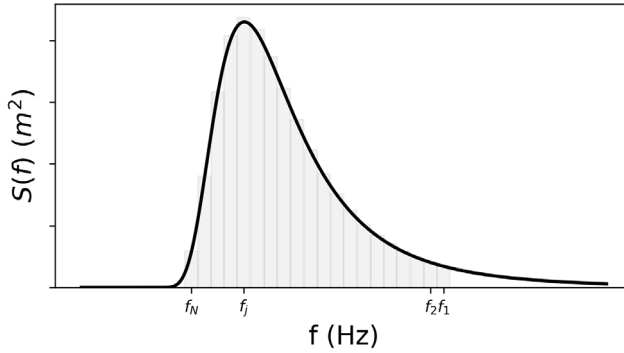


Figure 2.6: Illustration of the continuous variance density spectrum.

From the variance density spectrum it is possible to define several characteristic parameters:

1. n order moment m_n :

$$m_n = \int_0^{\infty} f^n S(f) df. \quad (2.39)$$

where f is the wave frequency and $S(f)$ is the variance density spectrum.

2. 0 order moment m_0 :

$$m_0 = \int_0^{\infty} S(f) df. \quad (2.40)$$

which corresponds to the area under the spectrum, and therefore the amplitude variance, σ , is given by:

$$\sigma = \sqrt{m_0}. \quad (2.41)$$

3. The significant wave height:

$$H_s \approx H_{m_0} = 4\sqrt{m_0}. \quad (2.42)$$

4. The peak period, T_p , defined as the period corresponding to the wave frequency with the highest spectral density, f_p :

$$T_p = \frac{1}{f_p} \quad \text{where} \quad f_p = f|_{S(f)=max}. \quad (2.43)$$

2.2.3 Construction of irregular waves from variance density spectrum

It is possible to construct a time series of surface elevation from the variance density spectrum. First order irregular waves can be obtained by superposing N regular wave components. The surface elevation can be obtained by:

$$\eta(t) = \sum_{j=1}^N a_j \cdot \cos(\varphi_j). \quad (2.44)$$

The amplitude of each component is obtained by:

$$a_j = \sqrt{2S(f_j)\Delta f}, \quad (2.45)$$

where $S(f_j)$ is the spectral density of the j -th wave component and Δf is the wave frequency interval:

$$\Delta f = \frac{f_{max} - f_{min}}{N}, \quad (2.46)$$

where f_{max} and f_{min} are the upper and lower limits of the frequency range. The wave phase is obtained by:

$$\varphi_i = kx - \omega t + \varphi_{rand}, \quad (2.47)$$

where k is the wave number, ω is the angular frequency and φ_{rand} is a random value between 0 and 2π .

There are different density spectra available in literature, but in this research the Pierson-Moskovitz and the JONSWAP spectrum are utilized. A Pierson-Moskovitz spectrum is typically used to describe fully developed sea states, while the JONSWAP spectrum is used to describe partially developed sea states.

The Pierson-Moskovitz irregular wave spectrum is defined by:

$$S_{P-M,j}(f) = \frac{B}{f_j^5} e^{-\frac{C}{f_j^4}}, \quad (2.48)$$

where,

$$\begin{aligned} B &= \frac{5}{16} \frac{H_s^2}{T_p^4}, \\ C &= \frac{5}{4} \frac{1}{T_p^4}. \end{aligned} \quad (2.49)$$

The JONSWAP irregular wave spectrum is defined by Equation 2.50:

$$S_{J-S}(f) = \alpha \frac{B}{f_j^5} e^{-\frac{C}{f_j^4}} * \gamma^\beta, \quad (2.50)$$

where,

$$\begin{aligned} \alpha &= \frac{0.0624}{0.23 + 0.0336\gamma - \left(\frac{0.185}{1.9+\gamma}\right)}, \\ B &= \frac{H_s^2}{T_p^4}, \\ C &= \frac{5}{4} \frac{1}{T_p^4}, \\ \gamma &= 3.3, \\ \beta &= e^{-\frac{(f_j - f_p)^2}{2\sigma^2 f_p^2}}, \\ \sigma &= 0.07 \quad \text{when } f_j < f_p \quad \text{or} \quad \sigma = 0.09 \quad \text{when } f_j > f_p. \end{aligned} \quad (2.51)$$

2.2.4 Conversion of irregular surface elevation into variance spectrum

To convert surface elevation into the variance spectrum, it is necessary to decompose the irregular wave into its regular wave components. This is done by using the Fourier Transformations. The present research uses a Fast Fourier Transformation, which is an algorithm to carry out Discrete Fourier Transformations (Aggarwal (2015)). The Fourier theorem states that a continuous variable, $x(t)$, measured over a finite duration over a wave period, t_T , in a interval $[-t_T/2, t_T/2]$, can be represented as the summation of sinusoidal wave components:

$$x(t) = \frac{a_0}{2} + \sum_{n=1}^{\infty} \left(a_n \cos\left(\frac{2\pi j t}{T}\right) + b_n \sin\left(\frac{2\pi j t}{T}\right) \right) = \sum_{n=0}^{\infty} (a_n \cos(\omega_n t) + b_n \sin(\omega_n t)), \quad (2.52)$$

where a_0, b_0, a_j and b_j are the Fourier coefficients given by:

$$\begin{aligned} a_0 &= \frac{1}{t_T} \int_{-t_T/2}^{t_T/2} x(t) dt, \\ b_0 &= 0, \\ a_j &= \frac{2}{t_T} \int_{-t_T/2}^{t_T/2} x(t) \cos(\omega_j t) dt, \\ b_j &= \frac{2}{t_T} \int_{-t_T/2}^{t_T/2} x(t) \sin(\omega_j t) dt. \end{aligned} \quad (2.53)$$

By rewriting Equation 2.52 in terms of a complex number, and by considering that it corresponds with the surface elevation of an irregular wave:

$$x(t) = \eta(t) = \sum_{-\infty}^{\infty} A_j e^{iw_j t}, \quad (2.54)$$

where,

$$\begin{aligned} A_0 &= \frac{1}{a_0}, \\ A_j &= \frac{1}{2}(a_j - ib_j), \\ A_{-j} &= \frac{1}{2}(a_j + ib_j). \end{aligned} \quad (2.55)$$

A_{-j} represents the complex conjugate A_j^* of A_j . The spectral density $S(f)$ is obtained as the sum of the variances of all Fourier components within the chosen spectral resolution, Δf :

$$S(f)\Delta(f) = 2 \sum_{\Delta f} A_j A_j^*. \quad (2.56)$$

2.3 Hydrodynamics of a floating body

2.3.1 Problem decomposition

It is possible to describe the total wave field around a generic floating body in the ocean as the superposition of an incident, diffracted and radiated wave fields. The incident wave field can be defined as a plane propagating wave in absence of the body. The diffracted wave field is obtained when the body is kept fixed under the incident wave field, and the radiated wave field is generated by forcing an harmonic oscillation of the body in still water. The description of the hydrodynamics of a floating body included in this Section is mainly based on the work by Alves (2016a).

Similarly to the linear wave theory, it is required to find a velocity potential for the total wave field, ϕ_{tot} , that not only satisfies the Laplace equation and the boundary conditions at the sea bed and the water free surface. ϕ_{tot} also has to meet a boundary condition over the body mean wetted surface and a boundary condition at infinity, also known in literature as the radiation condition. Therefore ϕ_{tot} can be decomposed as:

$$\phi_{tot} = \phi_I + \phi_D + \phi_R, \quad (2.57)$$

where ϕ_I , ϕ_D and ϕ_R represent the incident, diffracted and radiated velocity potentials, respectively. ϕ_I does not respect the boundary condition at the body

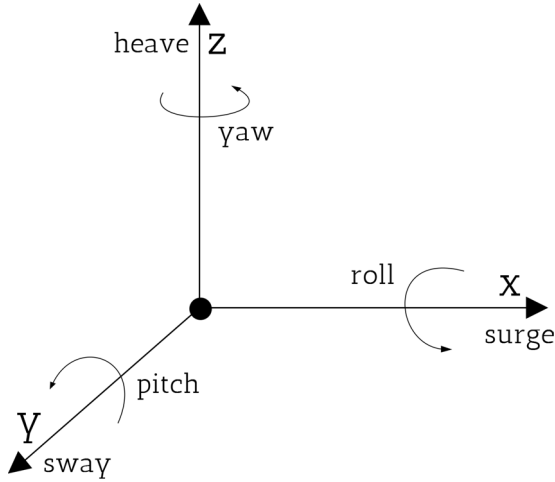


Figure 2.7: 6 degrees of freedom of a free floating body. Three translations: surge, moving left and right on the x-axis, sway moving forwards and backwards on the y-axis, and heave, moving up and down on the z-axis. Three rotations: roll, rotating on the x-axis, pitch, rotating on the y-axis, and yaw, rotating on the z-axis (Figure adopted from Verbrugghe (2018)).

nor the radiation condition, hence the complex amplitude can be computed directly using Equation 2.58:

$$\hat{\phi}_I = \frac{iga}{w} \frac{\cosh[k(d+z)]}{\cosh(kh)} e^{-ik(x \cos(\theta) + y \sin(\theta))}, \quad (2.58)$$

where a is the wave amplitude and θ is the angle between the direction of propagation of the incident wave and the x-axis.

To find a solution for the radiated $\hat{\phi}_R$ and the diffracted $\hat{\phi}_D$ complex amplitudes the body and the radiation boundary conditions are applied solving the radiation and diffraction problems, respectively.

The radiated complex amplitude, $\hat{\phi}_R$, can be expressed by:

$$\hat{\phi}_R = i\omega \sum_{j=1}^J z_j \hat{\phi}_j, \quad (2.59)$$

where J indicates the total number of oscillatory modes of the body, z_j is the complex amplitude of the body motion in mode j , and $\hat{\phi}_j$ is the radiation velocity potential per unit displacement amplitude in mode j . In the case of rigid body motion, j identifies with each one of the 6 rigid degrees of freedom (DOF) included in Figure 2.7.

The radiation velocity potential, $\hat{\phi}_R$, has to fulfil the Laplace Equation, the boundary condition at the sea bed, Equation 2.5 and the two boundary conditions

at the surface elevation, Equations 2.8 and 2.9, as well as the boundary condition on the body:

$$\frac{\partial \phi_j}{\partial n} = v_j n_j, \quad (2.60)$$

where n_j denotes the unit vector normal to the body surface. Moreover, it has to fulfil the radiation condition at infinity. According to this boundary condition, the wave field should appear undisturbed or similar to the incident wave field far from the oscillatory body's centre. This is expressed by:

$$\phi_i \propto (kr)^{1/2} e^{-ikr} \text{ as } r \rightarrow \infty, \quad (2.61)$$

where r is the radial distance from the body.

The diffraction velocity potential, ϕ_D , has to satisfy the Laplace Equation 2.4, the boundary condition at the sea bed, Equation 2.5, the two boundary conditions at the surface elevation Equations 2.8 and 2.9 and the radiation boundary condition (Equation 2.61). The diffracted wave is generated by the interaction between the body and the incident wave when the body is fixed. Thus, it must satisfy the body boundary condition of Equation 2.60 at the surface of the body, S_B , ensuring that there is a continuity between the incident, ϕ_I , and diffracted, ϕ_D , velocity potentials. Hence, the complex diffracted amplitude, $\hat{\phi}_D$, can be derived from :

$$\frac{\partial \hat{\phi}_D}{\partial n} = -\frac{\partial \hat{\phi}_I}{\partial n} \text{ on } S_B. \quad (2.62)$$

2.3.2 Equation of motion: single degree of freedom WEC

To understand the mechanics of wave energy conversion it is necessary to understand the motion response of bodies under wave action. The generic equation of motion for a DOF WEC will be derived in this section in the frequency-domain.

A single DOF WEC can be compared to a simple spring-mass-damper system with one DOF, subjected to an external harmonic force in the direction of the degree of freedom (Figure 2.8). In accordance with linear wave theory it is assumed that the fluid motion and the motion amplitude of the WEC are sufficiently small for viscous effects to be neglected. According to Newton's law, the general motion equation in the time-domain is given by:

$$m\ddot{z}(t) = F_{pe}(t) + F_{re}(t), \quad (2.63)$$

where m is the total inertia of the WEC, z is the displacement, $\ddot{z}(t)$ is the acceleration, F_{pe} is the force due to external hydrodynamic and hydrostatic pressure, and F_{re} is the reaction force. In accordance to linear wave theory, considering the oscillatory motion of the waves and the WEC to be harmonic it is possible to decompose each term of Equation 2.63 in its spacial and temporal dependencies. Therefore,

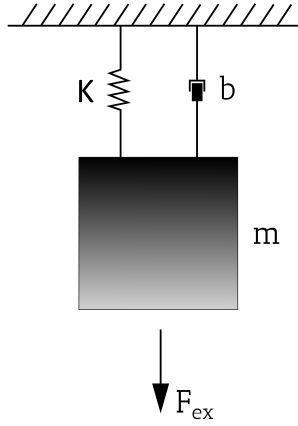


Figure 2.8: Illustration of a spring-mass-damper system. K is the spring stiffness, b is the system damping and m is the mass (Figure adapted from Verbrugghe (2018)).

all forces acting on the WEC can be described by a complex amplitude and the sinusoidal time dependence, $e^{i\omega t}$. Thus, the WEC displacement, $z(t)$, velocity, $\dot{z}(t)$, and acceleration, $\ddot{z}(t)$, become:

$$z(t) = \text{Re}\{\hat{z}(\omega)e^{i\omega t}\}, \quad (2.64)$$

$$\dot{z}(t) = \text{Re}\{i\omega\hat{z}(\omega)e^{i\omega t}\}, \quad (2.65)$$

$$\ddot{z}(t) = \text{Re}\{-i\omega^2\hat{z}(\omega)e^{i\omega t}\}, \quad (2.66)$$

where $\hat{\cdot}$ denotes the complex amplitude. Hence, in the frequency-domain Equation 2.63 can be rewritten as:

$$-\omega^2 m \hat{z}(\omega) = \hat{F}_{pe}(\omega) + \hat{F}_{re}(\omega). \quad (2.67)$$

The force due to the external pressure on the body, F_{pe} , can be decomposed in the hydrostatic and hydrodynamic pressure:

$$\hat{F}_{pe}(\omega) = \hat{F}_{hys}(\omega) + \hat{F}_{hyd}(\omega), \quad (2.68)$$

where the first term represent the hydrostatic restoring force due to gravity and buoyancy that tends to bring the body back to equilibrium, and the second term represent the hydrodynamic force acting on the WEC. Additionally, the reaction forces \hat{F}_{re} , can also be decomposed in two components:

$$\hat{F}_{re}(\omega) = \hat{F}_{PTO}(\omega) + \hat{F}_m(\omega), \quad (2.69)$$

where the first term is the reaction force of the power take off (PTO) system of the WEC, and the second is the constraint caused by the mooring system used to keep the WEC fixed in place.

2.3.3 Forces

After having described the equation of motion in the frequency-domain and identified the different forces acting on the WEC, the different forces to solve the boundary element problem that has been described in Section 2.3.1 is obtained.

The potential flow hydrodynamic force, F_{hyd} results from the integration of the dynamic pressure on the mean wetted body surface, S_b . Using the Bernoulli equation the dynamic pressure can be derived from the velocity potential, disregarding second order terms, as:

$$p_e = -\rho \frac{\partial \phi}{\partial t}. \quad (2.70)$$

Therefore, the linear hydrodynamic force is obtained from:

$$F_{hyd} = \int_{S_b} p_e n dS_b = \rho \int_{S_b} \frac{\partial \phi}{\partial t} n dS_b. \quad (2.71)$$

The decomposition of the velocity potential included in Section 2.3.1 allows writing the complex amplitude of the hydrodynamic force as:

$$\hat{F}_{hyd} = i\omega\rho \int_{S_b} \hat{\phi}_I n dS_b + i\omega\rho \int_{S_b} \hat{\phi}_D n dS_b - \omega^2\rho \int_{S_b} \sum_{j=1}^N \hat{z}\varphi_j n dS_b. \quad (2.72)$$

Solving the first term of the equation the Froude-Krylov force, \hat{F}_{FK} , is obtained from integrating the incident wave velocity potential, $\hat{\phi}_I$, over the mean wetted surface of the motionless body, S_b . That is the force acting on the body as if the body is not disturbing the incident wave field. The second term of the equation is the diffraction force, \hat{F}_{diff} , obtained integrating the diffracted velocity potential, $\hat{\phi}_D$, over the mean wetted surface of the body, S_b . The sum of the Froude-Krylov force and the diffraction force is referred in literature as the excitation force, \hat{F}_e , accounting for the effect of the incident waves on the body.

The third term of Equation 2.72 represents the wave radiation force, F_{rad} . This force is caused by the displacement of the water in the vicinity of the body when the body moves. The hydrodynamic radiation force of a floating body can be derived using an electric analogy, as described in Folley (2016a), and is given by:

$$\hat{F}_{rad} = -i\omega B_{hyd} \hat{z} + \omega^2 M_A \hat{z}. \quad (2.73)$$

It consists on a first term proportional to the velocity of the body and a second term proportional to the acceleration of the body. The first is multiplied by the hydrodynamic damping coefficient, B_{hyd} , which refers to a dissipative effect related to the energy transmitted to the water by the body oscillations through waves that propagate away from the body. The latter is multiplied by the added mass coefficient, M_A , which corresponds to an inertial increase due to the water displacement when the body is moving.

The hydrostatic force, F_{hys} , is the resulting force between the balance of the buoyancy of the WEC and gravity. It can be derived from the integration of the hydrostatic pressure over the body wetted surface under undisturbed conditions. For small amplitude body motions, it is possible to linearise the hydrostatic force, becoming proportional to the displacement. Thus the complex amplitude of the hydrostatic force, \hat{F}_{hys} , is expressed directly as:

$$\hat{F}_{hys} = -K\hat{z}, \quad (2.74)$$

where K_H is the hydrostatic coefficient.

Finally the reaction forces are calculated. Typically the reaction forces comprise the effect of the PTO system used to generate electricity and the mooring mechanism used to keep the WEC in place. Both problems have a complex nonlinear behaviour that will need to be linearised in order to keep the superposition principle valid.

In the frequency-domain the PTO reaction force can be linearised with two components: one proportional to the velocity, represented by a damper, and the other proportional to the body motion, represented by a spring. Hence, the complex amplitude of the force generated by the PTO, \hat{F}_{PTO} , is given by:

$$\hat{F}_{PTO} = -i\omega B_{PTO}\hat{z} - K_{PTO}\hat{z}, \quad (2.75)$$

where B_{PTO} is the power take off damping and K_{PTO} is the power take off spring coefficient.

The complex amplitude of the mooring force, \hat{F}_m , can be simply given by:

$$\hat{F}_m = -K_m\hat{z}, \quad (2.76)$$

where K_m represents the mooring spring stiffness.

2.3.4 Complex amplitude of the body motion

Introducing the forces caused by the external pressure, Equations 2.72 and 2.74, and the resulting expressions of the reaction forces, Equations 2.75 and 2.76, into the motion Equation 2.67, the complex amplitude of the WEC motion is obtained as:

$$\hat{z} = \frac{\hat{F}_e}{[-\omega^2(m + M_A) + K + K_{PTO} + K_m] + i\omega(B_{hyd} + B_{PTO})}. \quad (2.77)$$

2.3.5 Power absorption

The most common parameter used to evaluate the performance of WECs in terms of power capture is the power absorption. The mean power absorbed of a WEC corresponds to the mean power consumed by the mechanical damper of the PTO equipment during a wave period. Assuming sinusoidal waves, the mean absorbed power is given by:

$$P_a = \frac{1}{2} B_{PTO} \omega^2 |\hat{z}|^2, \quad (2.78)$$

where B_{PTO} is the PTO damping and \hat{z} is the complex amplitude of the WEC motion.

2.4 The wave propagation model MILDwave

The wave propagation model employed within this research is the mild-slope model MILDwave developed at the Coastal Engineering Research Group of Ghent University in Belgium (Troch (1998); Troch and Stratigaki (2016)). In the past years, MILDwave has been widely used in the modelling of "far field" effects of WEC arrays (Beels et al. (2010a); Stratigaki et al. (2011); Balitsky et al. (2017); Verbrugge et al. (2017); Tomey-Bozo et al. (2018)) as it has proven to be a robust and efficient numerical model for calculating wave propagation through WEC arrays and over large coastal areas.

2.4.1 Governing equations

MILDwave is a phase-resolving model based on the depth-integrated mild-slope equations of Radder and Dingemans (1985) given in Equations 2.79 and 2.80. MILDwave describes the wave transformations (shoaling and refraction) of regular, irregular and short-crested waves with a narrow frequency band propagating above mildly varying bathymetries.

$$\frac{\partial \eta}{\partial t} = B\phi - \nabla(A\nabla\phi), \quad (2.79)$$

$$\frac{\partial \phi}{\partial t} = -g\eta. \quad (2.80)$$

Values A and B are calculated using Equations 2.81 and 2.82, respectively:

$$A = \frac{CC_g}{g}, \quad (2.81)$$

$$B = \frac{\omega^2 - k^2 CC_g}{g}. \quad (2.82)$$

The mild-slope equations (Equations 2.79 and 2.80) are discretized and then resolved using a finite difference scheme that consists of a two-step space-centered, time-staggered computational grid, as detailed in Brorsen and Helm-Petersen (1998). The domain is uniformly divided in grid cells of dimensions dx and dy and central differences are used both for spatial and time derivatives. Both η and ϕ are calculated at the center of each grid cell at different time steps, $(n + \frac{1}{2})\Delta t$ and $(n + 1)\Delta t$ using Equations 2.83 and 2.84 :

$$\begin{aligned}
 \eta_{i,j}^{n+\frac{1}{2}} &\simeq \eta_{i,j}^{n-\frac{1}{2}} + B_{i,j} \phi_{i,j}^n \Delta t \\
 &- \frac{A_{i+1,j} - A_{i-1,j}}{2\Delta x} \frac{\phi_{i+1,j}^n - \phi_{i-1,j}^n}{2\Delta x} \Delta t \\
 &- A_{i,j} \frac{\phi_{i-1,j}^n - 2\phi_{i,j}^n + \phi_{i+1,j}^n}{\Delta x^2} \Delta t \\
 &- \frac{A_{i,j+1} - A_{i,j-1}}{2\Delta y} \frac{\phi_{i,j+1}^n - \phi_{i,j-1}^n}{2\Delta y} \Delta t \\
 &- A_{i,j} \frac{\phi_{i,j-1}^n - 2\phi_{i,j}^n + \phi_{i,j+1}^n}{\Delta y^2} \Delta t,
 \end{aligned} \tag{2.83}$$

$$\phi_{i,j}^{n+1} \simeq \phi_{i,j}^n - g\eta_{i,j}^{n+\frac{1}{2}} \Delta t. \tag{2.84}$$

MILDwave uses an internal wave generation line near the offshore boundary by applying the source term addition method introduced by Lee and Suh (1998) where the source term propagates with the energy velocity. According to this method, an additional surface elevation with the desired energy η^* is added to the calculated surface elevation η at the wave generation line for each time step and is given by Equation 2.85:

$$\eta^* = 2\eta_I \frac{C_e \Delta t}{\Delta x} \cos \theta. \tag{2.85}$$

The internal wave generation can be a single generation line (Figure 2.9 (A)), a combination of 2 straight generation lines (Figure 2.9 (B)) or an arc (2.9 (C)). To avoid unwanted reflection in the numerical basin absorbing sponge layers are placed at the open boundaries (hatched areas in Figures 2.9 A-D).

The numerical absorption of waves in the sponge layer is obtained multiplying the calculated surface elevation at each time step with an absorption function that decreases from 1 to 0 over the width of the sponge layer. Elliptical and sinusoidal absorption functions have been defined in MILDwave as detailed in Equations 2.86 and 2.87:

$$S_1(b) = \sqrt{1 - \left(\frac{lb}{B_S}\right)^2}, \tag{2.86}$$

$$S_2(b) = \frac{1}{2} \left(1 + \cos \left(\pi \frac{lb}{B_S} \right) \right). \tag{2.87}$$

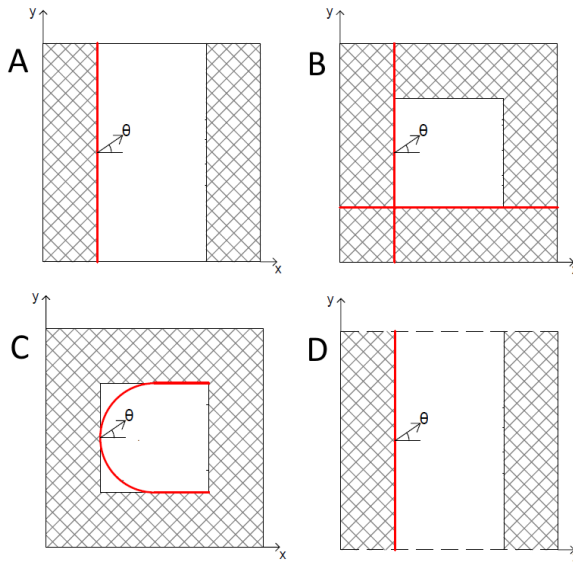


Figure 2.9: MILDwave wave generation types for rectangular numerical wave basins. Figure adapted from Vasarmidis et al. (2019).

where B_S is the length of the sponge layer and l_b the distance from the outside boundary to the start of the sponge layer.

2.4.2 Periodic lateral boundaries

Periodic lateral boundaries have been implemented in MILDwave by Vasarmidis et al. (2019) allowing the model to create homogeneous wave fields of oblique regular, long-crested and short-crested irregular waves. Figure 2.10 (D) shows the schematics of internal wave generation using a single wave generation line parallel to the y-axis combined with periodic lateral boundaries at the top and bottom of the numerical domain. The information reaching one end of the domain enters the opposite end.

Figure 2.10 shows an schematic of the periodic lateral boundaries implementation. A layer of ghost cells is present next to each vertical boundary, acting as fully reflective walls while the periodic boundaries are represented by dashed line in the x-axis direction (Figure 2.10 (A)). At the position of the periodic boundaries, Equation 2.83 is solved as the horizontal boundaries were next to each other (Figure 2.10 (B)). The bathymetry close to both lateral boundaries has to be identical between each other to ensure continuity.

The implementation of periodic lateral boundaries leads to a more homogeneous wave field than the "L" and arc shape previously used in MILDwave (Figure 2.9 A,B and C, respectively). As a result, no wave diffraction problems are caused due to the intersection of sponge layers or different wave generation lines.

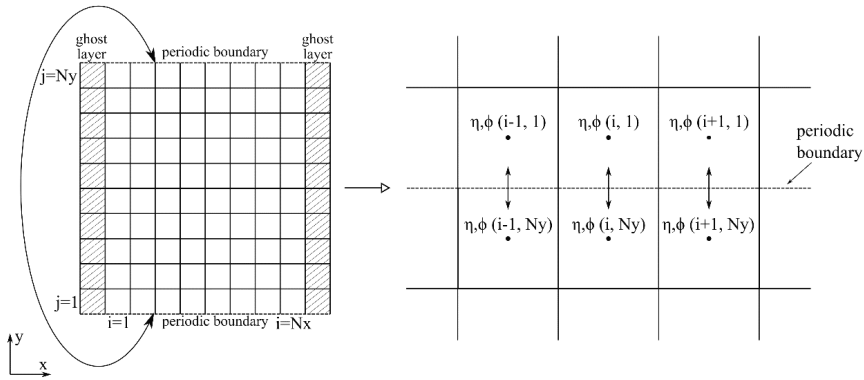


Figure 2.10: MILDwave periodic boundaries implementation. The information reaching one end of the domain enters the opposite end. Figure adopted from Vasarmidis et al. (2019).

2.5 The wave-structure Interaction solver NEMOH

In this research, the wave-structure interaction selected chosen to solve the diffraction/radiation problem introduced in Section 2.3.1 is the open-source potential flow BEM solver NEMOH, developed at Ecole Centrale de Nantes by Babarit and Delhommeau (2015). NEMOH is based on linear potential flow theory (Alves (2016a)) and employs the panel method to solve the velocity potential on the mean wetted surface of the body. In this section, a short description of the potential flow theory is included, as well as the numerical solution provided by NEMOH.

2.5.1 Potential Flow Theory

Potential flow theory has been widely used in numerical modelling of WEC arrays and it is based on the following assumptions:

1. The fluid is incompressible
2. The flow is irrotational
3. The flow is inviscid
4. The motion amplitudes of the modelled floating bodies are much smaller than the wavelength
5. The sea bed is flat

Under these conditions the water velocity, \vec{u} , can be expressed in terms of the

velocity potential, $\phi(x, y, z, t)$, according to:

$$\vec{u} = \nabla\phi, \quad (2.88)$$

and assuming that the fluid is incompressible, the continuity equation becomes:

$$\nabla\vec{u} = 0. \quad (2.89)$$

Introducing Equation 2.88 in Equation 2.89 results in the Laplace equation:

$$\nabla^2\phi = 0. \quad (2.90)$$

2.5.2 Solution of the boundary value problem

The Laplace Equation 2.90 must be satisfied by the velocity potential in the whole fluid domain, Ω , and thus the linear boundary value problem described in Section 2.3.1 becomes in NEMOH:

$$\nabla^2\phi = 0 \quad M \in \Omega, \quad (2.91)$$

$$\frac{\partial\phi}{\partial n} = f(M) \quad M \in S_B, \quad (2.92)$$

$$\frac{\partial\phi}{\partial n} = 0 \quad M \in S_{bed}, \quad (2.93)$$

$$\frac{\partial^2\phi}{\partial t^2} + g\frac{\partial\phi}{\partial n} = 0 \quad z = 0 \quad M \in S_{FS}, \quad (2.94)$$

$$\sqrt{R}\left(\frac{\partial\phi}{\partial n} - ik\right)(\phi - \phi_0) \rightarrow 0 \quad R \rightarrow \infty \quad M \in S_\infty. \quad (2.95)$$

where, $M(x, y, z)$ is a given point in the fluid domain, $f(M)$ is a scalar function, ϕ_0 is the incident wave potential at infinity, S_B is the body free surface, S_{FS} is the free surface, S_{bed} is the sea bed condition on the body, i is the imaginary number part, and S_∞ is the boundary condition on the infinity as shown in Figure 2.11:

NEMOH obtains a numerical solution of a boundary-integral equation, formulated using Green functions. The solution satisfies the aforementioned boundary conditions transforming the flow problem into a problem of source distribution on the body surface. Hence, NEMOH computes the solutions for the diffraction and radiation problems giving the following outputs:

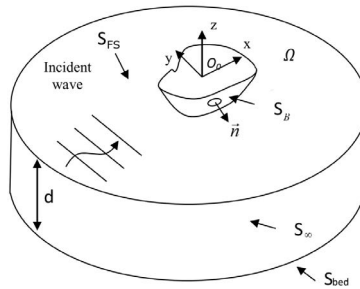


Figure 2.11: Linear boundary value problem solved in NEMOH. (Figure adapted from Babarit and Delhommeau (2015))

1. First order hydrodynamic coefficients: added mass coefficient, M_A , hydrodynamic damping, B_{hyd} and excitation force, F_e
2. Far field coefficients in terms of a Kochin function
3. The pressure field on the body surface
4. Near field complex free surface elevation for the diffracted and radiated waves

The near field complex free surface elevation for the diffracted and radiated waves will be used in the coupling methodology described in the next section as input values for the wave propagation model.

Chapter 3

MILDwave - NEMOH Coupled Model

3.1 Introduction

As it has been pointed out in Chapter 1, it is not possible to accurately predict the "far field" and "near field" effects of off-shore structures using a single numerical model. Wave-structure interaction solvers, typically used for solving the "near field" effects, are very computationally demanding, even for solving a single structure in a very limited spatial grid. On the contrary, wave propagation models can solve wave propagation in really large domains. However, these models lack a correct implementation of wave-structure interactions.

To overcome the limitation of both approaches to calculate "far field" and "near field" effects of off-shore structures, a one-way coupled model between the wave propagation model MILDwave and the wave-structure interaction solver NEMOH has been developed within this research. These two models have been chosen as they provide fast and accurate solutions within linear theory for wave propagation and wave-structure interaction calculations, respectively. The theoretical background of both models has been detailed in Chapter 2.

This Chapter will deal with applying a generic coupling methodology, first introduced by Stratigaki (2014), between MILDwave and NEMOH. The work presented by Stratigaki (2014) established the basis for coupling wave propagation models and wave-structure interaction solvers to study both "far field" and "near field" effects of WEC arrays. Additionally, this research included a first implementation of the generic coupling methodology for a single body under regular wave conditions between MILDwave and the wave-structure interaction solver WAMIT.

The present work extended this initial coupled model to a fully functional numerical tool by:

1. Optimizing the internal wave generation boundary to provide a correct phase matching between the incident and the perturbed waves.

2. Introducing irregular long- and short-crested wave generation.
3. Validating the numerical tool through numerical and experimental test cases.

Section 3.2 of this chapter presents a description of the generic coupling methodology, on which the MILDwave-NEMOH coupled model is based. In Section 3.3 the generic coupling methodology is applied between the wave propagation model MILDwave and NEMOH. A detailed description of the coupling implementation and the coupling algorithm is provided in Sections 3.3.2 and 3.3.3, respectively. Section 3.4 presents a numerical validation of the coupled model covering a wide range of wave conditions, WEC types and WEC array layouts. A sensitivity analysis is performed in Section 3.5 for various simulation parameters to define the optimal input for the model to obtain accurate and fast solutions. The results of the numerical validation are included in Section 3.6 and discussed in Section 3.7. The concluding remarks are summarized in Section 3.8.

3.2 Generic Coupling Methodology

The MILDwave - NEMOH coupled model presented in this research is based on a generic coupling methodology first introduced by Stratigaki (2014), who presented a coupled model between the wave propagation model MILDwave and the wave-structure interaction solver WAMIT.

The objective of the coupling methodology is to obtain the total wave field around a (group of) structure(s), as a superposition of the incident and the perturbed (which is a combination of the diffracted, radiated and reflected waves) wave fields. The incident wave field propagation and transformation is calculated over a large domain using a wave propagation numerical model. The perturbed wave field is simulated using a wave-structure interaction solver over a restricted domain around the structure(s), namely the coupling region.

The general strategy for the coupling methodology consists of four steps as shown in Figure 3.1. Firstly (Step 1), a wave propagation model is used to obtain the incident wave field at the location of the structure(s) when the structure(s) is (are) not present. Secondly (Step 2), the obtained wave field from Step 1 is used as input for the wave-structure interaction solver at the location of the structure(s). Then the motion of the structure(s) is solved and an accurate solution of the perturbed wave fields around the structure(s) is obtained. Thirdly (Step 3), the perturbed wave field is used as input in the wave propagation model and is propagated throughout a large domain. This is done by prescribing an internal wave generation boundary around the structure(s) location. Finally (Step 4), the total wave field due to the presence of the structure(s) is obtained as the superposition of the incident wave field and the perturbed wave field in the wave propagation model.

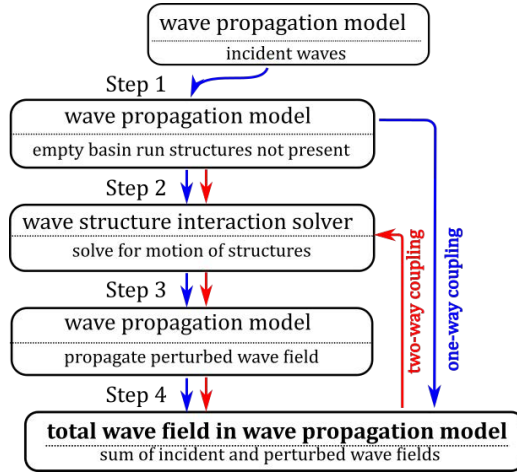


Figure 3.1: Flow chart of the generic coupling methodology between a wave-structure interaction solver and a wave propagation model.

The aforementioned coupling methodology can also be classified into a one-way or two-way coupling depending on how the information in Step 4 is transferred. Figure 3.2 shows the schematics of a one-way and a two-way coupling, respectively. The inner model domain corresponds to the location of the structure(s), where the "near field" effects are solved. The outer model domain corresponds to the area where the "far field" effects are evaluated.

In a one way-coupling, the wave field for each numerical problem is calculated independently. Thus, the main coupling mechanism is the superposition of two different simulations obtained in the wave propagation model: an incident wave field calculated intrinsically, and a perturbed wave field calculated using a wave generation boundary.

Alternatively, in a two-way coupling both numerical models are run at the same time with a two-way transfer of information between them. Consequently, there is an exchange of information in each simulation time step and as a result Steps 2, 3 and 4 of the coupling methodology are re-calculated each time.

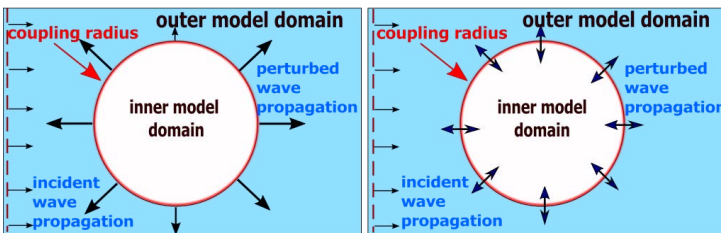


Figure 3.2: Schematic of a one-way coupling (left) and two-way coupling (right). In the inner model domain the motions of the studied structure(s)/WEC(s) are solved. Both the inner model domain and the outer model domain representations are not to scale.

Nevertheless, both solutions are able to obtain the far field effects of the structure(s) at a reasonable computational cost and accuracy taking into account bathymetric effects and wave transformation processes, with an accurate description of the perturbed wave field around the structure(s).

The proposed coupling methodology is a generic tool that can be applied in the following cases:

1. Any wave-structure interaction solver that solves wave-structure interactions is suitable for generating the input parameters for the internal wave generation boundary. Models based on potential flow theory (e.g. BEM Verbrughe et al. (2017); Alves (2016b)), or solving the fully nonlinear Navier-Stokes equations (e.g. CFD Devolder et al. (2018) or SPH Verbrughe et al. (2018)) or analytically obtained far field coefficients (Babarit et al. (2013)) can be used.
2. Any phase-resolving or phase-averaging wave propagation models where an internal wave generation boundary can be introduced.
3. Any kind of floating or fixed structure(s) such as wave energy converters (WECs), floating breakwaters, off-shore wind turbines or platforms.

The principles of this generic coupling methodology have been used in literature to couple different models and examples can be found in Verbrughe et al. (2017, 2018); Tomey-Bozo et al. (2018), both using the Stratigaki et al. (2014) methodology; and Rijnsdorp et al. (2018).

3.3 MILDwave-NEMOH coupled model

In this section the aforementioned coupling methodology is demonstrated between the wave propagation model MILDwave and the wave-structure interaction solver NEMOH. As indicated in Chapter 1, these two models have been used extensively in the recent years to model "near field" and "far field" effects of WEC arrays. The author finds worth pursuing the application of the generic coupling methodology between them as the first offers fast and accurate solutions of waves propagating over large domains, and the latter resolves the hydrodynamic interactions of floating structures at a reasonable computational cost. MILDwave is a time-domain model and NEMOH a frequency-domain model, therefore the coupling methodology applied needs to be one way only (executing both models independently), due to the fact that frequency-domain models are time invariant.

3.3.1 Basis of the MILDwave-NEMOH coupled model

To apply the one way coupling methodology concept described in Section 3.2, NEMOH is coupled into MILDwave following the four steps included in Figure 3.2, performing three different simulations:

1. A first simulation is performed in MILDwave to obtain the incident wave field in the time-domain, without any floating structure in the numerical basin. The wave characteristics at the coupling location are computed and used as input values for NEMOH.
2. A second simulation is performed in NEMOH to calculate the perturbed wave field around the floating structure at the coupling location in the frequency-domain.
3. A third simulation is performed in MILDwave to obtain the perturbed wave field in the time-domain. The perturbed wave field from NEMOH is transformed from the frequency-domain to the time-domain and coupled into MILDwave by prescribing an internal wave generation boundary.
4. Finally, the total wave field is obtained as the combination of the incident and perturbed wave fields calculated in MILDwave in the time-domain.

3.3.1.1 Generation of the Incident Wave Field

The incident wave field is calculated using the wave propagation model MILDwave in the time-domain. It is possible to simulate regular waves, and long-crested and short-crested irregular waves. However, it is not possible to perform a direct calculation of irregular waves using a one-way coupling as it is necessary to ensure the correct matching between each incident and perturbed wave regular component. Consequently, in this section details are provided on obtaining the incident regular waves and correctly calculating the irregular waves as a superposition of different linear regular wave components which is described in Chapter 2. The same structure is used when demonstrating the perturbed wave field calculation and the total wave field calculation.

The incident wave field for a linear regular wave is generated intrinsically in MILDwave. The numerical set-up of MILDwave is illustrated in Figure 3.3. Waves are generated along a linear offshore wave generation boundary (as illustrated in Figure 2.9) by applying the boundary condition of linear regular waves' generation:

$$\eta_{I,reg}(x, y, t) = a \cos(\omega t - k(x \cos \theta + y \sin \theta)), \quad (3.1)$$

where $\eta_{I,reg}$ is the incident regular wave surface elevation. To minimize unwanted wave reflection, absorption layers are placed down-wave and up-wave in the numerical wave basin.

By applying the superposition principle, a first order irregular wave is represented as the finite sum of N regular wave components characterized by their wave amplitude, a_j , and wave period, T_j , derived from the wave spectral density, S_j :

$$\eta_{I,irr}(x, y, t) = \sum_{j=1}^N a_j \cos(\omega_j t - k_j(x \cos \theta_j + y \sin \theta_j) + \varphi_j), \quad (3.2)$$

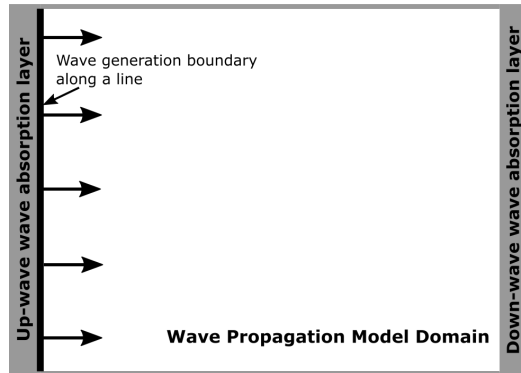


Figure 3.3: Sketch of the incident wave propagation in MILDwave. The black thick line corresponds to the wave generation line and the grey areas correspond to wave absorption layers used down-wave and up-wave the numerical domain.

where,

$$a_j = \sqrt{2S_j(f_j) \cdot \Delta f_j}, \quad (3.3)$$

where $\eta_{I,irreg}$ is the incident irregular wave surface elevation and a_j is the wave amplitude, ω_j is the wave angular frequency, f_j is the wave frequency, k_j is the wave number, θ_j is the wave direction and φ_j is the incident phase angle, of each wave frequency component j . φ_j is selected randomly between $-\pi$ and π to avoid local attenuation of $\eta_{I,irreg}$.

To generate a long-crested irregular wave, θ_j is equal to the mean direction of wave propagation, θ_{mean} , for all wave frequency components. In the case of short-crested waves the wave directions, θ_j , introduced in Equation (3.2) will be obtained for each frequency using the Sand and Mynett (1987) method.

According to this method, the wave spectrum is discretized in N_f frequency components. The wave propagation angles θ_j are selected randomly according to the cumulative distribution function of the directional spreading function, $D(f, \theta)$, and are assigned to each wave frequency component. This model provides an accurate representation of the targeted spreading function shape as shown in Vasarmidis et al. (2019). The spreading function of Frigaard et al. (1997) is employed:

$$D(f, \theta) = \frac{1}{\sqrt{\pi}} \frac{\Gamma(s_1 + 1)}{\Gamma(s_1 + \frac{1}{2})} \cos^{2s_1}(\theta - \theta_{mean}), \quad (3.4)$$

with,

$$-\frac{\pi}{2} < \theta - \theta_{mean} < \frac{\pi}{2}, \quad (3.5)$$

where s_1 is the directional spreading parameter, Γ is the Gamma function.

Hence, the values of s_1 can be determined for different directional spreading, given by:

$$\sigma_\theta = \sqrt{2 - \frac{2\Gamma^2(s_1 + 1)}{\Gamma(s_1 + \frac{1}{2})\Gamma(s_1 + \frac{3}{2})}}, \quad (3.6)$$

where σ_θ is the standard deviation of the directional spreading.

3.3.1.2 Calculation of the perturbed wave field

The perturbed wave field in the time-domain for a regular wave is obtained in two steps and the employed numerical set-up is illustrated in Figure 3.4. First, a frequency-dependent simulation is performed using NEMOH to obtain the complex perturbed wave field around the (group of) structure(s). NEMOH resolves the wave frequency-dependent wave radiation problem for each (of the) structure(s) and the diffraction over a predetermined numerical grid with the wave phase angle $\varphi = 0$ at the center of the domain. The resulting radiated and diffracted wave fields for each frequency, f_j , depend on the shape and number of floating structure(s), the number of DOF considered, the local constant water depth and the wave period.

The complex radiated wave field of all the bodies is obtained as a superposition of the complex radiated wave field for each body calculated using NEMOH. The diffracted wave field is given for all structures. Equations 3.7 and 3.8 describe the complex radiated and diffracted wave fields, respectively:

$$\hat{\eta}_{rad} = \sum_{k=1}^J i a \omega \tilde{X}_k(\omega) |\hat{\eta}_{rad,k}| e^{i\varphi_{rad}}, \quad (3.7)$$

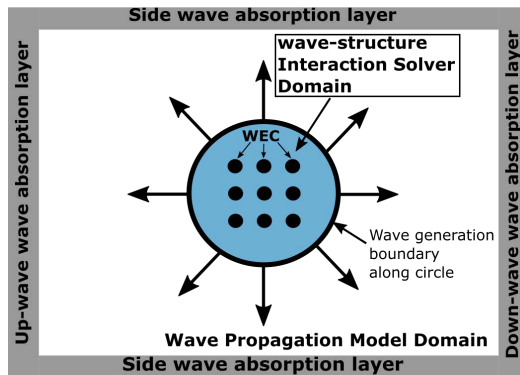


Figure 3.4: Sketch of the perturbed wave propagation in MILDwave. The black circle corresponds to the circular wave generation boundary which surrounds the NEMOH numerical domain (blue area). The smaller black solid circles indicate the locations of the WECs. The grey areas correspond to wave absorption layers down-wave, up-wave and at the sides of the numerical domain.

$$\hat{\eta}_{dif} = a|\hat{\eta}_{dif}|e^{i\varphi_{dif}}, \quad (3.8)$$

where $\hat{\eta}_{rad}$ is the radiated wave field, $\hat{\eta}_{dif}$ is the diffracted wave field, φ_{rad} and φ_{dif} correspond to the radiated and diffracted wave phase angles, respectively, J is the total number of floating WECs and \tilde{X} is the Response Amplitude Operator (RAO) vector for one DOF of the J WECs given by:

$$\tilde{X} = \tilde{F}_{ex} \cdot [-(\mathbf{m} + \mathbf{M}_A)\omega^2 - i\omega(\mathbf{B}_{hyd} + \mathbf{B}_{PTO}) + \mathbf{K}_H]^{-1}, \quad (3.9)$$

here \tilde{F}_{ex} is the excitation force vector of the J WECs, \mathbf{m} is the WEC's mass matrix, \mathbf{M}_A is the added mass matrix, \mathbf{B}_{hyd} is the hydrodynamic damping coefficient matrix, \mathbf{B}_{PTO} is the Power Take-Off (PTO) damping coefficient matrix and \mathbf{K}_H is the hydrodynamic stiffness matrix.

The radiated and diffracted complex wave fields are added to obtain the complex perturbed wave field, η_{pert} :

$$\hat{\eta}_{pert} = \hat{\eta}_{dif} + \hat{\eta}_{rad}. \quad (3.10)$$

Secondly, the perturbed wave field is transformed from the frequency-domain to the time-domain and imposed into MILDwave using an internal circular or rectangular wave generation boundary (Figure 3.4). To ensure phase matching between the incident and perturbed wave fields, the phase angle obtained from NEMOH has to be corrected with the phase angle of the incident regular wave in the center of the internal wave generation boundary. Waves are forced away from the wave generation boundary by imposing values of free surface elevation $\eta_b(x, y, t)$ as described by Equation 3.11:

$$\eta_b(x, y, t) = a_{I,c}|\hat{\eta}_{pert}|\cos(\varphi_{pert,NM,c} + \varphi_{I,c} - \omega t), \quad (3.11)$$

where η_{pert} is the perturbed complex wave field from the frequency-domain, $a_{I,c}$ and $\varphi_{I,c}$ are the wave amplitude and the wave phase angle of the incident wave, respectively, and $\varphi_{pert,NEMOH}$ is the phase angle of the perturbed wave at the center of the internal wave generation boundary, c . To avoid unwanted wave reflection, wave absorption layers or relaxation zones are implemented up-wave, down-wave and also in the sides of the MILDwave numerical domain (Figure 3.4).

As in the case for the calculation of the irregular incident wave field, the irregular perturbed wave field is calculated as the finite sum of N regular perturbed wave components characterized at the center of the wave generation boundary by their wave amplitude, $a_{c,j}$, derived from the wave spectrum:

$$\eta_{pert,irr}(x, y, t) = \sum_{j=1}^N a_{c,j}|\hat{\eta}_{pert,j}|\cos(\varphi_{pert,NM,c,j} + \varphi_{I,c,j} - \omega_j t), \quad (3.12)$$

where

$$a_{c,j} = \sqrt{2S_{c,j}(f_j) \cdot \Delta f_j}, \quad (3.13)$$

and $\eta_{pert,irr}$ is the perturbed irregular wave surface elevation where $S_{c,j}$ is the spectral density, and $\varphi_{I,c,j}$ is the incident phase angle and $\varphi_{pert,NM,c,j}$ is the perturbed phase angle in NEMOH of each frequency component at the center of the internal wave generation boundary, c . $\varphi_{I,c,j}$ is selected randomly between $-\pi$ and π to avoid local attenuation of the surface elevation.

This methodology for calculating irregular waves is valid both for long-crested and short-crested waves. The phase angle of the perturbed wave obtained in NEMOH is dependent on the incident wave direction of each wave frequency. Thus, the wave direction of each frequency is implicitly considered when prescribing the internal circular or rectangular wave generation boundary and forcing away the perturbed wave field. In the case of long-crested waves it corresponds with the mean direction, while in the case of short-crested waves each direction corresponds with the random direction of the incident wave component.

3.3.1.3 Calculation of the total wave field

The regular total wave field is obtained as the superposition of the incident and perturbed regular wave fields obtained in the MILDwave numerical domain as:

$$\eta_{tot,reg}(x, y, t) = \eta_{I,reg}(x, y, t) + \eta_{pert,reg}(x, y, t), \quad (3.14)$$

where, η_{tot} is the total regular wave surface elevation, and $\eta_{I,reg}$ and $\eta_{pert,reg}$ are the incident and perturbed regular wave surface elevation.

Consequently, the irregular total wave field is obtained as the superposition of the irregular incident and perturbed wave fields, which are at the same time obtained as a superposition of N regular wave simulations:

$$\eta_{tot,irr}(x, y, t) = \sum_j^N \eta_{I,reg,j}(x, y, t) + \sum_j^N \eta_{pert,reg,j}(x, y, t), \quad (3.15)$$

where, $\eta_{tot,irr}$ is the total irregular wave surface elevation, and $\eta_{I,reg,j}$ and $\eta_{pert,reg,j}$ are the incident and perturbed wave surface elevation of each f_j , respectively.

3.3.2 MILDwave-NEMOH coupled model implementation

The numerical implementation of the coupled model has been programmed using Python (2019). MILDwave and NEMOH can be initialized from Python using a command-line interface (CLI). This allows the coupled model to have a common work space for both programs, where it is possible to call and follow the execution of

the different processes independently, check intermediately the results, and ensure that the information transfer between them is performed correctly. The numerical implementation has been divided into four processes:

1. Python shell.
2. MILDwave process.
3. NEMOH process.
4. Python Coupling process.

The first process is defining the Python shell. It acts as the simulation preprocessor, as the interface to call the other three processes of the simulation and as the post processor. It creates the input files for the coupled model based on the user input, launches the execution of each MILDwave and NEMOH process (Processes 2 and 3) independently and it generates the total wave surface elevation once all the processes are finished.

The second process takes place in the MILDwave. It runs a regular wave simulation using a CLI version of MILDwave. For a regular incident or perturbed wave simulation the MILDwave CLI is called providing the regular incident wave surface elevation in the whole numerical domain. It also generates the wave amplitudes and wave phases at the coupling location.

The third process takes place in NEMOH. The wave-structure interactions are simulated in the frequency-domain and employing a smaller domain using a CLI version of NEMOH. For a single regular wave or for N regular waves it calculates the perturbed wave field around the structure(s) that has been defined in the Python shell during Process 1.

The fourth process includes the Python Coupling. This is a communication Python script called by the Python Shell from Process 1 that connects the results from Process 2 in MILDwave and Process 3 in NEMOH. It generates the input parameters for the wave internal circular or rectangular wave generation boundary used to perform a MILDwave perturbed wave simulation.

3.3.3 MILDwave-NEMOH coupled model algorithm

In this section, the practical implementation of the coupled model algorithm will be discussed for the case of irregular waves. The algorithm for regular waves is a simplification of the irregular waves case computed for a single wave component.

The basic simulation for the coupled model is running a single incident regular wave in MILDwave. This allows coding the coupled model with a parallel algorithm where a large number of regular wave components are computed at the same time. Parallel coding allows the coupled model to perform at an efficient computational time, even though irregular waves are calculated as a superposition of regular waves. The coupling algorithm is illustrated in Figure 3.5 and consists of six tasks. Each task is performed sequentially, storing the output results on a dedicated simulation folder, until they are called and used by the subsequent step task as indicated in Figure 3.5.

1. Task 1: Variables initialization.
2. Task 2: Incident wave calculation in the time-domain.
3. Task 3: Perturbed wave calculation in the frequency-domain.
4. Task 4: Coupling input files generation.
5. Task 5: Perturbed wave calculation in the time-domain.
6. Task 6: Total wave calculation.

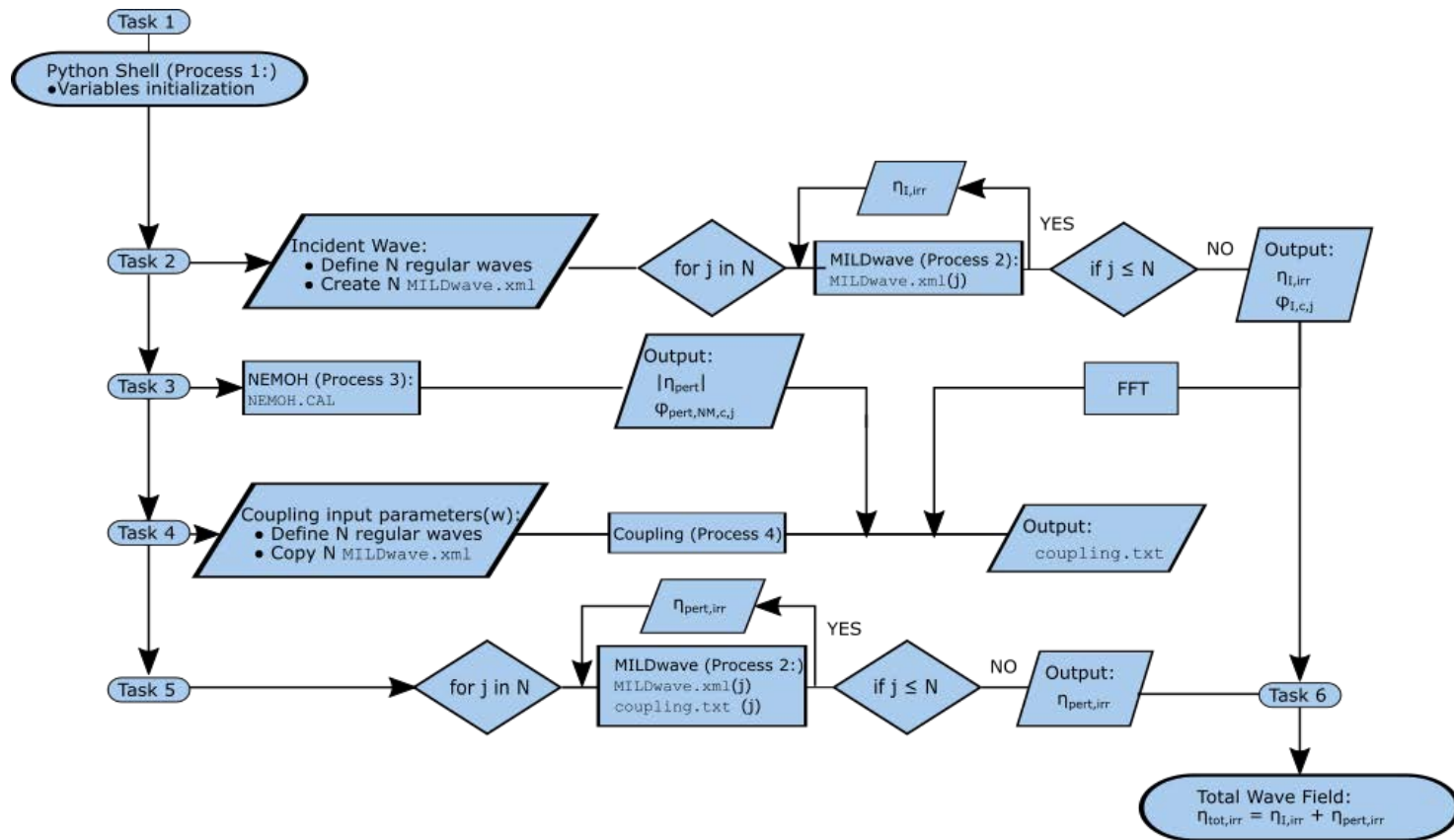


Figure 3.5: Implementation of the coupling algorithm.

3.3.3.1 Initialization - Task 1

In the first task the coupling algorithm runs the Python Shell (Process 1) to initialize all the computational variables:

1. Numerical basin parameters: width, length, bathymetry, coupling region, grid size, MILDwave grid, NEMOH grid.
2. Wave Parameters: wave type, wave height, wave period, mean wave direction.
3. Structure parameters: shape, number.
4. Simulation parameters: time step, simulation time, time series of surface elevation, number of components of the wave spectra.

The main input files for MILDwave and NEMOH are created using the selected parameters and saved on a main dedicated folder to perform the simulations.

3.3.3.2 Incident wave calculation in the time-domain - Task 2

In the second task, the Python Shell creates a sub-folder structure for running several times the MILDwave Process in parallel, for the incident wave simulation. This sub-folder structure contains a specific MILDwave input file for each regular wave component. Using the same numerical domain for all simulations, MILDwave requires different time steps based on the Courant-Friedrichs-Lewy criterion to obtain a convergent solution of the free surface elevation. To ensure an identical time series length and a random phase for each regular wave component each regular wave component input file is calculated from the main simulation parameters.

A new MILDwave time step for each regular wave is calculated based on the Courant-Friedrichs-Lewy condition, considering that is a multiple of the simulation time step:

$$\Delta t_{reg,j} = \frac{\Delta t_{sim}}{t_{step,j}} < \frac{\Delta x}{C_j}, \quad (3.16)$$

where $\Delta t_{reg,j}$ is the time step for each regular wave simulation, Δt_{sim} is the simulation time step, Δx is the grid size, C_j is the wave celerity of each regular wave component and $t_{step,j}$ is a natural number. A new time series of surface elevation is defined for each regular wave component. The time series length has to be equal for all simulations and it is obtained from the simulation time step. However, the simulation time to start saving each time series varies for each regular wave. Thereby, a random phase for each regular time series is obtained. The time to start computing the new time series is based on the group celerity and the width of the numerical basin to obtain an optimal computational time:

$$\text{time series}_j = \{t_{j,ini}, \dots, t_{j,n}, \dots, t_{j,fin}\}, \quad (3.17)$$

where,

$$t_{j,ini} = \frac{l_{domain}}{C_{g,j}} + t_{ramp}, \quad (3.18)$$

$$t_{j,n} = t_{j,n-1} + \Delta t_{reg,j} \cdot \Delta t_{step,j} = t_{j,n-1} + \Delta t_{sim}, \quad (3.19)$$

$$t_{j,fin} = t_{j,1} + t_{tot}, \quad (3.20)$$

where $t_{j,ini}$, $t_{j,n}$, and $t_{j,fin}$ are the initial, the n^{th} and the final time components of the regular wave surface elevation time series, respectively, and t_{tot} is the time series duration. t_{ramp} is the MILDwave internal ramping time to generate a regular wave and l_{domain} is the maximum distance from the wave generation line to the end of the numerical domain following the wave direction. Resulting in a total computational time for each regular wave simulation of:

$$t_{sim,j} = t_{j,ini} + t_{tot}, \quad (3.21)$$

where $t_{sim,j}$ is the simulation time for each wave component. Finally to ensure phase matching between the incident and the perturbed regular waves the initial time of the time series has to be a multiple of the regular wave period. Therefore:

$$t_{j,ini} = \left[\frac{t_{j,ini}}{T_j} \right] \cdot T_j. \quad (3.22)$$

Once the MILDwave input files for each regular wave component have been created, the Python Shell calls Process 2 in MILDwave, in parallel, to resolve the different regular wave simulations depending on the number of cores available. The parallelization has been implemented in Python using the "Subprocess" module. The regular wave executables are divided into groups of regular wave periods depending on the number of cores available. Then each group is run in parallel until all the simulations included are finished. Afterwards, the surface elevation for those simulations are added together and saved in the root incident wave simulation folder obtaining a temporal irregular wave surface elevation. The memory occupied by each regular wave is cleared, but the wave phase information at $t_{j,ini}$ at the coupling location is kept. The process is repeated until all the regular simulations are completed obtaining the incident irregular wave surface elevation as a superposition of regular waves.

Algorithm 3.1: Illustration of the implementation of the parallelization of Process 2 in MILDwave from the coupled model source code: mw_utilities_run.py

```

f_runs = [dir_Tnn[ii*n:(ii + 1)*n] for ii in range((len(dir_Tnn) + n - 1)//n)]

for subdir_mw in f_runs:
    execute_mw(dir_exe, subdir_mw)

    if os.path.exists(os.path.join(main_dir, 'eta.npy')):
        eta_irr = np.load('eta.npy')
    else:
        eta_irr = 0
    for dir_name in subdir_mw:
        with open('eta.bin') as feta:
            eta_irr += np.fromfile(feta)
        os.remove('eta.bin')
    np.save(main_dir, eta_irr)
    del eta_irr

def execute_mw(dir_exe, subdir_mw):
    cmds_list = [[dir_exe, 'MILDwave.xml']]
    procs_list = [Popen(cmd) for cmd in cmds_list]
    for proc in procs_list:
        proc.wait()

```

3.3.3.3 Perturbed wave calculation in the frequency-domain - Task 3

In the third task, the Python Shell calls Process 3 in NEMOH which solves the wave-structure interactions for the total number of components of the wave spectrum in a single numerical simulation. As a result, the perturbed wave field in the frequency-domain is obtained at the coupling location as a superposition of the radiated and diffracted complex wave fields. The results are stored in the main dedicated folder.

3.3.3.4 Coupling input parameters - Task 4

In the fourth task, the Python Shell calls Process 4, Coupling Process, to generate the input files needed to run the perturbed wave simulation in the time-domain. A sub-folder directory for the perturbed regular waves simulations is created copying the MILDwave input files from the incident wave sub-directory. Then a coupling input file, "coupling.txt", prescribing the internal wave generation boundary for the simulation is obtained for each regular wave. This file combines the results from the incident wave and NEMOH.

The coupling input file for each regular wave contains the following information for Equation 3.11:

1. The x and y coordinates of the internal wave generation boundary in the MILDwave domain.
2. The wave amplitude at each coordinate of the internal wave generation boundary calculated as $a_{I,c} \cdot |\eta_{pert}|$.
3. The wave phase of each coordinate of the internal wave generation boundary obtained as $\varphi_{pert,NM,c} + \varphi_{I,c}$.

$a_{I,c}$ is derived from the free surface elevation at the coupling location for the incident wave. A Fast Fourier Transformation (FFT) has been implemented in

Python using the "scipy.signal.welch" module. Using the spectral density contained in each wave frequency component, the amplitude of each regular wave is obtained in the frequency-domain. $|\eta_{pert}|$ and $\varphi_{pert,NM,c}$, and $\varphi_{I,c,t_j,ini}$ are directly obtained from the NEMOH and MILDwave simulations, respectively.

As a result, the algorithm for the implementation of a circular, squared or rectangular internal wave generation boundary has been coded as:

Algorithm 3.2: Generation of the coupling input file in Task 4 using Process 4 from the coupled model source code: coupling.py. The coupling input file contains the internal wave generation boundary used in Task 5 by Process 2 to perform a perturbed wave simulation in the time-domain.

```

pert_wave=amp_mw*pert_wave_nm*np.exp(1j*phase_mw[[center_ymw , center_xmw ]])

if MW.CPL['circ']:
    center_x = 0
    center_y = 0
    center_xmw = 0
    center_ymw = 0

    mask1 = np.sqrt((X-center_x)**2+(Y-center_y)**2)
        < MW.CPL['radius'] + dx
    mask2 = np.sqrt((Xmw-center_xmw)**2+(Ymw-center_ymw)**2)
        < MW.CPL['radius'] + dy

    yynm, xxnm = np.where(mask1)
    yymw, xxmw = np.where(mask2)

elif MW.CPL['rect']:
    xxh = int(NEM_GRID['Nx']/2) - int(MW.CPL['length']/(NEM_GRID['dx'] *2))
    yyh = int(NEM_GRID['Ny']/2) - int(MW.CPL['width']/(NEM_GRID['dy']*2))
    xxh_mw = int(MW_ini['Nx']/2) - int(MW.CPL['length']/(NEM_GRID['dx']*2))
    yyh_mw = int(MW_ini['Ny']/2) - int(MW.CPL['width']/(NEM_GRID['dy']*2))
    mask1 = np.zeros((np.shape(Y)[0], np.shape(X)[1]), dtype=bool)
    mask1[yyh:yyh+int(MW.CPL['width']/(NEM_GRID['dy']))],
        xxh:xxh+int(MW.CPL['length']/(NEM_GRID['dx']))] = True
    mask2 = np.zeros((np.shape(Ymw)[0], np.shape(Xmw)[1]), dtype=bool)
    mask2[yyh_mw:yyh_mw+int(MW.CPL['width']/(NEM_GRID['dy']))],
        xxh_mw:xxh_mw+int(MW.CPL['length']/(NEM_GRID['dx']))] = True
    yynm, xxnm = np.where(mask1)
    yymw, xxmw = np.where(mask2)

```

3.3.3.5 Perturbed wave calculation in the time-domain - Task 5

In the fifth task, the Python Shell calls again Process 2 in MILDwave in the subfolder structure, now for the perturbed wave simulation. Identically to the incident wave simulation, N regular wave simulations are computed in parallel, obtaining the perturbed irregular wave surface elevation as a superposition of regular waves. The internal wave generation boundary input conditions included in "coupling.txt" are transformed from the frequency-domain to the time-domain in Process 2 in MILDwave using the following algorithm:

Algorithm 3.3: Perturbed wave generation used in Task 5 by Process 2 from the MILD-wave source code: Calculations.ccp

```

case WaveGenerationSettings:: GenerationType:: coupling:

int xxh;
int yyh;

for (int i = 1; i <= nemoh_data.size(); i++)
|{
|  xx = floor(mGlobals->nemoh_data[i - 1][0]);
|  yy = floor(mGlobals->nemoh_data[i - 1][1]);
|
|  eta_inc = nemoh_data[i - 1][2] * cos(nemoh_data[i - 1][3] - MPITwt);
|
|  mGlobals->eta[xx][yy] = eta_inc;
|}

```

3.3.3.6 Total wave calculation in the time-domain - Task 6

Finally in the sixth task, the Python Shell superposes the results from the incident and the perturbed waves obtained in Tasks 2 and 5 resulting in the total surface elevation. From this results, it is possible to obtain relevant characteristics of the wave field such as the disturbance coefficient, the spectral density or the wave energy at any given location in the numerical basin.

3.4 Numerical validation of the MILDwave-NEMOH coupled model

A numerical validation is carried out by comparing the results from the MILDwave-NEMOH coupled model to those obtained from the numerical model NEMOH. This is done to ensure that the perturbed wave is correctly transferred from NEMOH to the MILDwave-NEMOH coupled model. The coupled model has been applied in a series of numerical test cases for different structure(s) and wave conditions.

3.4.1 Test Cases

The numerical validation aims to comprise a wide range of wave conditions, WEC types and array configurations. It demonstrates the application of the coupled model for a fixed wave height $H = 2.0$ m, different wave periods, a fixed width and length of the numerical domain (800 m \times 800 m), a fixed wave direction $\theta_{mean} = 0^\circ$ and two spreading parameters s_1 .

The regular waves selected include wave periods of $T = 6, 8$ and 10 seconds. The irregular wave set consists of a significant wave height of $H_s = 2.0$ m and peak periods $T_p = 6, 8$ and 10 seconds. A spreading parameter of $s_1 = 0$ is used for simulating long-crested irregular waves and $s_1 = 15.8$ is used for short-crested irregular waves. The range of the wave periods is selected from 6 to 10 seconds. This range includes values closer to the resonance period (T_r) of the WECs studied, for which the WEC motions are large, and values far from T_r where the motions of the WECs are reduced. This reproduces possible operational wave conditions for the WEC array.

Two different type of WEC(s) are studied:

1. Heaving Cylindrical Wave Energy Converter (HCWEC): is a disc shaped heaving buoy WEC with a diameter, \varnothing_{HC} , of 20 m, a height, h_{HC} of 4 m, and a draft, d_{HC} of 2 m. These WECs are designed to be deployed in deep water at depths around 30 m. This shape has been selected as it is one of the most investigated WEC types with several prototypes reaching pre-commercial WEC array testing stage. An illustration of the HCWEC modelled is depicted in Figure 3.6.
2. Oscillating Wave Surge Wave Energy Converter (OSWEC): the second structure chosen is a bottom-fixed pitching flap driven by the surge motion of the waves. These WECs are designed to be deployed in shallow water at depths of 10 - 20 m. The simulated WEC has dimensions of 20 m width, w_{OS} , 1 m thickness, t_{OS} , and 12 m height, h_{OS} and it is deployed at a water depth of 10 m. It is hinged at the sea bed with pitching motion about its bottom end. The OSWEC together with the HCWEC are two of the most investigated WEC types with several prototypes been developed over the past years. An illustration of the OSWEC modelled in NEMOH is shown in Figure 3.7.

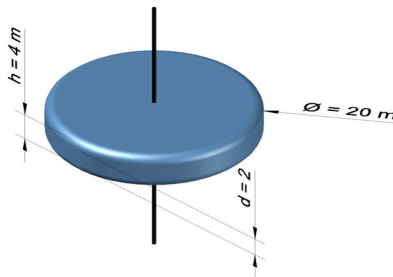


Figure 3.6: Sketch of the Heaving Cylindrical WEC used for the numerical validation.

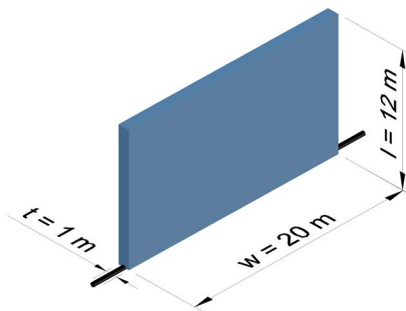


Figure 3.7: Sketch of the Oscillating Wave Surge WEC used for the numerical validation.

Firstly, each WEC is modelled independently over a constant bathymetry with a depth corresponding to that at the expected deployment site. Secondly, each WEC is modelled for two staggered array configurations of five and nine WECs. This type of configuration has been selected as it has been used in a wide number of studies and has shown to maximize the total power output of the WEC array, and thus maximizes the array impact on the surrounding wave field. Figure 3.8 (A) shows the staggered configuration of 5 HCWECs (H1), in green color and of 9 HCWECs (H2) combining the green and black solid circles. Identically, Figure 3.8 (B) shows the two staggered configurations of 5 (O1) and 9 (O2) OSWECs, indicated in green, and green and black, respectively.

Combining the different wave conditions, WEC types and WEC array layouts two sets of numerical test cases have been generated and are included in Tables 3.1 and 3.2, respectively:

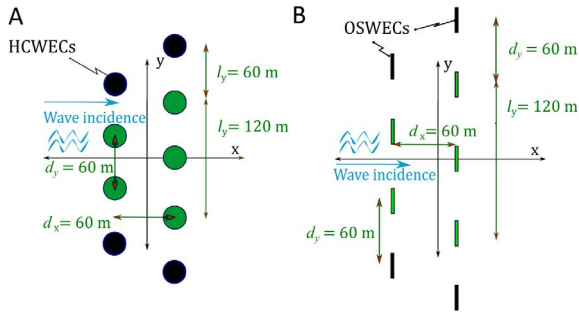


Figure 3.8: Plane (top) view of all different array layouts used for the numerical validation. (A) 5 and 9 HCWEC arrays, and (B) 5 and 9 OSWEC arrays.

Table 3.1: Numerical test cases for the Heaving Cylindrical Wave Energy Converter (HCWEC). The water depth, d , is 30 m, the width of the domain is 800 m and the length of the domain is 800 m.

Test Case Number	Wave Type	H (m)	T (s)	s_1 (-)	WEC (array)
1	REG	2	6	0	Single
2	REG	2	8	0	Single
3	REG	2	10	0	Single
4	REG	2	6	0	H2
5	REG	2	8	0	H2
6	REG	2	10	0	H2
7	IRREG	2	6	0	Single
8	IRREG	2	8	0	Single
9	IRREG	2	10	0	Single
10	IRREG	2	6	0	H1
11	IRREG	2	8	0	H1
12	IRREG	2	10	0	H1
13	IRREG	2	6	0	H2
14	IRREG	2	8	0	H2
15	IRREG	2	10	0	H2
16	IRREG	2	6	15.8	H2
17	IRREG	2	8	15.8	H2
18	IRREG	2	10	15.8	H2

Table 3.2: Numerical test cases for the Oscillating Wave Surge Energy Converter (OSWEC). The water depth, d , is 10 m, the width of the domain is 800 m and the length of the domain is 800 m.

Test Case Number	Wave Type	H (m)	T (s)	s_1 (-)	WEC (array)
19	REG	2	6	0	Single
20	REG	2	8	0	Single
21	REG	2	10	0	Single
22	REG	2	6	0	O2
23	REG	2	8	0	O2
24	REG	2	10	0	O2
25	IRREG	2	6	0	Single
26	IRREG	2	8	0	Single
27	IRREG	2	10	0	Single
28	IRREG	2	6	0	O1
29	IRREG	2	8	0	O1
30	IRREG	2	10	0	O1
31	IRREG	2	6	0	O2
32	IRREG	2	8	0	O2
33	IRREG	2	10	0	O2
34	IRREG	2	6	15.8	O2
35	IRREG	2	8	15.8	O2
36	IRREG	2	10	15.8	O2

3.4.2 Numerical set-up in MILDwave

In MILDwave, simulations are carried out in two types of numerical wave basins (see A and B in Figure 3.9) with an effective domain (area not covered by the wave absorbing sponge layers) extended in the x and y axis, and a constant water depth of 30 m and 10 m for the HCWEC and the OSWECs, respectively.

For the simulations performed to obtain the incident wave field, waves are generated using a linear wave generation line located at the left side of the numerical domain with two equally sized wave absorbing sponge layers placed up-wave (left) and down-wave (right), as indicated in Figure 3.9 (A).

For the simulations carried out to obtain the perturbed wave field, waves are generated using an internal wave generation boundary (Figure 3.9 (B)). The type of wave generation boundary used is discussed in Section 3.5, performing a sensitivity analysis between the circular and rectangular wave generation boundaries implemented in the model and different extensions. Four equally sized wave absorbing sponge layers are placed at all sides of the numerical domain.

The total dimensions of the total numerical wave basin in MILDwave are not always the same, as the length of the wave absorbing sponge layers (B_s) is different

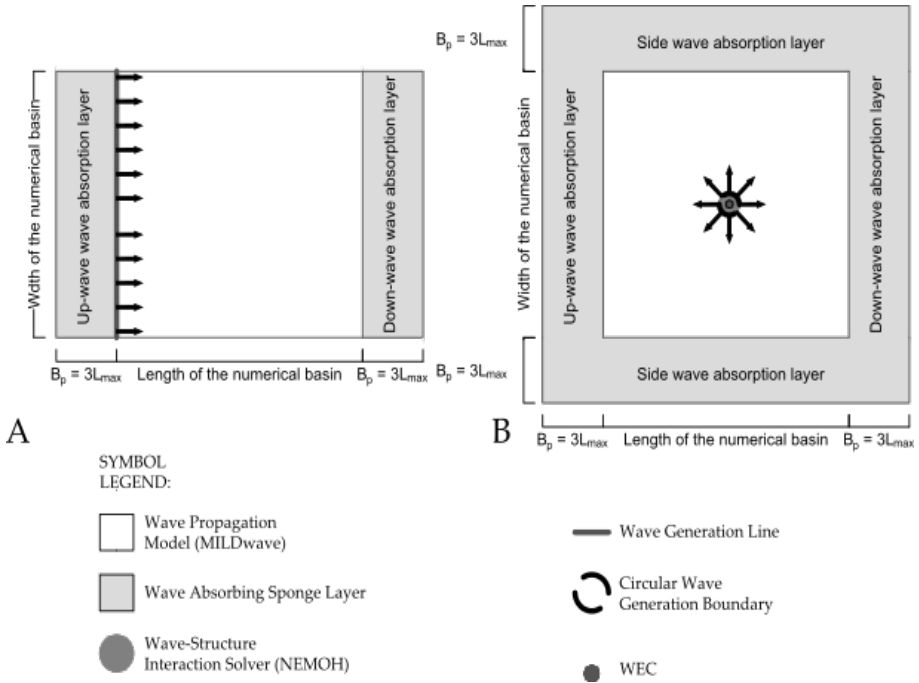


Figure 3.9: Set-up of the different numerical wave basins used in MILDwave. (A) Empty Numerical wave basin and (B) Numerical wave basing with a single WEC.

for each set of wave conditions and depends on L . For regular waves the recommendation by Beels (2009) are followed to use $B = 3xL$, as the wave reflection coefficient drops to 1 %. As irregular waves are obtained as a superposition of N_f regular wave components, B_s is calculated using the maximum L of the discretized spectra, L_{max} , which corresponds to T_{max} .

The total wave field of the MILDwave-NEMOH coupled model is obtained as the superposition of the numerical results from the domains of Figure 3.9 (A) and, Figure 3.9 (B), respectively.

3.4.3 Numerical set-up in NEMOH

NEMOH simulations are carried out in a numerical domain of 800 m width, and 800 m length and constant water depth of 30 m and 10 m for the HCWEC and the OSWECs, respectively. The HCWEC and OSWEC have been discretized using 200 and 300 panels, respectively. The effect of the WEC's PTO system is taken into account adding the suitable external damping coefficient, B_{PTO} , in the equation of motion (Equation 3.9).

For the numerical validation test cases, the optimal $B_{PTO,opt}$ that maximizes the energy conversion for a single WEC in regular waves is used (Cargo et al. (2012)) using as input the peak angular frequency, ω_p . It can be derived from the

following expression:

$$B_{PTO,opt} = \sqrt{(B_{hyd}^2 + (\omega_p(M + M_A) - \frac{K_H}{\omega_p})^2)}. \quad (3.23)$$

The $B_{PTO,opt}$ results have been summarized in Table 3.3.

Table 3.3: Optimal $B_{PTO,opt}$ used in the MILDwave-NEMOH coupled model numerical validation.

	$B_{PTO,opt}$		
	$T = 6 \text{ s}$	$T = 8 \text{ s}$	$T = 10 \text{ s}$
HCWEC [$kg \cdot s^{-1}$]	$1.14 \cdot 10^6$	$1.84 \cdot 10^6$	$2.74 \cdot 10^6$
OSWEC [$kg \cdot m^2 s^{-2}$]	$107.92 \cdot 10^6$	$102.36 \cdot 10^6$	$86.17 \cdot 10^6$

3.4.4 Criteria Used for the numerical validation

The comparison between the MILDwave-NEMOH coupled model and NEMOH is assessed by calculating the K_d disturbance values, as defined in Equations 3.24 and 3.26 for regular waves, and Equations 3.25 and 3.27 for irregular waves. K_d is defined as the ratio between the numerically calculated local total wave height, H_{tot} , and the incident wave height, H_I , imposed along the linear wave generation boundary. In the MILDwave-NEMOH coupled model the $K_{d,coupled}$ is obtained in the time-domain for regular waves as:

$$K_{d,cp,reg} = \frac{H_{tot}}{H_I} = \frac{\sqrt{8 \cdot \sum_t^{\Delta t} (\eta_{I,reg,t} + \eta_{pert,reg,t})^2 \cdot \frac{dt}{\Delta t}}}{H_I}, \quad (3.24)$$

$$K_{d,cp,irr} = \frac{H_{s,tot}}{H_{s,I}} = \frac{4 \cdot \sqrt{\sum_t^{\Delta t} (\eta_{I,irr,t} + \eta_{pert,irr,t})^2 \cdot \frac{dt}{\Delta t}}}{H_{s,I}}, \quad (3.25)$$

where $\eta_{I,reg,t}$, $\eta_{I,irr,t}$, $\eta_{pert,reg,t}$ and $\eta_{pert,irr,t}$ are the free surface elevation for regular and irregular incident and perturbed waves in each time step dt , from the domains of Figure 3.9 (A) and, Figure 3.9 (B), respectively, and Δt is the time window over which the K_d is computed. In NEMOH, the $K_{d,NEMOH}$ is obtained in the frequency-domain as:

$$K_{d,reg,NM} = \frac{|\hat{\eta}_{tot,reg,freq}|}{H_I}, \quad (3.26)$$

$$K_{d,irr,NM} = \frac{|\hat{\eta}_{tot,irr,freq}|}{H_{s,I}}, \quad (3.27)$$

where $|\hat{\eta}_{tot,reg,freq}|$ and $|\hat{\eta}_{tot,irr,freq}|$ are the absolute value of free surface elevation for the complex total wave obtained in the frequency-domain for regular and irregular waves, respectively.

The K_d value is an useful parameter that has been used extensively in literature to study wave field variations ((Beels et al., 2010b, 2011; Stratigaki, 2014; Troch and Stratigaki, 2016; Verbrugge et al., 2017; Sismani et al., 2017; Tomey-Bozo et al., 2018; Stratigaki et al., 2011)). $K_d > 1$ and $K_d < 1$ indicate increase and decrease of the local wave height, respectively. When studying WEC arrays, increases in the local wave height indicates the presence of "hot spots" (Iglesias and Carballo (2010)), defined as areas of high wave energy concentration. Instead, decrease in the local wave height indicates the so-called "wake" effects, which result in an area of reduced wave energy.

To evaluate K_d differences between the MILDwave-NEMOH coupled model and NEMOH, four different outputs have been generated:

1. K_d contour plots of the entire numerical domain;
2. K_d cross-sections along the length of the numerical domain (parallel to the wave propagation direction);
3. Contour plots of the "Relative Difference" between the obtained K_d values (RD_{K_d}) defined as:

$$RD_{K_d} = \frac{(K_{d,NEMOH} - K_{d,coupled})}{K_{d,NEMOH}} \cdot 100 \quad \% \quad ; \quad (3.28)$$

4. The Root Mean Square Error between K_d values obtained using the MILDwave-NEMOH coupled model and NEMOH for the entire numerical domain ($RMSE_{K_d,G}$):

$$RMSE_{K_d,G} = \sqrt{\frac{\sum_{i=1}^G (K_{d,NEMOH} - K_{d,coupled})^2}{G}} \cdot 100 \quad \% \quad , \quad (3.29)$$

where G is the number of grid points of the numerical domain.

3.5 Sensitivity analysis

Before performing the numerical simulations for the test cases listed in Tables 3.1 and 3.2, a sensitivity analysis is carried out to ensure a converging result of the regular and irregular waves simulations, while keeping the computational time low. Five critical parameters have been identified in the MILDwave-NEMOH coupled model affecting the convergence of the results:

1. The type of internal wave generation boundary.
2. The dimensions of the internal wave generation boundary.
3. The computational grid cell size (d_x and d_y).

4. The number of regular wave components, N .
5. The directional spreading function $D(f, \theta)$.

The first three parameters are important for all type of waves generated, the fourth parameter is specific of irregular waves and the fifth parameter is specific of short-crested irregular waves. In the following sections, each of the parameters will be analysed to obtain a general guideline of recommended simulation parameters for the MILDwave-NEMOH coupled model.

The sensitivity analysis has been performed for all regular and irregular Test Cases of Table 3.1 and for a single HCWEC. Nevertheless, in this section it is only demonstrated for Test Cases 2, 13 and 18. The convergence of the MILDwave-NEMOH model is assessed in terms of K_d values and the simulation parameters that lead to a convergent result, keeping the computational time low, are selected.

3.5.1 Internal wave generation boundary

The influence of the internal wave generation boundary has been evaluated using the three types that can be prescribed with the MILDwave-NEMOH coupled model: a circular, squared and rectangular wave generation boundary. The dimensions of any internal wave generation boundary have to be defined in relation to the structure(s) geometry inside it. A minimum distance from the center of the internal wave generation boundary to the outside limit needs to be equal to the distance from its center to the furthest structure plus a wave propagation area. The extension of the wave propagation area is studied in Section 3.5.2 with respect to the wavelength.

For the considered Test Case 2 of a single HCWEC, the circular wave generation boundary has a coupling radius, $R_c = 0.5L + 0.5\phi_{HC}$ (Figure 3.10 (A)), the squared wave generation boundary has a width and length = $L + \phi_{HC}$ (Figure 3.10 (B)), and the rectangular wave generation boundary has a width = $2L + \phi_{HC}$ and a length = $L + \phi_{HC}$ (Figure 3.10 (C)). The rest of the simulation parameters have been kept constant and are included in Table 3.4.

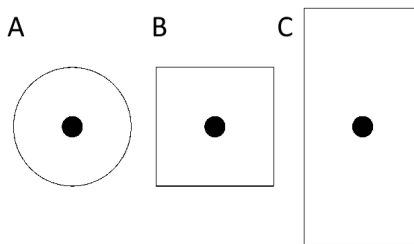


Figure 3.10: Sketch of the different internal wave generation boundaries used in the simulation sensitivity analysis. Circular (A), squared (B) and rectangular wave generation boundaries.

Table 3.4: Simulation parameters used for the internal wave generation boundary sensitivity analysis.

Test Case 2		
Parameter	Symbol	Value
Wave Height	H	2.0 m
Wave Period	T	8.0 s
Grid cell size x-axis	d_x	$L/20 = 4.8$ m
Grid cell size y-axis	d_y	$L/20 = 4.8$ m
Simulation time	t_{sim}	600 s
Time step	Δt	$T/20 = 0.4$ s
Water Depth	d	30.0 m

Figure 3.11 shows the K_d results for Test Case 2 and for the circular internal wave generation boundary. The K_d for the different internal wave generation boundaries is presented using two longitudinal cross-sections across the center of the domain; at $y = 0$ m, and at $y = -200$ m in Figures 3.12 and 3.13, respectively. The same simulation is performed in NEMOH and plotted together with the MILDwave-NEMOH coupled model results.

It can be observed that all the internal wave generation boundaries slightly overestimate the K_d . Nevertheless, the difference between all of them and NEMOH never exceeds 2 %. In Figure 3.13 a small phase shift between the K_d calculated by MILDwave-NEMOH coupled model and NEMOH is observed towards the edge of the numerical basin. This is caused due to the different way MILDwave and NEMOH obtain the K_d in the far field. MILDwave uses a planar wave approximation to propagate the perturbed wave field, while NEMOH uses the Kochin-Functions to calculate the far field complex amplitudes.

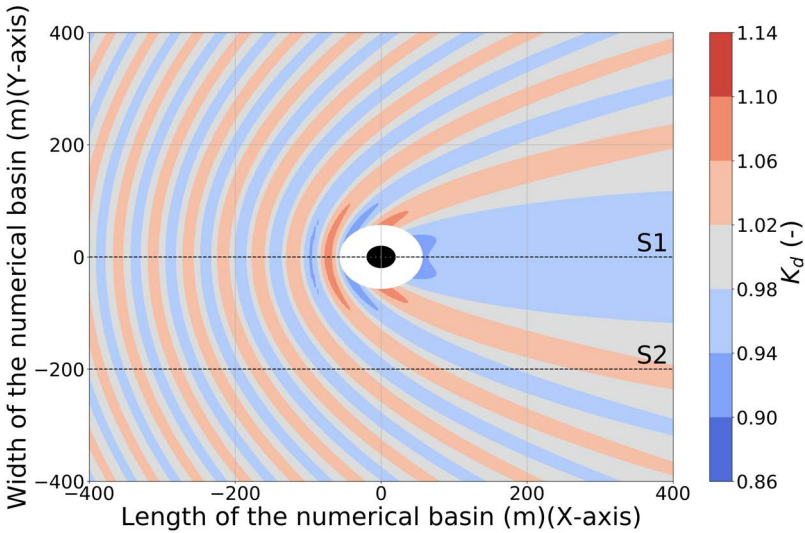


Figure 3.11: K_d disturbance coefficient results for a single HCWEC interacting with a regular wave with $H = 2.0$ m and $T = 8.0$ s. The results are obtained using the MILDwave-NEMOH coupled model for Test Case 2. The coupling region is filled using a white solid circle which includes the WEC (indicated by using a black solid circle). Incident waves are generated from the left to the right. S1 and S2 indicate the location of cross-sections.

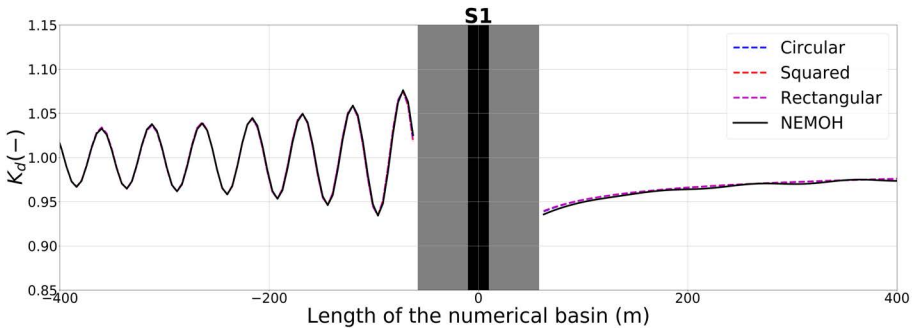


Figure 3.12: K_d disturbance coefficient results for the MILDwave-NEMOH coupled model along one longitudinal cross-section S1 as indicated in Figure 3.11 for a single HCWEC interacting with a regular wave of $H = 2$ m and $T = 8$ s. The results are obtained using the MILDwave-NEMOH coupled model with different internal wave generation boundaries for Test Case 2. The coupling region is filled in gray colour and includes the WEC's cross-section, which is indicated by a black vertical area.

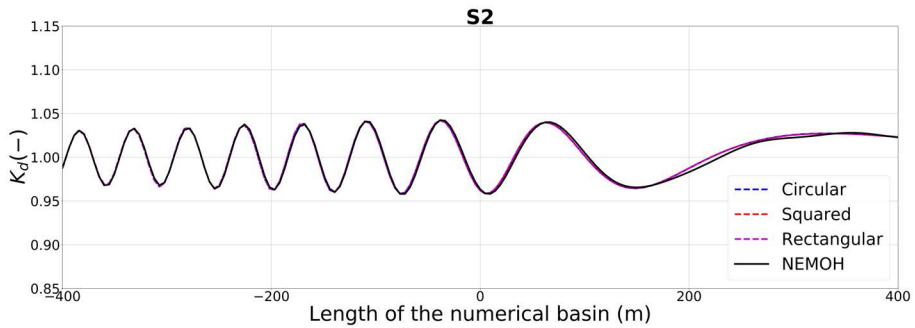


Figure 3.13: K_d disturbance coefficient results for the MILDwave-NEMOH coupled model along one longitudinal cross-section S2 as indicated in Figure 3.11 for a single HCWEC interacting with a regular wave of $H = 2$ m and $T = 8$ s. The results are obtained using the MILDwave-NEMOH coupled model with different internal wave generation boundaries for Test Case 2.

Therefore it can be concluded that any of the three types of wave generation boundaries studied can be used to obtain a convergent solution. For the rest of the simulations in this manuscript, a circular wave generation boundary has been employed.

3.5.2 Dimensions of the internal wave generation boundary

As reported in Section 3.5.1, R_c can be obtained as:

$$R_c = 0.5L + 0.5\phi_{HC}. \quad (3.30)$$

The length of R_c has been studied for different propagation areas in relation to the wavelength. A sensitivity analysis has been performed using Test Case 2, by running 5 simulations with simulation parameters of Table 3.4. Different R_c ranging from $0.2L + 0.5\phi_{HC}$ to $2L + 0.5\phi_{HC}$ have been tested. K_d value are calculated over a longitudinal cross-section across the center of the domain and the results for the different simulations are included in Figure 3.14:

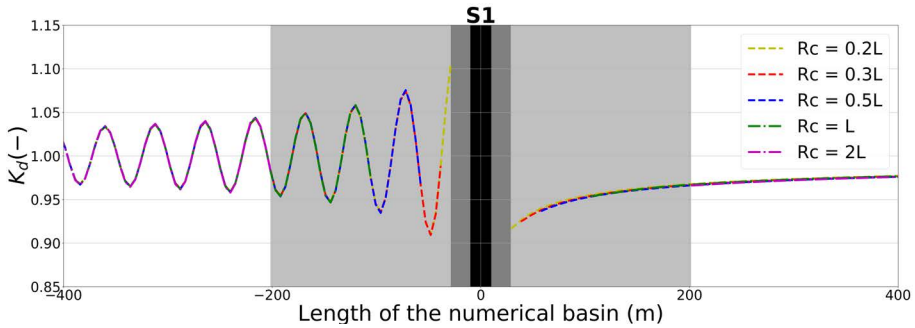


Figure 3.14: K_d disturbance coefficient results for the MILDwave-NEMOH coupled model along one longitudinal cross-section S1 as indicated in Figure 3.11 for a single HCWEC interacting with a regular wave of $H = 2$ m and $T = 8$ s. The results are obtained using the MILDwave-NEMOH coupled model with different coupling radii for Test Case 2. The inner coupling radius is filled in dark grey colour and includes the WEC's cross-section, which is indicated by a black vertical area, and the external coupling radius is filled in light grey.

In Figure 3.14, it is observed that for the three largest coupling radii the same convergent results are achieved. Even for the two shortest R_c , the difference between the different simulations never exceeds 2%. Therefore, any coupling radius in the range studied would be suitable to perform the simulations. For the rest of the simulations, a $R_c = 0.5L + 0.5\phi_{HCWEC}$ has been chosen.

3.5.3 Grid cell size

3.5.3.1 Regular Waves

The grid cell size resolution has been studied for regular waves with respect to the wavelength, L . The internal circular wave generation boundary previously defined and the simulation parameters of Table 3.4 are employed. Five different grid cell sizes have been used: $d_x = d_y = L/10$, $L/20$, $L/25$, $L/30$ and $L/40$. K_d values for the different grid sizes are presented using longitudinal cross-sections across the center of the domain; at $y = 0$ m, and at $y = -200$ m in Figures 3.15 and 3.16, respectively.

It can be seen that in the lee of the coupling region the K_d results have converged for all grid cell sizes. On the contrary, in the front of the coupling region it is observed that the coarsest grid cell size is not able to capture in detail wave reflection, showing spikes in the crests and troughs. Furthermore, looking at a distance of $-y = 200$ m from the center of the domain a phase shift between the coarsest grid cell size and the rest of the grid cell sizes tested can be noticed. Therefore, it can be concluded that a minimum grid cell size $d_x = d_y = \frac{L}{20}$ is necessary to ensure a K_d convergent solution in regular waves.

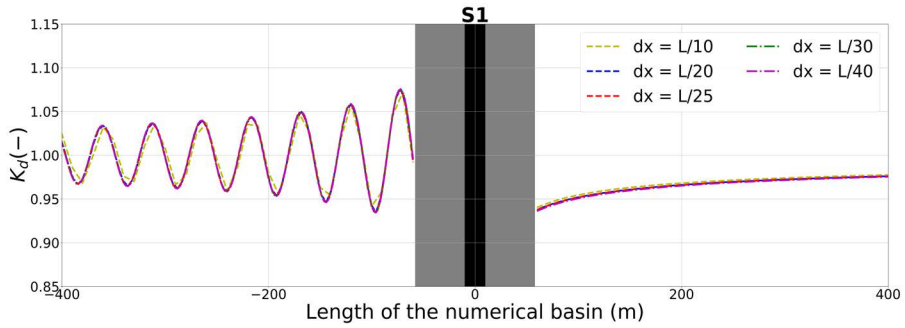


Figure 3.15: K_d disturbance coefficient results for the MILDwave-NEMOH coupled model along one longitudinal cross-section S1 as indicated in Figure 3.11 for a single HCWEC interacting with a regular wave of $H = 2$ m and $T = 8$ s. The results are obtained using the MILDwave-NEMOH coupled model with different grid size resolutions for Test Case 2. The coupling region is filled in gray colour and includes the WEC's cross-section, which is indicated by a black vertical area.

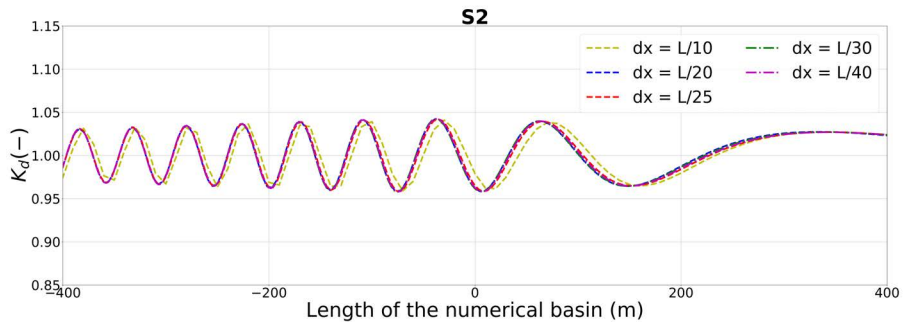


Figure 3.16: K_d disturbance coefficient results for the MILDwave-NEMOH coupled model along one longitudinal cross-section S2 as indicated in Figure 3.11 for a single HCWEC interacting with a regular wave of $H = 2$ m and $T = 8$ s. The results are obtained using the MILDwave-NEMOH coupled model with different grid size resolutions for Test Case 2.

3.5.3.2 Irregular Waves

Considering the coupling implementation detailed in Section 3.3.1 it is reasonable to assume that for an irregular wave calculation the optimal grid cell size would be $d_x = d_y = L_{min}$ and the optimal coupling radius propagation length $= 0.5L_{min}$. L_{min} is the minimum wavelength of the N regular wave components that are simulated. If the latter does not affect the simulation time, a too fine grid cell size for the high period regular wave components will increase the computational time considerably. To illustrate this, the total simulation time for the regular wave simulations used for the regular wave grid cell size sensitivity analysis is shown in Table 3.5.

As it can be observed the computational time increases considerably with the

Table 3.5: Computational time for the Test Case 2 grid size sensitivity analysis

Test Case Number	Grid cell size (m)	Computational time (s)
2	$L/10 = 10$	20
2	$L/20 = 4.8$	50
2	$L/25 = 4$	120
2	$L/30 = 3$	162
2	$L/40 = 2$	300

grid cell size and thus it can be computationally very demanding when applying the model in large coastal areas. Therefore, it is more reasonable to study the convergence of the K_d in irregular waves with respect to the peak wavelength L_p . Three different simulations for Test Case 13 have been performed using $d_x = d_y = L_p/25$, $L_p/30$ and $L_p/40$ for all regular wave components. The irregular wave simulation parameters are included in Table 3.6.

The numerical spectral density in MILDwave, $S_{n,M}(f)$ is obtained at the center of the coupling region for the incident wave simulation. The comparison with the theoretical spectral density $S_t(f)$ is shown in Figure 3.18. The K_d in the entire numerical domain for Test Case 13 and $d_x = d_y = L_p/40$ is illustrated in Figure 3.17. Two longitudinal cross-sections including the K_d for all grid cell sizes, are drawn through: the centre of the domain, at $y = 0$ m (S1) and at $y = -200$ m (S2), in Figure 3.20.

Table 3.6: Simulation parameters for the irregular wave grid cell size sensitivity analysis

Test Case 13		
Parameter	Symbol	Value
Significant wave height	H_s	2.0 m
Peak wave period	T_p	6.0 s
Spectrum	Pierson–Moskowitz	[-]
Grid cell size x-axis	d_x	1.4 1.8 2.0 m
Grid cell size y-axis	d_y	1.4 1.8 2.0 m
Total simulation time	t_{sim}	3000 s
Time step	Δt	$T_p/20 = 0.3$ s
Water depth	d	30.0 m

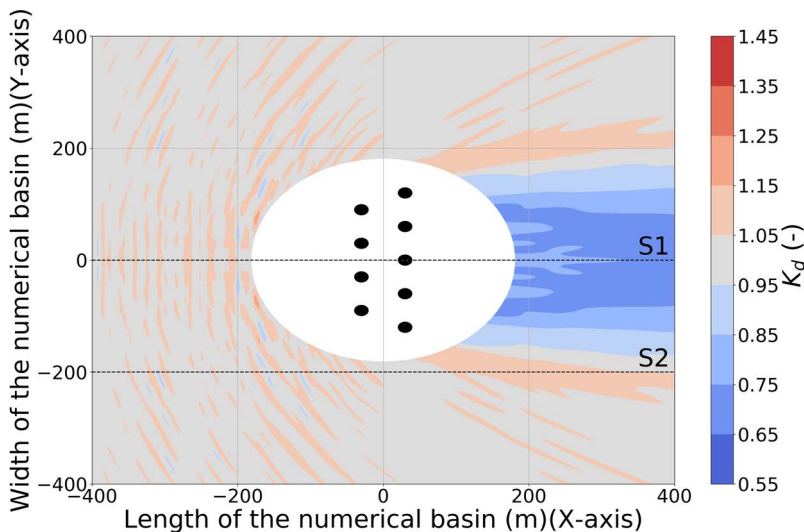


Figure 3.17: K_d disturbance coefficient results for a 9-HCWEC array interacting with an irregular wave with $H_s = 2.0$ m and $T_p = 6.0$ s. The results are obtained using the MILD-NEMOH coupled model for Test Case 13. The coupling region is filled using a white solid circle which includes the WECs (indicated by using a black solid circles). Incident waves are generated from the left to the right. S1 and S2 indicate the location of cross-sections.

As expected, with the finest grid cell size resolution it is possible to obtain an accurate representation of the theoretical spectrum. When reducing the grid cell size resolution, it can be observed in Figure 3.18 that high frequency waves are carrying more energy than in the theoretical spectrum. This is because, these waves have a smaller wavelength and the number of grid points per wavelength is not sufficient to provide a good representation. Nevertheless, the wave height and wave period obtained in each numerical simulation do not differ much from the target wave height and period as seen in Table 3.7.

Furthermore, it is reasonable to assume that the wave spectrum concentrates over a limited bandwidth around the peak frequency. As shown in Sheng and Li (2017), for the same spectra used in this sensitivity analysis, 50 % of the energy is concentrated within a bandwidth of 0.05 Hz around the peak wave period.

Table 3.7: Significant wave height, H_s , and peak period, T_p , achieved during the irregular waves grid size sensitivity analysis simulations.

Simulation	H_s	Target H_s	T_p	Target T_p
$d_x = d_y = L_p/25$	2.024 m	2.0 m	7.877 s	8.0 s
$d_x = d_y = L_p/30$	2.043 m	2.0 m	7.877 s	8.0 s
$d_x = d_y = L_p/40$	2.018 m	2.0 m	7.877 s	8.0 s

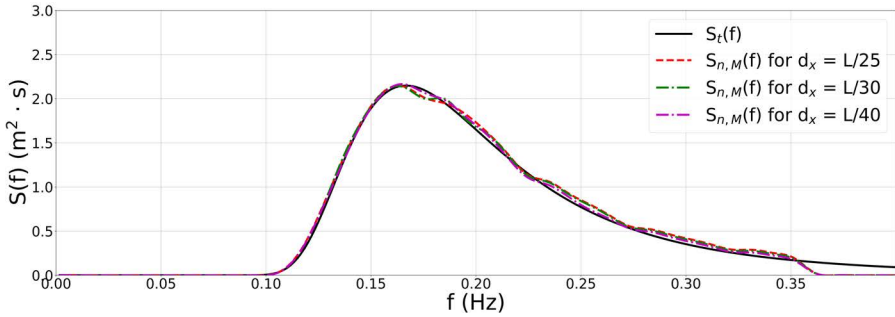


Figure 3.18: Numerical wave spectrum $S_{n,M}(f)$ generated at the centre of the MILDwave numerical domain for an incident irregular wave with $H_s = 2.00$ m and $T_p = 6.0$ s and different grid cell sizes $d_x (=d_y)$.

Consequently, the regular waves included in these bandwidth will have a higher impact in the perturbed wave field than the regular wave components of the higher frequency band. Therefore, it is reasonable to assume that a certain error in the high frequency band of the spectra will not have a major impact when calculating the perturbed wave field around the structure(s). This can be seen in Figure 3.19, showing a cross-section of the perturbed wave field across the center of the domain. For a grid cell size larger than $d_x = d_y = L/25$, convergence is obtained between the different simulations. The difference between the K_d disturbance coefficient values never exceeds a 5% between each simulation.

However, the cross-sections of the total wave field in Figure 3.20, indicate a large difference between the studied grid cell size resolutions. A convergent result with NEMOH is obtained for $d_x = d_y = L_p/40$. The small phase-shift noticed in

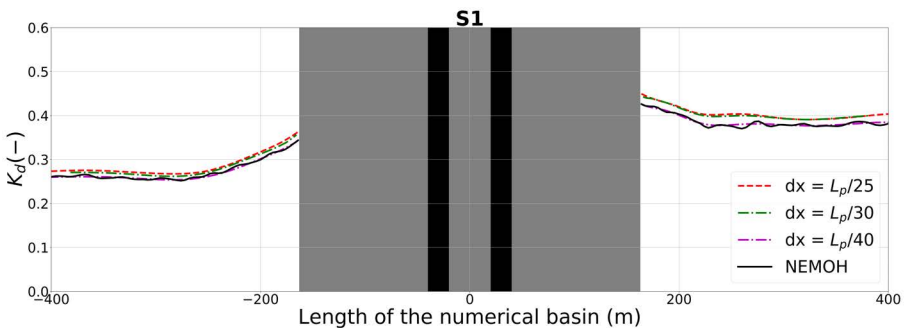


Figure 3.19: Perturbed wave field K_d disturbance coefficient results along one longitudinal cross-section S1 as indicated in Figure 3.17 for a 9-HCWE array interacting with an irregular wave of $H_s = 2$ m and $T_p = 6$ s. The results are obtained for the MILDwave-NEMOH coupled model and NEMOH obtained using different grid cell size resolutions for Test Case 13. The coupling region is filled in gray colour and includes the WECS' cross-section, which are indicated by black vertical areas.

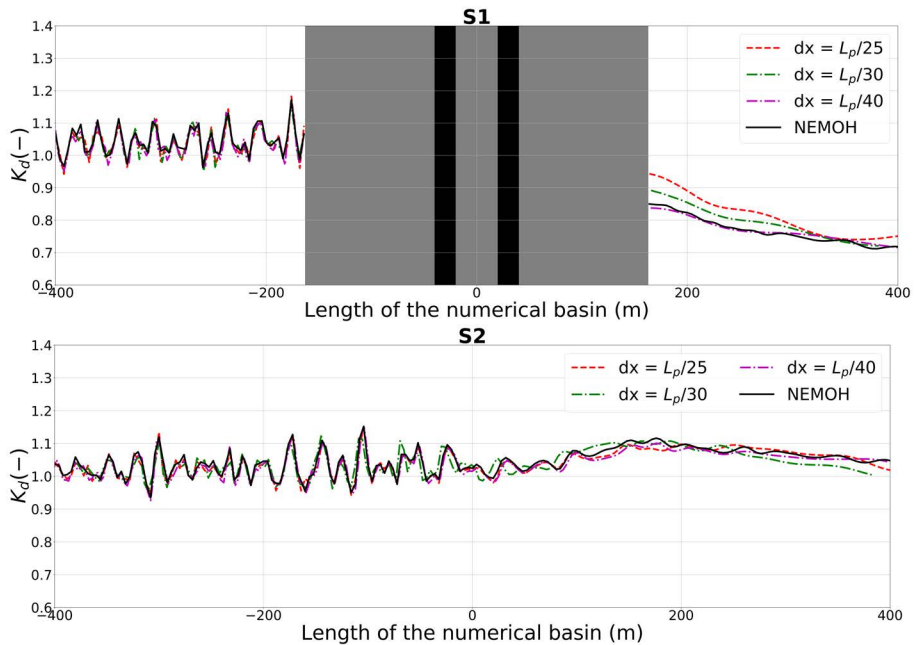


Figure 3.20: K_d disturbance coefficient results along two longitudinal cross-sections S1 (up) and S2 (bottom) as indicated in Figure 3.17 for a 9-HCWEC array interacting with an irregular wave of $H_s = 2$ m and $T_p = 6$ s. The results are obtained using the MILDwave-NEMOH coupled model and for NEMOH different grid cell size resolutions for Test Case 13. The coupling region is filled in gray colour and includes the WEC's cross-section, which is indicated by a black vertical area.

Figure 3.16 due to the coarse MILDwave grid cell size is affecting the K_d calculation close to the coupling region, where the radiation effects of the high frequencies are still important. An incorrect match of the incident and the perturbed wave cannot represent the constructive or destructive interactions of the different wave components correctly close to the WECs. Nevertheless, it can be noticed that towards the end of the numerical basin all the K_d simulations do not differ more than a 5% from each other. The further away from the WECs, the less important is the effect of the phase-shift in the high-frequency band as the contribution of the high frequency components to the far-field effects becomes smaller.

As a result, a selection has been made to obtain accurate and computationally viable simulations with the MILDwave-NEMOH coupled model. If a high accuracy of the spectra is needed and a good resolution in the near field is required a grid size equal to $L_p/40$ should be used. If an overestimation in the wave-structure interactions on the high frequency bandwidth of the spectra is acceptable, a grid size equal to $L_p/30$ is sufficient. For the rest of this chapter a grid size, $d_x = d_y = L_p/40$ has been chosen.

3.5.4 Number of regular wave components

The numerical wave spectrum generated at the center of the MILDwave domain, $S_{n,M}(f)$, for different N_f for Test Case 7 are compared to the theoretical wave spectrum, $S_t(f)$, in Figure 3.21. All the simulation parameters included in Table 3.6 are kept constant and $d_x = d_y = L_p/40$. Simulations are performed for $N_f = 15, 20$ and 40 . There is a good agreement between $S_{n,M}(f)$ and $S_t(f)$ for 20 and 40 regular wave components with a slight amount of spurious energy for high wave frequencies that is not reduced when increasing N_f . The accuracy gained by increasing N_f from 20 to 40 is not significant, as the $S_{n,M}(f)$ peak and the energy contained within the $S_{n,M}(f)$ curve is practically the same. Nonetheless, as indicated in Table 3.8, an increment of 1.8 points in the computational time is observed when moving from 20 to 40 regular wave components. Consequently, it is concluded that increasing N_f is not required and therefore N_f is kept to 20 to reduce the computational time.

Finally, a longitudinal cross-section for each simulation across the center of the domain, at $y = 0$ m (S1) is shown in Figure 3.22. As expected, there is a convergent K_d in the lee of the coupling region. In front of the coupling region, it is not possible to achieve an identical K_d , as different regular wave components are solved in each case. This causes different reflected waves on the structure(s) superposing with different locations for the constructive and destructive effects. Nevertheless, the magnitude of this reflections range from 0.97 to 1.03 K_d value

Table 3.8: Computational time in hours (h) for Test Case 7 number of regular wave components sensitivity analysis

Test Case Number	Regular wave components	Computational time (h)
7	$N_f = 15$	2.71
7	$N_f = 20$	3.55
7	$N_f = 40$	6.40

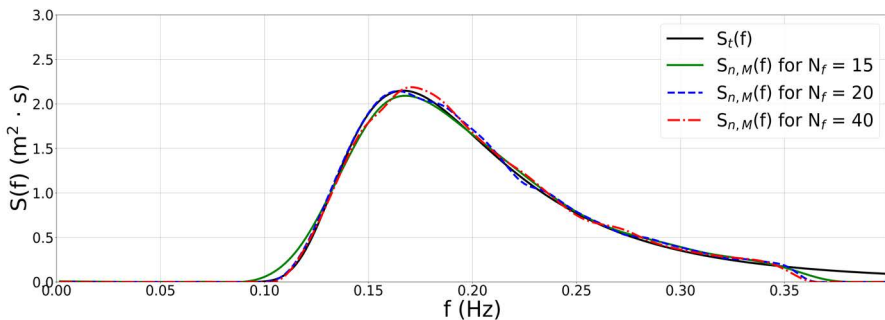


Figure 3.21: Numerical wave spectrum $S_{n,M}(f)$ generated at the centre of the MILDwave numerical domain for an incident irregular wave with $H_s = 2$ m and $T_p = 6$ s using a different number of regular wave components, N_f .

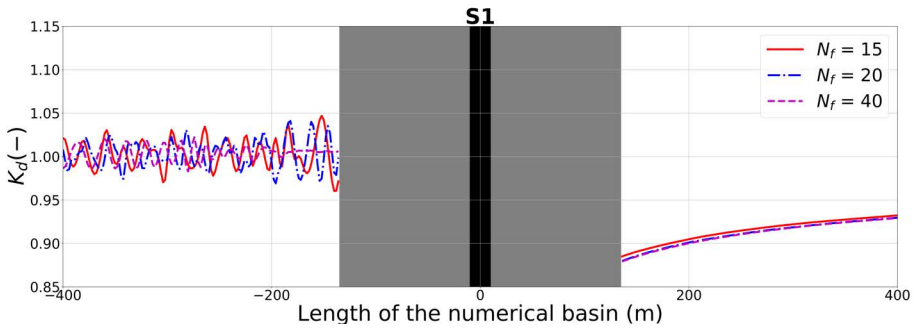


Figure 3.22: K_d disturbance coefficient results along one longitudinal cross-sections S1 as indicated in Figure 3.17 for Test Case 7, with $H_s = 2$ m and $T_p = 6$ s. The results are obtained using the MILDwave-NEMOH coupled model with different regular wave components, N_f . The coupling region is filled in gray colour and includes the WEC's cross-section, which is indicated by a black vertical area.

for all the simulations.

3.5.5 Directional spreading function

The last part of the sensitivity analysis is to obtain the correct normalised spreading function distribution for different short-crested irregular wave simulations. The methodology introduced in Section 3.3.1.1 randomly assigns a wave direction θ for each frequency of the discretized spectra, causing that each simulation will generate a different normalised spreading function.

Ten different simulations with $H_s = 2.0$ m, $T_p = 8.0$ s and $s_1 = 15.8$ have been performed using the parameters included in Table 3.9. A normalised spreading function close to the theoretical one is obtained for all the test cases, as illustrated in Figure 3.23. Figure 3.23 shows the normalised spreading function, $D(f, \theta)_i$, for four simulations and the normalised theoretical spreading function, $D(f, \theta)_t$.

Table 3.9: Simulation parameters used in the directional spreading function sensitivity analysis

Parameter	Symbol	Value
Significant wave height	H_s	2.0 m
Peak wave period	T_p	8.0 s
Spectra	Pierson–Moskowitz	[-]
Directional spreading parameter	s_1	15.8
Grid cell size x-axis	d_x	4.0 m
Grid cell size y-axis	d_y	4.0 m
Simulation time	t_{sim}	4000 s
Time step	Δt	$T_p/20 = 0.4$ s
Water depth	d	30.0 m

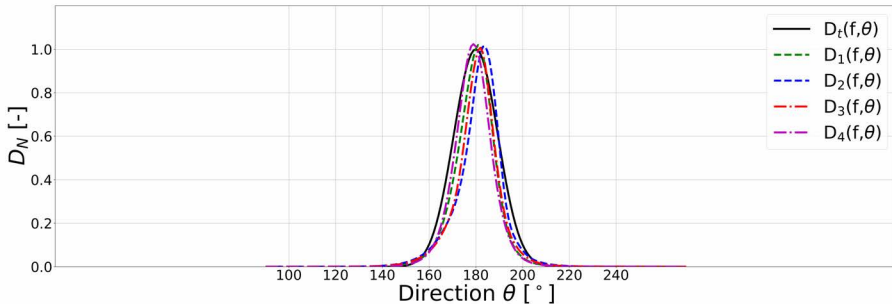


Figure 3.23: Normalised spreading function distributions D_N generated at the centre of the MILDwave numerical domain for an incident irregular wave with $H_s = 2$ m and $T_p = 8$ s using different randomly generated short-crested sea states with $s_1 = 15.8$.

Still, the wave frequencies where the WEC is extracting more energy will not necessarily be close to the θ_{mean} as they are randomly assigned. Consequently an asymmetric diffraction and radiation pattern interacting with the incident wave field will be generated. Therefore, for comparing the effect on the total wave field of short-crested irregular waves to those of long-crested waves it is not possible to use a single simulation (one sea-state). An average of the K_d over a different number of simulations should be used instead, to assess the impact of short-crested waves. In this way it is possible to account for the different wave attack angles of the frequencies of the discretized spectra close to the absorb bandwidth of the WEC(s). There, more energy will be extracted from the waves and that is randomly changed in each simulation. Figure 3.24 shows the $K_{d,avg}$ for a total of $M = 10$ simulations with a randomly generated directional spectra in each case, using the simulation parameters included in Table 3.9 and a single HCWEC. It can be seen that the average tends to be symmetric along the x-axis corresponding with $\theta_{mean} = 0^\circ$, with waves propagating from left to right.

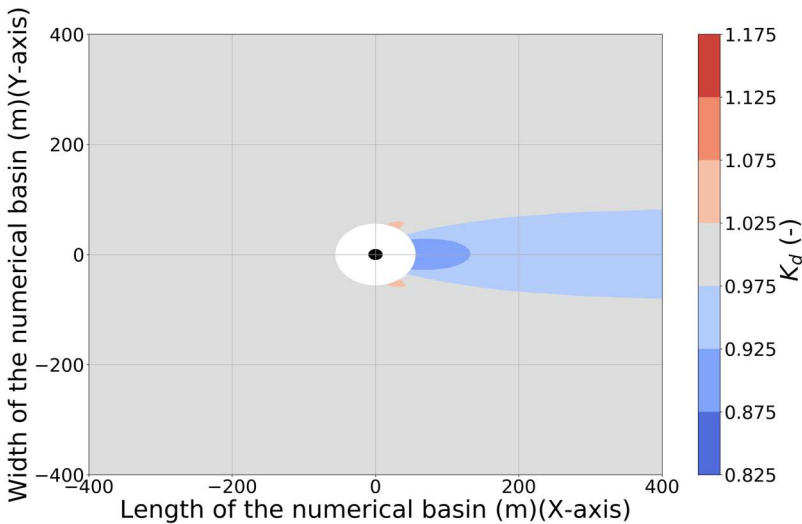


Figure 3.24: K_d disturbance coefficient results for a single HCWEC interacting with an irregular wave with $H_s = 2.0$ m, $T_p = 8.0$ s and $s_1 = 15.8$. The results are obtained using the MILDwave-NEMOH coupled model. The coupling region is filled using a white solid circle which includes the WEC (indicated by using a black solid circle). Incident waves are generated from the left to the right.

3.6 Numerical validation results

An extensive comparison will be made for three relevant Test Cases: Test Case 13, Test case 18 and Test Case 31.

3.6.1 Test Case 13

As described in Table 3.1, Test Case 13 consists on simulating a nine HCWEC array under the effect of long-crested irregular waves with $H_s = 2.0$ m and $T_p = 6$ s. Two numerical simulations are performed, one in the MILDwave-NEMOH coupled model and one in NEMOH. The simulation results are compared to determine if there is a correct exchange of information between the MILDwave and NEMOH domains through the coupling interface. The simulation parameters used for the MILDwave-NEMOH coupled model and NEMOH simulations are included in Tables 3.10 and 3.11, respectively.

The K_d results are illustrated in Figures 3.25 and 3.26 for the MILDwave-NEMOH coupled model and NEMOH, respectively. The coupling region is indicated using a white solid circle and is not considered for the comparison. In both figures it is possible to observe a diffraction-reflection pattern in front and around the WEC array with increased values of K_d and an area of reduced K_d in the lee of the array. The magnitude of both areas are within the same range for both numerical models.

Table 3.10: Simulation parameters for the Test Case 13 using the MILDwave-NEMOH coupled model.

Test Case 13		
Parameter	Symbol	Value
Significant wave Height	H_s	2.0 m
Peak wave Period	T_p	6.0 s
Spectra	Pierson–Moskowitz	PM
MILDwave effective length of the Basin	-	807.8 m
MILDwave effective width of the Basin	-	807.8 m
Grid cell size x-axis	d_x	1.4 m
Grid cell size y-axis	d_y	1.4 m
Simulation time	t_{sim}	3000 s
Time step	Δt	$T_p/20 = 0.3$ s
Water depth	d	30.0 m
Internal wave generation boundary	Circular	$R_c = 182.7$ m
NEMOH length of the basin	-	392.0 m
NEMOH width of the basin	-	392.0 m

Table 3.11: Simulation parameters for the Test Case 13 using NEMOH.

Test Case 13		
Parameter	Symbol	Value
Significant wave height	H_s	2.0 m
Peak wave period	T_p	6.0 s
Spectra	Pierson–Moskowitz	PM
Grid cell size x-axis	d_x	4.0 m
Grid cell size y-axis	d_y	4.0 m
Water depth	d	30.0 m
NEMOH length of the basin	-	800.0 m
NEMOH width of the basin	-	800.0 m

For the numerical validation, K_d values obtained with the MILDwave-NEMOH coupled model and with NEMOH are compared by means of the relative difference in K_d , RD_{K_d} . A RD_{K_d} contour plot for Test Case 13 is illustrated in Figure 3.27. The MILDwave-NEMOH coupled model provides lower K_d results than NEMOH in the wave reflection zone up-wave of the WECs as indicated by positive values of RD_{K_d} . The magnitude of the wake effects down-wave is lower for the MILDwave-NEMOH coupled model as indicated by negative values of RD_{K_d} . The maximum and minimum values of RD_{K_d} are 3.69 % and - 3.48 %, respectively. As seen in Figure 3.27, these values are located close to the coupling region towards the lee of the WEC array, where the radiation effects have a high impact in the wave field. In this area, the influence of the high wave frequency components of the

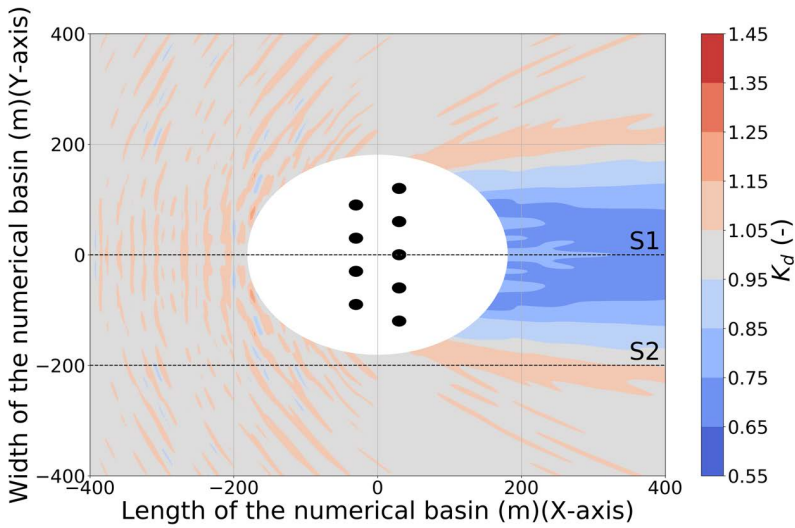


Figure 3.25: K_d disturbance coefficient results for a 9-HCWEC array interacting with an irregular wave with $H_s = 2.0$ m and $T_p = 6.0$ s. The results are obtained using the MILDwave-NEMOH coupled model for Test Case 13. The coupling region is filled using a white solid circle which includes the WECs (indicated by using black solid circles). Incident waves are generated from the left to the right. S1 and S2 indicate the location of cross-sections.

spectra on the perturbed wave field is still significant. It is not perfectly modelled in MILDwave due to the small phase-shift with coarse grid cell size compared to the wavelength.

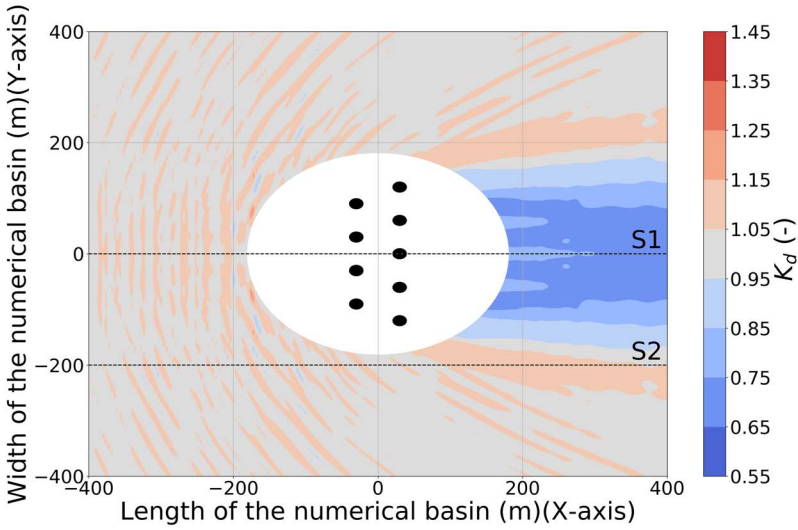


Figure 3.26: K_d disturbance coefficient results for a 9-HCWEC array interacting with an irregular wave with $H_s = 2.0$ m and $T_p = 6.0$ s. The results are obtained using NEMOH for Test Case 13. The coupling region is filled using a white solid circle which includes the WECs (indicated by using black solid circles). Incident waves are generated from the left to the right. S1 and S2 indicate the location of cross-sections.

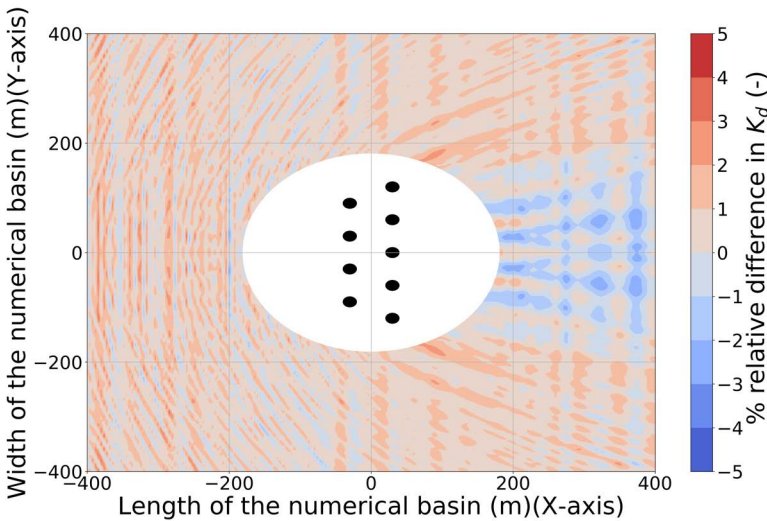


Figure 3.27: Relative difference (%) in K_d disturbance coefficient, RD_{K_d} between the MILDwave-NEMOH coupled model and NEMOH for a 9-HCWEC array interacting with an irregular wave with $H_s = 2.0$ m and $T_p = 6.0$ s. The results are obtained for Test Case 13. The coupling region is filled using a white solid circle which includes the WECs (indicated by using black solid circles).

To have a closer look to the comparison between the K_d results from the MILDwave-NEMOH coupled model and NEMOH, two longitudinal cross-sections (indicated in Figure 3.28) are drawn: through the centre of the domain, at $y = 0$ m (S1), and at $y = -200$ m (S2). Again, the coupled zone is filled using gray colour. There is very good agreement for K_d results between the MILDwave-NEMOH coupled model and NEMOH. By evaluating the cross-sections for the rest of the Test Cases of the HCWEC, included in Appendix B, it is observed that: the MILDwave-NEMOH coupled model K_d values are lower in the wave reflection and diffraction regions in front and at the side of the WECs, and higher in the region where "wake effects" occur in the lee of the WECs, compared to NEMOH.

This difference is related to the number of WECs simulated and the hydrodynamic interactions between the WECs and the incident wave. In general, the difference between the two models increases with the number of WECs and is affected by the WEC array impacts on the incident wave field. This is clear when looking at the results from Test Case 13 in Figure 3.27. The RD_{K_d} in the lee of the array, oscillates between negative and positive values. Even though, the grid resolution is fine, the high frequency components phase shift is influencing the superposition between the incident and the perturbed wave field in the coupled

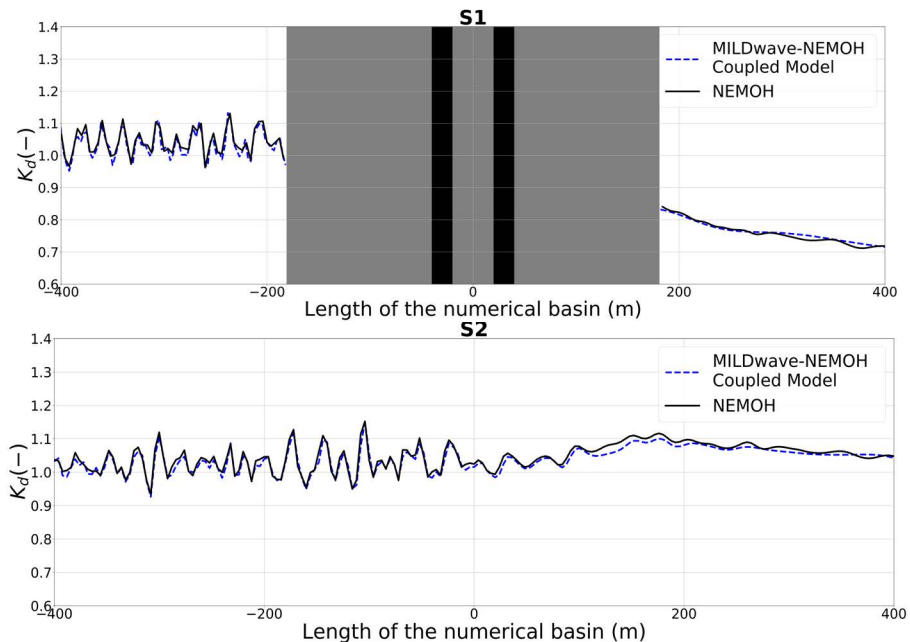


Figure 3.28: K_d disturbance coefficient results along two longitudinal cross-sections S1 (up) and S2 (bottom) as indicated in Figure 3.25 for a 9-HCWEC array interacting with an irregular wave of $H_s = 2$ m and $T_p = 6$ s. The results are obtained using the MILDwave-NEMOH coupled model and NEMOH for Test Case 13. The coupling region is filled in gray colour and includes the WECs' cross-sections, which are indicated by black vertical areas.

model.

3.6.2 Test Case 31

As defined in Table 3.2, Test Case 31 consists on simulating a nine OSWEC array under the effect of long-crested irregular waves with $H_s = 2.0$ m and $T_p = 6$ s. Similarly, results from the MILDwave-NEMOH coupled model are compared to NEMOH results. The simulation parameters used are included in Tables 3.12 and 3.13, respectively.

K_d results are illustrated in Figures 3.29 and 3.30 for the MILDwave-NEMOH coupled model and NEMOH, respectively. In both figures it is possible to observe

Table 3.12: Simulation parameters for the Test Case 31 using the MILDwave-NEMOH coupled model.

Test Case 31		
Parameter	Symbol	Value
Significant wave height	H_s	2.0 m
Peak wave period	T_p	6.0 s
Spectra	Pierson–Moskowitz	[-]
MILDwave effective length of the Basin	-	807.8 m
MILDwave effective width of the Basin	-	807.8 m
Grid size x-axis	d_x	1.4 m
Grid size y-axis	d_y	1.4 m
Simulation time	t_{sim}	3000 s
Time step	Δt	$T_p/20 = 0.3$ s
Water depth	d	10.0 m
Internal wave generation boundary	Circular	$R_c = 182.7$ m
NEMOH length of the Basin	-	392.0 m
NEMOH width of the Basin	-	392.0 m

Table 3.13: Simulation parameters for the Test Case 31 using NEMOH.

Test Case 31		
Parameter	Symbol	Value
Significant wave height	H_s	2.0 m
Peak wave period	T_p	6.0 s
Spectra	Pierson–Moskowitz	[-]
Grid cell size x-axis	d_x	4.0 m
Grid cell size y-axis	d_y	4.0 m
Water Depth	d	10.0 m
NEMOH length of the basin	-	800.0 m
NEMOH width of the basin	-	800.0 m

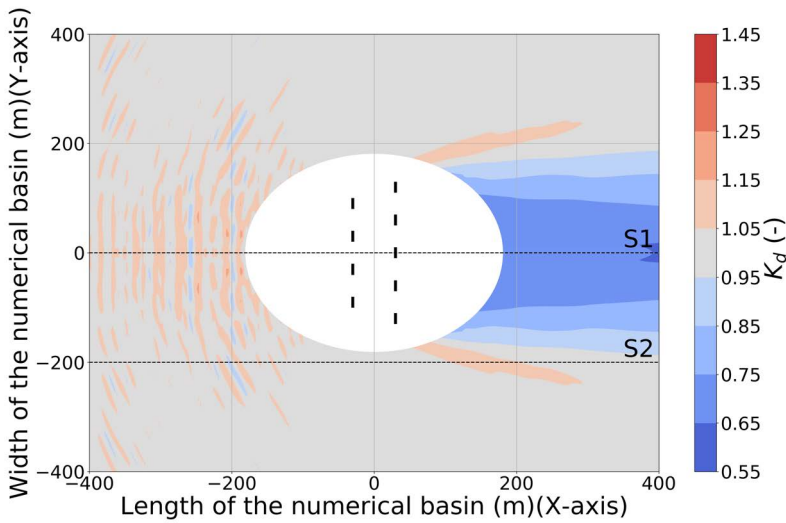


Figure 3.29: K_d disturbance coefficient results for a 9-OSWEC array interacting with an irregular wave with $H_s = 2.0$ m and $T_p = 6.0$ s. The results are obtained using the MILDwave-NEMOH coupled model for Test Case 31. The coupling region is filled using a white solid circle which includes the WECs (indicated by using black solid rectangles). Incident waves are generated from the left to the right. S1 and S2 indicate the location of cross-sections.

a diffraction-reflection pattern in front of the WEC array with increased values of K_d and an area of reduced K_d in the lee of the array. The wave field on the sides of the array is almost not affected as expected for an OSWEC. The magnitude of both areas are within the same range for both numerical models with similar contour lines.

A RD_{K_d} contour plot for Test Case 31 is illustrated in Figures 3.31. Like in Test Case 13, the MILDwave-NEMOH coupled model provides lower K_d results than NEMOH in the wave reflection zone up-wave of the WECs, and higher K_d results than NEMOH in the lee of the WEC array. The maximum and minimum values of RD_{K_d} are 3.17 % and - 4.32 %, respectively. Identically to Test Case 13, these values are located close to the coupling region towards the lee of the WEC array, where the radiation effects have a high impact in the wave field.

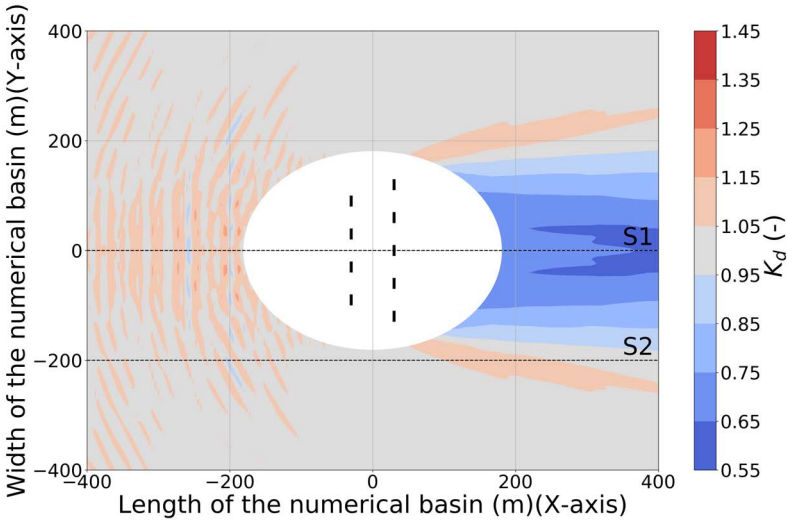


Figure 3.30: K_d disturbance coefficient results for a 9-OSWEC array interacting with an irregular wave with $H_s = 2.0$ m and $T_p = 6.0$ s. The results are obtained using NEMOH for Test Case 31. The coupling region is filled using a white solid circle which includes the WECs (indicated by using black solid rectangles). Incident waves are generated from the left to the right. S1 and S2 indicate the location of cross-sections.

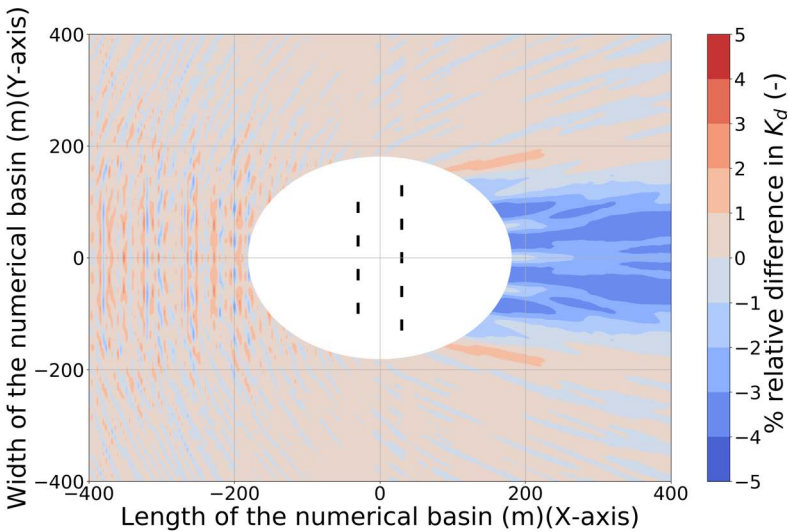


Figure 3.31: Relative difference (%) in K_d disturbance coefficient, RD_{K_d} between the MILDwave-NEMOH coupled model and NEMOH for a 9-OSWEC array interacting with an irregular wave with $H_s = 2.0$ m and $T_p = 6.0$ s. The results are obtained for Test Case 31. The coupling region is filled using a white solid circle which includes the WECs (indicated by using black solid rectangles).

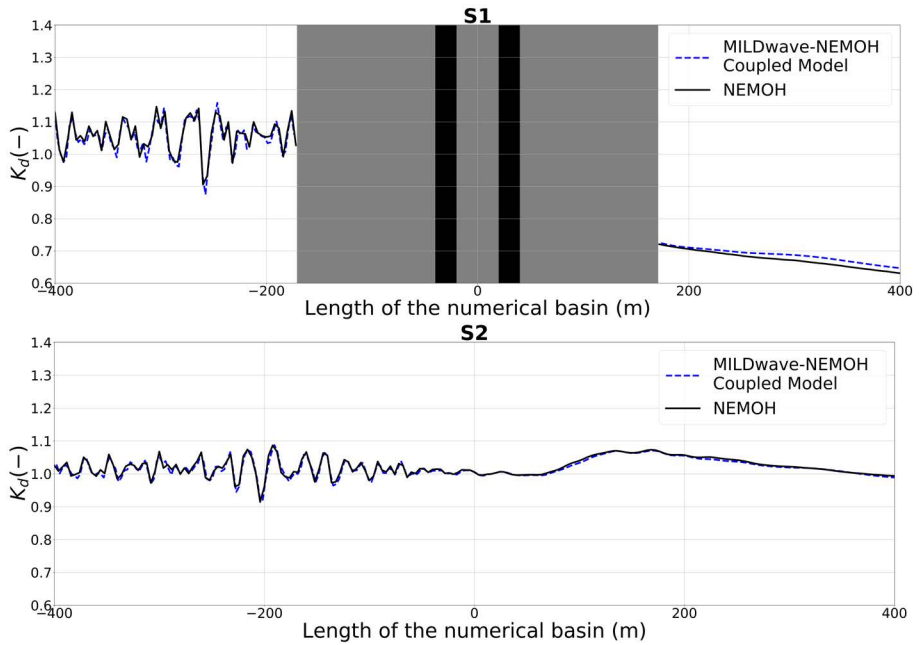


Figure 3.32: K_d disturbance coefficient results along two longitudinal cross-sections S1 (up) and S2 (bottom) as indicated in Figure 3.25 for a 9-OSWEC array interacting with an irregular wave of $H_s = 2$ m and $T_p = 6$ s. The results are obtained using the MILDwave-NEMOH coupled model and NEMOH for Test Case 31. The coupling region is filled in gray colour and includes the WECs' cross-sections, which are indicated by black vertical areas.

K_d results from the MILDwave-NEMOH coupled model and NEMOH at two longitudinal cross-sections (indicated in Figure 3.32) are drawn: through the centre of the domain, at $y = 0$ m (S1) and at $y = -200$ m (S2). There is a very good agreement for K_d results between the MILDwave-NEMOH coupled model and NEMOH.

3.6.3 Test Case 16

Test Case 16 consists on simulating a nine HCWEC array under the effect of short-crested irregular waves with $H_s = 2.0$ m, $T_p = 6.0$ s and $s_1 = 15.8$. Similarly, Test Case 16 has been simulated using the MILDwave-NEMOH coupled model and NEMOH. The simulation parameters are included in Table 3.14 and 3.15, respectively.

K_d results are illustrated in Figures 3.33 and 3.34 for the MILDwave-NEMOH coupled model and NEMOH, respectively. In both figures it is possible to observe a diffraction-reflection pattern in front of the WEC array with increased values of K_d and an area of reduced K_d in the lee of the array.

As discussed in Section 3.5.5, it is not possible to obtain a symmetric wake

Table 3.14: Simulation parameters for the Test Case 16 using the MILDwave-NEMOH coupled model.

Test Case 16		
Parameter	Symbol	Value
Significant wave height	H_s	2.0 m
Peak wave Period	T_p	6.0 s
Spectra	Pierson–Moskowitz	[-]
Directional spreading parameter	s_1	15.8
MILDwave effective length of the Basin	-	807.8 m
MILDwave effective width of the Basin	-	807.8 m
Grid cell size x-axis	d_x	1.4 m
Grid cell size y-axis	d_y	1.4 m
Simulation time	t_{sim}	3000 s
Time step	Δt	$T_p/20 = 0.3$ s
Water depth	d	30.0 m
Internal wave generation boundary	Circular	$R_c = 182.7$ m
NEMOH length of the Basin	-	392.0 m
NEMOH width of the Basin	-	392.0 m

Table 3.15: Simulation parameters for the Test Case 16 using NEMOH.

Test Case 16		
Parameter	Symbol	Value
Significant wave height	H_s	2.0 m
Peak wave period	T_p	6.0 s
Spectra	Pierson–Moskowitz	[-]
Directional spreading parameter	s_1	15.8
Grid cell size x-axis	d_x	4.0 m
Grid cell size y-axis	d_y	4.0 m
Water depth	d	30.0 m
NEMOH length of the Basin	-	800.0 m
NEMOH width of the Basin	-	800.0 m

effect of a WEC array under short-crested irregular waves. Nevertheless, for a single random simulation, the magnitude of both wake areas are within the same range for both numerical models. The extents of this areas are similar, with maximum and minimum values of RD_{K_d} of 3.35 % and - 1.6 %, respectively as seen in Figure 3.35. Additionally, the numerically obtained normalised spreading function distribution has a good agreement with the theoretical one as shown in Figure 3.36.

Finally, K_d results from the MILDwave-NEMOH coupled model and NEMOH at two longitudinal cross-sections (indicated in Figure 3.37) are drawn: through the centre of the domain, at $y = 0$ m (S1) and at $y = -200$ m (S2). There is very

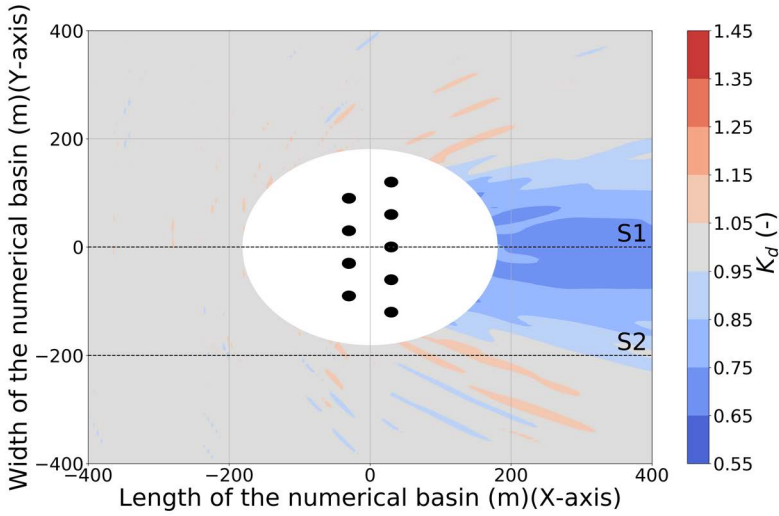


Figure 3.33: K_d disturbance coefficient results for a 9-HCWE array interacting with an irregular wave with $H_s = 2.0$ m , $T_p = 6.0$ s and $s_1 = 15.8$ [-]. The results are obtained using the MILDwave-NEMOH coupled model for Test Case 16. The coupling region is filled using a white solid circle which includes the WECs (indicated by using black solid circles). Incident waves are generated from the left to the right. S1 and S2 indicate the location of cross-sections.

good agreement for K_d results between the MILDwave-NEMOH coupled model and NEMOH. Therefore, it can be concluded that a randomly generated short-crested sea state can be correctly transferred between MILDwave and NEMOH.

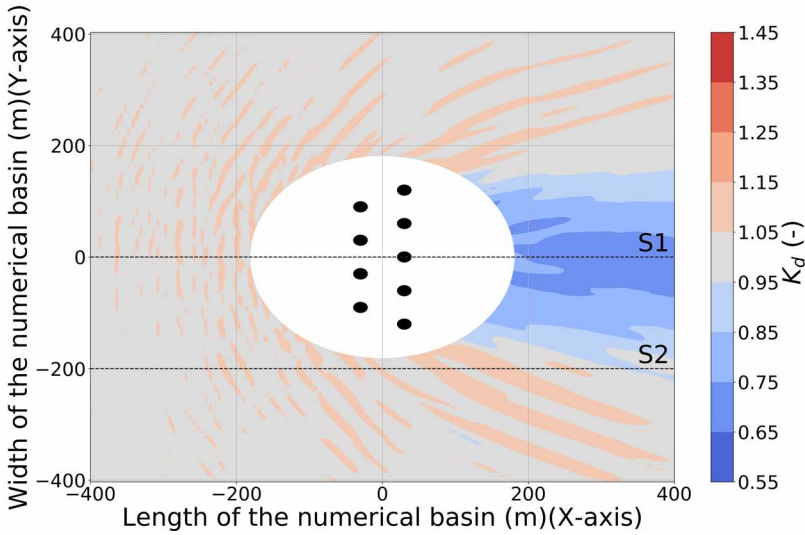


Figure 3.34: K_d disturbance coefficient results for a 9-HCWEC array interacting with an irregular wave with $H_s = 2.0$ m , $T_p = 6.0$ s and $s_1 = 15.8$ [-]. The results are obtained using NEMOH for Test Case 16. The coupling region is filled using a white solid circle which includes the WECs (indicated by using black solid circles). Incident waves are generated from the left to the right. S1 and S2 indicate the location of cross-sections.

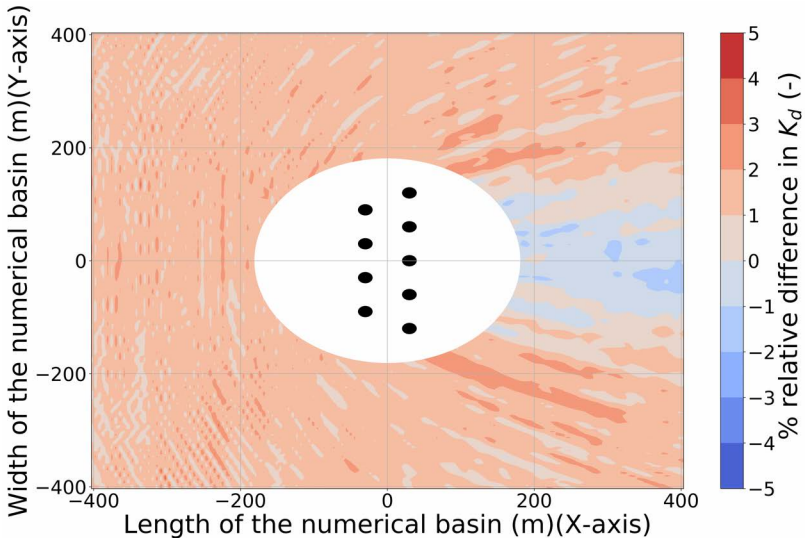


Figure 3.35: Relative difference (%) in K_d disturbance coefficient, RD_{K_d} between the MILDwave-NEMOH coupled model and NEMOH for a 9-HCWEC array interacting with an irregular wave with $H_s = 2.0$ m , $T_p = 6.0$ s and $s_1 = 15.8$ [-]. The results are obtained for Test Case 16. The coupling region is filled using a white solid circle which includes the WECs (indicated by using black solid circles).

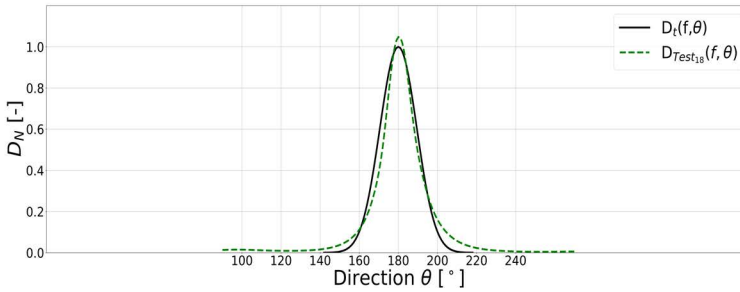


Figure 3.36: Normalised spreading function distributions D_N generated at the centre of the MILDwave numerical domain for an incident irregular wave with $H_s = 2$ m and $T_p = 6$ s and $s_1 = 15.8$ for Test Case 16.

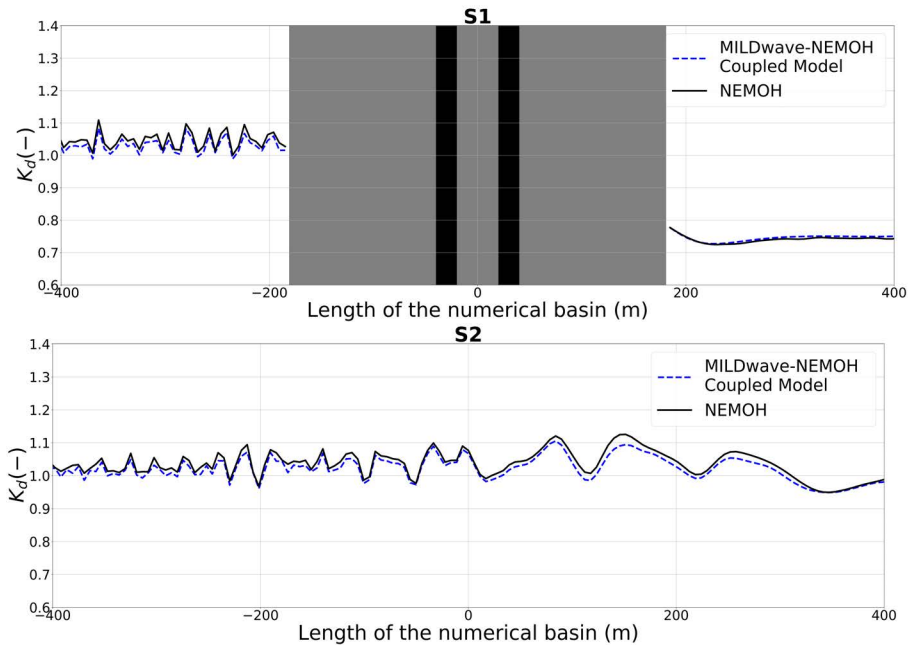


Figure 3.37: K_d disturbance coefficient results along two longitudinal cross-sections S1 (up) and S2 (bottom) as indicated in Figure 3.25 for a 9-HCWE array interacting with an irregular wave of $H_s = 2$ m, $T_p = 6$ s and $s_1 = 15.8$ [-]. The results are obtained using the MILDwave-NEMOH coupled model and NEMOH for Test Case 16. The coupling region is filled in gray colour and includes the WECS' cross-sections, which are indicated by black vertical beams.

3.6.4 Comparison Summary

Similar conclusions for Test Cases 13, 16 and 31 can be withdrawn for all the test cases studied. There is a correct transfer of information between MILDwave and NEMOH in the MILDwave-NEMOH coupled model as seen in the cross-sections drawn at $y = 0$ m and $y = -200$ m. A good agreement between both numerical simulation results shown in terms of obtained K_d . Nevertheless, the K_d is typically underestimated in the wave reflection zone up-wave the WEC(s) (array) and overestimated down-wave the WEC(s) (array) with higher values of K_d obtained.

As it can be observed in the RD_{K_d} contour plots, the magnitude of the RD_{K_d} depends on the number and the type of WEC(s) studied. When the number of WEC(s) is increased, RD_{K_d} increases. Furthermore, this increase in RD_{K_d} is higher for those wave conditions that are within the absorption band-width of the WEC. The higher the wave-structure interaction is, the higher the overestimation or underestimations that the MILDwave-NEMOH coupled model will generate when transferring the information.

To summarize the results for all the test cases included in Tables 3.1 and 3.2, the Root-Mean-Square-Error for the K_d , $RMSE_{K_d,G}$, over all the grid points of the numerical domain has been obtained and included in Figures 3.38 and 3.39, respectively. A maximum value of $RMSE_{K_d,G}$ of 1.49 % and 2.59 % is obtained for the HCWEC and OSWEC respectively. The maximum and minimum error between the MILDwave-NEMOH coupled model and NEMOH is never higher than 5% for all test cases and it is mainly located close to the coupling region at the lee of the WEC(s) (array).

3.6.5 Computational Time

The computational time for the test cases in the MILDwave-NEMOH coupled model with a wave period of 6 s have been summarized in Table 3.16. The results are similar for all test cases as the numerical simulations have an equivalent number of grid points. This is the most limiting factor in both models in obtain-

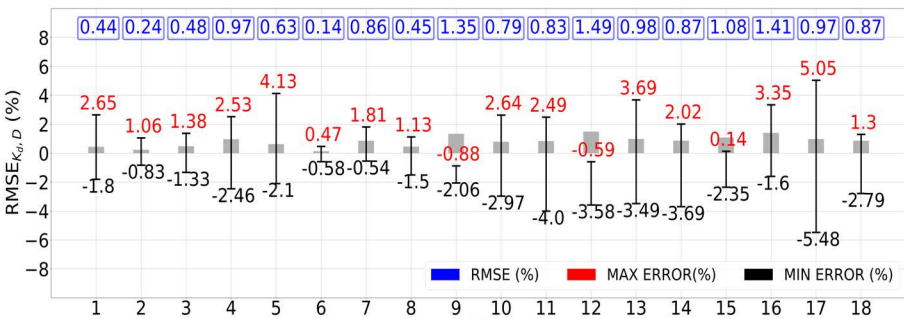


Figure 3.38: Root-Mean-Square-Error for the K_d , $RMSE_{K_d,G}$, over the entire numerical domain. Comparison between the MILDwave-NEMOH coupled model and NEMOH for all Test Cases of Table 3.1 performed for a heaving cylindrical WEC.

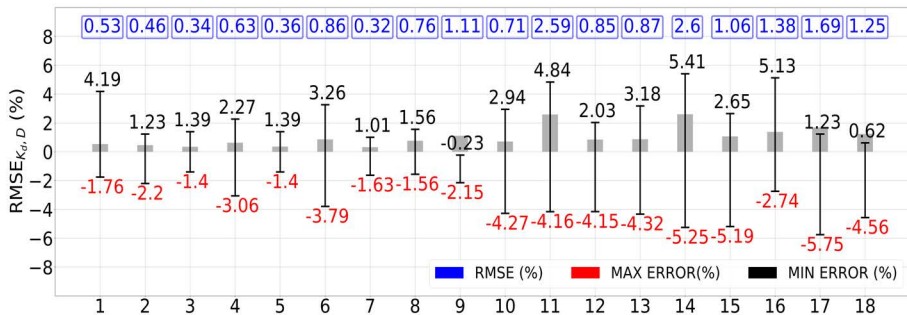


Figure 3.39: Root-Mean-Square-Error for the K_d , $RMSE_{K_d,G}$, over the entire numerical domain. Comparison between the MILDwave-NEMOH coupled model and NEMOH for all Test Cases of Table 3.2 performed for and oscillating wave surge WEC.

ing a fast solution if the rest of the simulation parameters are kept constant. All the simulations have been performed using 10 cores (Intel(R) Core(TM) i7-8700 CPU@3.2GHz).

It can be observed that in NEMOH, simulations with a single body are solved rapidly. However when the number of bodies, J , and frequency components, N_f is increased, the computational time increases rapidly. Almost nine hours are required for simulating short-crested waves (Test Case 16).

In the MILDwave domain, the number of bodies present does not affect the computational time, as it can be seen for Test Case 1 and 4 and Test Cases 7, 10 and 13. Moreover, the computational time increase in MILDwave is not as significant as the increase observed in NEMOH for short-crested waves. Showing that in terms of computational effort NEMOH can become a limiting factor of the coupled model when large WEC arrays need to be studied. For Test Case 16 modelling a 9-HCWE array under the effect of short-crested irregular waves, the NEMOH Process takes 8.71 h to finish, while the two MILDwave Processes take 8.29.

Considering the fine grid cell size resolution that has been used to perform the numerical validation, it is concluded that the MILDwave-NEMOH coupled model

Table 3.16: Computational Time in hours (h) for the MILDwave-NEMOH coupled model.

Test Case Number	J, Number of Bodies [-]	NEMOH	Incident Wave	Perturbed Wave	Computational time
1	1	0.01	0.1	0.1	0.21
4	9	0.22	0.1	0.1	0.42
7	1	0.09	1.61	1.85	3.55
10	5	1.5	1.61	1.85	4.96
13	9	3.55	1.61	1.85	7.01
16	9	8.71	3.88	4.41	17.0

is a cost-efficient numerical tool for the estimation of "far field" effects. The MILDwave-NEMOH coupled model will perform simulations at a higher computational time than phase-averaged wave propagation models in trade-off a better representation of the hydrodynamics and wave transformations around the WEC array. In relation with phase-resolving wave propagation models the MILDwave-NEMOH coupled model will provide high speed solution as MILDwave is an efficient tool providing accurate results in cases that non-linear effects are not important

Looking at the coupled model algorithm it can be seen that three different simulations are performed. Consequently, when studying possible WEC array deployment locations at a specific water depths at a coastal area, it is possible to perform one NEMOH simulation, one incident wave run in MILDwave and several perturbed wave runs in MILDwave. This results in a speed up of the calculations dealing with the increased NEMOH computational time.

Moreover, the coupled model algorithm has been parallelized, see Section 3.3.3, which allows the use of High Performance Clusters (HPC) to perform high computational time simulations like irregular short-crested waves over coastal areas. This will result on even faster simulations using the MILDwave-NEMOH coupled model.

3.7 Discussion

A sensitivity analysis for the MILDwave-NEMOH coupled was performed using the different simulation parameters of Section 3.5 to achieve a convergent solution with NEMOH results. The results show that a circular or rectangular internal wave generation boundary can be used with similar results.

As a guideline, to study the "near field" and "far field" effects around a WEC(s) (arrays) a grid cell size equal to $L/25$ for regular waves and $L_p/40$ for irregular waves should be used in order to obtain an accurate solution close to the coupling region. For instance, in case there is only the need to study the "far field" effects, the grid cell size for irregular waves can be increased to $L_p/30$ or $L_p/25$. This is because the radiation effects are diminished with the distance, and in the "far field" the wake effect K_d tends to 1 due to the effect of diffraction. By reducing the grid cell size in irregular waves it is then possible to decrease the computational time considerably.

In long-crested irregular waves, keeping a small N_f for discretizing the irregular waves spectra, using a $d_x = d_y = \frac{L_p}{40}$ and a simulation time representing 500 waves is sufficient to obtain a good representation of the target irregular long-crested sea state. Increasing the N_f or the simulation time will not lead to a significant increase in the accuracy of the obtained K_d results.

For short-crested irregular waves, the minimum N_f used should be at least 50 to obtain a correct representation of the normalized spreading function. As discussed in Section 3.5.5, to study "far field" effects of WEC arrays, a single simulation is not sufficient. Instead, a number of ten simulations is recommended to obtain an average of the K_d in the numerical domain. This allows to account for the different wave attack angles of the discretized spectra close to the absorption bandwidth of the WEC(s).

Section 3.6 demonstrates that the MILDwave-NEMOH coupled model can accurately propagate the perturbed wave field around different WEC types and (array) configurations for the here employed linear wave theory based coupling. The results of the MILDwave-NEMOH coupled model are compared with NEMOH results. Small discrepancies between NEMOH and the MILDwave-NEMOH coupled model are found close to the coupling region in the lee of the WEC (array). These discrepancies are more relevant when the number of WEC(s) modelled is increased and the wave-structure interactions between the WEC(s) and the incident wave is higher, as shown in Figures 3.38 and 3.39. Though the Root-Mean-Square-Error for the K_d remains below 2 %. This shows, that the complexity of the hydrodynamic interactions when modelling the "far field" effects is not influential.

Nevertheless, the coupling of MILDwave and NEMOH has some limitations. Firstly, despite the fact that the computational time for simulating different WEC arrays in this study is reasonable (the longest recorded computational time was that for Test Case 16, which lasted 17 hours on 10 cores (Intel(R) Core(TM) i7-8700 CPU@3.2GHz)), it can increase considerably when increasing the number of WECs. For an array of J WECs with six DOFs, the computational time for a BEM model increases as σ^{6J} , with increased computational time in larger numerical domains. Secondly, irregular waves are calculated as a superposition of regular waves. It has been proven that is possible to obtain very good results with a low N_f , however, if a higher resolution of the $S_{n,M-N}(f)$, depending on the study case requirements, would lead to an exponential increase of the computational time. Thirdly, NEMOH calculations can only be performed at a constant bathymetry introducing a limitation in that way. Moreover, MILDwave is applied for mild slope bathymetries limiting the MILDwave-NEMOH coupled model to coastal regions with a mild slope lower than $\frac{1}{3}$. Finally, a realistic modelling of the WEC PTO system is required to maximize the WEC (array) power output and quantify WEC effects on the surrounding wave field (Child (2011)). Modelling a resistive PTO system allows us to obtain a cost-efficient simulation regarding computational times, but may result in an overestimation of the incident wave power absorbed by the WEC(s). Realistic PTO systems lead to a reduction of the power output due to losses and differences between the predicted optimum damping and the optimum damping that can be achieved in operational conditions. The control and optimization of the PTO system, however, as shown in Balitsky et al. (2018), does not have a significant influence on the wave field in the "far field".

In terms of limitations of the general coupling methodology employed to obtain the MILDwave-NEMOH coupled model, these depend each time on the type of models that are coupled. Specifically, for coupling between two linear models such as MILDwave and NEMOH, the resulting coupled model will provide conservative results in study cases when nonlinear phenomena are dominating. On the other hand, the above limitations can be overcome when applying the proposed coupling methodology, for nonlinear models. However, the use of nonlinear models needs to be justified for each specific study case, as they often introduce computational instability and high computational costs.

Examples of nonlinear WEC modelling can be found for PTO control studies such as the work by Giorgi and Ringwood (2018) where the authors investigated

the importance of an accurate representation of PTO behavior using a nonlinear Froude-Krylov model. Other nonlinear studies such as the work by Ransley et al. (2017) have focused on survivability analysis of a single WEC using CFD. Additionally, Verbrugge et al. (2018) proposed a nonlinear coupling methodology between OceanWave3D and SPH that if further developed could also be applied for survivability analysis of WEC arrays. Even though there has been an increase in the computational power available studies of WEC arrays have only been reported by Agamloh et al. (2008); McCallum (2017); Devolder et al. (2018) studying WEC array interactions using nonlinear models under regular wave conditions. It can be concluded, that in terms of WEC array interactions linear wave models are still more commonly used as they offer a better trade-off in terms of accuracy and computational time.

3.8 Conclusions

In this chapter, a generic coupling methodology for modelling both near and far field effects of floating structures and WECs is presented. This generic coupling methodology has been applied between the mild-slope wave propagation model MILDWave and the BEM wave-structure interaction solver NEMOH. This resulted in a one-way coupled model for simulating "near field" and "far field" effects of offshore structures. The coupled model consists on a nested NEMOH zone that acts as an internal wave generation boundary on a larger MILDwave numerical domain. The total wave field due to the presence of the structure(s), is obtained as a superposition of an incident wave field, calculated intrinsically in MILDwave and a perturbed wave field obtained also in MIDLwave using NEMOH as an internal wave generation boundary.

THE MILDwave-NEMOH coupled model has been programmed in Python where three processes for running MILDwave, NEMOH and generating the internal wave generation boundary are controlled by a fourth process, namely the Python Shell. This Python Shell ensures that the information between the different models is transferred correctly and that the results obtained from the different simulations can be combined to obtain the near and far field effects.

A series of numerical validation test cases are introduced in Section 3.4 to demonstrate the ability of the coupled model to transfer the information between NEMOH and MILDwave propagating waves in the far field. Wave propagation of three different types: regular, long-crested and short-crested irregular waves has been used for different wave conditions, for two types of WECs, both alone and in several array configurations.

The results from the MILDwave-NEMOH coupled model have been compared to NEMOH, that is used as a benchmark for evaluating the accuracy of the coupled model when transferring information in the near-field. The model showed a good agreement with NEMOH for all the considered test cases, with Root-Mean-Square-Error values for the K_d lower than 2 % and a maximum and minimum relative difference in K_d always below $\pm 5\%$.

The coupled model introduced has the following advantages:

1. As MILDwave correctly models coastal transformations, it is possible to extend the NEMOH numerical domain and simulate "far field" effects over large coastal areas.
2. The Python Shell can be updated to include a fifth process acting as a wave-to-wire model including different types of PTOs.
3. The Python Shell connecting MILDwave and NEMOH ensures that there is a correct transfer of information between the models, reducing to the minimum the need of altering their source code.
4. The MILDwave-NEMOH coupled model algorithm is parallelized, which allows the possibility to perform simulations on very large domains with a fine grid resolution and a high number of frequencies using High Performance Clusters (HPC).

Nevertheless, the MILDwave-NEMOH coupled model has some limitations:

1. Its applicability is limited to linear and weakly nonlinear wave conditions. It provides accurate results out of the surf zone where non-linear phenomena is taking place. In case of breaking waves, extreme wave conditions and when H_s and T_p do not lay within the linear wave theory it cannot be applied. Furthermore, for non linear WEC array interactions including turbulence modelling, the appearance of viscous forces or the need to perform PTO active control the model cannot also be applied.
2. The computational time can increase considerably if a large number of frequencies and WECs or a complex PTO type is modelled introducing a wave-to-wire process.
3. The extension of the WEC array is limited to a uniform non-movable bed.
4. Increasing the number of WECs can significantly increase the simulation time.

In the next chapter, the MILDwave-NEMOH coupled model will be validated against experimental tests, using the existing WEC array data-set of the WECwakes project (Stratigaki et al. (2014)).

Chapter 4

Experimental validation of the MILDwave-NEMOH coupled model

4.1 Introduction

In this fourth chapter of the thesis, an experimental validation is performed by comparing the results from the MILDwave-NEMOH coupled model to WEC array experimental data from the WECwakes project (Stratigaki (2014); Stratigaki et al. (2014, 2015)). Even though it has been demonstrated in Chapter 3 that the information between MILDwave and NEMOH is transferred correctly at the coupling interface, experimental validation is required to study the accuracy and the applicability of the coupled model.

The experimental validation of the demonstrated generic coupled model is carried out by comparing the results from the MILDwave-NEMOH coupled model to those obtained from the numerical model NEMOH and the WEC array experimental data from the WECwakes project (Stratigaki (2014); Stratigaki et al. (2014, 2015)).

The chapter is outlined as follows: firstly, the WEC array experimental data-set is presented in Section 4.2. A validation test case is described in Sections 4.3 and the results are presented in Section 4.4. In Section 4.4.2.3, the accuracy of the MILDwave-NEMOH coupled model to replicate "near field" effects and simulate "far field" effects of WEC farms is discussed. Finally, conclusions are drawn in Section 4.5.

4.2 WECwakes experimental data-set

In the WECwakes project, arrays consisting of up to 25 WECs were tested to study "near field" and "far field" effects of heaving point absorber type WECs. The

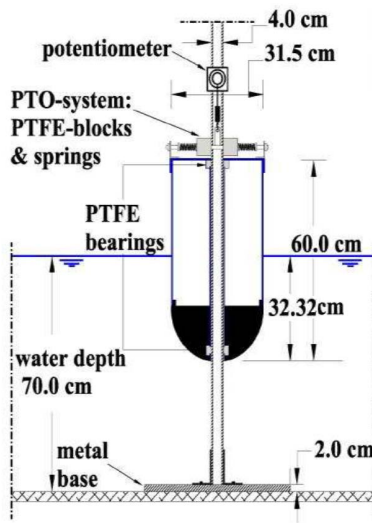


Figure 4.1: Definition sketch of a WEC used in the WECwakes project. Adopted from Stratigaki et al. (2014, 2015).

experiments were conducted in the Shallow Water Wave Basin of the Danish Hydraulic Institute (DHI), Hørsholm, Denmark. Each of the 25 WECs tested consists of a WEC buoy heaving through an inox metal vertical shaft mounted on a metal flat base installed at the bottom of the wave basin (Figure 4.1). Each WEC buoy consists of a cylindrical body and a spherical bottom with a diameter of 0.315 m. The draft of the WEC buoy is 0.323 m. The water depth is fixed to 0.700 m. The PTO system is composed of PTFE (Teflon) blocks placed at the top of the WEC buoy, which cause energy dissipation and damping of the WEC heave motion due to friction through contact of the PTFE blocks against the inox metal vertical shaft. Moreover, the contact of the inner part of the WEC buoy against the vertical shaft causes additional friction.

The DHI wave basin is 22 m wide and 25 m long and the overall water depth can be maximum 0.8 m. Forty-four piston type wave paddles, each of a width of 0.5 m generate waves along one end of the wave basin (red filled area, Figure 4.2). By testing different WEC array configurations during the WECwakes project under a wide range of sea states, a large experimental data-set has been generated and is publicly available for numerical validation purposes and for WEC array design guidelines. The wave field around the WECs has been recorded using 41 resistive wave gauges (WGs) distributed in the wave basin as shown in Figure 4.3. A potentiometer is installed at the top of each WECs buoy to measure its heave displacement (Figure 4.1). Furthermore two load cells were installed in the 5 WECs located on the central column of WECs to measure wave induced surge forces on the WECs.

The WECwakes project led to a data-base of 591 tests focusing on different array geometrical configurations (arrays are composed from 1-25 WECs) and wave

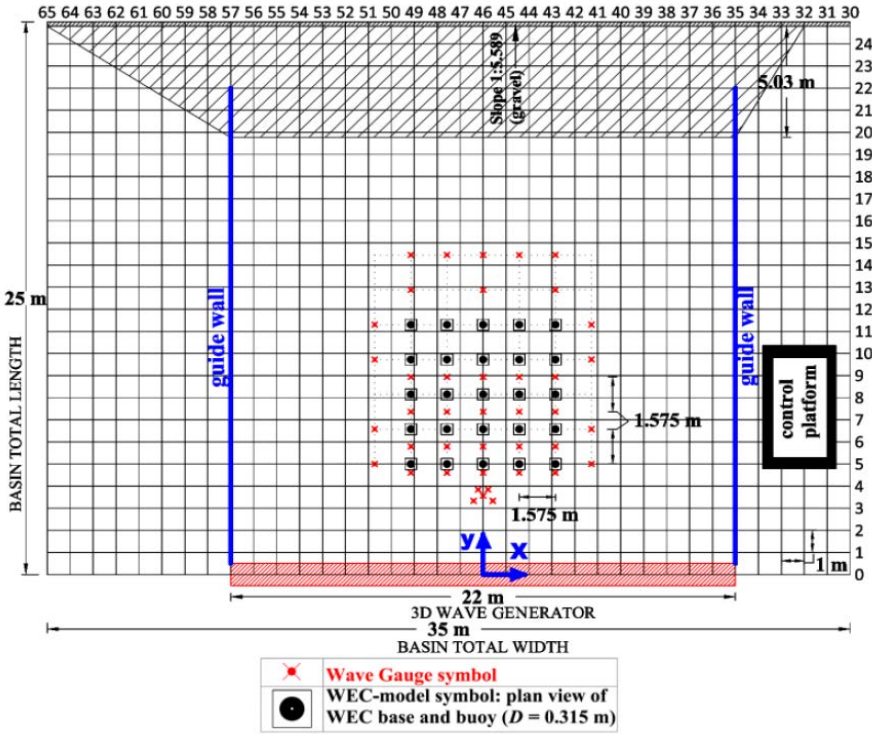


Figure 4.2: Plan view of the WECwakes experimental set-up in the DHI wave basin as a 5 × 5 rectilinear array. The red crosses indicate the position of all the wave gauges installed in the DHI wave basin during the experiments and the black circles indicate the locations of the different WECs. The wave paddles are denoted by the red filled area at the bottom of the figure while the black filled area at the top of the figure represents the wave absorbing gravel beach. Two guide walls were installed at the sides of the basin, denoted using blue thick lines. Figure adopted from Stratigaki (2014).

characteristics. For the present experimental validation, three different WEC configurations are selected: a single WEC, an array of five WECs arranged in a 1 × 5 WEC layout and an array of nine WECs arranged in a 3 × 3 WEC layout (see Figure 4.3 (B-D)). A total of 15 wave gauges located in the front, leeward and sides of the WEC array configurations are used to compare the significant wave height, H_s , and the spectral density, S , between the MILDwave-NEMOH coupled model and the experimental data-set. The separating distance between the different WECs is equal to 1.575 m (centre-to-centre distance). The incident regular wave conditions used to generate waves are $H = 0.074$ m and $T = 1.18$ s and 1.26 s. The incident irregular wave conditions used to generate waves during the experiments tests are defined by a JONSWAP spectrum with $H_s = 0.104$ m, and two peak wave periods of $T_p = 1.18$ s and 1.26 s.

4.3 Experimental validation strategy

4.3.1 Validation Test Cases

A validation "Test Case" (Table 4.1) program based on the WECwakes experimental data-set has been designed for different regular and irregular wave cases and WEC (array) configurations:

Table 4.1: Experimental test cases from the WECwakes project data-set. The water depth, d , is 0.7 m, the width of the domain is 22.0 m and the length of the domain is 22.0 m.

Test Case Number	Wave Type	H (m)	T (s)	s_1 (-)	WEC (array)	WEC buoy motion (-)
37	REG	0.074	1.26	0	3x3	Damped
38	IRREG	0.104	1.18	0	1x1	Damped
39	IRREG	0.104	1.26	0	1x1	Damped
40	IRREG	0.104	1.26	0	1x5	No motion
41	IRREG	0.104	1.26	0	1x5	Damped
42	IRREG	0.104	1.18	0	3x3	Damped
43	IRREG	0.104	1.26	0	3x3	Damped

4.3.2 Criteria used for the experimental validation

Together with the criteria used in Section 3.4.4, the validation of results obtained from the MILDwave-NEMOH coupled model against WECwakes experimental data is carried out using data recorded at the 15 numerical and experimental WGs, respectively, as these are illustrated in Figure 4.3 (A). For each WG, two different outputs have been generated:

1. Surface elevation plots comparing the surface elevation between the MILDwave-NEMOH coupled model and the WECwakes experimental data for the 15 WGs for the Test Cases of regular waves.
2. The Root Mean Square Error between the surface elevation, $\eta_{n,M-N}$, of the MILDwave-NEMOH coupled model and the $\eta_{WECwakes}$ of the WECwakes experimental data for the 15 WGs, $RMSE_{\eta_{WG}}$:
3. Spectral density plots comparing the wave spectra between the MILDwave-NEMOH coupled model and the WECwakes experimental data for the 15 WGs for the test cases of irregular waves.
4. The Root Mean Square Error between the K_d of the MILDwave-NEMOH coupled model and the $K_{d,WW}$ of the WECwakes experimental data for the 15 WGs, $RMSE_{K_d,WG}$:

$$RMSE_{K_d,WG} = \sqrt{\frac{\sum_{i=1}^Q (K_{d,WW} - K_{d,MN})^2}{Q}} \cdot 100 \quad \% \quad (-) \quad (4.1)$$

where Q is the number of Test Cases.

The different "Test Cases" included in Table 4.1 are performed both using the MILDwave-NEMOH coupled model, and NEMOH. NEMOH simulation results are used: (1) as input for the MILDwave-NEMOH coupled model, and (2) as a benchmark for the validation of the MILDwave-NEMOH coupled model, which is also compared with WECwakes data. The author finds important, not only to validate the MILDwave-NEMOH coupled model against experimental data, but to assess the accuracy of NEMOH when representing the WECWakes WEC characteristics.

4.3.3 Numerical set-up in MILDwave

In MILDwave, simulations are carried out in two types of numerical wave basins (see A and B-D in Figure 4.3) with an effective domain (area not covered by the wave absorbing sponge layers) of 22 m width and 22 m length, and a constant water depth of 0.700 m. Four equally sized effective numerical domains are used. For the simulations performed to obtain the incident wave field, waves are generated using a linear wave generation line located at the left side of the numerical domain with two equally sized wave absorbing sponge layers placed up-wave (left) and down-wave (right) (see Figure 4.3 (A)).

For the simulations carried out to obtain the perturbed wave field, waves are generated using an internal circular wave generation boundary (Figure 4.3 (B-D)). The three different WEC (arrays) configurations of Table 4.1 are simulated using different coupling radii for the circular wave generation boundary (see Figure 4.3 (B-D)). Each coupling radius is obtained following the recommendations of Chapter 3 as 0.3 times the wavelength (L) plus the radius of the WEC or the distance from the centre of the circular area to the most distant WEC for a single WEC and a WEC array, respectively. Four equally sized wave absorbing sponge layers are placed at all sides of the numerical domain.

The dimensions of the total numerical wave basin in MILDwave are not always the same, as the length of the wave absorbing sponge layers (B_S) is different for each set of wave conditions and depends on L . As irregular waves are obtained as a superposition of N_f regular wave components, B_p is calculated using the maximum L of the discretized spectra, L_{max} , which corresponds to T_{max} . An increase of B_s causes a decrease of wave reflection, and as pointed out in Beels (2009) for $B_p = 3xL_{max}$, the wave reflection coefficient drops to 1 %.

The total wave field of the MILDwave-NEMOH coupled model is obtained as the superposition of the numerical results from the domains of Figure 4.3 (A) and, Figure 4.3 (B), (C), (D) for a single WEC, five WECs and nine WECs, respectively.

4.3.4 Numerical set-up in NEMOH

NEMOH simulations are carried out in a numerical domain of 22 m width and 22 m length, with a constant water depth of 0.700 m. The effect of the WEC's PTO system is taken into account adding the suitable external damping coefficient, B_{PTO} , in the equation of motion (Equation 3.9). The value for B_{PTO} is estimated

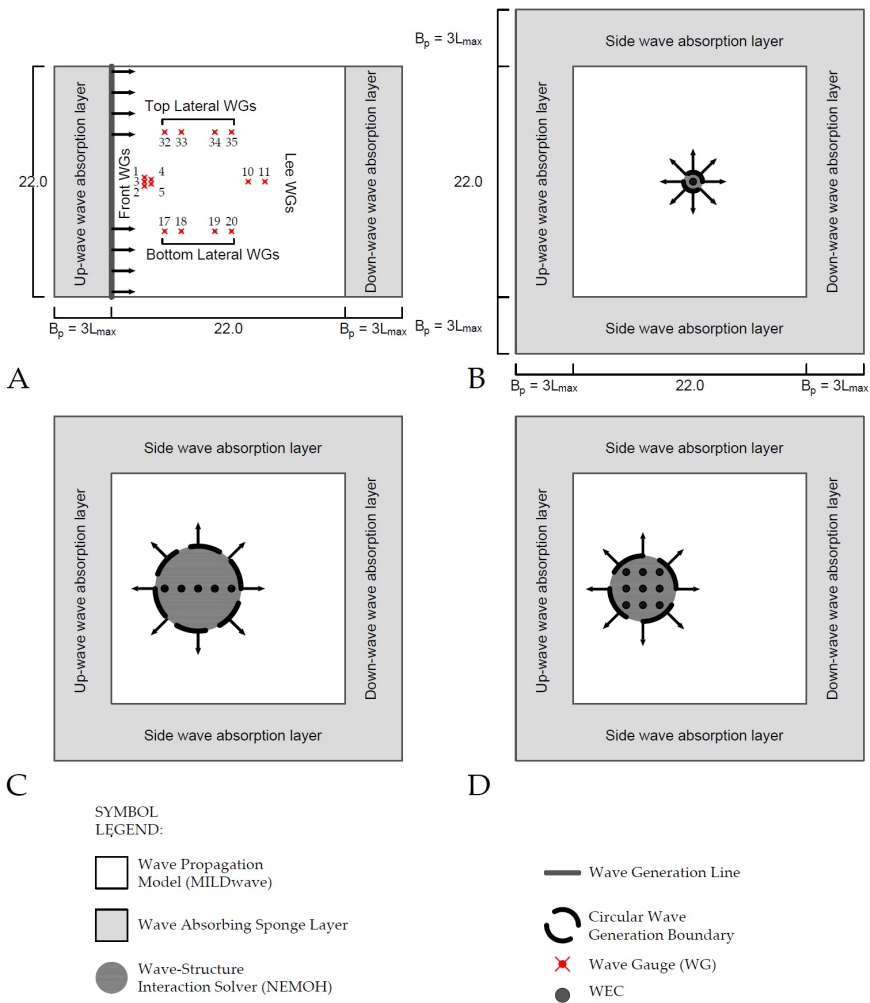


Figure 4.3: Set-up of the different numerical wave basins used in MILDwave. The wave gauges (WGs) are represented by the x symbol and numbered as they appear in the WECwakes experimental data-set. (A) Empty Numerical wave basin and layout of WGs; (B) Numerical wave basing with a single WEC; (C) numerical wave basin with an array of 5 WECs (1 column, 1x5); (D) numerical wave basin with an array of 9 WECs (3 columns and 3 rows, 3 x 3).

empirically to account for (i) the PTO system itself (PTFE blocks against vertical shaft), (ii) damping of the WEC's motion due to the presence of water between the WEC vertical shaft and the WEC buoy (Devolder et al. (2018)) and (iii) additional friction caused by the wave induced surge forces pushing the WEC buoy against its vertical shaft bearings (Figure 4.1) (Devolder et al. (2018)). Note that the WECs have been modelled in NEMOH, without the shaft bearings, and also that

regular waves are generated. An external damping $B_{PTO} = 28.5$ kg/s as indicated by Devolder et al. (2017) is further used.

4.4 Experimental validation results

4.4.1 Regular waves results

For Test Case 37 there is a good agreement between the NEMOH-MILDwave coupled model and the experimental data as it can be seen in Figure 4.4. However, it can be noticed that wave gauges 1, 10, 20, 32 and 33 show small differences on the surface elevation pattern.

The error of the free surface elevation for each wave gauge is included in Figure 4.5. It can be seen that the best agreement is obtained in front of the WEC array (WG 1-5) and in the wake of the array (WG 11) with an error ranging from 3-5 %. The highest difference is also obtained in the wake of the array (WG10), close to the WEC array with an error of 11 %. While evaluating these high differences it has to be considered that experimental data are intrinsically nonlinear (Stratigaki et al. (2014)). nonlinear effects such as viscosity or the friction between the shaft and the WECs cannot be modelled with the coupling methodology employed as it is based on linear wave theory. When the wave propagates further from the WEC these nonlinearities are reduced and therefore the agreement between experimental and numerical data is better. Finally, on the sides of the coupling region the error ranges from 6 to 9 % showing that the numerical model is not accurately representing the wave diffraction around the WEC array.

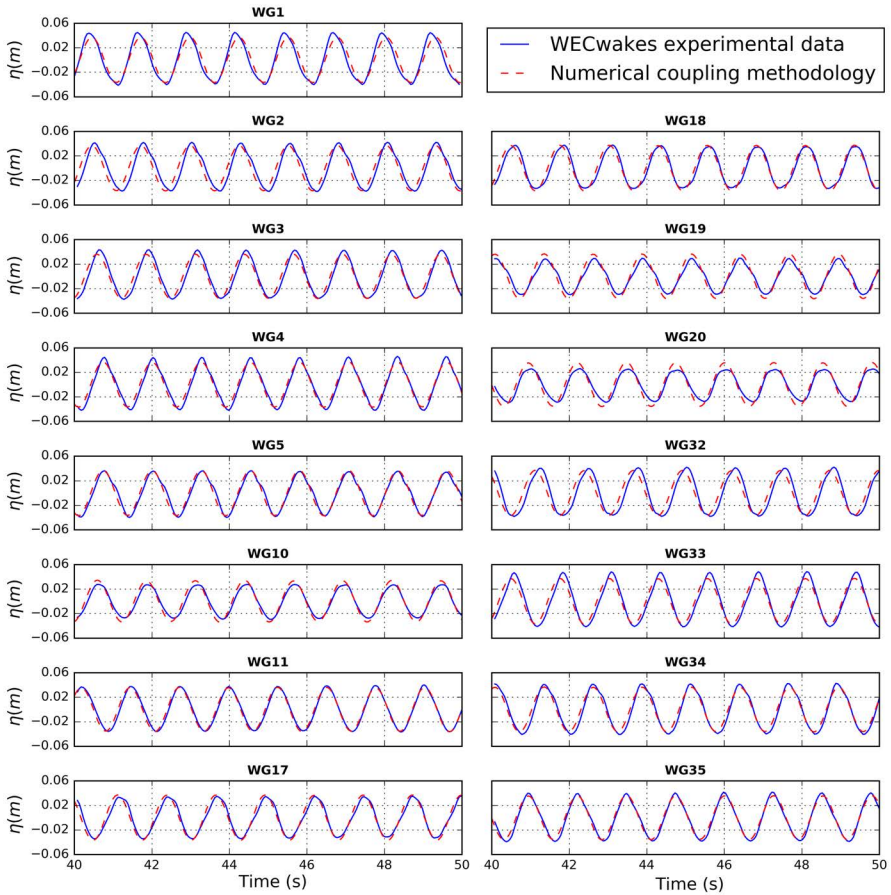


Figure 4.4: surface elevation η for the NEMOH-MILDwave coupled model and the WECwakes experimental data for a total of 15 wave gauges shown in Figure 4.3 (A).

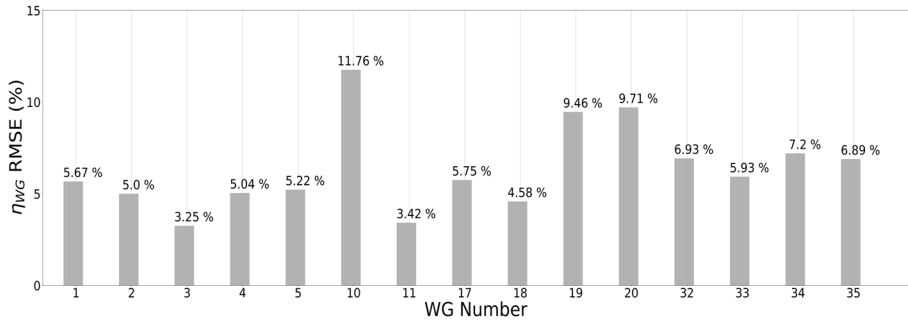


Figure 4.5: Root Mean Square Error (RMSE) values for the free surface elevation η for the 15 wave gauges analyzed from the data set (see Figure 4.3 (A)).

4.4.2 Irregular waves results

4.4.2.1 Comparison between MILDwave-NEMOH coupled model and NEMOH

Using the MILDwave-NEMOH coupled model for the Test Cases included in Table 4.1 the total wave field around one, five and nine WECs, respectively, is simulated using the numerical domain of Figure 4.3 (B), (C) and (D), respectively. In this section, only the results of Test Case 43 are included as the considerations made are valid for all the Test Cases. K_d results for Test Case 43 are illustrated in Figure 4.6. The coupling region in the MILDwave-NEMOH coupled model is filled using a white solid circle and is not considered for the experimental validation.

As a benchmark, K_d values obtained with the MILDwave-NEMOH coupled model and with NEMOH are compared by means of the RD_{K_d} . A contour plot for Test Cases 43 is illustrated in Figure 4.7. The results are in accordance with the findings of Chapter 3. The MILDwave-NEMOH coupled model provides lower K_d results than NEMOH in the wave reflection zone up-wave of the WECs indicated by positive values of RD_{K_d} , while the magnitude of the wake effects are smaller for the MILDwave-NEMOH coupled model as indicated by negative values of RD_{K_d} . A maximum and minimum value of RD_{K_d} are 4 % and - 4 %, respectively, is obtained.

To have a closer look to the comparison between the K_d results from the MILDwave-NEMOH coupled model and NEMOH, for Test Cases 43, two longitudinal cross-sections (indicated in Figure 4.6) are drawn: through the centre of the domain, at $y = 0$ m (S1) and through the location of WGs 17,18,19 and 20 (see Figure 4.3 (A)), at $y = 4.75$ m (S2). Again, the coupled zone is filled in gray in cross-section. There is very good agreement for K_d results between the MILDwave-NEMOH coupled model and NEMOH.

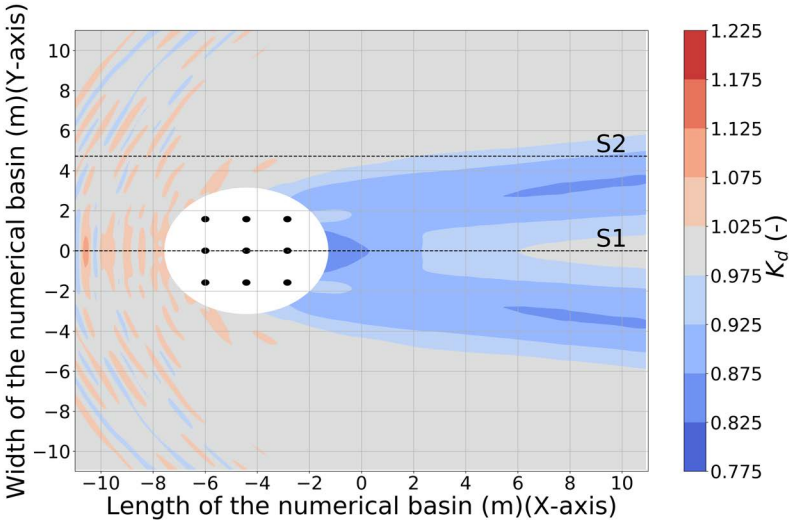


Figure 4.6: K_d disturbance coefficient results for a 9 WEC array interacting with an irregular wave with $H_s = 0.104$ m and $T_p = 1.26$ s. The results are obtained using the MILDwave-NEMOH coupled model for Test Case 43. The coupling region is filled using a white solid circle which includes the WECs (indicated by using black solid circles). Incident waves are generated from the left to the right. S1 and S2 indicate the location of cross-sections.

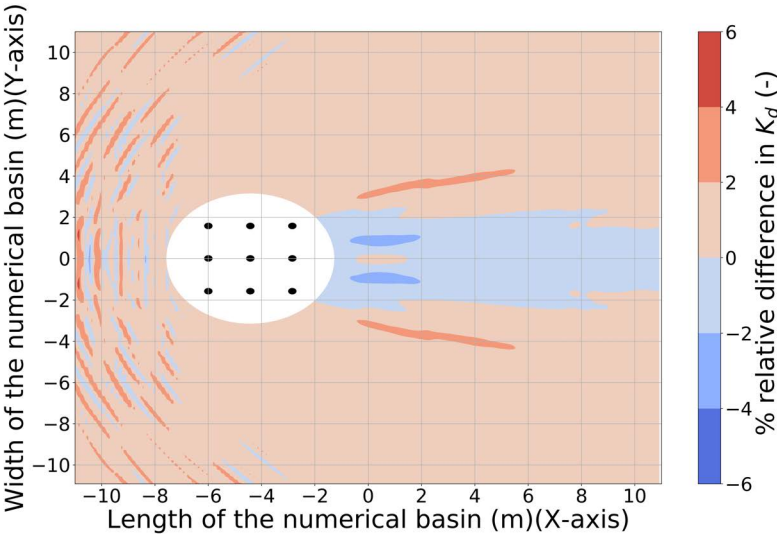


Figure 4.7: Relative difference (%) in K_d disturbance coefficient, RD_{K_d} between the MILDwave-NEMOH coupled model and NEMOH for a 9 WEC array interacting with an irregular wave with $H_s = 0.104$ m and $T_p = 1.26$ s. The results are obtained for Test Case 43. The coupling region is filled using a white solid circle which includes the WECs (indicated by using black solid circles).

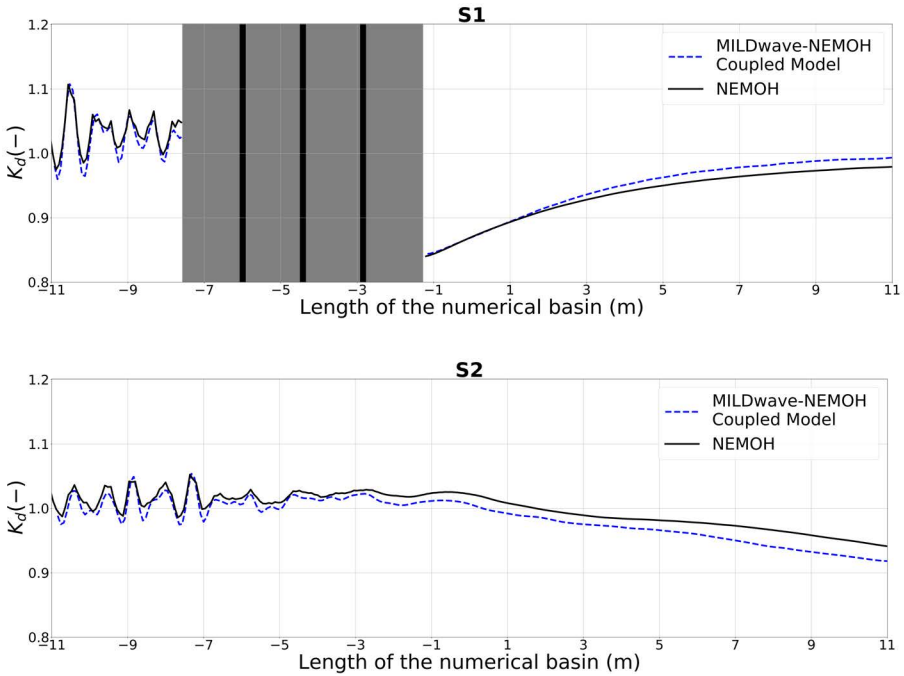


Figure 4.8: K_d disturbance coefficient results along two longitudinal cross-sections S1 (up) and S2 (bottom) as indicated in Figure 4.6 for a 9 WEC array interacting with an irregular wave of $H_s = 0.104$ m and $T_p = 1.26$ s. The results are obtained using the MILDwave-NEMOH coupled model and NEMOH for Test Case 43. The coupling region is filled in gray colour and includes the WECs' cross-sections, which are indicated by black vertical areas.

To complete the comparison, K_d results obtained for each considered Test Case are included in Appendix C. Similar conclusions for Test Cases 43 are drawn: the MILDwave-NEMOH coupled model provides lower K_d results than NEMOH in the wave reflection zone up-wave of the WECs, and decreased magnitude of the wake effects down-wave of the WECs indicated by positive and negative values of RD_{K_d} , respectively. These differences in the RD_{K_d} between the two models appear close to the coupling and increase when more WECs are simulated. These RD_{K_d} differences are slightly increased when moving away from the coupling region.

The results for all irregular wave Test Cases of Table 4.1 are then summarized by calculating the $RMSE_{K_d,D}$ over all the grid points of the numerical domain. Figure 4.9 reports that $RMSE_{K_d,D}$ values remain below 1.60 % for the simulated Test Cases.

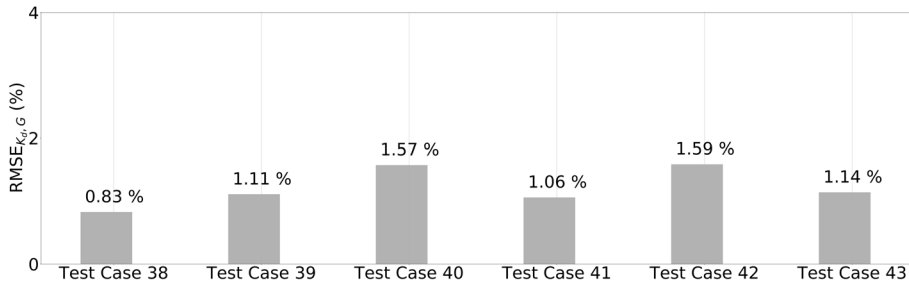


Figure 4.9: Root-Mean-Square-Error for the K_d , $RMSE_{K_d, D}$, over the entire numerical domain. Comparison between the MILDwave-NEMOH coupled model and NEMOH for all test cases of Table 4.1.

4.4.2.2 Comparison between the MILDwave-NEMOH coupled model and the WECwakes experimental data-set

Results for Test Case 43 are shown in Figures 4.10 and 4.11 for the 15 WGs shown in Figure 4.3 (A). The K_d values from the MILDwave-NEMOH coupled model and from the experimental measurements, $K_{d, MN}$ and $K_{d, WW}$, respectively, and numerical (using MILDwave-NEMOH coupled model) and experimental results of $S_{n, M-N}(f)$ and $S_{WECwakes}(f)$, respectively are plotted in Figures 4.10 and 4.11. The MILDwave-NEMOH coupled model and the experimental data have a good agreement in the WGs in the lee of the WECs where wake effects take place and in the Bottom Lateral WGs (see Figure 4.3 (A)) for both the K_d and $S(f)$.

To complete the validation of the MILDwave-NEMOH coupled model against experimental data, the $RMSE_{K_d, WG}$ is calculated between the $K_{d, MN}$ and the $K_{d, WECwakes}$ for all Test Cases of Table 4.1. Figure 4.12 shows the $RMSE_{K_d, WG}$ obtained for each WG of Figure 4.3 (A). The K_d obtained for the numerical data differs maximal by 10.0 % from the experimental data. The $RMSE_{K_d, WG}$ ranges between 2.0 % to 10.0 %, while the highest agreement is observed at the WGs located in the lee of the WECs and at the Bottom Lateral WGs. The largest

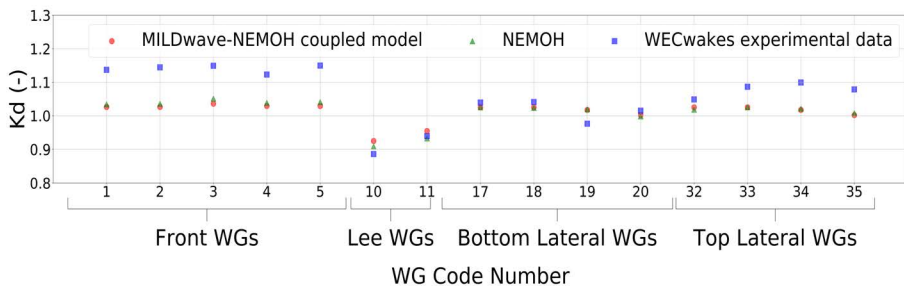


Figure 4.10: Comparison of the K_d disturbance coefficient between the MILDwave-NEMOH coupled model and the WECwakes experimental data for all 15 WGs of Figure 4.3 (A) for Test Case 43.

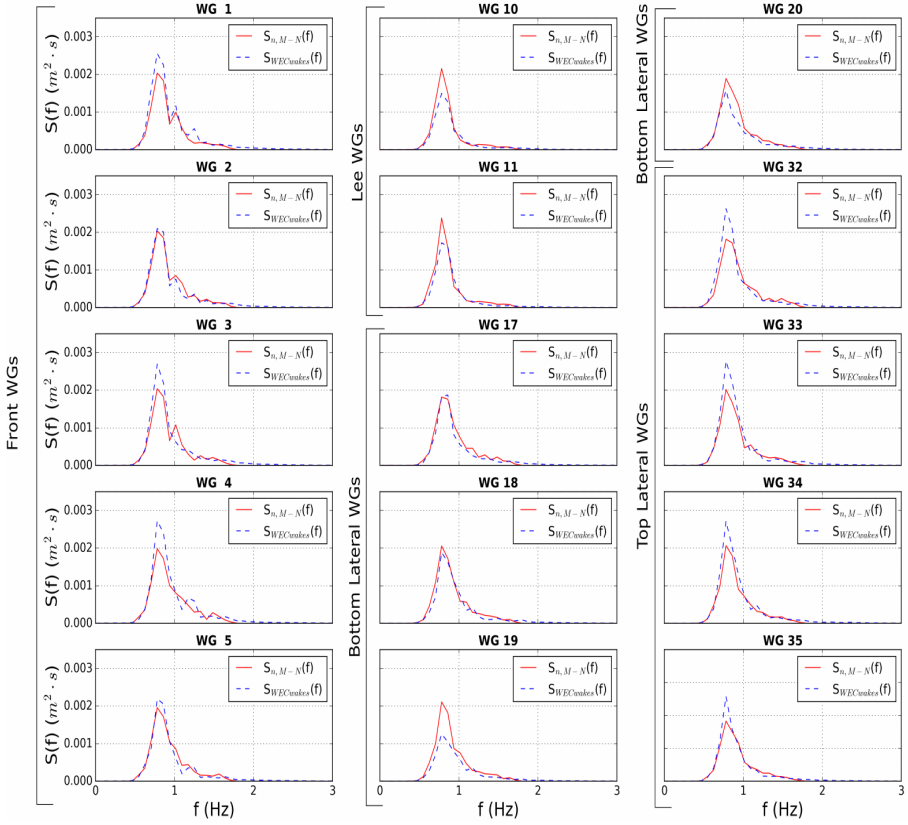


Figure 4.11: Comparison between the spectral density $S_{n,M-N}(f)$ obtained using the MILDwave-NEMOH coupled model, and the spectral density from the WECwakes experimental data, $S_{WECwakes}(f)$ for all 15 WGs of Figure 4.3 (A) for Test Case 43.

$RMSE_{K_d, WG}$ are obtained in the front WGs and at the Top Lateral WGs.

4.4.2.3 Discussion

Section 4.4.2.2 demonstrates that the MILDwave-NEMOH coupled model can accurately propagate the perturbed wave field around different WEC (array) configurations for the here employed linear wave theory based coupling. The results of the MILDwave-NEMOH coupled model are compared against NEMOH results. Small discrepancies between NEMOH and the MILDwave-NEMOH coupled model are found close to the coupling wave generation circle in front of and in the lee of the WEC (array). These discrepancies increase as the number of WECs modelled increases, as seen in the K_d contour plots included in Appendix C. Though, they remain between $\pm 4\%$. This shows, as pointed out in Chapter 3, that the complexity of the hydrodynamic interactions when modelling the "far field" effects is not influential.

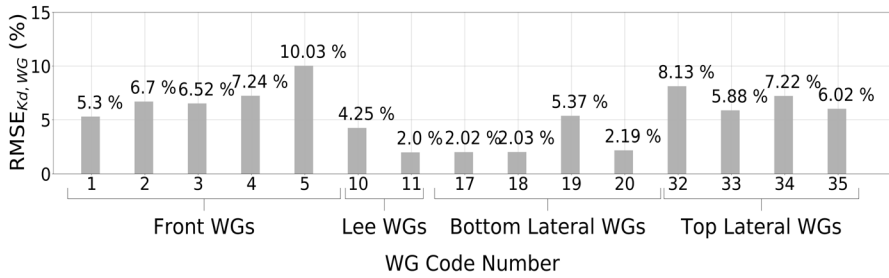


Figure 4.12: Root-Mean-Square-Error for the K_d for all 15 WGs, $RMSE_{K_d, WG}$, of Figure 4.3 (A). Comparison between the MILDwave-NEMOH coupled model and the WECwakes experimental data-set.

Validation of the MILDwave-NEMOH coupled model against the experimental WECwakes data is performed in Section 4.4 showing a good agreement for the different Test Cases used in this study. An error in predicting the K_d values measured at 15 WGs from the WECwakes tests is quantified in terms of $RMSE_{K_d, WG}$ (%). $RMSE_{K_d, WG}$ values range from 2.0 % to 10.0 % being the WGs in front of the WECs the ones with the least correspondence with the experimental data. On the contrary, for WGs that are further away from the WECs a better agreement is obtained. Similarly to the regular waves test case, the difference within the Front WGs arises due to the viscosity nonlinear effect of the friction between the WEC shafts and the WEC buoys that cannot be represented with the BEM-based coupling methodology employed, as BEM is based on linear wave theory. This friction is causing the experimental WEC buoy to have smaller motion amplitude than the numerical one obtained in the BEM solver. Thus the WEC is absorbing less energy from the incoming waves yielding a higher wave reflection in front of the WEC (array). Finally, the asymmetry in the K_d results between the Bottom and the Top Lateral zones is caused by the nonlinear behaviour of the WECs in the experimental model and unwanted wave reflection in the wave basin that cannot be modelled in the MILDwave-NEMOH coupled model. In the MILDwave-NEMOH coupled model all the WECs of the array have an identical behaviour as shown by the symmetric values of K_d given for the top and the bottom lateral zones in Figure 4.10 and the symmetric total wave field shown in Figure 4.6. Despite this, the following considerations have to be made: (1) a linear coupled model is compared to experimental data that is inherently nonlinear, as confirmed by Verbrugge et al. (2017) who reported that the incident wave is a weakly nonlinear Stokes second order wave. (2) moreover, the experimental PTO system behaves as a Coulomb damper, yet in the numerical model it is approximated as a linear damper.

For all Test Cases of Table 4.1 the $RMSE_{K_d, D}$ by comparing the MILDwave-NEMOH coupled model to NEMOH remains below 2.0 %, while by comparing the $RMSE_{K_d, WG}$ for the 15 WGs of Figure 4.3 (A) between the MILDwave-NEMOH coupled model and the WECwakes experimental data this never exceeds 10.0 %. Therefore, it can be concluded that the coupling methodology can be used to

extend the numerical domain for simulating an irregular long-crested wave using the MILDwave-NEMOH coupled model, and thus simulate "far field" effects of WEC farms and arrays in a cost effective way.

4.5 Conclusions

In this chapter, an experimental validation of the MILDwave-NEMOH coupled model has been presented. Test Cases from the WECwakes experimental data-set have been considered for different WEC (array) configurations and wave conditions, and performed using the MILDwave-NEMOH coupled model and NEMOH.

First the surface elevation was compared between the MILDwave-NEMOH coupled model and the WECwakes data-set, obtaining a good agreement with a maximum difference in the $RMSE_{\eta, WG}$ of 12 %. Then, for the irregular wave Test Cases the total wave field evaluated in terms of K_d was compared between the MILDwave-NEMOH coupled model and NEMOH. The MILDwave-NEMOH coupled model showed a good agreement with NEMOH for all the considered Test Cases, with an $RMSE_{K_d, D}$ below 2 %. Next, the model was validated against irregular experimental WECwakes data obtaining a satisfactory agreement, with a $RMSE_{K_d, WG}$ smaller than 10 % for all test cases.

Despite some discrepancies between the numerical and experimental results, which are mainly caused due to the inherent nonlinear behaviour of the experiments, it has been demonstrated that the proposed coupled model between the wave propagation model MILDwave and the BEM solver NEMOH can accurately simulate the hydrodynamic behaviour of a WEC array and obtain the modified total wave field in the "near field" for irregular long-crested wave conditions. As MILDwave correctly models coastal transformations processes it is possible to extend the numerical domain and simulate "far field" effects over large coastal areas.

Chapter 5

Numerical Applications of the MILDwave-NEMOH Coupled Model

5.1 "Far field" effects of WEC arrays over varying bathymetry

The first application of the developed MILDwave-NEMOH coupled model is to study the "far field" effects of WEC arrays over large domains. This is done by extending the NEMOH numerical domain and including a varying bathymetry. This allows to overcome the NEMOH limitation to fixed bottom depths and small spatial resolution. To illustrate these applications, wake effects of the nine HCWEC array used in Chapter 3 have been simulated over an extended MILDwave-NEMOH numerical domain with a constant depth of 40.0 m and a mild-slope varying bathymetry.

An effective domain of 3000 m in the x-axis and 1600 m in the y-axis has been defined as it provides a large enough area to demonstrate the capabilities of the numerical model and study the "far field" effects of a WEC array. The WEC array is located at the centre of the numerical domain where a fixed and a varying bathymetry (as sketched in Figure 5.1) have been implemented. The varying bathymetry consists of a linear mild slope of $m = 0.02$ in the x-axis direction. The water depth decreases towards the positive direction of the x-axis from 40 m to 20 m depth. At a water depth of 20 m a constant bathymetry is extended for 400 m corresponding with the deployment site of the array, and with the NEMOH numerical domain. Afterwards the depth is decreased until reaching 5 m at the end of the numerical basin. The water depth in the model ranges from 40 m to 5 m, which is enough to induce shoaling effects in the incident waves, while avoiding wave breaking.

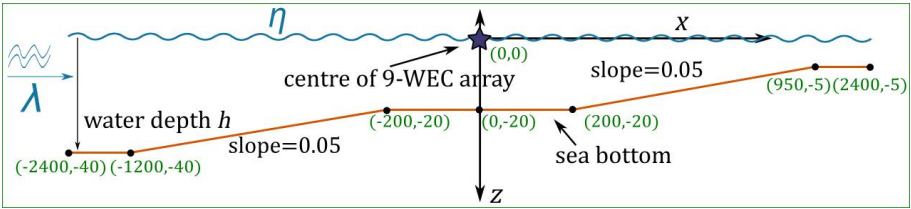


Figure 5.1: Water depth view showing the location of the 9-HCWE array. x-z plane (side) profile. The bathymetry is located at the right side. The 9-HCWE array is located at the center of the domain.

The same irregular wave conditions and PTO damping defined in Chapter 3 for long-crested irregular waves have been used as input wave conditions. A summary of the 6 different simulations are included in Tables 5.1 and 5.2 for a constant and a varying bathymetry, respectively.

Table 5.1: Simulation parameters for MILDwave-Coupled model constant bathymetry simulations using a Pierson Moskowitz spectra and a water depth, $d = 40$ m.

Parameter	Symbol	Test 44	Test 45	Test 46
Significant wave height	H_s	2.0 m	2.0 m	2.0 m
Peak wave period	T_p	6.0 s	8.0 s	10.0 s
Number of frequencies	N_f	20	20	20
Grid cell size x-axis	d_x	1.4 m	2.0 m	3.5 m
Grid cell size y-axis	d_y	1.4 m	2.0 m	3.5 m
Simulation time	t_{sim}	3000 s	4000 s	5000 s
Time step	Δt	0.3 s	0.4 s	0.5 s
Coupling radii	R_c	171.5 m	193.0 m	215.25
NEMOH length of the basin	-	400.0 m	400.0 m	450.0 m
NEMOH width of the basin	-	400.0 m	400.0 m	450.0 m

Figure 5.2 and 5.3 show the K_d results for the three different wave conditions over a constant and a varying bathymetry, respectively. In front of the WEC array a small reflection pattern is visible, while in the lee of the WEC array a high reduction in the wave height can be observed identified by lower K_d values. The magnitude of the wake effects varies for the different periods studied due to the different absorption capacities of the WECs modelled. As indicated by Tomey-Bozo et al. (2018) the WEC power extraction reaches a saturation point at certain sea states depending on the device, instead of incrementing with the wave conditions. As a consequence, for the same WEC array when the peak period is increased, the wave power absorption will have less impact on the disturbance coefficient K_d .

Together with the influence of the different incident wave conditions, the varying bathymetry is changing the magnitude of the wave radiation and wave diffraction effects. In contrast with the constant bathymetry case, where the extension of the wake effects can reach at least 1400 m down-wave the location of the WEC array, over a varying bathymetry the extents of the wake effects tends to be reduced

Table 5.2: Simulation parameters for MILDwave-Coupled model varying bathymetry simulations using a Pierson Moskowitz spectra and a slopping bathymetry.

Parameter	Symbol	Test 47	Test 48	Test 49
Significant wave height	H_s	2.0 m	2.0 m	2.0 m
Peak wave period	T_p	6.0 s	8.0 s	10.0 s
Number of frequencies	N_f	20	20	20
Grid cell size x-axis	d_x	1.4 m	2.0 m	3.5 m
Grid cell size y-axis	d_y	1.4 m	2.0 m	3.5 m
Simulation time	t_{sim}	3000 s	4000 s	5000 s
Time step	Δt	0.3 s	0.4 s	0.5 s
Coupling radii	R_c	171.5 m	193.0 m	215.25
NEMOH length of the basin	-	400.0 m	400.0 m	450.0 m
NEMOH width of the basin	-	400.0 m	400.0 m	450.0 m

specially for the higher period. Shoaling effects are expected to be higher on waves with a larger wavelength, and consequently shoaling has a higher impact on the wake effects of high wave periods, which are lower. Only for $T_p = 6$ s the array total wave field modification outweighs the shoaling effects and thus has the WEC array an impact both up-wave and down-wave. For $T_p = 8$ and 10 s, the effect of the WEC array is practically nil in the region down-wave the WEC array where the shoaling effects are much greater than the wake effects.

Finally, the MILDwave-NEMOH coupled model allows to directly study the wave spectral density, $S(f)$, in any point of the domain. $S(f)$ is affected by the depth variations and the presence of the WEC array.

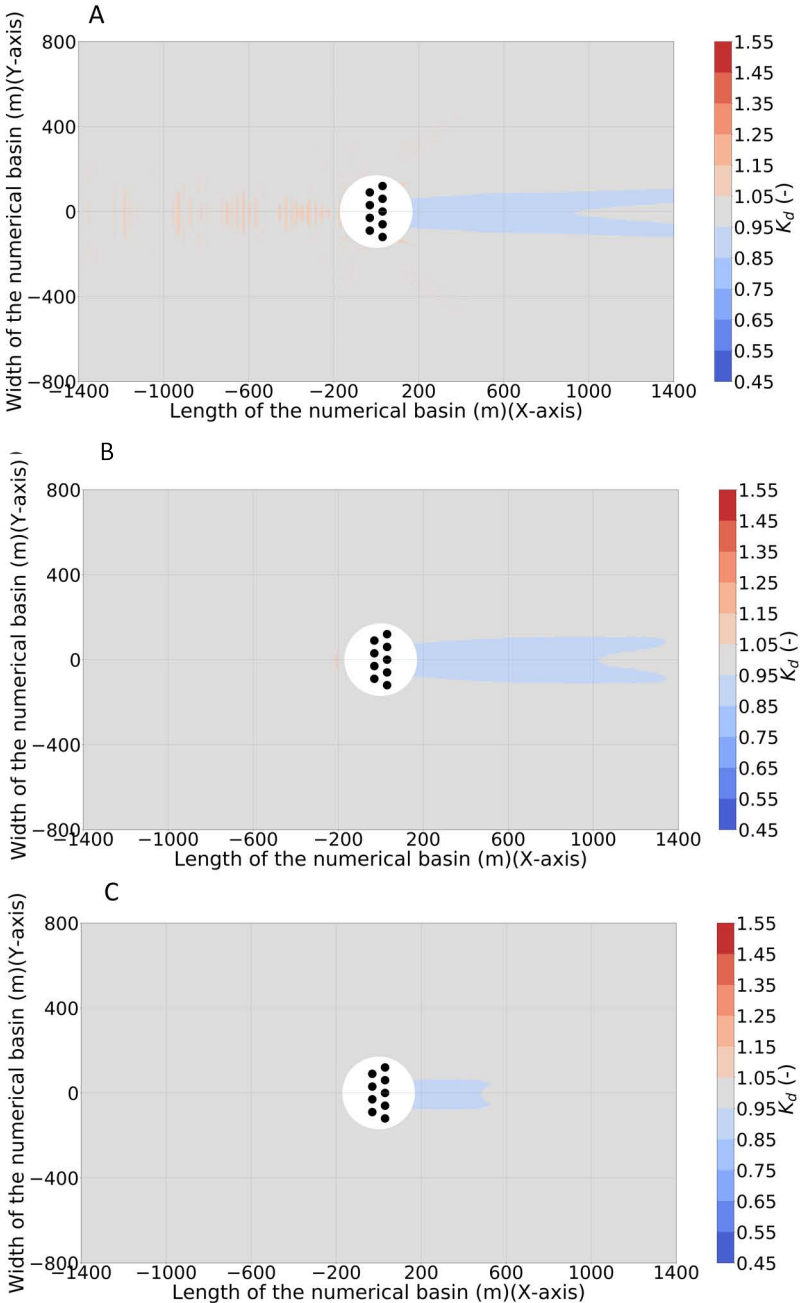


Figure 5.2: K_d results for Test Case 44 (A), Test Case 45 (B) and Test Case 46 (C). The coupling region is filled using a white solid circle which includes the WECs (indicated by using black solid circles). Incident waves are generated from the left to the right.

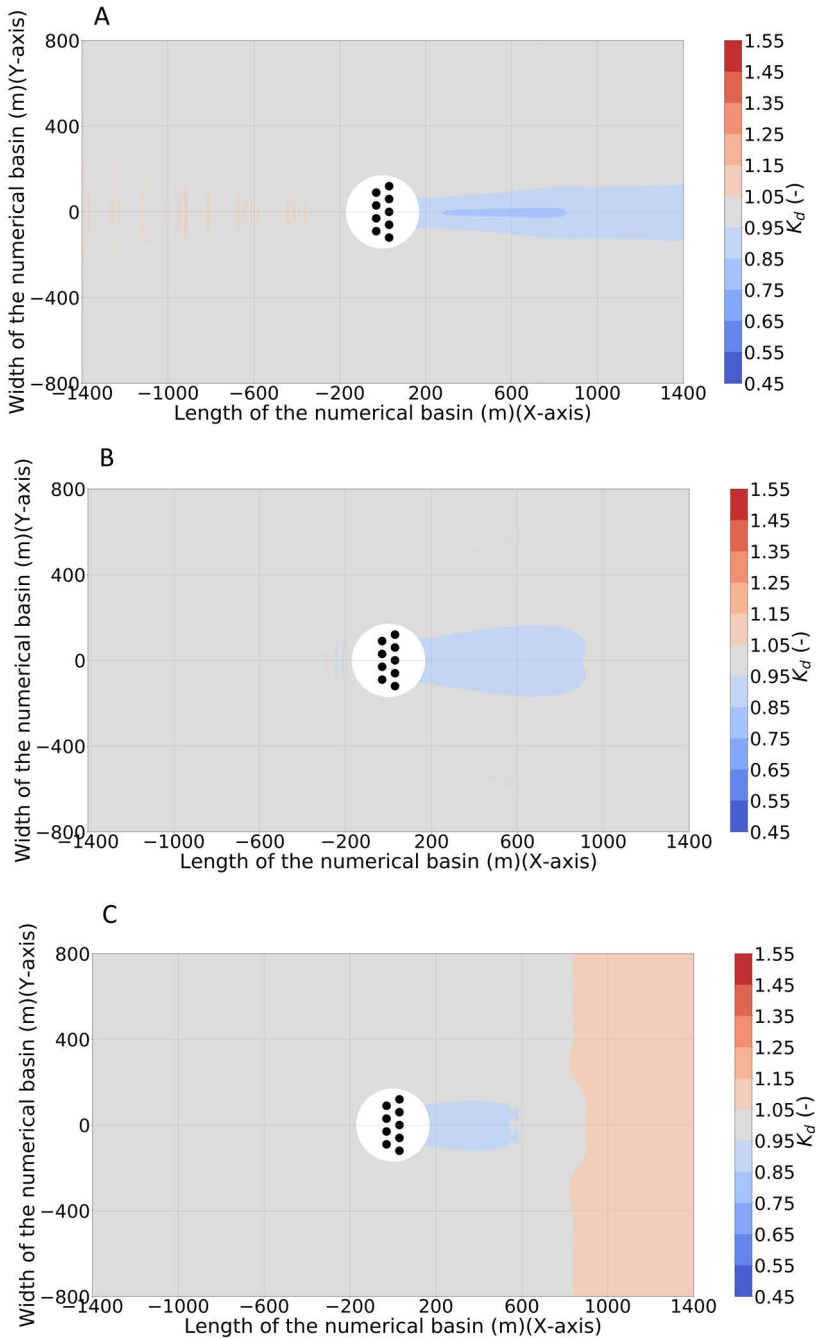


Figure 5.3: K_d results for Test Case 47 (A), Test Case 48 (B) and Test Case 49 (C). The coupling region is filled using a white solid circle which includes the WECs (indicated by using black solid circles). Incident waves are generated from the left to the right.

5.2 "Far field" effects of WEC arrays in irregular long-crested and short-crested waves

One of the main achievements of this PhD is the capability to simulate "far field" effects of irregular short-crested waves. From an analysis of the literature presented in Chapter 1.1 only three investigations have been found using short-crested irregular waves for WEC array modelling. The majority of them focusses either on regular or long-crested irregular waves modelling even though real ocean waves are short-crested. Borgarino et al. (2012) studied WEC array layout optimization of arrays of heaving cylindrical WECs, Götteman et al. (2018) performed a similar study using also heaving cylindrical WECs, while Tay and Venugopal (2017) studied the hydrodynamics interactions of oscillating wave surge WECs. The analysis of this investigations shows that the performance of WEC arrays changes in short-crested sea states. A change in the performance of the WEC array will then have an impact in the "far field" effects.

The second application of the MILDwave-NEMOH coupled model is to study the difference in the "far field" effects of WEC arrays under long-crested and short-crested irregular waves. To illustrate this application, the wake effects of the 5 heaving cylindrical WEC and the 5 oscillating WEC arrays used in Chapter 3 to numerically validate the coupled model, have been simulated on an extended MILDwave-NEMOH numerical domain with a constant depth of 30.0 m and 10.0 m, respectively. An effective domain of 2000 m in the y-axis and 2000 m in the x-axis has been defined as it provides a large enough area to demonstrate the capabilities of the numerical model to simulate WEC array interactions in short-crested waves. The WEC array is located at the centre of numerical domain and the simulation parameters used for the calculations are included in Table 5.3

Table 5.3: Simulation parameters for the MILDwave-NEMOH coupled model for long and short-crested irregular waves with $H_s = 2.0$ m and $T_p = 8.0$ s obtained using a Pierson–Moskowitz spectrum.

Parameter	Test 50	Test 51	Test 52	Test 53
WEC Type	HCWEC	HCWEC	OSWEC	OSWEC
N_f	20	50	20	50
s_1	0.0	15.8	0.0	15.8
d_x	2.0 m	2.0 m	2.0 m	2.0 m
d_y	2.0 m	2.0 m	2.0 m	2.0 m
t_{sim}	5000 s	5000 s	5000 s	5000 s
Δt	0.4 s	0.4 s	0.4 s	0.4 s
R_c	120.75 m	120.75 m	120.75 m	120.75 m
NEMOH length of the basin	400.0 m	400.0 m	400.0 m	400.0 m
NEMOH width of the basin	400.0 m	400.0 m	400.0 m	400.0 m

5.2.1 Disturbance coefficient calculation for long and short-crested irregular waves

Results for the K_D for Test Case 50 and 51 are shown in Figures 5.4 and 5.5, respectively. The coupling region in the MILDwave-NEMOH coupled model is filled using a white solid circle and is not considered for the comparison. For the long-crested wave case, Figure 5.4, the total wave field obtained is symmetric over the x-axis showing almost no reflection in front of the WEC, while a "wake effect" is clearly visible in the lee of the WEC(s). Around the x-axis at distance of $x = 500$ m there is a small asymmetry in the "wake effect" due to the coarse grid resolution used for visualization.

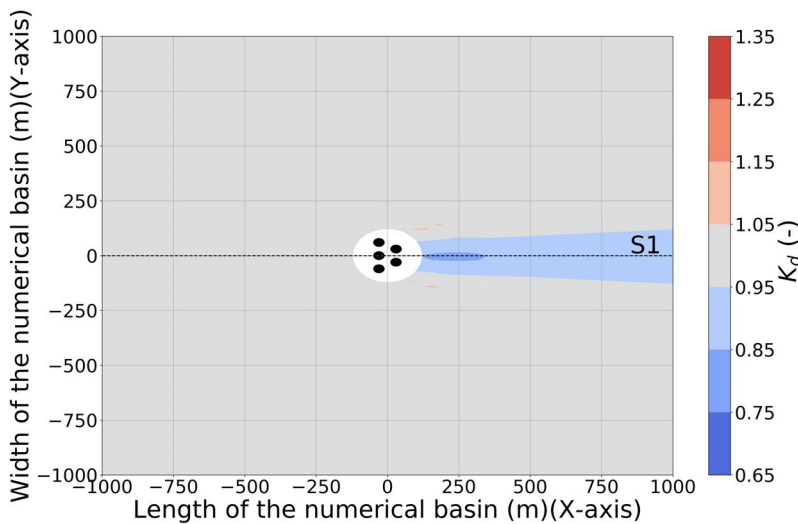


Figure 5.4: K_d disturbance coefficient results for a 5-HCWEC array interacting with an irregular wave with $H_s = 2.0$ m, $T_p = 8.0$ s and $s_1 = 0.0$ [-]. The results are obtained using the MILDwave-NEMOH coupled model for Test Case 50. The coupling region is filled using a white solid circle which includes the WECs (indicated by using black solid circles). Incident waves are generated from the left to the right. S1 indicates the location of a cross-section.

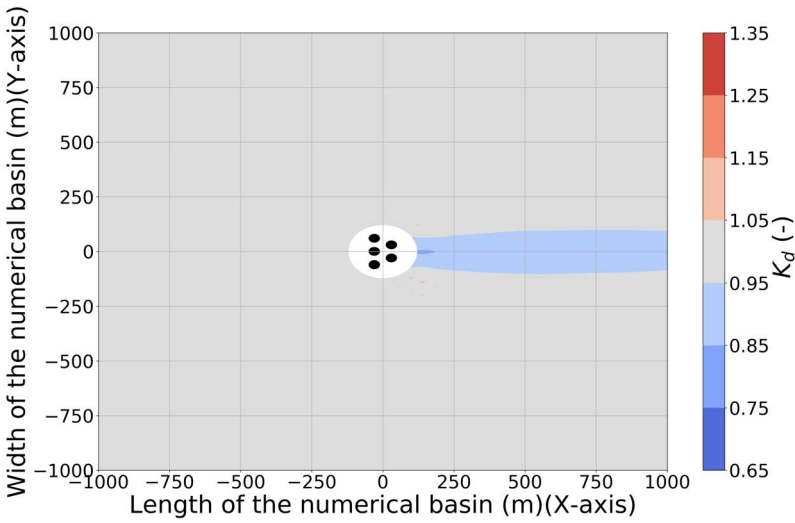


Figure 5.5: K_d disturbance coefficient results for a 5-HCWEC array interacting with an irregular wave with $H_s = 2.0$ m , $T_p = 8.0$ s and $s_1 = 15.8$ [-]. The results are obtained using the MILDwave-NEMOH coupled model for Test Case 51. The coupling region is filled using a white solid circle which includes the WECs (indicated by using black solid circles). Incident waves are generated from the left to the right.

For the short-crested wave case, in Figure 5.5 the same effect can be seen: there is almost no reflection in front of the coupling region, with a "wake effect" appearing in the lee of the WEC(s) that has a smaller magnitude than the one from long-crested irregular waves. Furthermore, in this case it can be seen that there is no symmetry around the x-axis. It is not possible to obtain a symmetric wake effect of a WEC(s) in short-crested waves using a single sea-state, and only one simulation.

The methodology employed randomly assigns a wave direction θ for each frequency of the discretized spectra, meaning that the frequencies where the WEC is extracting more energy (close to the resonance period of the device) will not necessarily be close to the θ_{mean} and therefore will be generating an asymmetric diffraction and radiation pattern that is interacting with the incident wave field.

To help understand this behaviour in short-crested waves results for the surface elevation, η of the incident, perturbed and total wave field for Test Cases 49 and 50 are shown in Figures 5.6,5.7 and 5.8; and Figures 5.9,5.10 and 5.11 respectively at the simulation time $t = 100$ s. Test Cases 52 and 53 have been chosen as the 5 OSWEC array will have the biggest impact in the incident wave field and therefore modifications of the surface elevation around the WEC array are more visible. The coupling region in the MILDwave-NEMOH coupled model is filled using a white solid circle.

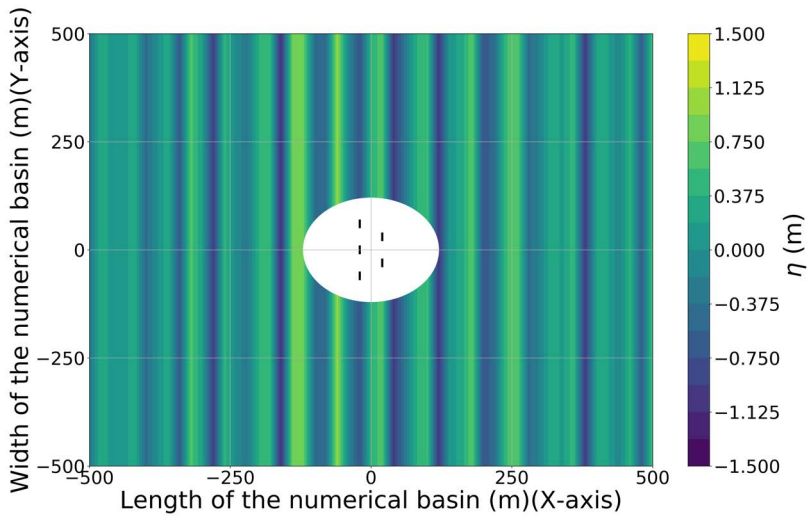


Figure 5.6: Incident η (m) results for a 5-OSWEC array interacting with an irregular wave with $H_s = 2.0$ m, $T_p = 8.0$ s and $s_1 = 0.0$ [-]. The results are obtained using the MILDwave-NEMOH coupled model for Test Case 52. The coupling region is filled using a white solid circle which includes the WECs (indicated by using black solid rectangles). Incident waves are generated from the left to the right.

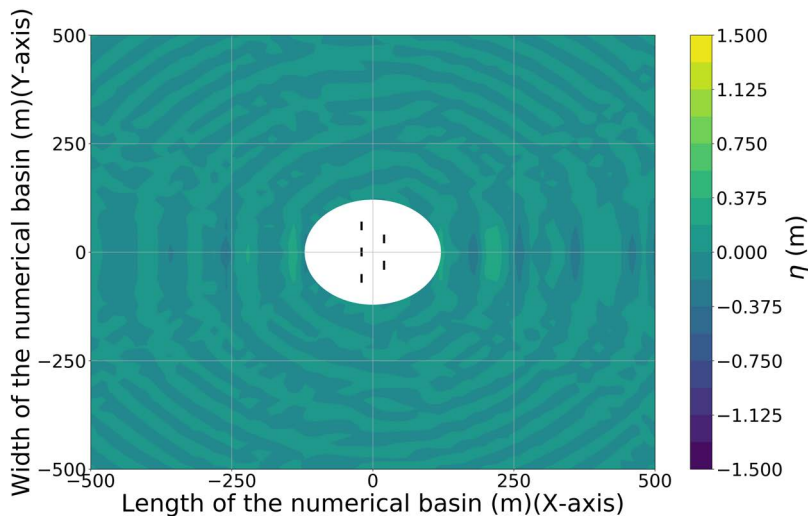


Figure 5.7: Perturbed η (m) results for a 5-OSWEC array interacting with an irregular wave with $H_s = 2.0$ m, $T_p = 8.0$ s and $s_1 = 0.0$ [-]. The results are obtained using the MILDwave-NEMOH coupled model for Test Case 52. The coupling region is filled using a white solid circle which includes the WECs (indicated by using black solid rectangles). Incident waves are generated from the left to the right.

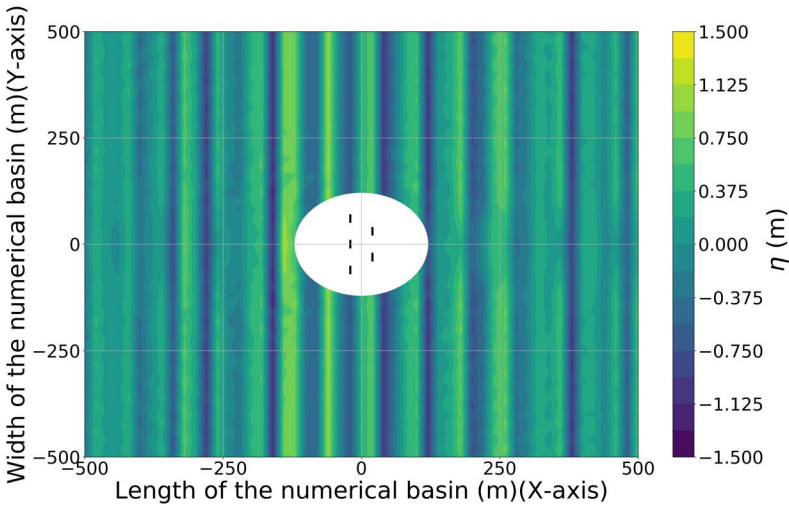


Figure 5.8: Total η (m) results for a 5-OSWEC array interacting with an irregular wave with $H_s = 2.0$ m , $T_p = 8.0$ s and $s_1 = 0.0$ [-]. The results are obtained using the MILDwave-NEMOH coupled model for Test Case 52. The coupling region is filled using a white solid circle which includes the WECs (indicated by using black solid rectangles). Incident waves are generated from the left to the right.

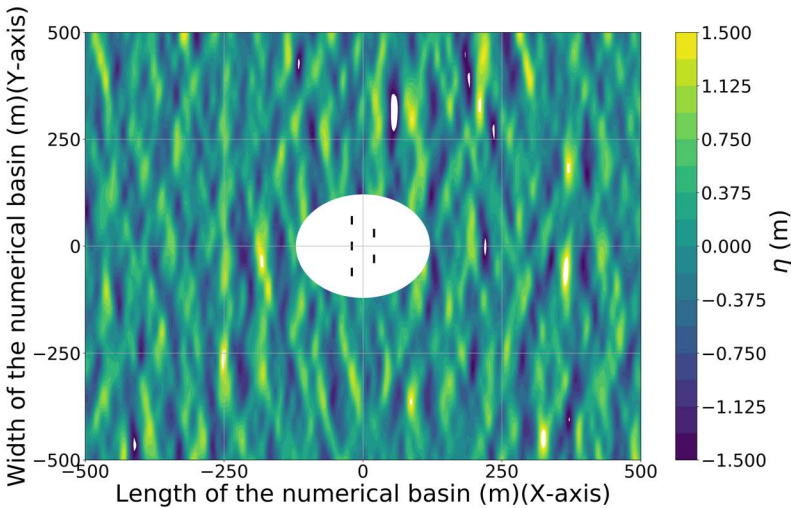


Figure 5.9: Incident η (m) results for a 5-OSWEC array interacting with an irregular wave with $H_s = 2.0$ m , $T_p = 8.0$ s and $s_1 = 15.8$ [-]. The results are obtained using the MILDwave-NEMOH coupled model for Test Case 53. The coupling region is filled using a white solid circle which includes the WECs (indicated by using black solid rectangles). Incident waves are generated from the left to the right.

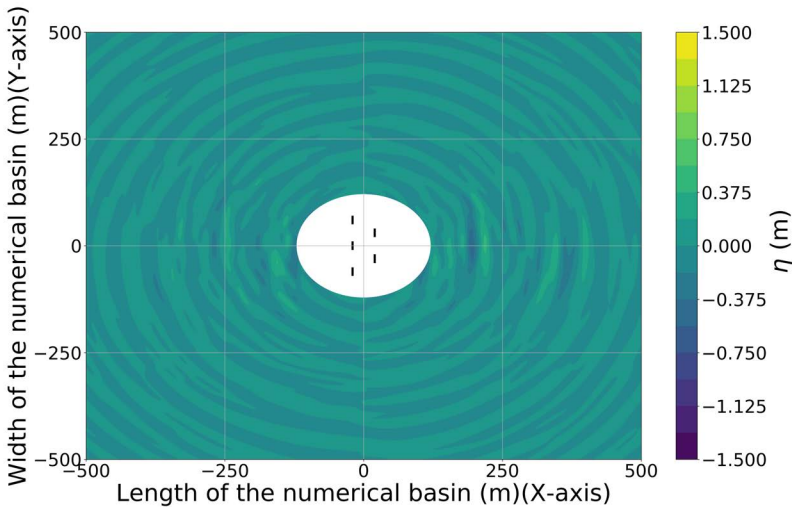


Figure 5.10: Perturbed η (m) results for a 5-OSWEC array interacting with an irregular wave with $H_s = 2.0$ m , $T_p = 8.0$ s and $s_1 = 15.8$ [-]. The results are obtained using the MILDwave-NEMOH coupled model for Test Case 53. The coupling region is filled using a white solid circle which includes the WECs (indicated by using black solid rectangles). Incident waves are generated from the left to the right.

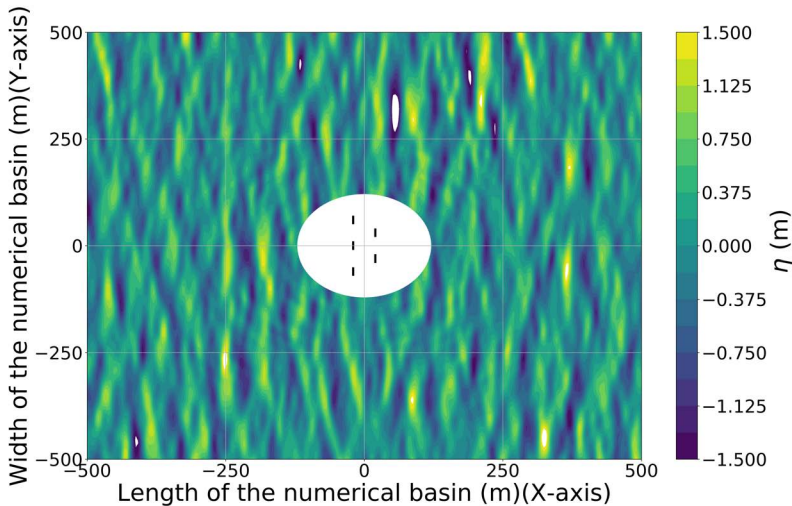


Figure 5.11: Total η (m) results for a 5-OSWEC array interacting with an irregular wave with $H_s = 2.0$ m , $T_p = 8.0$ s and $s_1 = 15.8$ [-]. The results are obtained using the MILDwave-NEMOH coupled model for Test Case 53. The coupling region is filled using a white solid circle which includes the WECs (indicated by using black solid rectangles). Incident waves are generated from the left to the right.

For the long-crested waves (Figure 5.8) it is possible to see the effect of the OSWEC array in surface elevation, η in front and in the lee of the coupling region. However, for the short-crested waves (Figure 5.11) the effect of the WEC array in η is smaller and it is only possible to distinguish a small reduction in η in the lee of the WEC array close to the coupling region.

Looking at Figures 5.7 and 5.9 a difference in the perturbed surface elevation can be seen. In the case of long-crested waves the perturbed wave pattern is symmetric according to the x -axis, which is not the case for short-crested waves with the propagating direction changing in each time step.

Therefore for comparing the effect on the total wave field of short-crested irregular waves to those of long-crested waves it is not possible to use a single simulation (one sea-state) and then obtain the K_D for short-crested waves. An average of the K_D over a different number of simulations should be used instead, to assess the impact of short-crested waves. In this way it is possible to account for the different incident angles of the frequencies of the discretized spectra close to the resonance period of the WEC(s), where more energy will be extracted from the waves and that is randomly changed in each simulation.

Figure 5.12 shows the $K_{D,avg}$ for Test Case 51 in Table I for a total of $M = 10$ simulations with a randomly generated directional spectra in each case. It can be seen that the average tends to be symmetric over the x -axis corresponding with $\theta_{mean} = 0^\circ$. It can be observed that in front of the coupling region there is almost no reflection, while the "wake effect" in the lee is smaller than for a single simulation, Figure 5.5. Nevertheless, the wake effect is smaller than the one generated by long-crested irregular waves.

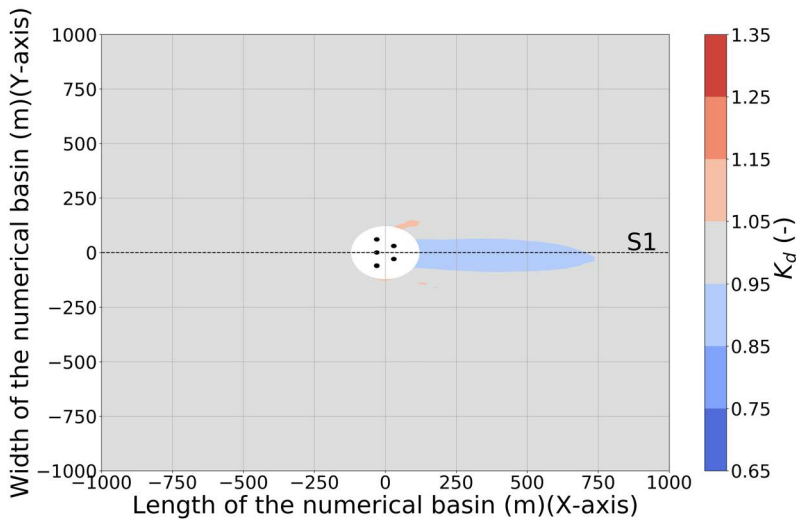


Figure 5.12: Average K_d disturbance coefficient results for a 5-HCWEC array interacting with an irregular wave with $H_s = 2.0$ m , $T_p = 8.0$ s and $s_1 = 15.8$ [-]. The results are obtained using the MILDwave-NEMOH coupled model for Test Case 51. The coupling region is filled using a white solid circle which includes the WECs (indicated by using black solid circles). Incident waves are generated from the left to the right. S1 indicates the location of a cross-section.

5.2.2 Comparison between long and short-crested irregular waves

To understand the difference in the "wake effects" of WEC(s) interacting with irregular long and short-crested waves longitudinal, cross-sections drawn through the center of the numerical domain for the different Test Cases included in Table I. Figure 5.13 show the results for the 5 HCWEC array, and Figure 5.14 shows the results for a 5 OSWEC array.

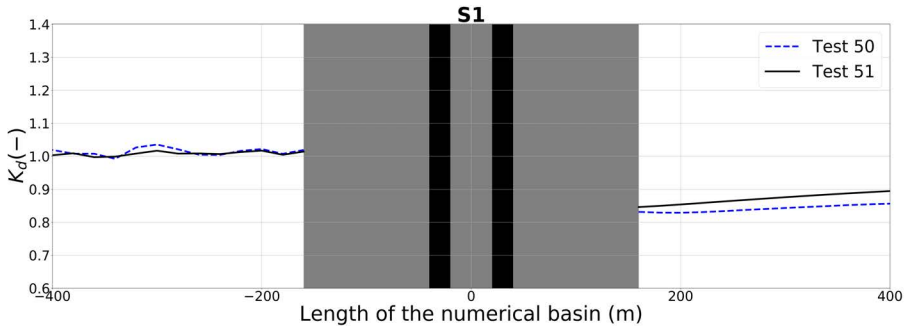


Figure 5.13: K_d disturbance coefficient results along one longitudinal cross-sections S1 as indicated in Figure 5.4 for a 5-HCWE array. The results are obtained using the MILDwave-NEMOH coupled model and NEMOH for Test Cases 50 and 51. The coupling region is filled in gray colour and includes the WECs' cross-sections, which are indicated by black vertical areas.

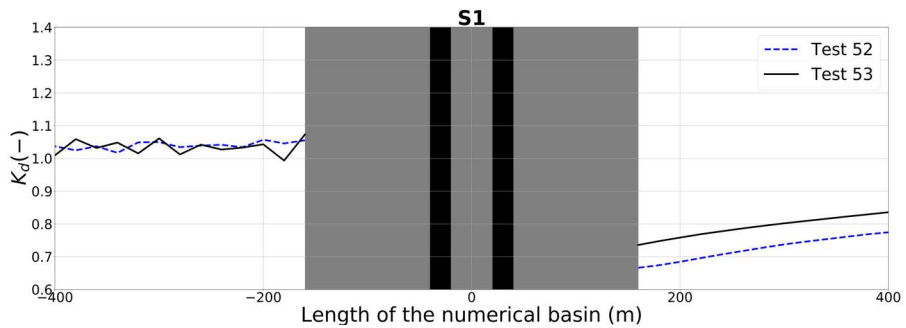


Figure 5.14: K_d disturbance coefficient results along one longitudinal cross-sections S1 as indicated in Figure 5.4 for a 5-OSWEC array. The results are obtained using the MILDwave-NEMOH coupled model and NEMOH for Test Cases 52 and 53. The coupling region is filled in gray colour and includes the WECs' cross-sections, which are indicated by black vertical areas.

The "wake effects" of OSWEC are greater than those of HCWEC for the same wave conditions, as they have a wide absorption bandwidth. Furthermore, for both cases there are bigger wake effects for long-crested irregular waves than for short-crested irregular waves. Lower values of K_D in the lee of the array can be observed, since the waves are coming from multiple directions and thus reducing the "lee side" effect.

For the case of the 5 WEC arrays there is a K_D difference of 2.4% for the HCWEC and 6.7% for the OSWEC between long-crested and short-crested irregular waves. This difference in the K_D for irregular and short-crested waves is showing that the impact of WEC arrays under short-crested waves is less than that of irregular long-crested waves. Combining this results with the findings of Section 5.1, it is possible to suggest that the "wake effects" of WEC arrays under short-

crested irregular waves will be further reduced when modelling a real bathymetry where shoaling effects are taking place.

Finally, a trend is noticed when increasing the number of WECs of the array. The difference in K_D between long-crested and short-crested waves is increased. This observation is also valid when increasing the impact of the WEC modelled, the K_D reduction of OSWEC in the lee of the array is larger than for HCWEC.

It can be concluded based on the current results that to avoid over estimating the "wake effects" of WEC arrays it is necessary to study them under short-crested waves. The difference in the assessed impact between long and short-crested irregular waves can differ substantially when increasing the number of WEC of the array and the WEC type.

5.3 "Far field" effects of WEC arrays over a real bathymetry

The north coast of Galicia has been identified in numerous studies as a suitable location for wave energy exploitation (Iglesias et al. (2009); Carballo et al. (2015)). The coastal area of Burela (Galicia, NW Spain) has been identified by Arean et al. (2017) as a suitable location for the installation of a wave energy farm. Nevertheless, this area is of high environmental value and many sea-related activities such as fishing or cargo shipping occur in its vicinity. Therefore, it would be interesting not only to study the viability of a WEC farm in terms of annual power production, but to characterize the impact in the wave field that such a project could have.

A preliminary coastal impacts case study has been set-up using the 9 oscillating cylindrical WEC array described in Chapter 3 in Cape Estaca de Bares to illustrate how the MILDwave-NEMOH coupled model can be a useful tool when designing WEC farm projects. This region is close to the area identified by Arean et al. (2017) to install a WEC farm project. A decision was made to use this bathymetry instead of the one at the location proposed by Arean et al. (2017), to stay within the applicability of the model for mild-slope bathymetries.

Figure 5.15 shows the location of the study area. A rectangular region of 5000 m \times 2600 m has been considered for the demonstration and is indicated in Figure 5.15 by a black rectangular area. For the incident wave simulation two equally sized sponge layers of 900 m were placed at the left and right sides of the numerical domain. For the perturbed wave simulation, four equally sized sponge layers of 900 m were placed at all sides of the numerical domain. The bathymetry data (Figure 5.16) were obtained from the EMODnet bathymetry data-base (European Marine Observation and Data Network (2019)). The bathymetry was modified to include a constant depth in the coupling location as indicated by a black dashed circle in Figure 5.17. An incident sea state of $T_p = 8$ s and $H_s = 2.0$ m was considered as the deep water boundary. This is the most probable incident wave condition recorded at the Estaca de Bares off-shore buoy. The wave buoy information was obtained from the "Puertos del Estado" database (Puertos del Estado (2019)). The 9-HCWEC array has been deployed at $x = -500$ m and $y = 0$ m at a depth of 35 m.

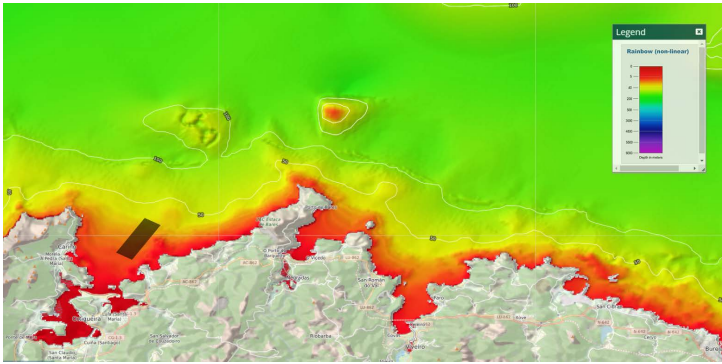


Figure 5.15: Map of the coastal area of Burela. The studied area is hatched using a black rectangle

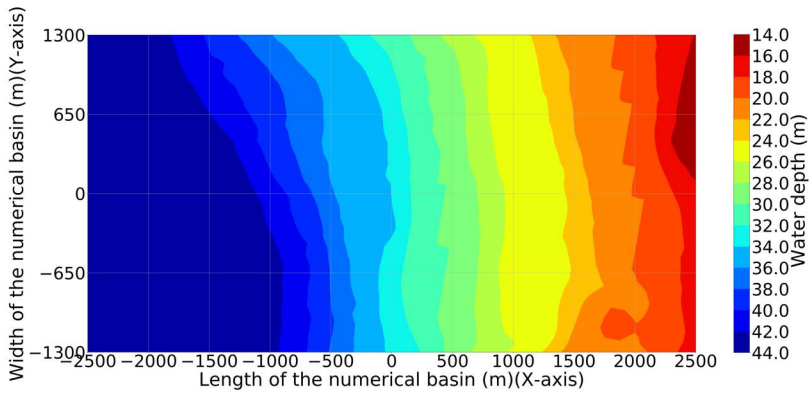


Figure 5.16: Plan view of the water depth contours in the coastal area of Burela.

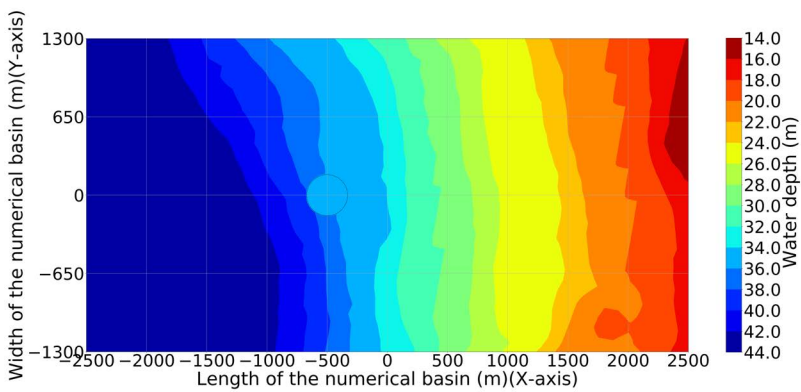


Figure 5.17: Modified bathymetry used in the MILDwave-NEMOH coupled model.

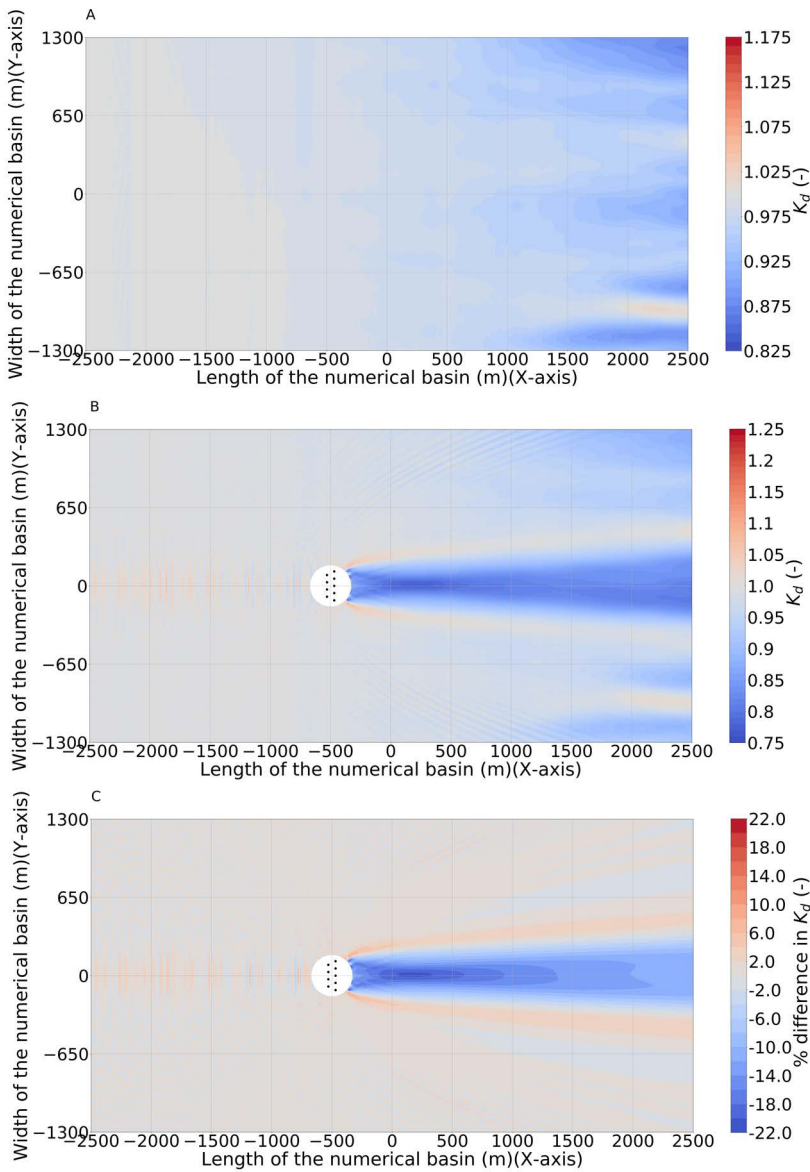


Figure 5.18: (A) K_d disturbance coefficient results for an irregular wave with $H_s = 2.0$ m and $T_p = 8.0$ s. (B) K_d disturbance coefficient results for a 9-HCWE array interacting with an irregular wave with $H_s = 2.0$ m and $T_p = 8.0$ s. (C) % difference between K_d disturbance coefficient results for simulation (A) and (B), respectively. The results are obtained using the MILDwave-NEMOH coupled model. The coupling region is filled using a white solid circle which includes the WECs (indicated by using black solid circles).

Figure 5.18 (A) shows the K_d disturbance coefficient values in the study area

if the 9-HCWEC array was not present. Figure 5.18(B) shows the K_d disturbance coefficient with the 9-HCWEC array. Figure 5.18 (C) illustrates the % different between both scenarios.

A wave height reduction up to 22 % is found immediately in the lee of the WEC array. After 1500 m this wave height reduction has already decreased to values between 6 - 8%, showing that for small WEC arrays the impact on the near-shore wave climate remains low. At the sides of the WEC array there is a small wave height increment. This increment indicates that WEC arrays can induce areas of energy concentration close to them. The asymmetrical pattern seen in Figure 5.18(C) proves that bathymetrical effects have an influence on the "far field" effects of WEC arrays.

These results show that the MILDwave-NEMOH coupled model can be used to identify wave impacts of WEC arrays. Sometimes these impacts can turn out to be positive. In this case study, the induced areas of energy concentration close to the WEC array could be used to install another WEC arrays that could benefit from the increased wave energy available. Additionally, WEC arrays could be used to reduce the amount of wave energy on vulnerable coast lines. In this case, the wave energy flux at 2000 m from the array deployment location is almost restored due to the effect of diffraction, nonetheless for larger WEC arrays this would not be the case.

Chapter 6

Conclusions and Further Work

6.1 Summary of the key findings

In this doctoral research, a generic coupling methodology has been applied to study the hydrodynamic interactions of WEC arrays. The application of the generic coupling methodology resulted in the development of a coupled model between the linear wave propagation model MILDwave and the wave-structure interaction solver NEMOH. The coupled model is capable of simulating the “near field” and “far field” effects of WEC arrays over varying realistic bathymetries under the effect of regular and irregular long-crested and irregular short-crested waves.

The first part of the manuscript focused on the development of the MILDwave-NEMOH coupled model. In the coupled model, the total wave field due to the presence of the WEC array is obtained as a superposition of an incident and a perturbed wave field. The incident wave field is calculated intrinsically in MILDwave, without any WECs. The perturbed wave field is calculated in MILDwave, using NEMOH as an internal wave generation boundary. The superposition principle is valid as the generic coupling methodology has been applied between two linear models.

The coupled model has been programmed and parallelized through a Python algorithm that runs MILDwave, NEMOH and the coupling interface separately. This algorithm ensures a correct transfer of information between the two numerical models through the coupling interface, together with an increased computational performance of the simulations.

A numerical validation of the coupled model has been performed for different wave conditions, WEC types and array configurations. The results from the MILDwave-NEMOH coupled model were compared to NEMOH, used as a benchmark for the numerical validation. The numerical validation results showed that the coupled model can effectively transfer the “near field” information from the NEMOH domain into the MILDwave domain and propagate it into the “far field”.

In the second part of the manuscript an experimental validation of the MILDwave-NEMOH coupled model against WEC array experimental data was performed. The experimental validation showed that the coupled model can accurately simulate the hydrodynamic behaviour of WEC arrays in the “near field” for regular and irregular long crested wave conditions. Some discrepancies in the experimental validation results close to the coupling interface region, indicated that the coupled model can only be used for linear or weakly non-linear wave conditions.

Finally, the third part of the manuscript introduced a series of applications of the MILDwave-NEMOH coupled model. Two applications focused on studying “far field” effects of WEC arrays in varying bathymetries. They have shown the importance of shoaling and refraction when assessing “far field” effects of WEC arrays. The third application carried out a comparison between “far field” effects of WEC arrays under long-crested and short-crested irregular waves. Results indicated a reduction in the magnitude on the “far field” impacts of short-crested irregular waves compared to long-crested irregular waves.

Nevertheless a number of limitations have been identified for the MILDwave-NEMOH coupled model: (i) it is only applicable for linear and weakly non-linear wave conditions, (ii) the computational time can increase considerably for short-crested irregular wave simulations, large WEC arrays and large numerical domains, and (iii) the extension of the WEC array is limited to constant bathymetry locations.

6.2 Recommendations for future research

The developed coupled model has proven to be a useful tool to perform cost-efficient simulations of “far field” effects of WEC arrays. However, the coupled model has a lot of potential that could be extended in future research either by increasing the capabilities of the model itself or by performing numerical research based on the model capabilities:

1. Direct calculation of irregular waves

In the MILDwave-NEMOH coupled model irregular waves are obtained as superposition of regular wave components. The implementation of a direct calculation of the perturbed wave field in irregular waves for the internal wave generation boundary using a suitable wave-structure interaction solver, would lead to a computational speed up.

2. Multiple internal wave generation boundaries

The applicability of the coupled model has been exemplified for a single internal wave generation boundary. It would be valuable to consider implementing simultaneously different internal wave generation boundaries. This could prove useful to reduce the computational time when modelling WEC farms.

3. Wave-to-Wire Model

The PTO of the two WECs modelled has been implemented as a linear damping coefficient. If a more accurate representation of the PTO is needed,

the Python Shell Process offers the possibility of introducing a PTO simulator as a fifth independent process.

4. Simulating six DOFs WECs;
In this research a HCWEC and an OSWEC restricted to heave and surge motions, respectively have been modelled. However, NEMOH allows simulating full 6 DOFs which could be implemented in the coupled model.
5. Study "far field" effects under real ocean waves
The coupled model has shown the capability of modelling "far field" effects of WEC arrays under short-crested waves. This capability could be used to perform a parametric study of WEC array impacts under short-crested irregular waves.
6. Study "far field" effects under real bathymetries
The coupled model can be used with sloping and/or varying bathymetries. It would be valuable to compare the precision of the MILDwave-NEMOH coupled model with other studies performed using phase-resolving and phase-averaged models as indicated in Section 1.2.2. Different studies that have been performed at a wide range of locations such as the United Kingdom (Abanades et al. (2014)), Galicia (Carballo et al. (2015); Iglesias and Carballo (2014)), Spain (Rodriguez-Delgado et al. (2018)), Portugal (Rusu and Guedes Soares (2013); Bento et al. (2014); Onea and Rusu (2016); Rusu and Onea (2016)) and the Black Sea (Rusu and Diaconu (2014)), could be used for a comparison. Additionally, it would be interesting to compare the results from the different studies as the influence of WEC farms in the near shore is very case dependent and is highly influence by the seasonal variability of the wave climate and the bathymetry.
7. Study coastal morphodynamic changes
The results of the coupled model close to the near shore area can be used as input for numerical formulae or morphodynamic models such as XBeach (XBeach Open Source Community (2019)). The MILDwave-NEMOH coupled model can be used to obtain the time series of surface elevation at a certain depth and use it as the input for XBeach, or it can be directly coupled using a Python interface to transfer the information in the boundaries of the two models.

Appendix A

MILDwave-NEMOH original source code

This Appendix includes the main python based codes used to run the MILDwave-NEMOH coupled model. It was decided not to include the code used for the NEMOH process as it was only used to call the NEMOHO executable and has no added value to NEMOH itself. The Appendix includes the following python scripts:

1. "mw_nemoh_shell.py" (Algorithm A.1) is the python code used to execute the Python process.
2. "mw_utilities_run.py" (Algorithm A.2) is the python code used to execute the MILDwave process.
3. "coupling.py" (Algorithm A.3) is the python code used to execute the Coupling process.

Algorithm A.1: Python Shell: mw_nemoh_shell.py

```
"""
Created on Wed Oct 24 08:22:50 2018
@author: gveraofe
SCRIPT TO RUN A COUPLED SIMULATION
1. RUN NEMOH OR SELECT NEMOH RESULTS
2. RUN EB MW OR SELECT EXISTING EMPTY BASIN
3. RUN COUPLING FOLDERS OR SELECT A COUPLED FOLDER
4. INSTRUCTIONS MUST BE PLACED HERE AND NOT IN THE FUNCTIONS
"""
#FUNCTIONS FOR RUNNING MW
import os
import numpy as np
import sys
NEMOHDir = #DIRECTORY WHERE THE NEMOH PROGRAM IS LOCATED
CLI_dir = #Location of the CLI exe for MILDwave
#FUNCTIONS FOR RUNNING NEMOH
from MW_NEM.shared import nem_shell_utilities as nsu
from MW_NEM.shared import nem_utilities as ne
```

```

from MW_NEM_shared import meshTypes as mt
#
import mw_utilities_pre as pre
import mw_utilities_run as run
import mw_utilities_post as post
import coupling as cpl
import matplotlib.pyplot as plt
from xml.etree import ElementTree as et #Element Tree for modifying xml values
import time
import logging #writes log file with the simulation times
#
#
# 1.0 DEFINE SHELL PARAMETERS
#
#
print(f'Simulation_Started:_' + str(time.asctime()))
MW_sim = {}
MW_sim['run_name'] = 'ch4'
MW_sim['mw_dir'] = [""]
MW_sim['create_ini'] = True
MW_sim['run_NEMOH'] = False #RUN A NEW NEMOH SIMULATION OR USED AND EXISTING ONE
MW_sim['run_MW_EB'] = True #RUN AN INCIDENT WAVE IN MILDwave OR USE AND EXISTING ONE
MW_sim['run_MW_CPL'] = False #RUN A PERTURBED WAVE IN MILDwave OR USE AND EXISTING ONE
MW_sim['regular'] = True #REGULAR WAVE
MW_sim['irregular'] = False #IRREGULAR WAVE
MW_sim['directional'] = False #DIRECTIONAL IRREGULAR WAVE
MW_sim['interpolation'] = False #TODO REMOVE INTERPOLATION
MW_sim['Coupling'] = False #CREATE COUPLING FILES

for handler in logging.root.handlers[:]:
    logging.root.removeHandler(handler)
    logging.basicConfig(level=logging.DEBUG)

#
#
# 1.1 DEFINE MW INPUT WAVE CONDITIONS
#
#
MW_ini = {}
MW_ini = [{"_"} for _ in range(len(MW_sim['mw_dir']))]
if MW_sim['create_ini']:
    for ii in range(len(MW_ini)):
        MW_ini[ii]['mw_dir'] = MW_sim['mw_dir'][ii]
        MW_ini[ii]['depth'] = []
        if MW_sim['regular']:
            MW_ini[ii]['T'] = []
            MW_ini[ii]['H'] = []
            MW_ini[ii]['deg'] = []
            MW_ini[ii]['Nf'] = 1
        elif MW_sim['irregular']:
            MW_ini[ii]['Tp'] = []
            MW_ini[ii]['Hs'] = []
            MW_ini[ii]['spectra'] = 'PM'
            #JS for JONSWAP or PM for Pierson-Moskovitz
            MW_ini[ii]['fini'] = [1/(Tp+Tp*2/3) for Tp in MW_ini[ii]['Tp']]
            MW_ini[ii]['fend'] = [1/(Tp-Tp*1/3) for Tp in MW_ini[ii]['Tp']]
            MW_ini[ii]['Nf'] = 20
            MW_ini[ii]['deg'] = []
            if MW_sim['directional']:
                MW_ini[ii]['deg'] = []
                MW_ini[ii]['deg_main'] = []
                MW_ini[ii]['s1'] = []

pre.create_input(MW_sim, MW_ini[ii])

tree = et.parse(os.path.join(MW_sim['mw_dir'][ii], "MILDwave.xml"))

MW_ini[ii]['Nx'] = int(tree.find("./Nx").text)
MW_ini[ii]['Ny'] = int(tree.find("./Ny").text)
# left and right sponge layers
MW_ini[ii]['Lsponge'] = int(tree.find("./ixsL").text)

```

```

MW_ini[ii]['R sponge']=int(tree.find("./ixsR").text)

MW_ini[ii]['dx_bin_step'] = 2
MW_ini[ii]['dy_bin_step'] = 2

MW_ini[ii]['kd_x'] = []
MW_ini[ii]['kd_y'] = []
# for complete domain = MILDwave domain size -2
# snaphot if rest of simulations fails save initial conditions
MW = {'MW_sim' : MW_sim, 'MW_ini' : MW_ini}
np.savez(MW_sim['run_name'] + "_snap", **MW)
del MW

else:
    for ii in range(len(MW_ini)):
        MW = np.load(MW_sim['run_name'] + "_snap.npz")
        MW_ini[ii] = MW['MW_ini'][ii]
        del MW

#-----
#                               1.2 DEFINE COUPLING SIMULATION PARAMETERS
#-----
MW_CPL = [{ } for _ in range(len(MW_sim['mw_dir']))]
for ii in range(len(MW_sim['mw_dir'])):
    MW_CPL[ii]['circ'] = True #generates a circular coupling zone
    MW_CPL[ii]['rect'] = False#generates a rectangular coupling zone
    MW_CPL[ii]['output_check'] = False
    MW_CPL[ii]['frequency_check'] = 0#

if MW_sim['irregular']:
    MW_CPL[ii]['FFT_BLOCK'] = 512
    MW_CPL[ii]['Overlap'] = 0.5 #Between 0 < Overlap < 1

if MW_CPL[ii]['circ']:
    MW_CPL[ii]['radius'] = 50.0
    MW_CPL[ii]['ph_LOC_x'] = []
    MW_CPL[ii]['ph_LOC_y'] = []

#-----
#                               1.3 DEFINE MW SIMULATION EXECUTABLE PARAMETERS
#-----
MW_exe = { }
# change name
MW_exe['mw_cli'] = CLI_dir
MW_exe['mw_dir'] = MW_sim['mw_dir']
MW_exe['time_ramp'] = 300
MW_exe['time_Kd'] = 601
MW_exe['n_cores'] = 10
MW_OUT = { }
MW_OUT = [{ } for _ in range(len(MW_sim['mw_dir']))]

#-----
#                               1.4 DEFINE NEMOH SIMULATION PARAMETERS and RUN NEMOH
#-----
if MW_sim['run_NEMOH']:
    #data structure containing the Simulation Parameters for NEMOH
    NEM_ini = [{ } for _ in range(len(MW_sim['mw_dir']))]
    # different mw dirs must have the ability to have different nemoh runs
    for ii in range(len(MW_exe['mw_dir'])):
        print(f'Simulation_Started_NEMOH:_' + str(time.asctime()))
        logging.info('Simulation_Started_NEMOH:_' + str(time.asctime()))
        #lets' set these and the wave conditions depth etc. equal to the mw_dir so reg=reg
        NEM_ini[ii]['case_dir'] = MW_sim['mw_dir']
        NEM_ini[ii]['runNEMOH'] = MW_sim['run_NEMOH']
        NEM_ini[ii]['regular'] = MW_sim['regular']
        NEM_ini[ii]['irregular'] = MW_sim['irregular']
        NEM_ini[ii]['directional'] = False#MW_sim['directional']
        NEM_ini[ii]['interpolation'] = MW_sim['interpolation']

```

```

#
#                               1.4.1 WAVE CONDITIONS
#
NEM_ini[ii]['depth'] = [30.0]

if NEM_ini[ii]['regular']:
    NEM_ini[ii]['T'] = MW_ini[ii]['T']#[[1.26]]#define each T as list
    NEM_ini[ii]['H'] = MW_ini[ii]['H']#[[0.104]]#define each H as list
    NEM_ini[ii]['deg'] = MW_ini[ii]['deg']#[[0.0]]
    NEM_ini[ii]['Nf'] = 1
elif NEM_ini[ii]['irregular']:
    NEM_ini[ii]['T'] = MW_ini[ii]['T']#[1.26]
    NEM_ini[ii]['H'] = MW_ini[ii]['H']#[1.26]
    NEM_ini[ii]['Tp'] = MW_ini[ii]['Tp']#[1.26]
    NEM_ini[ii]['Hs'] = MW_ini[ii]['Hs']#[0.104]
    NEM_ini[ii]['spectra'] = MW_ini[ii]['spectra']
    NEM_ini[ii]['fini'] = MW_ini[ii]['fini']#0.7#0.705
    NEM_ini[ii]['fend'] = MW_ini[ii]['fend']#2.1#2.15
    NEM_ini[ii]['Nf'] = MW_ini[ii]['Nf']#20
    NEM_ini[ii]['deg'] = MW_ini[ii]['deg']#[[0.0]]
    if MW_sim['directional']:
        NEM_ini[ii]['deg'] = []
        NEM_ini[ii]['deg_main'] = MW_ini[ii]['deg_main']
        NEM_ini[ii]['s1'] = MW_ini[ii]['s1']

nsu.create_input(NEM_ini[ii]) #function name not class name

    if MW_sim['directional']:
        NEM_ini[ii]['deg'] = MW_ini[ii]['deg']

```

```

#
#                               1.4.2 GRID
#

```

```

NEM_GRID = {} #NEMOH input in meters!!!
NEM_GRID['Lg'] = []
NEM_GRID['Wg'] = []
NEM_GRID['dx'] = []
NEM_GRID['dy'] = []
NEM_GRID['Nx'] = []
NEM_GRID['Ny'] = []
if NEM_ini[ii]['interpolation']:
    NEM_GRID['dxN'] = []
    NEM_GRID['dxN'] = []
NEM_OUT=[{} for _ in range(len(MW_exe['mw_dir']))]
for ii in range(len(MW_exe['mw_dir'])):

```

```

#
#                               1.4.3 NEM BODY
#

```

```

NEM_BODY = [{} for _ in range(len(MW_exe['mw_dir']))]
NEM_BODY[ii]['dof'] = [0,0,1,0,0,0]
NEM_BODY[ii]['ndof'] = np.sum(NEM_BODY[ii]['dof'])

NEM_BODY[0]['nbody'] = 1
NEM_BODY[0]['xBody'] = [0]
NEM_BODY[0]['yBody'] = [0]
cylmesh = [0]*NEM_BODY[ii]['nbody']
NEM_BODY[ii]['cG'] = -1.
nPanels = 200
nsym = 0
NEM_BODY[ii]['rho'] = 1025.0
NEM_BODY[ii]['PTOtype'] = 'Bpto_L'
NEM_BODY[ii]['Bpto'] = 2.25 * 10**6
NEM_BODY[ii]['ptoProp'] = [0.0, NEM_BODY[ii]['Bpto'], 0.0]

```

```

#
#                               1.4.4 MESHING
#

```

```

os.chdir(os.path.join(NEMOHDDir, 'Calculation'))

```

```

    if not(os.path.isdir('mesh')) :
        os.mkdir('mesh')
    # and f'inresults folder
    if not(os.path.isdir('results')) :
        os.mkdir('results')
    for iB in range(NEM.BODY[ii]['nbody']):
        cylmesh[iB] = mt.shape()#diameter and draft

    if NEM.BODY[ii]['nbody'] > 1:
        mt.writeMesh(cylmesh[iB], './mesh/axisym {0:d}'.format(iB+1))
    else:
        mt.writeMesh(cylmesh[iB], './mesh/axisym')
    ne.createMeshOpt()
    (NEM.BODY[ii]['Mass'],NEM.BODY[ii]['Kh']) = ne.calcM(rho=1026.0)

#-----
#
#                               1.4.5. NEMOH SIMULATION PARAMETERS (ADVANCED OPTIONS)
#-----
# Basic Options (RAO calculation)
nrFreq = 1
NEM_advOps = {}
NEM_advOps['rhoW'] = 1025.0      #water density
NEM_advOps['dirCheck'] = True#Activate to change wave direction
NEM_advOps['dirStep'] = 1
NEM_advOps['irfCheck'] = False#Activate for IRF calculations
NEM_advOps['irfDur'] = 40.0
NEM_advOps['irfStep'] = 0.01
NEM_advOps['kochCheck'] = False#Activate to calculate Kochin Function
NEM_advOps['kochStart'] = 0.0
NEM_advOps['kochStop'] = 360.0
NEM_advOps['kochStep'] = 24
NEM_advOps['fsCheck'] = True#Activate to calculate free surface elevation
NEM_advOps['fsNx'] = NEM.GRID['Nx']
NEM_advOps['fsNy'] = NEM.GRID['Ny']
NEM_advOps['fsLengthX'] = NEM.GRID['Lg']
NEM_advOps['fsLengthY'] = NEM.GRID['Wg']
NEM_advOps['Show_Console'] = False #Toggle ON or OFF the WINDOWS CONSOLE

#-----
#
#                               1.4.6. RUNNING NEMOH
#-----

(NEM.OUT[ii]) = nsu.runNEM(nrFreq, NEM.ini[ii],
                          NEM.BODY[ii], NEM_advOps, NEM.GRID, NEMOHDDir)

#-----
#
#                               1.4.7. GENERATING COUPLING OUTPUTS FROM NEMOH
#-----

NEM = {'NEM.ini' : NEM.ini, 'NEM.GRID' : NEM.GRID,
       'NEM.BODY' : NEM.BODY, 'NEM_advOps' : NEM_advOps, 'NEM.OUT' : NEM.OUT}
np.savez('nem-'+MW.sim['run_name'],**NEM)

else :
    nemoh_dir = os.path.abspath(os.path.join(MW.sim['mw_dir'][0], '..'))
    NEM = np.load(os.path.join(nemoh_dir, 'nem_'+ MW.sim['run_name']+'.npz'))
    NEM_ini = NEM['NEM.ini']
    NEM_GRID = NEM['NEM.GRID'].item()
    NEM_BODY = NEM['NEM.BODY']
    NEM_advOps = NEM['NEM_advOps'].item()
    NEM_OUT = NEM['NEM.OUT']

#-----
#
#                               1.5.1 RUN MW EMPTY BASIN
#-----
if MW.sim['run_MW_EB']:
    for ii in range(len(MW.sim['mw_dir'])):
        if MW.sim['regular']:
            for ii in range(len(MW.sim['mw_dir'])):

```

```

        if MW_sim['regular']:
            pre.reg_init(MW_ini[ii],MW_exe)
            mwd = MW_exe['mw_dir'][ii]
            for Tjj in MW_ini[ii]['T']:
                run_type = 'EB'
                run.run_mw(MW_sim, MW_ini[ii], mwd, Tjj, MW_exe, run_type, Tnn="")
    elif MW_sim['irregular']: #TODO not checked!!!
        pre.irr_init(MW_ini[ii],MW_exe)
        mwd = MW_exe['mw_dir'][ii]
        for jj in range(len(MW_ini[ii]['Tp'])):
            Tjj = MW_ini[ii]['Tp'][jj]
            Tnn = MW_ini[ii]['T'][jj]
            run_type = 'EB'
            run.run_mw(MW_sim, MW_ini[ii], mwd, Tjj, MW_exe, run_type, Tnn)

```

```

#
#
#

```

1.5.2 CALCULATE MW INCIDENT WAVE KD

```

run_type = 'EB'

for ii in range(len(MW_exe['mw_dir'])):
    (MW_OUT[ii]['Kd.EB'],MW_OUT[ii]['x_vector'],MW_OUT[ii]['y_vector'])
    = post.kd_EB(MW_sim,MW_ini[ii],MW_exe)

```

```

#
#
#

```

1.5.3 RUN MW PERTURBED WAVE SIMULATION

```

if MW_sim['run_MW_CPL']:
    print(f'Simulation_Coupled_Wave_MW_Started:_{str(time.asctime())}')

    for ii in range(len(MW_sim['mw_dir'])):
        if MW_sim['Coupling']:

            cpl.coupling(MW_sim,MW_ini[ii],MW_exe,MW_OUT[ii],
                        ,MW_CPL[ii],NEM_ini,NEM_GRID,NEM_OUT[ii])
            mwd = MW_exe['mw_dir'][ii]
            if MW_sim['regular']:
                for jj in range(len(MW_ini[ii]['T'])):
                    Tjj=MW_ini[ii]['T'][jj]
                    for kk in range(len(MW_CPL[ii]['ph.LOC_x'])):
                        run_type = 'CP_'+LOC_+str(kk)
                        run.run_mw(MW_sim, MW_ini[ii], mwd, Tjj, MW_exe, run_type, Tnn="")
            elif MW_sim['irregular']:
                for jj in range(len(MW_ini[ii]['Tp'])):
                    Tjj = MW_ini[ii]['Tp'][jj]
                    Tnn = MW_ini[ii]['T'][jj]
                    for kk in range(len(MW_CPL[ii]['ph.LOC_x'])):
                        run_type = 'CP_'+LOC_+str(kk)
                        run.run_mw(MW_sim, MW_ini[ii], mwd, Tjj, MW_exe, run_type, Tnn)

```

```

#
#
#

```

1.5.4 CALCULATE KD PERTURBED WAVE SIMULATION

```

for ii in range(len(MW_sim['mw_dir'])):
    (MW_OUT[ii]['Kd.CP'],MW_OUT[ii]['x_vector'],MW_OUT[ii]['y_vector'])
    = post.kd_CP(MW_sim, MW_ini[ii], MW_CPL[ii], MW_exe)

```

```

#
#
#

```

1.5.5 CALCULATE MW TOTAL WAVE

```

for ii in range(len(MW_exe['mw_dir'])):
    MW_OUT[ii]['Kd.TW'] = post.total_wave(MW_sim, MW_ini[ii], MW_exe, MW_CPL[ii])

```

```

#create dictionary of dictionaries for saving all data
MW = {'MW_sim' : MW_sim, 'MW_ini' : MW_ini, 'MW_exe' : MW_exe,
      'MW_CPL[ii]' : MW_CPL[ii], 'MW_OUT' : MW_OUT}
np.savez(MW_sim['run_name'], '..', 'MW'),**MW

```

Algorithm A.2: MILDwave process: mw_nemoh_run.py

```

@author: gverao
Modified on Thu Feb 28 19:48:35 2019 by pbalitsk
functions Necessary for runnign MILDwave and calling the MW_CLI
run_mw set up the MILDwave runs and shuffle around the outputs
execute_mw -call subprocess to run mw_cli.exe

import numpy as np
import os
from xml.etree import ElementTree as et
import subprocess
import shutil
import time
from subprocess import Popen

def run_mw(MW_sim, MW_ini, mw_dir, Tjj, MW_exe, run_type, Tnn):

    dir_exe = MW_exe['mw_cli']
    dx_bin_step=MW_ini['dx_bin_step']
    if MW_sim['regular']:
        dir_data = 'data'
        T_dir= os.path.join(mw_dir, 'T_'+ '{:05.2f}'.format(Tjj), run_type)
        execute_mw(dir_exe, T_dir, MW_sim['regular'], dx_bin_step)
        tree = et.parse(os.path.join(T_dir, "MILDwave.xml"))
        time_length = float(truncate(np.float(tree.find("../etaOutput/end").text),3))
            - float(truncate(np.float(tree.find("../etaOutput/start").text),3))
        dt = np.float(tree.find("../etaOutput/increment").text)
            *np.float(tree.find("../delt").text)
        time_length = int(time_length/dt)*dt
        npoints = int((time_length/dt) * MW_ini['kd_x'] * MW_ini['kd_y'] )
        with open(os.path.join(T_dir, dir_data, 'eta.bin')) as feta:
            eta = np.fromfile(feta, dtype = np.float32, count = npoints, sep='')
            os.remove(os.path.join(T_dir, dir_data, 'eta.bin'))
            np.save(os.path.join(T_dir, dir_data, 'eta'), eta)
        del eta
    else: # Irregular
        n = MW_exe['n_cores']
        dir_data = 'data'
        Tp_dir = os.path.join(mw_dir, 'Tp_'+ '{:05.2f}'.format(Tjj))
        f_runs = [dir_Tnn[i * n:(i + 1) * n] for i in range((len(dir_Tnn)+n-1)//n)]
        tree = et.parse(os.path.join(Tp_dir, "MILDwave.xml"))
        time_length = float(truncate(np.float(tree.find("../etaOutput/end").text),3))
            -float(truncate(np.float(tree.find("../etaOutput/start").text),3))
        dt = np.float(tree.find("../etaOutput/increment").text)
            *np.float(tree.find("../delt").text)
        time_length = int(time_length/dt)*dt
        npoints = int((time_length/dt) * MW_ini['kd_x'] * MW_ini['kd_y'])

    for subdir_mw in f_runs:

        execute_mw(dir_exe, subdir_mw, MW_sim['regular'], dx_bin_step)

        if os.path.exists(os.path.join(Tp_dir, run_type, dir_data, 'eta.npy')):
            eta_irr = np.load(os.path.join(Tp_dir, run_type, dir_data, 'eta.npy'))
        else:
            eta_irr = 0

        for dir_name in subdir_mw:
            with open(os.path.join(dir_name, dir_data, 'eta.bin')) as feta:
                eta_irr += np.fromfile(feta, dtype = np.float32, count = npoints, sep='')
            os.remove(os.path.join(dir_name, dir_data, 'eta.bin'))

```



```

w = 2*np.pi / Tw
eta_instant = eta_phi+1j*phi_aux*w/9.81
phase = np.angle(eta_instant)
amp_aux = wave_ampw[nn]
pert_wave_aux = pert_wave[nn]
phase_aux = 1j*phase[[loc_y[kk]], [loc_x[kk]]]
pert_wave_coup = amp_aux*pert_wave_aux*np.exp(phase_aux)

Lgmw = (int(tree.find("./Nx").text)-1)*float(tree.find("./dx").text)
Wgmw = (int(tree.find("./Ny").text)-1)*float(tree.find("./dy").text)

xFS = np.arange(-NEM_GRID['Lg']/2.0,
NEM_GRID['Lg']/2.0+NEM_GRID['dx'], NEM_GRID['dy'])
xFS = xFS[:NEM_GRID['Nx']]
yFS = (-1)*np.arange(-NEM_GRID['Wg']/2.0,
NEM_GRID['Wg']/2.0+NEM_GRID['dy'], NEM_GRID['dy'])
yFS = yFS[:NEM_GRID['Ny']]
X, Y = np.meshgrid(xFS, yFS)
xFS_mw = np.arange(-Lgmw/2.0,
Lgmw/2.0+NEM_GRID['dx'], NEM_GRID['dx'])
#xFS_mw = xFS_mw[:Nx_mw]
yFS_mw = (-1)*np.arange(-Wgmw/2.0,
Wgmw/2.0+NEM_GRID['dy'], NEM_GRID['dy'])
#yFS_mw = yFS_mw[:Ny_mw]
Xmw, Ymw = np.meshgrid(xFS_mw, yFS_mw)

if MW_CPL['circ']:

    dx = NEM_GRID['dx']
    dy = NEM_GRID['dy']

    center_x = 0
    center_y = 0
    center_xmw = 0
    center_ymw = 0

    mask1 = np.sqrt((X-center_x)**2+(Y-center_y)**2)
    < MW_CPL['radius'] + dx
    mask2 = np.sqrt((Xmw-center_xmw)**2+(Ymw-center_ymw)**2)
    < MW_CPL['radius'] + dy

    yynm, xxnm = np.where(mask1)
    yymw, xxmw = np.where(mask2)

elif MW_CPL['rect']:
    xxh = int(NEM_GRID['Nx']/2) - int(MW_CPL['length']/(NEM_GRID['dx'] *2))
    yyh = int(NEM_GRID['Ny']/2) - int(MW_CPL['width']/(NEM_GRID['dy'] *2))
    xxh_mw = int(MW_ini['Nx']/2) - int(MW_CPL['length']/(NEM_GRID['dx'] *2))
    yyh_mw = int(MW_ini['Ny']/2) - int(MW_CPL['width']/(NEM_GRID['dy'] *2))
    mask1 = np.zeros((np.shape(Y)[0], np.shape(X)[1]), dtype=bool)
    mask1[yyh:yyh+int(MW_CPL['width']/(NEM_GRID['dy']))],
          xxh:xxh+int(MW_CPL['length']/(NEM_GRID['dx']))] = True
    mask2 = np.zeros((np.shape(Ymw)[0], np.shape(Xmw)[1]), dtype=bool)
    mask2[yyh_mw:yyh_mw+int(MW_CPL['width']/(NEM_GRID['dy']))],
          xxh_mw:xxh_mw+int(MW_CPL['length']/(NEM_GRID['dx']))] = True
    yynm, xxnm = np.where(mask1)
    yymw, xxmw = np.where(mask2)

amp = np.zeros((np.shape(xxnm)[0]))
phase = np.zeros((np.shape(xxnm)[0]))
amp[:] = np.abs(pert_wave_coup[yynm, xxnm])
phase[:] = np.angle(pert_wave_coup[yynm, xxnm])
#
#
#
fid = open(os.path.join(dir_cp_full[nn], 'nemoh_data.txt'), 'w')
for mm in range(np.shape(amp)[0]):
    fid.write((xxmw[mm]+xoff[kk], yymw[mm]+yoff[kk], amp[mm], phase[mm]))
fid.close()

```

5. CREATING NEMOH.DATA.TXT

```

def coupling_input_irregular(Nf, f, dir_Tp, MW_exe, MW_ini, MW_CPL):
    with open(os.path.join(dir_Tp, 'EB', 'data', 'eta.npy')) as feta:
        eta_irr = np.fromfile(feta, dtype = np.float32, count = npoints, sep='')

    WG[0][jj][tt] = eta_irr[tt][np.int(locy*dy_ini/dy), np.int(locx*dx_ini/dx)]

    fs = 1/dt

    df = (np.max(f)-np.min(f))/(np.shape(f)[0]-1)
    S_coupling_loc = []
    Hi_coupling_loc = []
    amp_coupling_loc = []
    for ww in range(len(WG[0])):
        S_coupling_aux = np.zeros(Nf)
        Hi_coupling_aux = np.zeros(Nf)
        amp_coupling_aux = np.zeros(Nf)
        fsd, S = signal.welch(WG[0][ww], fs, nperseg = MW_CPL['FFT_BLOCK'],
                             noverlap = MW_CPL['FFT_BLOCK'] * MW_CPL['Overlap'],
                             scaling = 'density')
        for ii in range(len(f)):
            for kk in range(1, np.shape(S)[0]):
                if fsd[kk-1] <= f[ii] <= fsd[kk]:
                    if f[ii] < (1/Tp):
                        S_coupling_aux[ii] = S[kk-1]
                        Hi_coupling_aux[ii] = 2.0 * np.sqrt(2.0*S_coupling_aux[ii]*df)
                        amp_coupling_aux[ii] = Hi_coupling_aux[ii]/2.0
                    else:
                        S_coupling_aux[ii] = S[kk]
                        Hi_coupling_aux[ii] = 2.0 * np.sqrt(2.0*S_coupling_aux[ii]*df)
                        amp_coupling_aux[ii] = Hi_coupling_aux[ii]/2.0
            S_coupling_loc.append(S_coupling_aux)
            Hi_coupling_loc.append(Hi_coupling_aux)
            amp_coupling_loc.append(amp_coupling_aux)
    return(amp_coupling_loc[0])

```

Appendix B

Numerical validation results

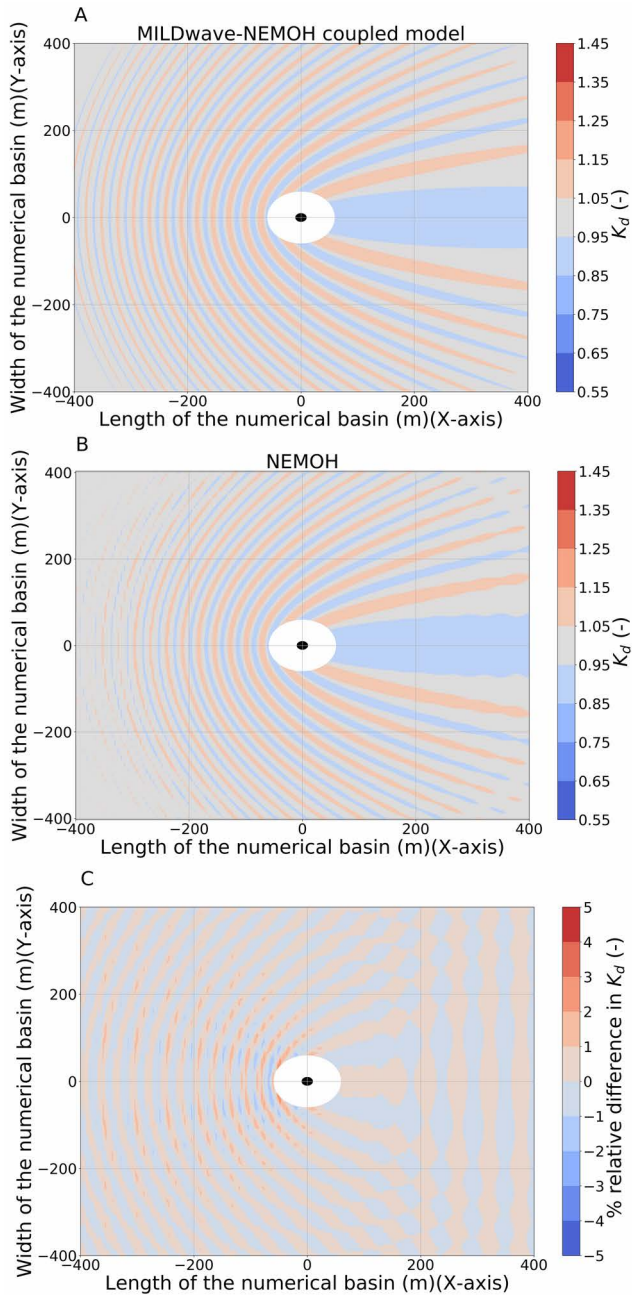


Figure B.1: Numerical validation results for Test Case 1: (A) K_d results for the MILDwave-NEMOH coupled model, (B) K_d results for NEMOH and (C) relative difference in K_d between the two models.

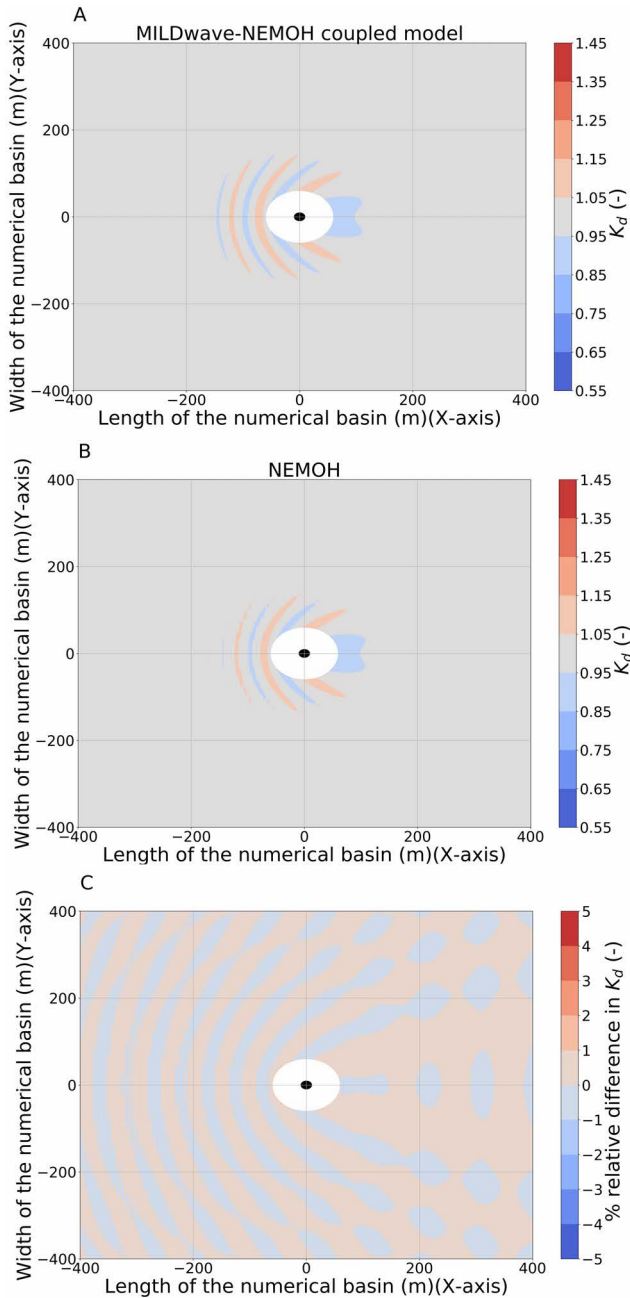


Figure B.2: Numerical validation results for Test Case 2: (A) K_d results for the MILDwave-NEMOH coupled model, (B) K_d results for NEMOH and (C) relative difference in K_d between the two models.

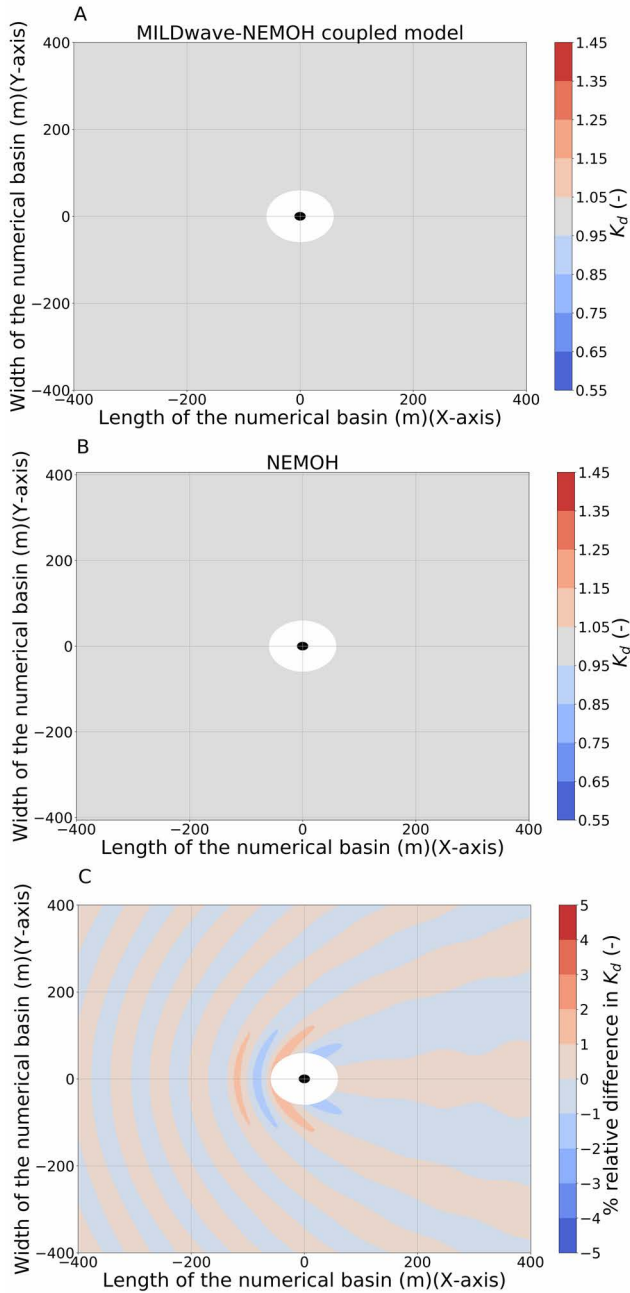


Figure B.3: Numerical validation results for Test Case 3: (A) K_d results for the MILDwave-NEMOH coupled model, (B) K_d results for NEMOH and (C) relative difference in K_d between the two models.

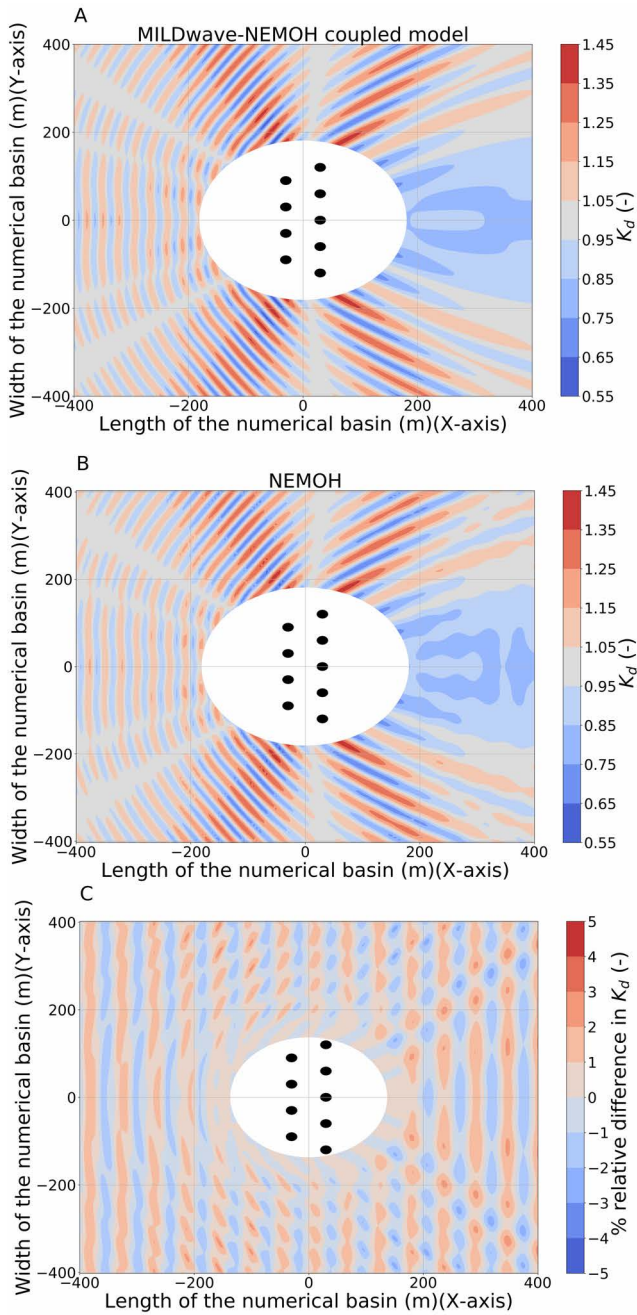


Figure B.4: Numerical validation results for Test Case 4: (A) K_d results for the MILDwave-NEMOH coupled model, (B) K_d results for NEMOH and (C) relative difference in K_d between the two models.

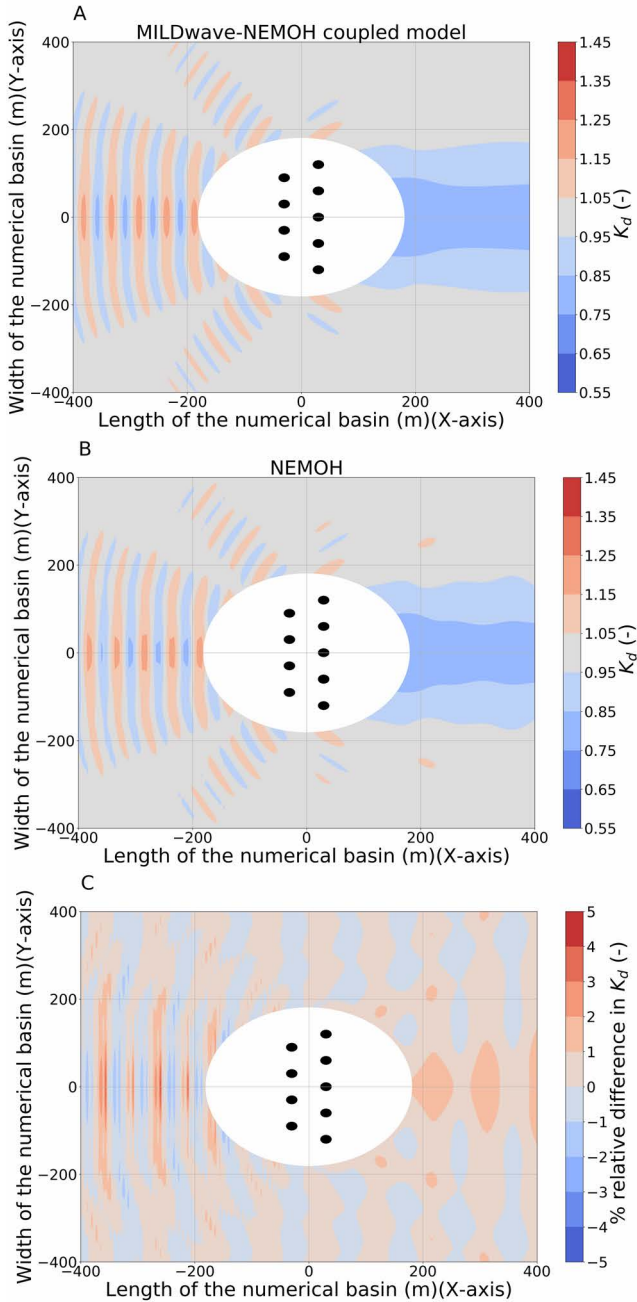


Figure B.5: Numerical validation results for Test Case 5: (A) K_d results for the MILDwave-NEMOH coupled model, (B) K_d results for NEMOH and (C) relative difference in K_d between the two models.

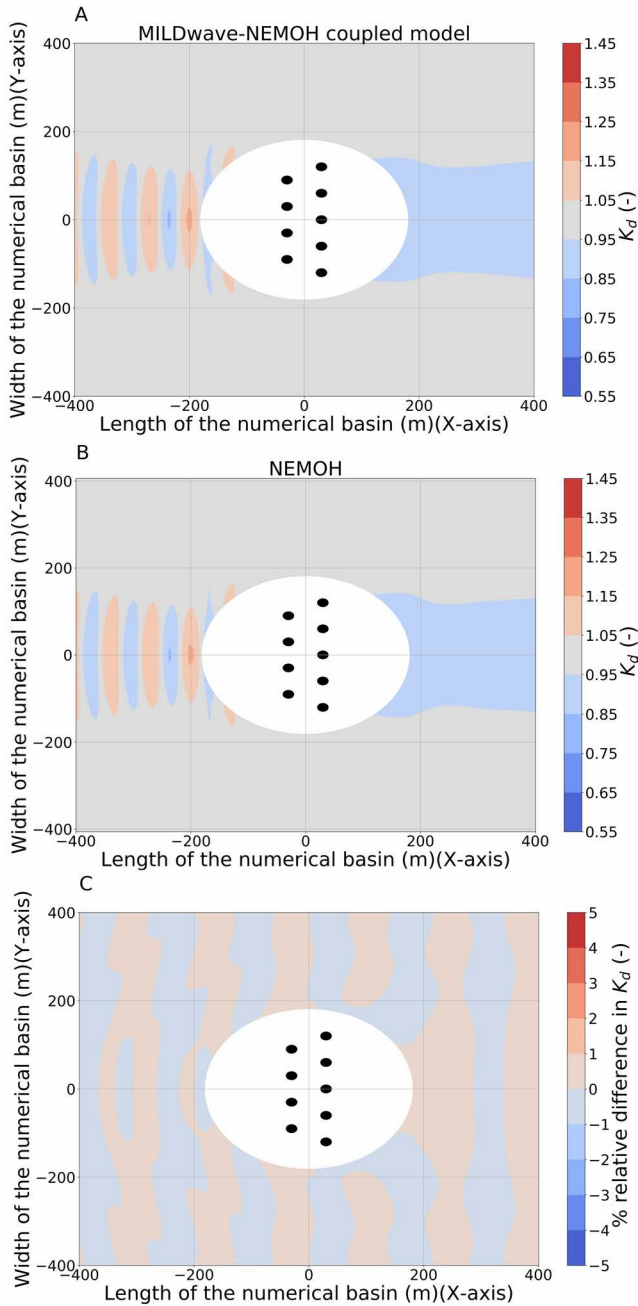


Figure B.6: Numerical validation results for Test Case 6: (A) K_d results for the MILDwave-NEMOH coupled model, (B) K_d results for NEMOH and (C) relative difference in K_d between the two models.

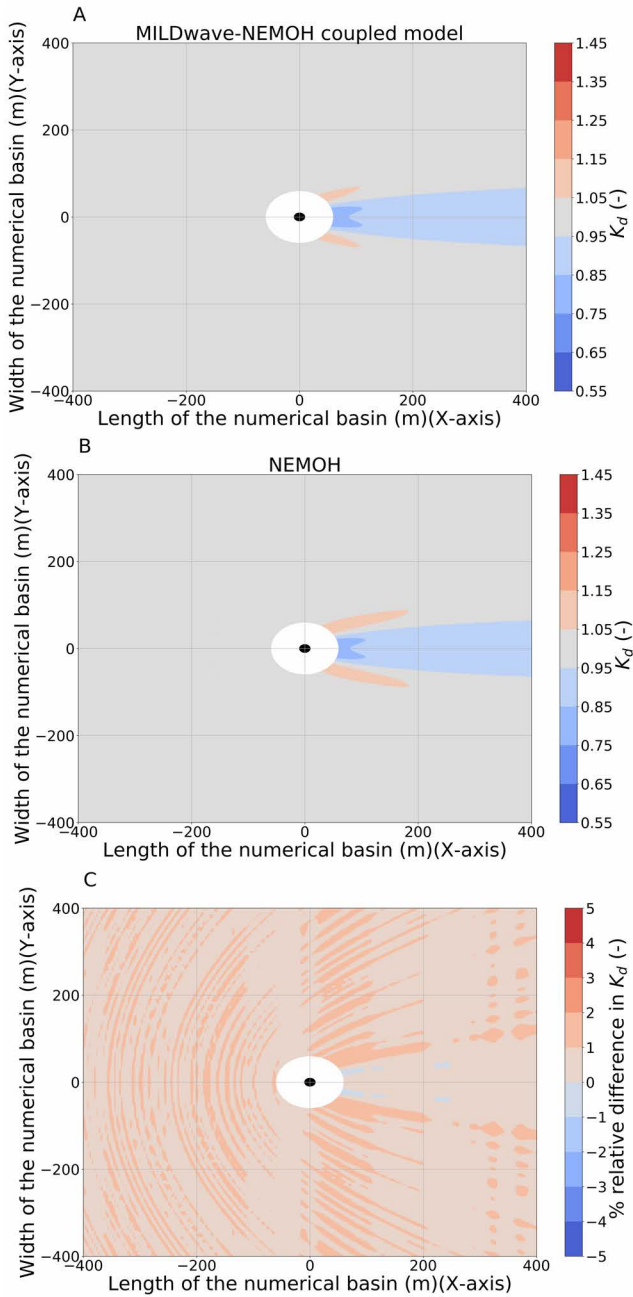


Figure B.7: Numerical validation results for Test Case 7: (A) K_d results for the MILDwave-NEMOH coupled model, (B) K_d results for NEMOH and (C) relative difference in K_d between the two models.

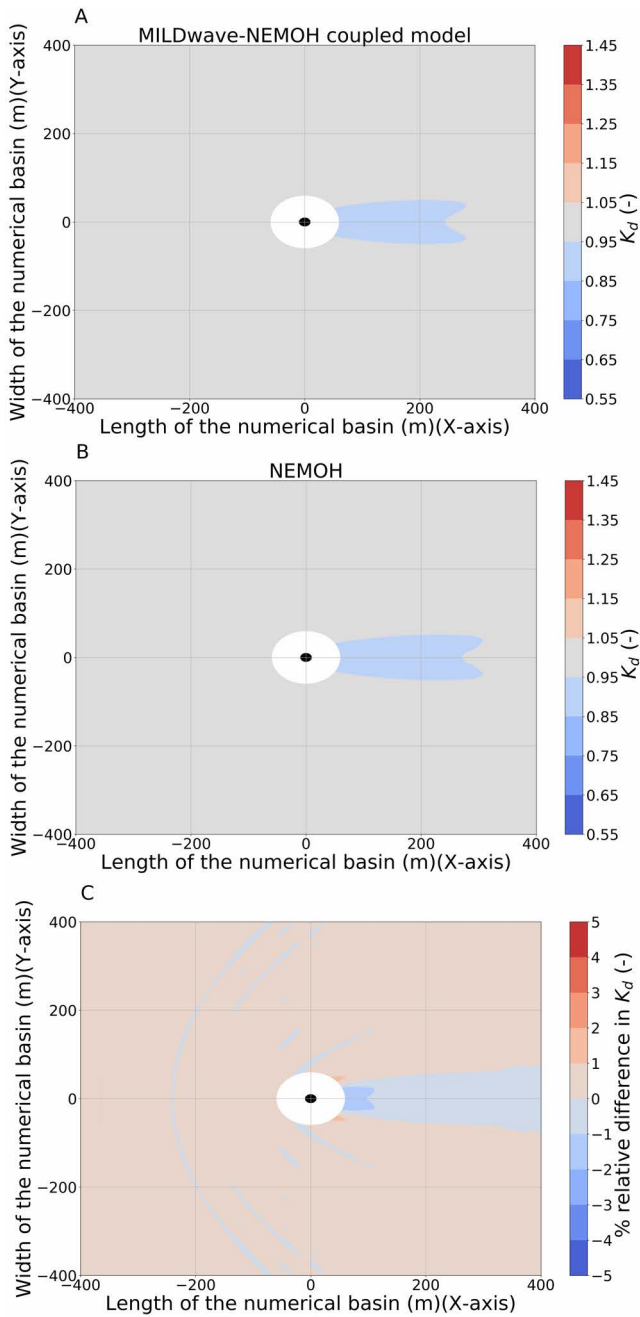


Figure B.8: Numerical validation results for Test Case 8: (A) K_d results for the MILDwave-NEMOH coupled model, (B) K_d results for NEMOH and (C) relative difference in K_d between the two models.

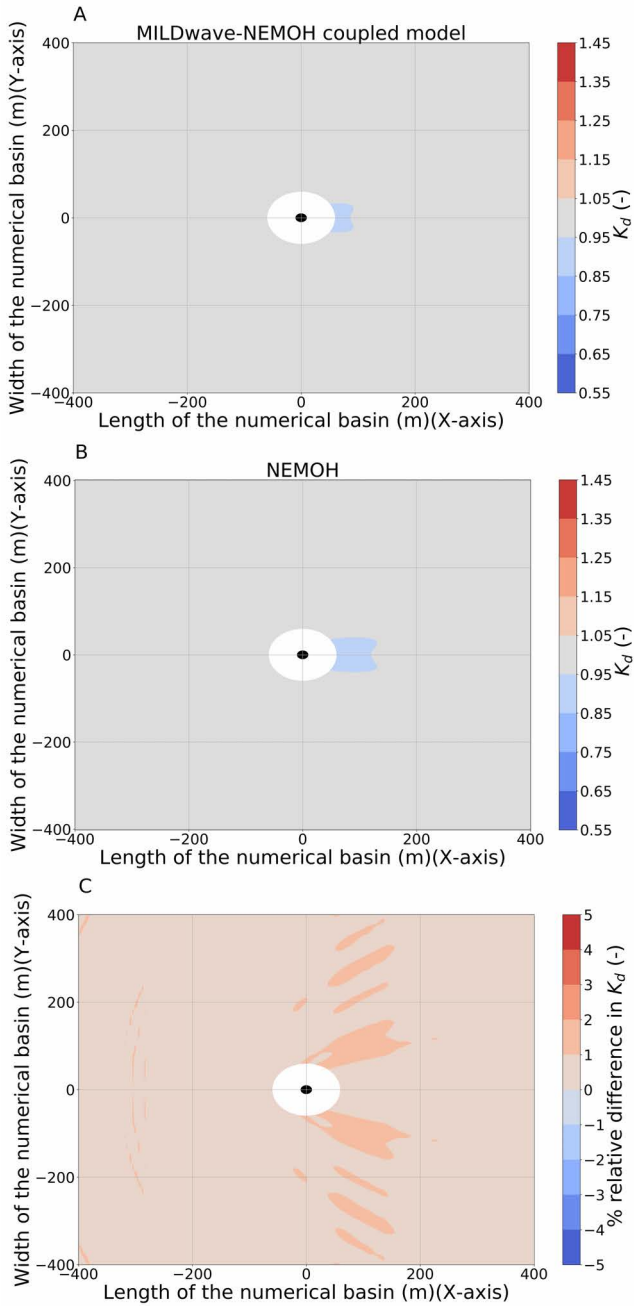


Figure B.9: Numerical validation results for Test Case 9: (A) K_d results for the MILDwave-NEMOH coupled model, (B) K_d results for NEMOH and (C) relative difference in K_d between the two models.

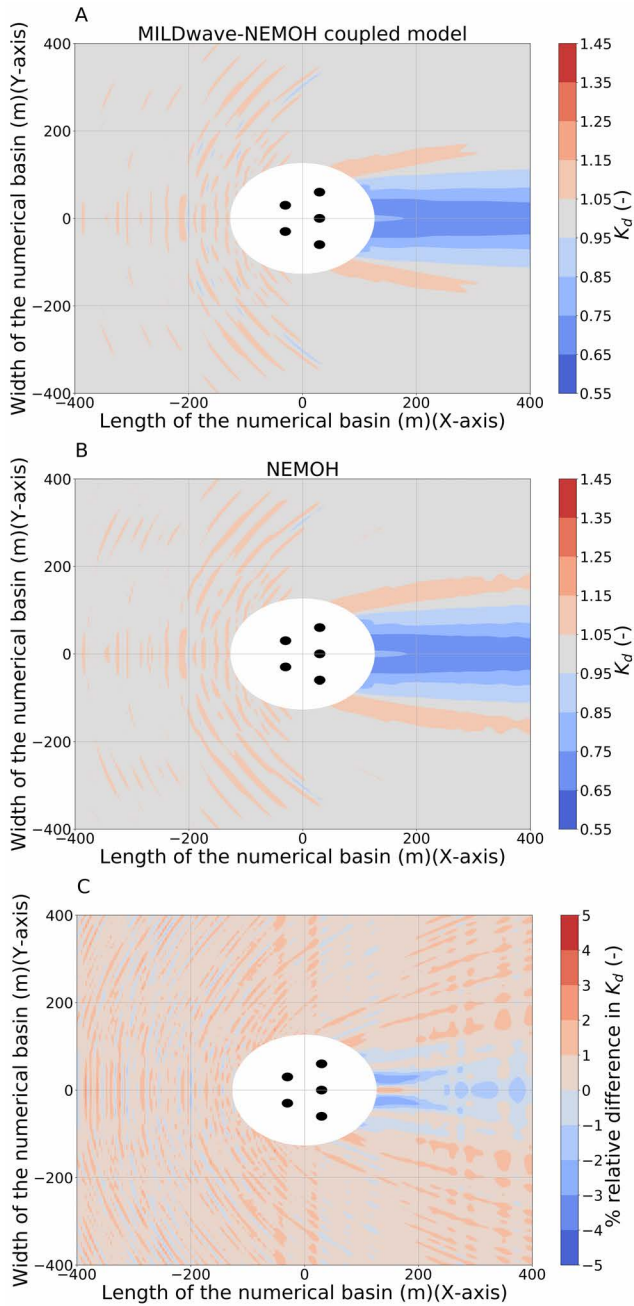


Figure B.10: Numerical validation results for Test Case 10: (A) K_d results for the MILDwave-NEMOH coupled model, (B) K_d results for NEMOH and (C) relative difference in K_d between the two models.

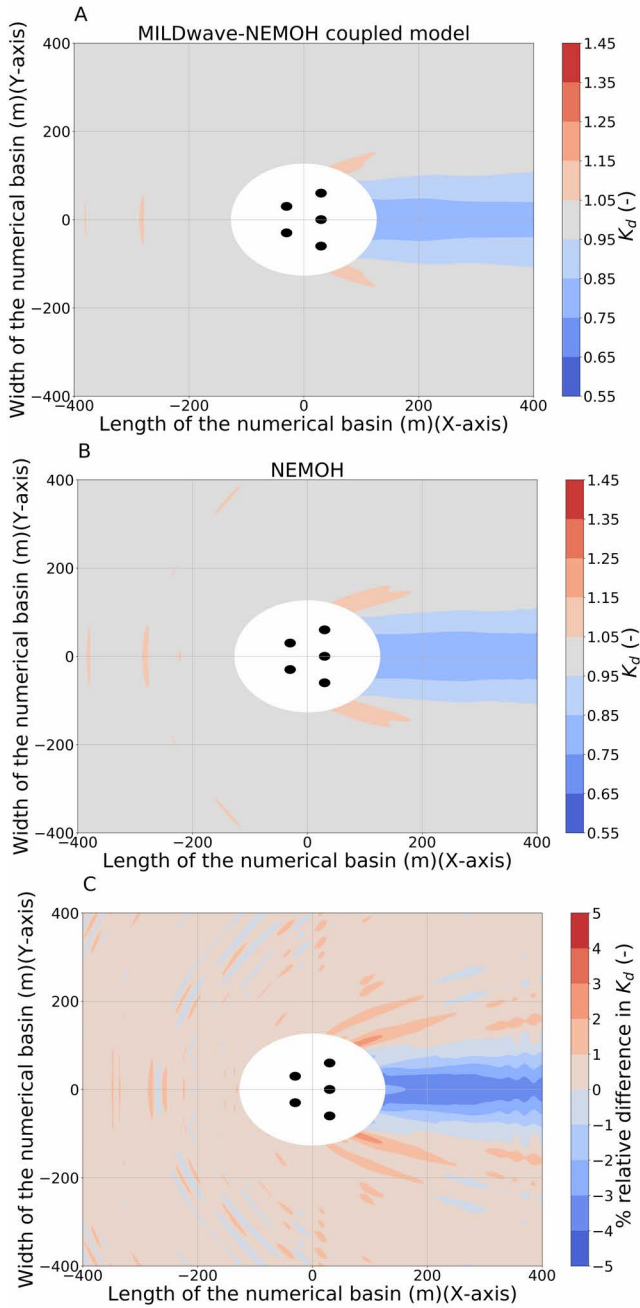


Figure B.11: Numerical validation results for Test Case 11: (A) K_d results for the MILDwave-NEMOH coupled model, (B) K_d results for NEMOH and (C) relative difference in K_d between the two models.

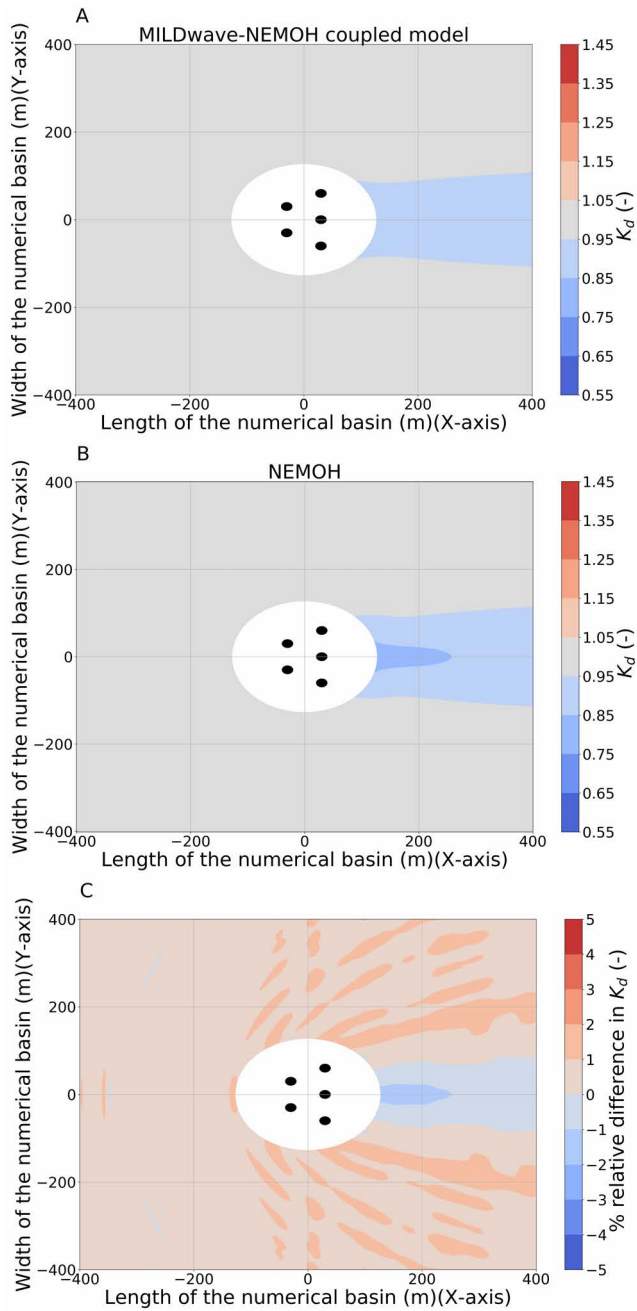


Figure B.12: Numerical validation results for Test Case 12: (A) K_d results for the MILDwave-NEMOH coupled model, (B) K_d results for NEMOH and (C) relative difference in K_d between the two models.

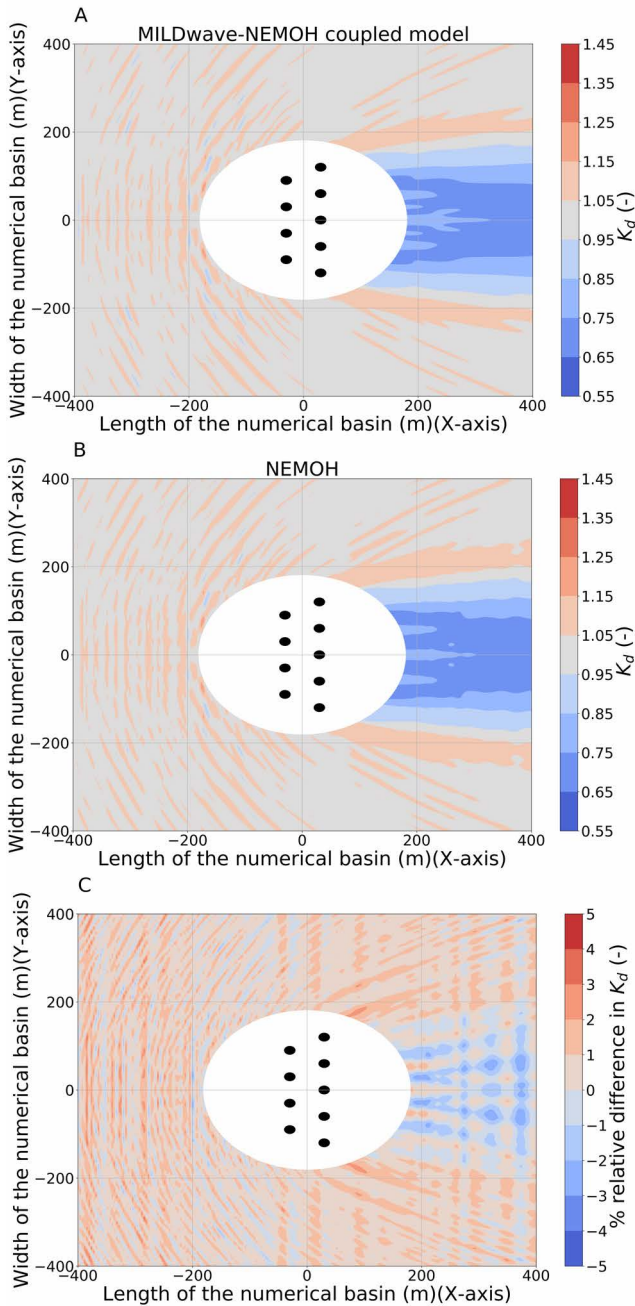


Figure B.13: Numerical validation results for Test Case 13: (A) K_d results for the MILDwave-NEMOH coupled model, (B) K_d results for NEMOH and (C) relative difference in K_d between the two models.

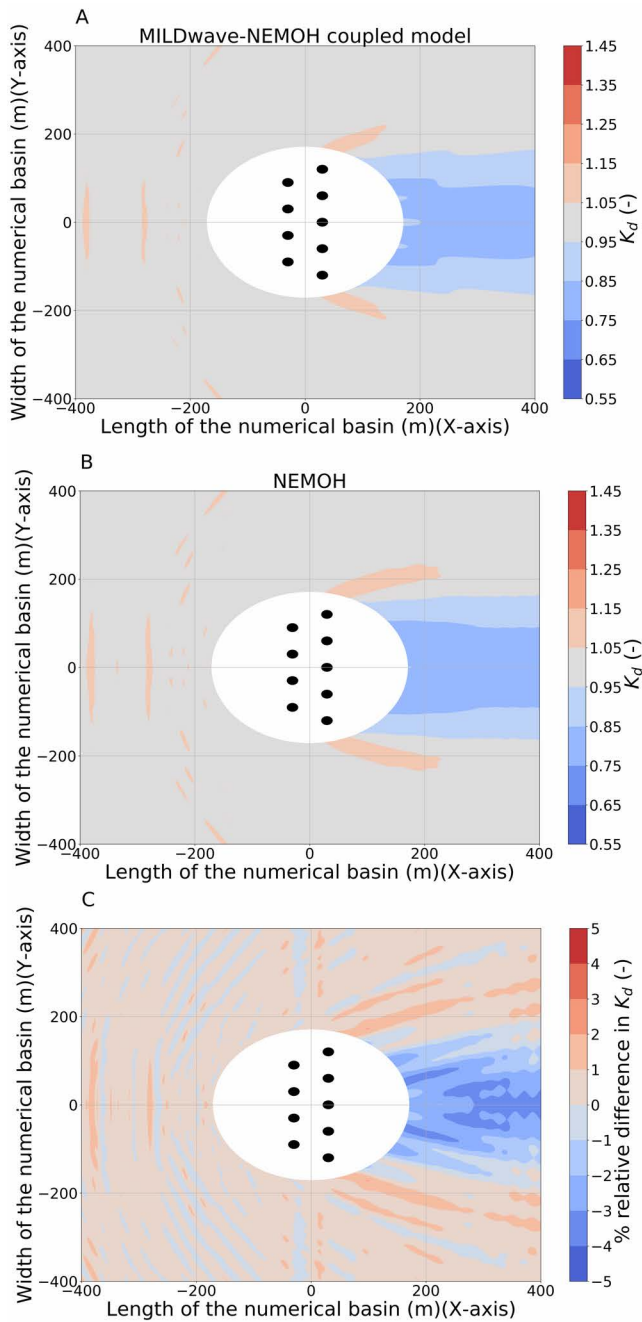


Figure B.14: Numerical validation results for Test Case 14: (A) K_d results for the MILDwave-NEMOH coupled model, (B) K_d results for NEMOH and (C) relative difference in K_d between the two models.

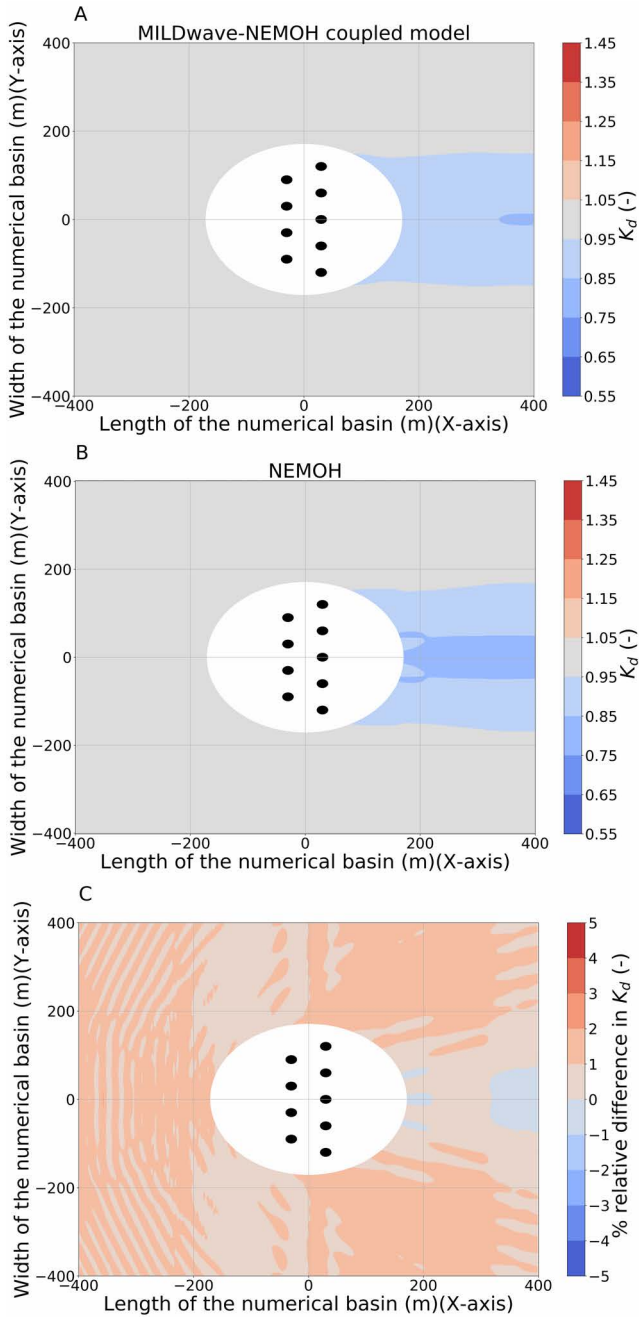


Figure B.15: Numerical validation results for Test Case 15: (A) K_d results for the MILDwave-NEMOH coupled model, (B) K_d results for NEMOH and (C) relative difference in K_d between the two models.

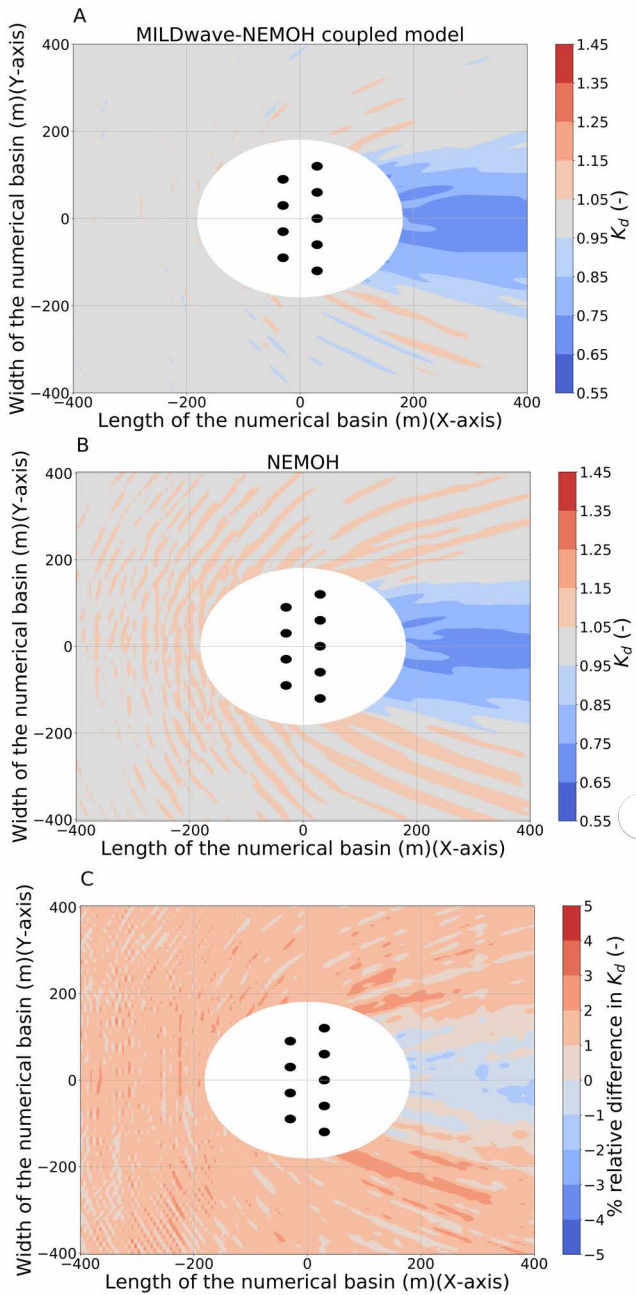


Figure B.16: Numerical validation results for Test Case 16: (A) K_d results for the MILDwave-NEMOH coupled model, (B) K_d results for NEMOH and (C) relative difference in K_d between the two models.

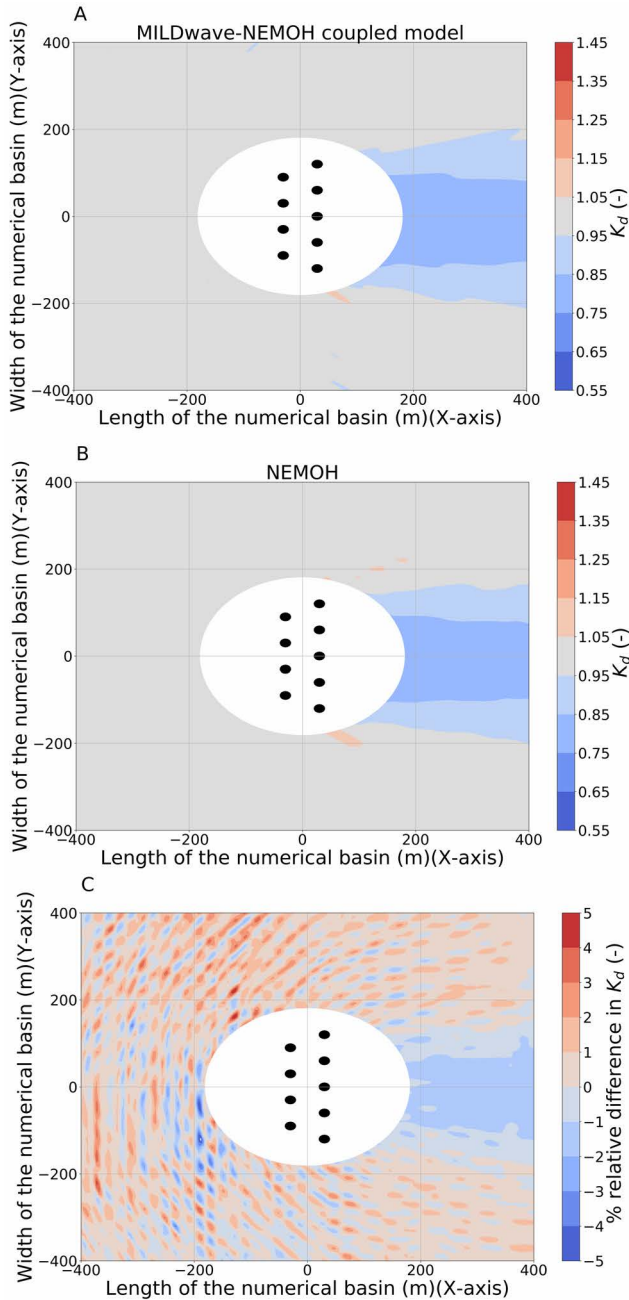


Figure B.17: Numerical validation results for Test Case 17: (A) K_d results for the MILDwave-NEMOH coupled model, (B) K_d results for NEMOH and (C) relative difference in K_d between the two models.

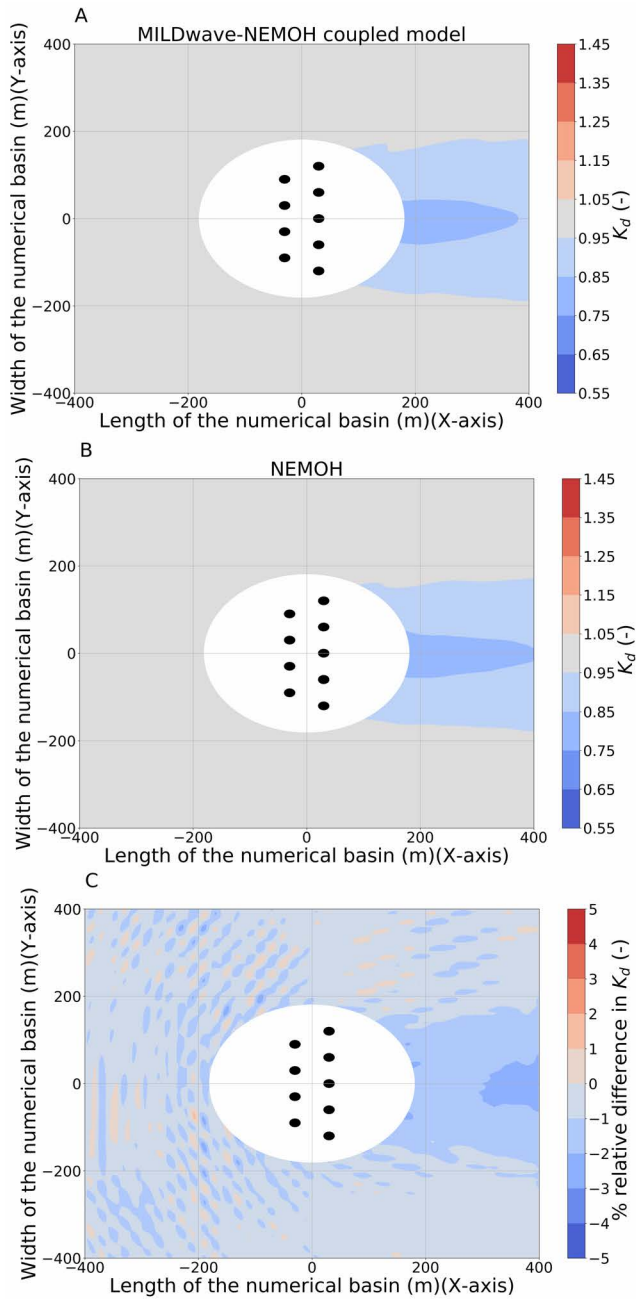


Figure B.18: Numerical validation results for Test Case 18: (A) K_d results for the MILDwave-NEMOH coupled model, (B) K_d results for NEMOH and (C) relative difference in K_d between the two models.

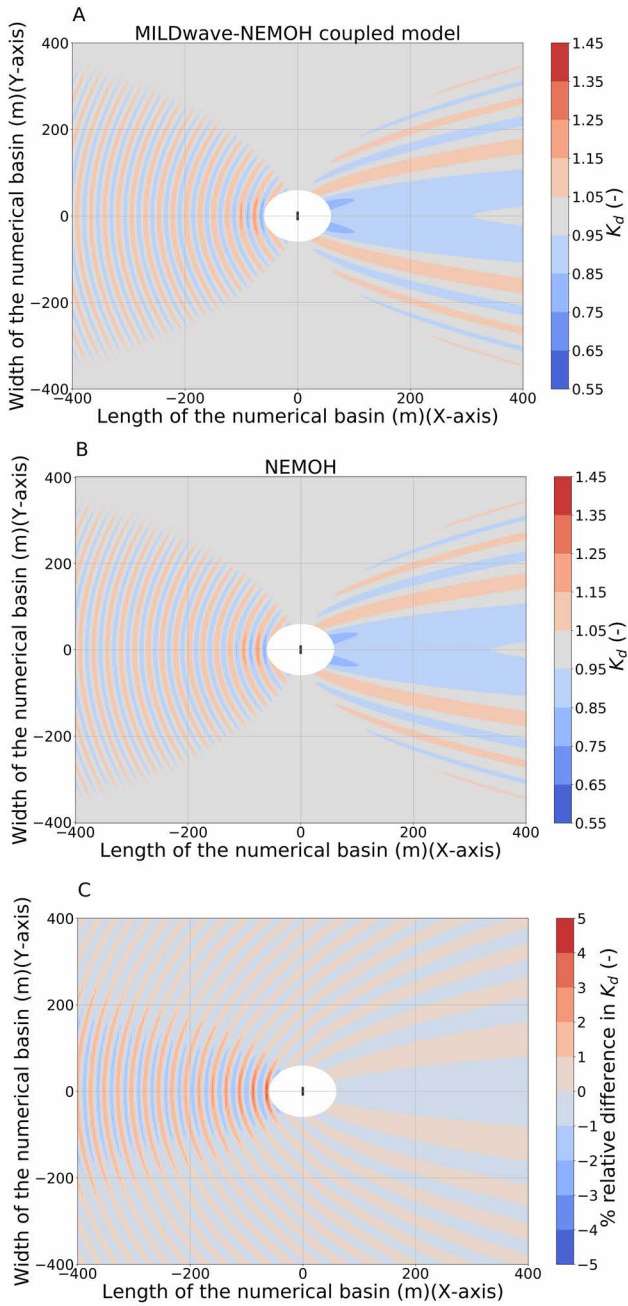


Figure B.19: Numerical validation results for Test Case 19: (A) K_d results for the MILDwave-NEMOH coupled model, (B) K_d results for NEMOH and (C) relative difference in K_d between the two models.

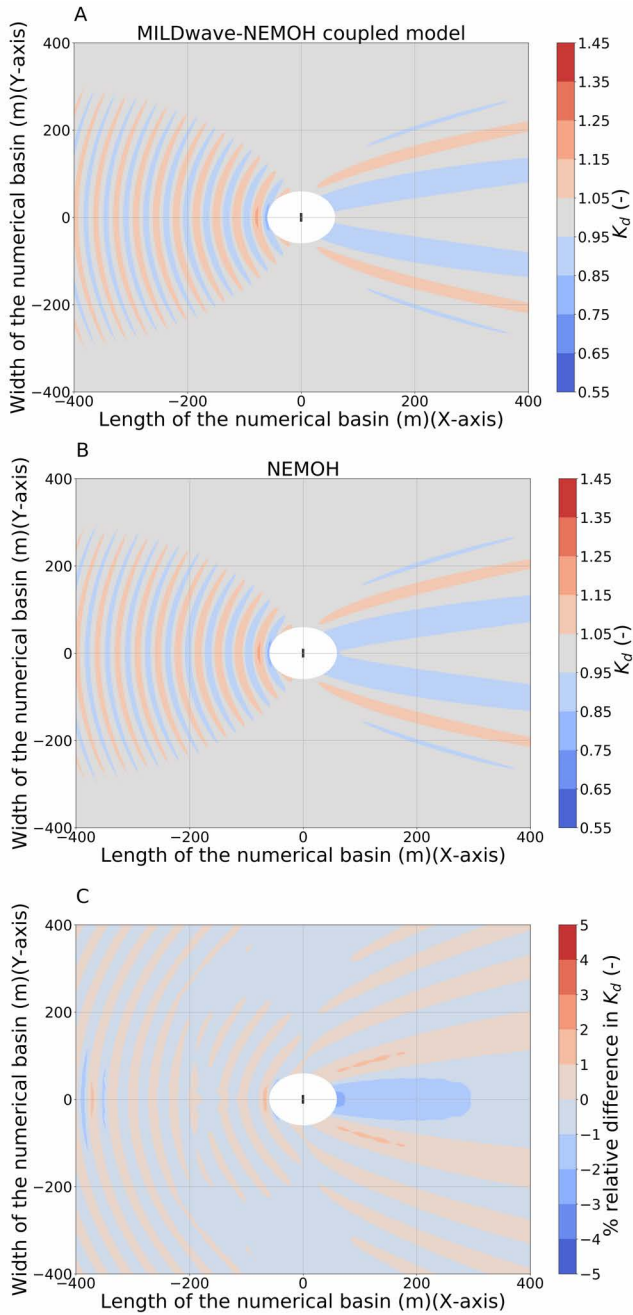


Figure B.20: Numerical validation results for Test Case 20: (A) K_d results for the MILDwave-NEMOH coupled model, (B) K_d results for NEMOH and (C) relative difference in K_d between the two models.

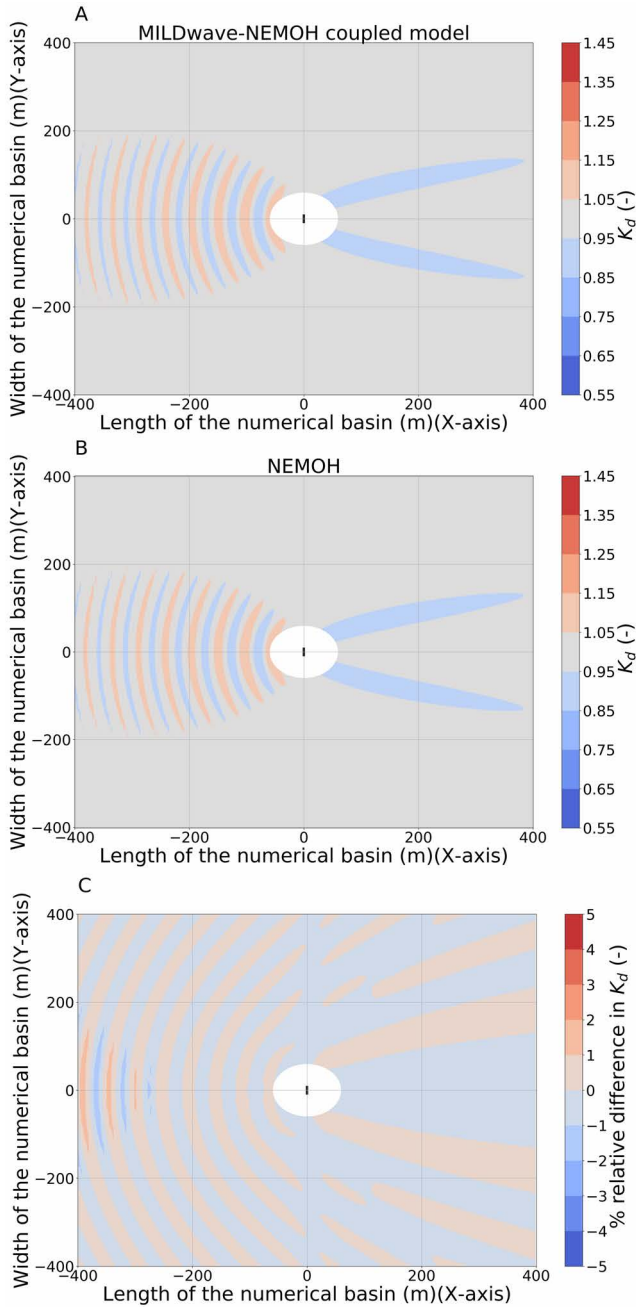


Figure B.21: Numerical validation results for Test Case 21: (A) K_d results for the MILDwave-NEMOH coupled model, (B) K_d results for NEMOH and (C) relative difference in K_d between the two models.

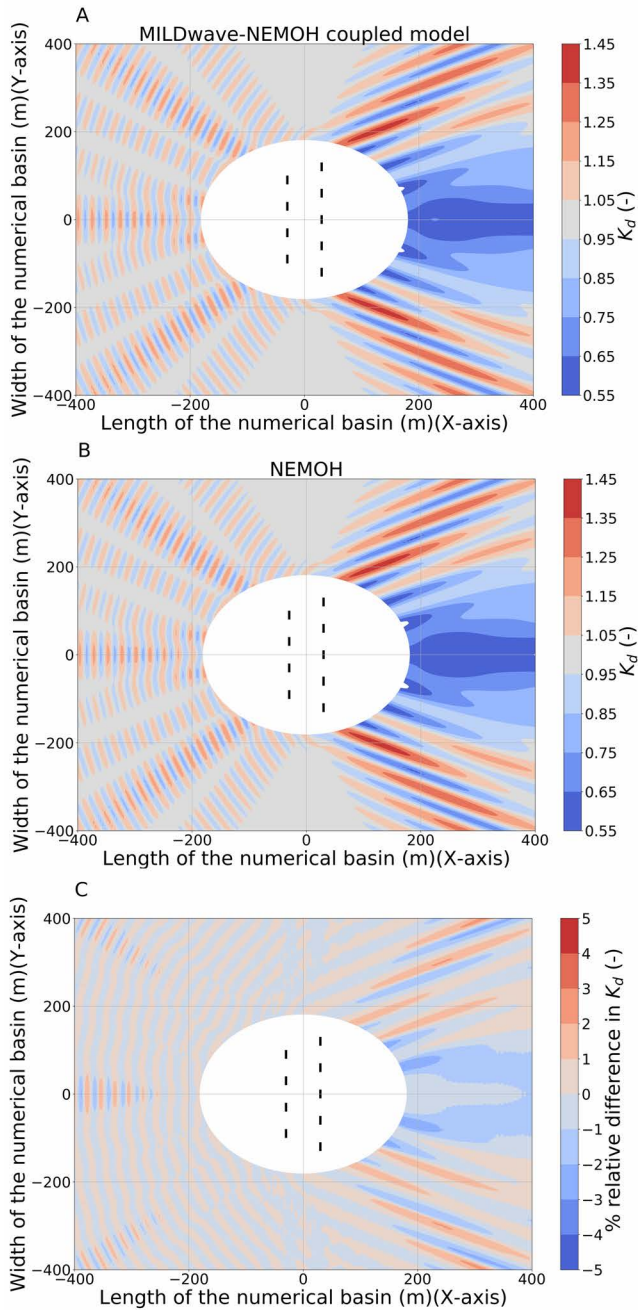


Figure B.22: Numerical validation results for Test Case 22: (A) K_d results for the MILDwave-NEMOH coupled model, (B) K_d results for NEMOH and (C) relative difference in K_d between the two models.

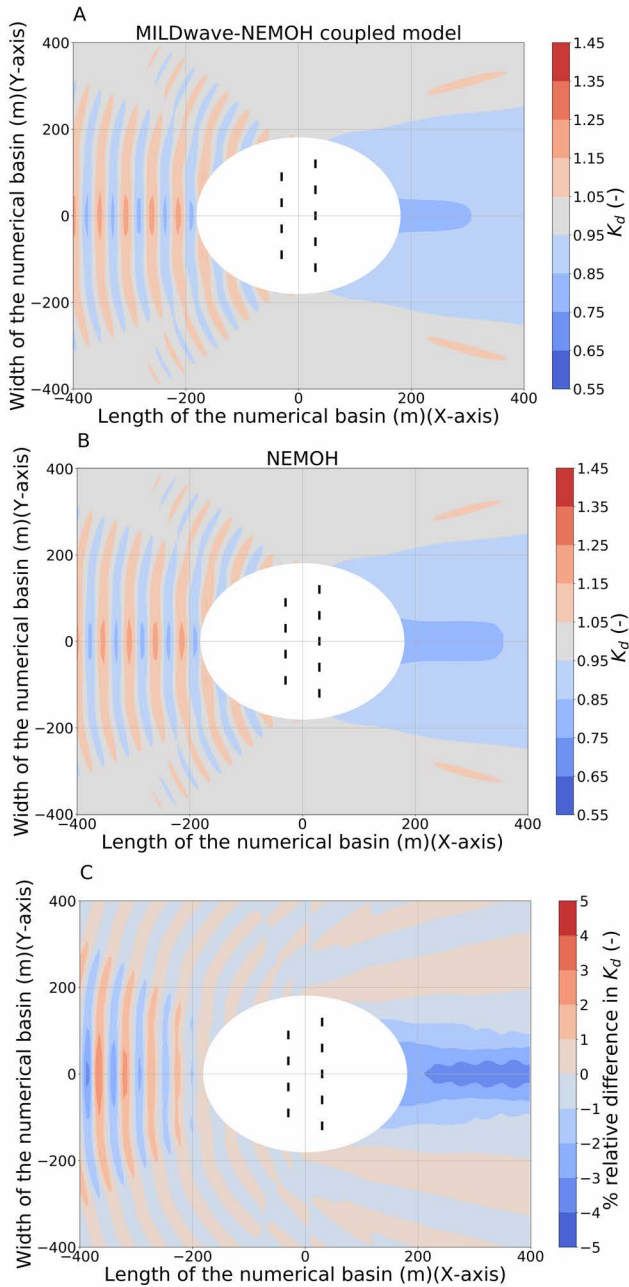


Figure B.23: Numerical validation results for Test Case 23: (A) K_d results for the MILDwave-NEMOH coupled model, (B) K_d results for NEMOH and (C) relative difference in K_d between the two models.

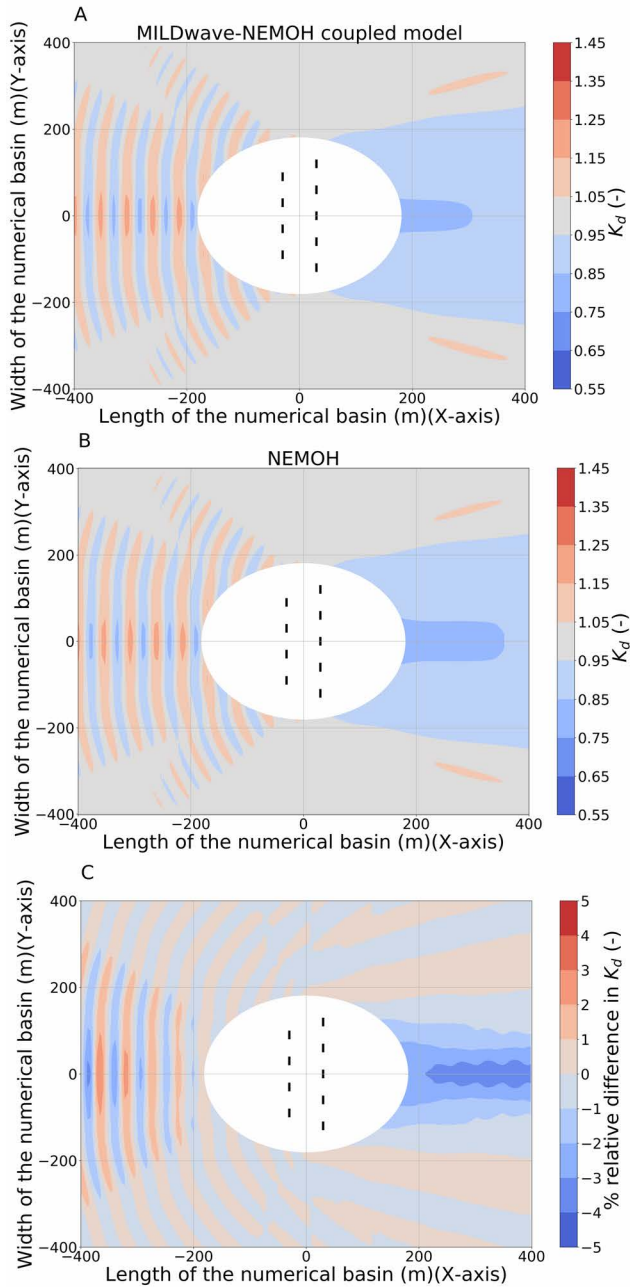


Figure B.24: Numerical validation results for Test Case 24: (A) K_d results for the MILDwave-NEMOH coupled model, (B) K_d results for NEMOH and (C) relative difference in K_d between the two models.

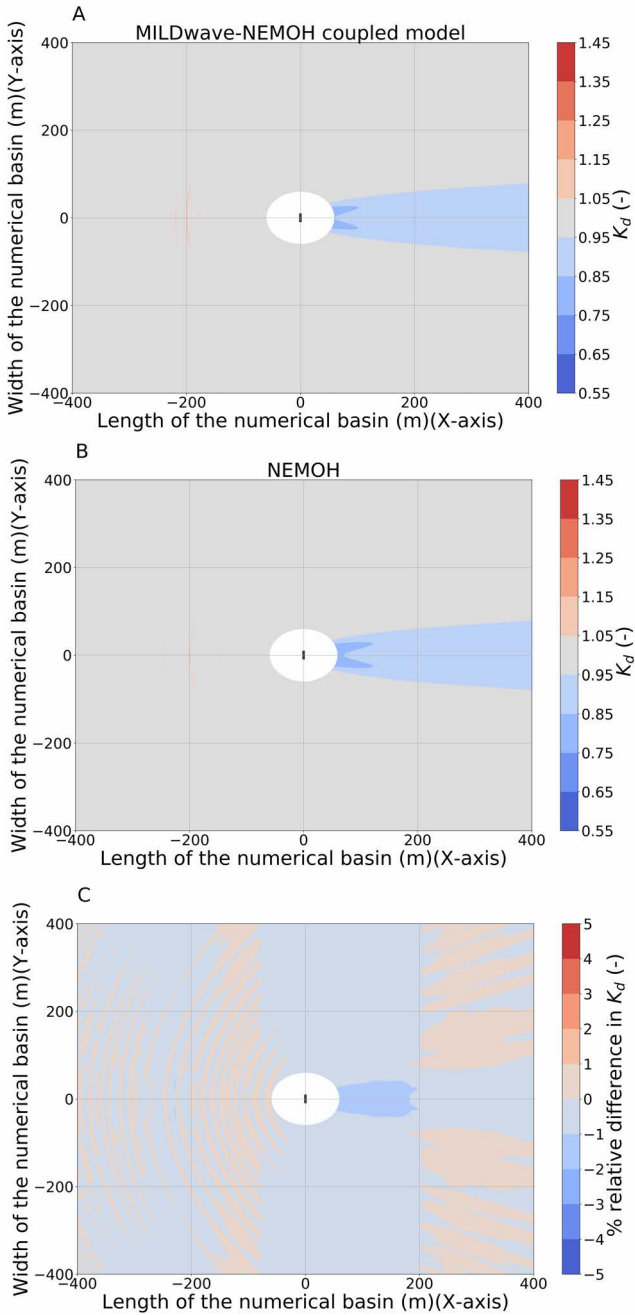


Figure B.25: Numerical validation results for Test Case 25: (A) K_d results for the MILDwave-NEMOH coupled model, (B) K_d results for NEMOH and (C) relative difference in K_d between the two models.

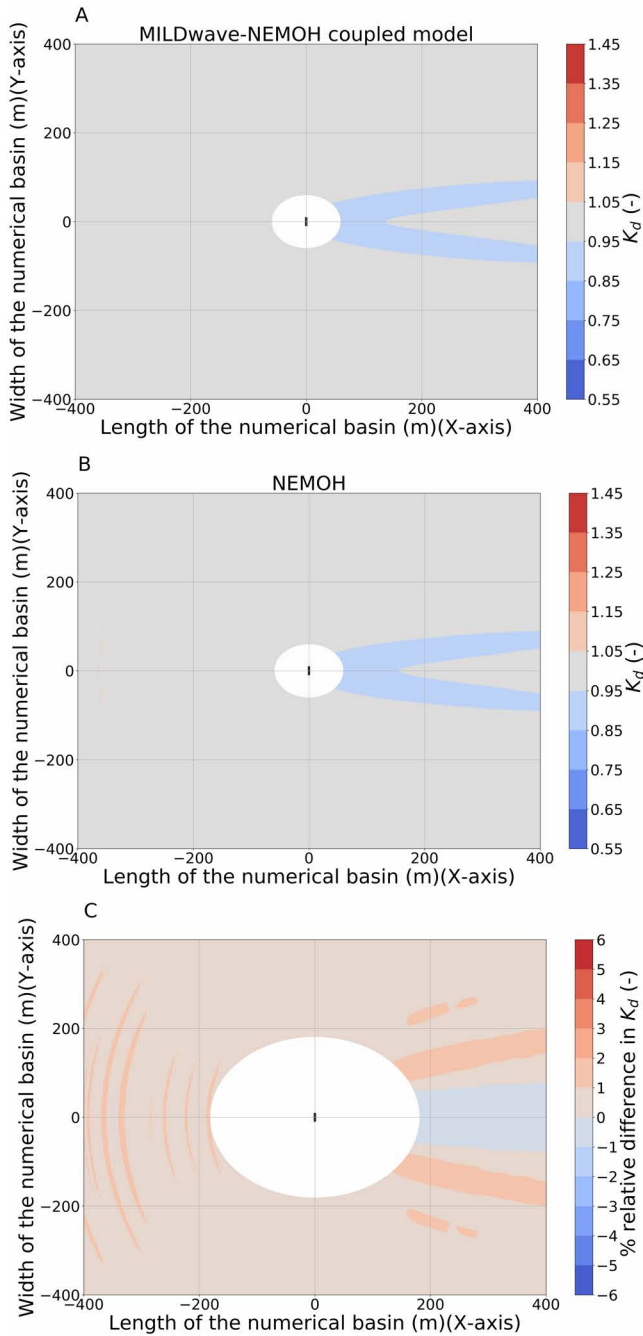


Figure B.26: Numerical validation results for Test Case 26: (A) K_d results for the MILDwave-NEMOH coupled model, (B) K_d results for NEMOH and (C) relative difference in K_d between the two models.

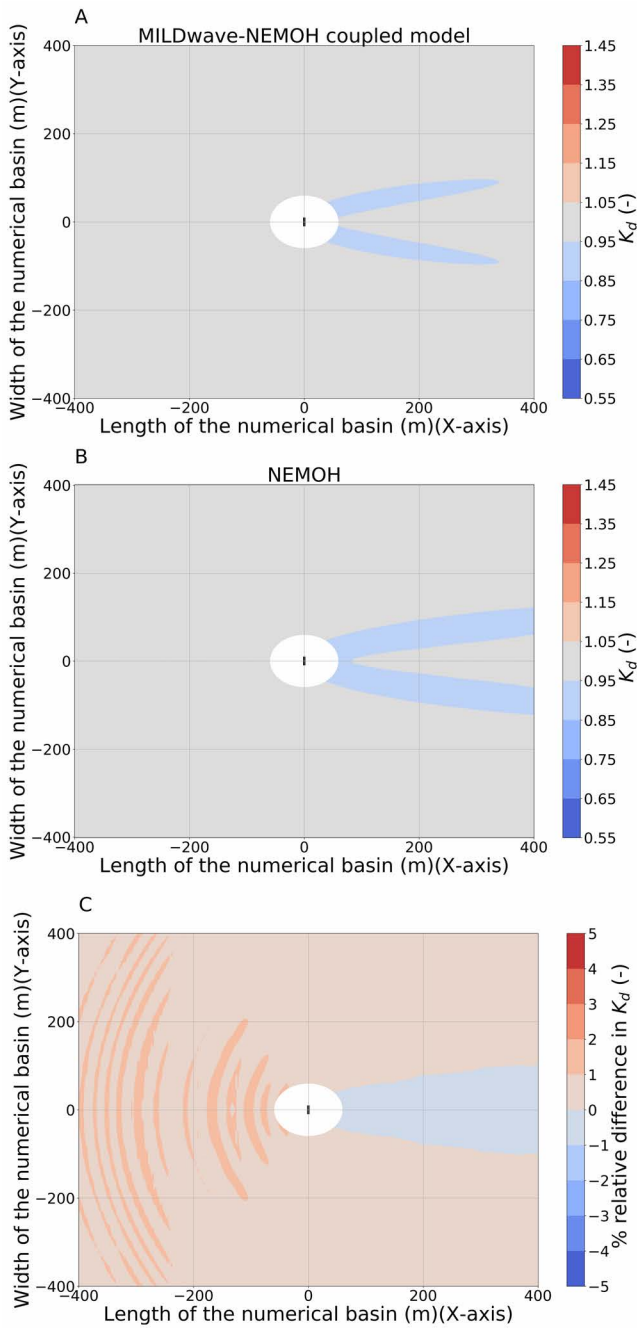


Figure B.27: Numerical validation results for Test Case 27: (A) K_d results for the MILDwave-NEMOH coupled model, (B) K_d results for NEMOH and (C) relative difference in K_d between the two models.

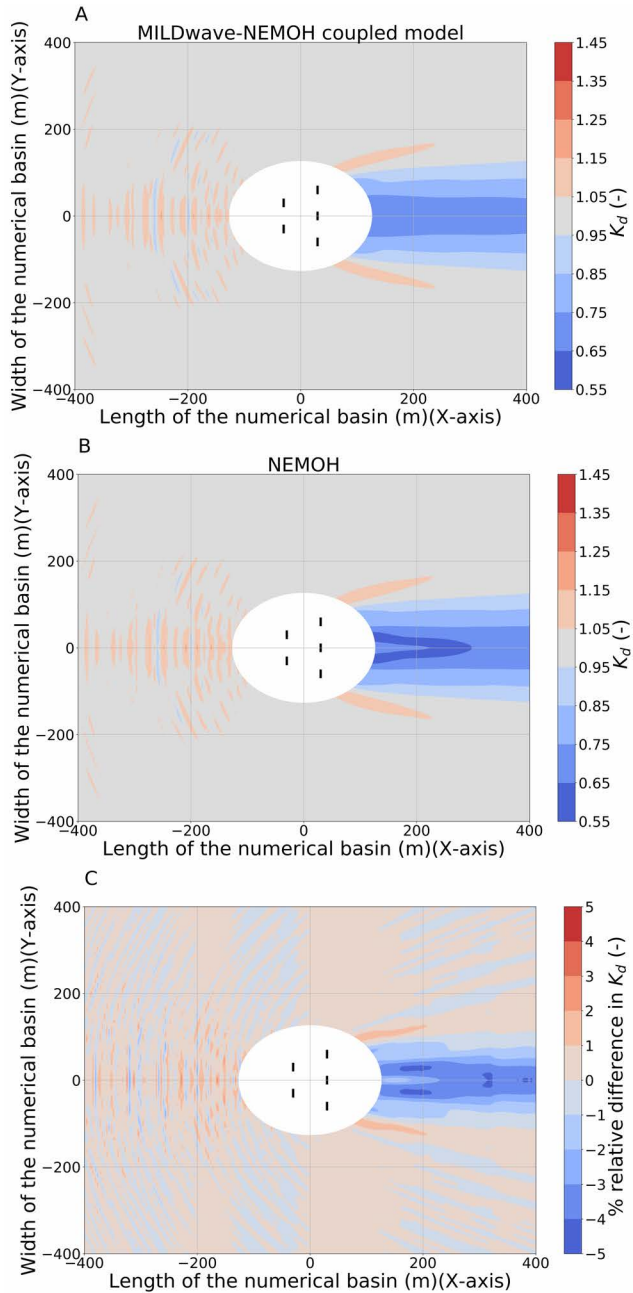


Figure B.28: Numerical validation results for Test Case 28: (A) K_d results for the MILDwave-NEMOH coupled model, (B) K_d results for NEMOH and (C) relative difference in K_d between the two models.

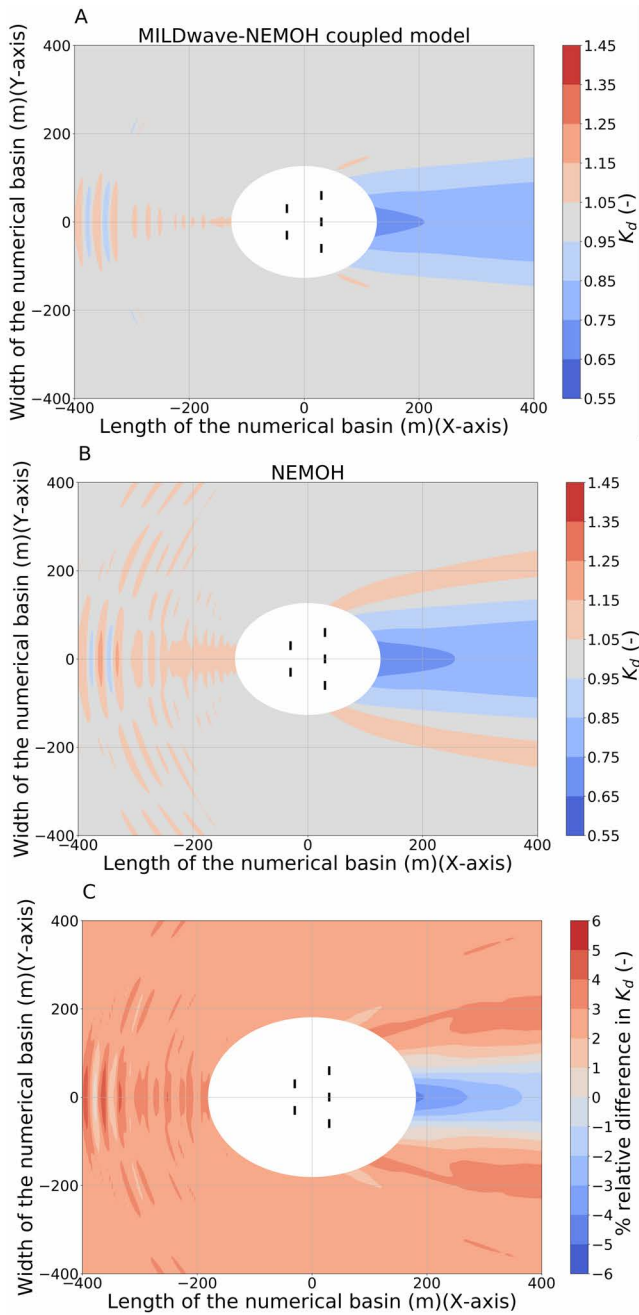


Figure B.29: Numerical validation results for Test Case 29: (A) K_d results for the MILDwave-NEMOH coupled model, (B) K_d results for NEMOH and (C) relative difference in K_d between the two models.

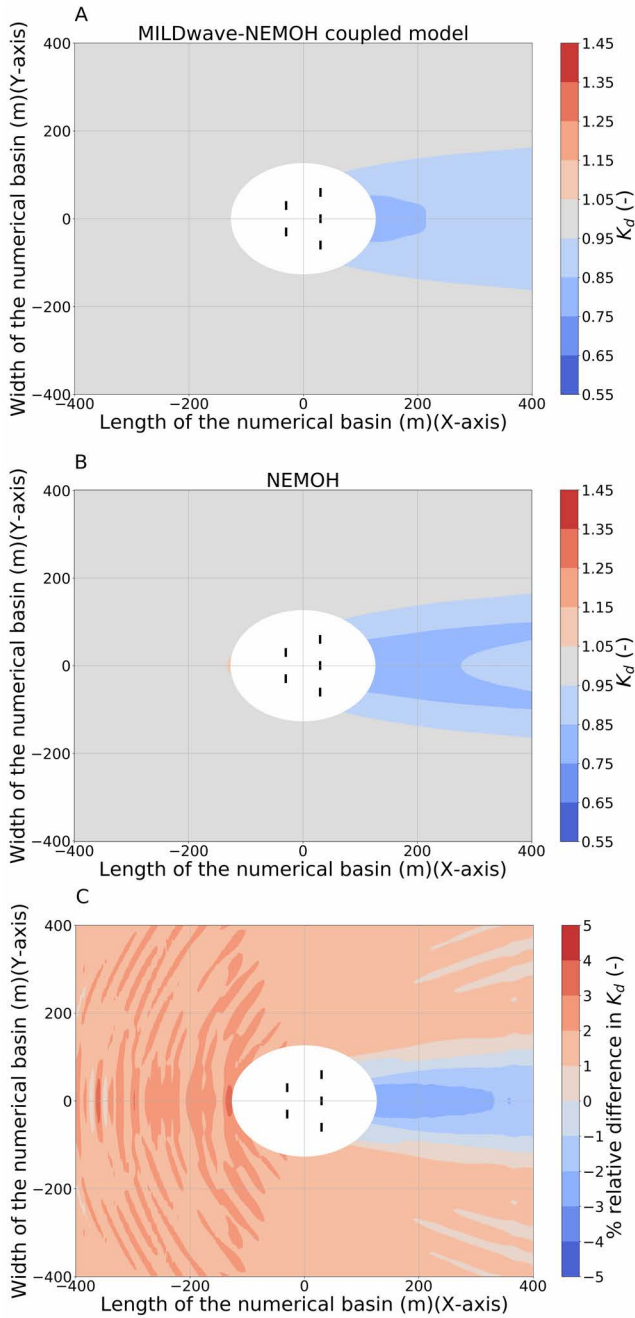


Figure B.30: Numerical validation results for Test Case 30: (A) K_d results for the MILDwave-NEMOH coupled model, (B) K_d results for NEMOH and (C) relative difference in K_d between the two models.

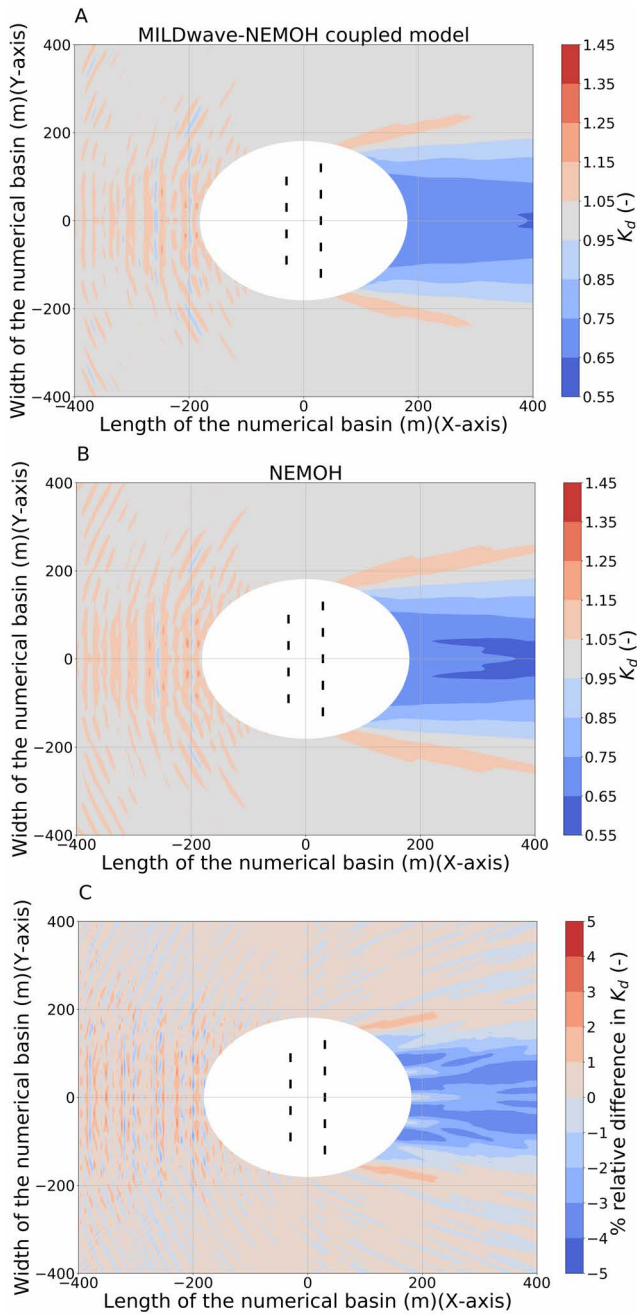


Figure B.31: Numerical validation results for Test Case 31: (A) K_d results for the MILDwave-NEMOH coupled model, (B) K_d results for NEMOH and (C) relative difference in K_d between the two models.

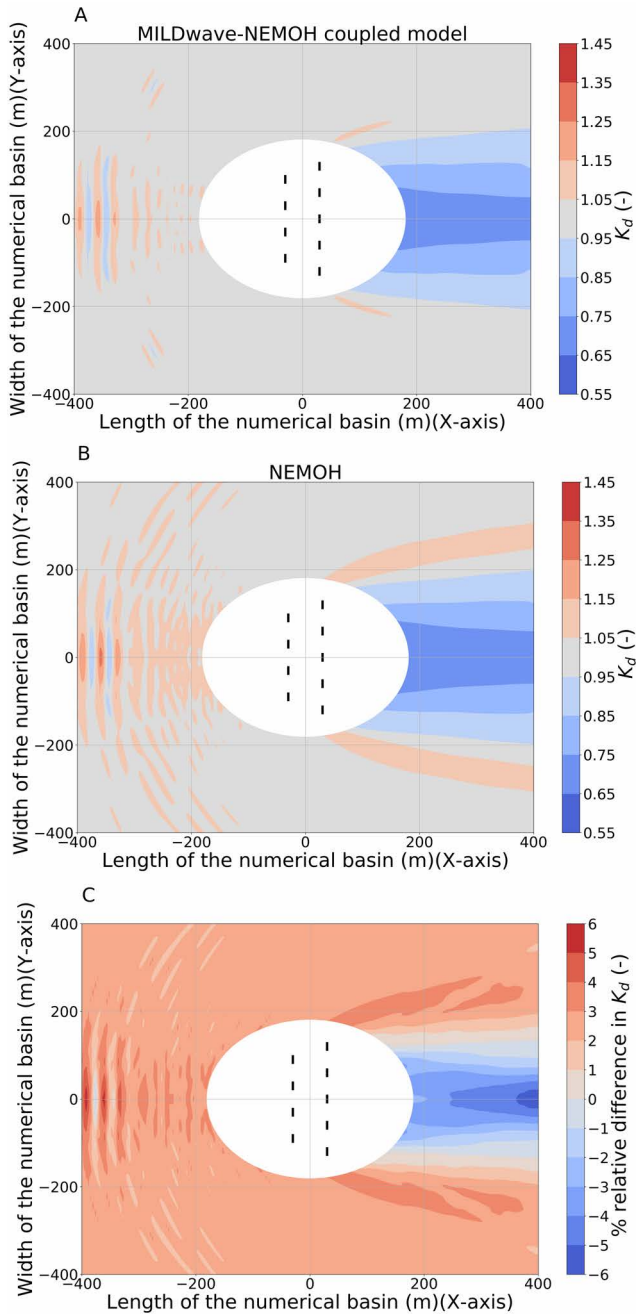


Figure B.32: Numerical validation results for Test Case 32: (A) K_d results for the MILDwave-NEMOH coupled model, (B) K_d results for NEMOH and (C) relative difference in K_d between the two models.

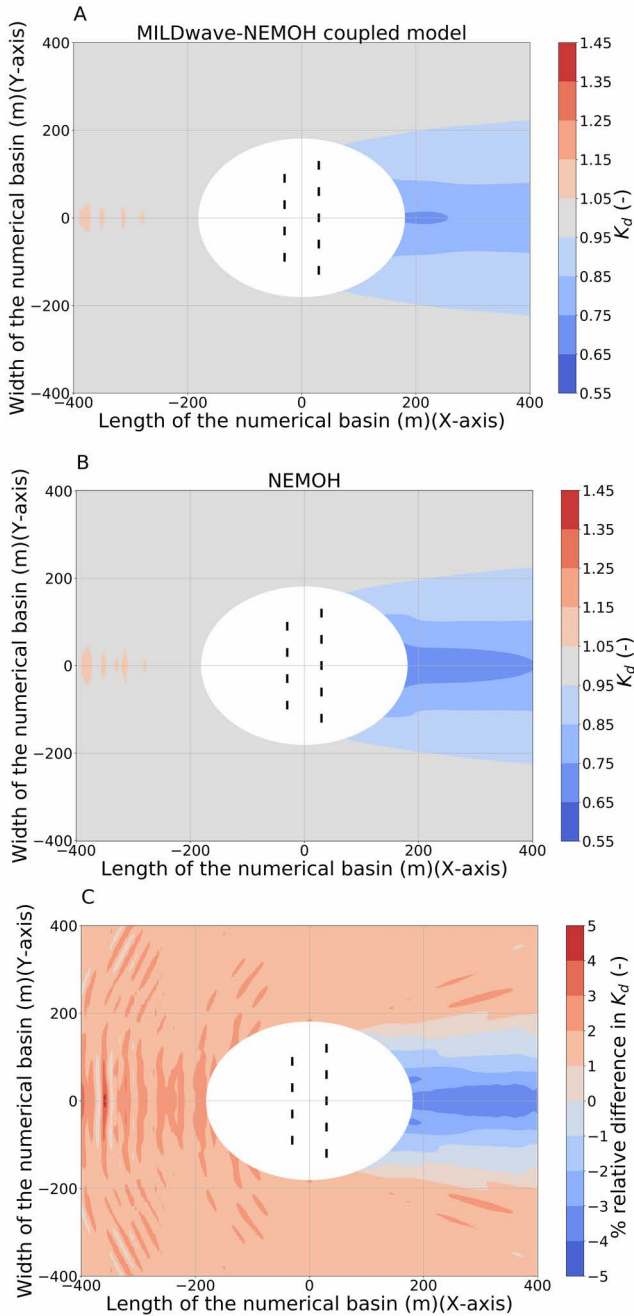


Figure B.33: Numerical validation results for Test Case 33: (A) K_d results for the MILDwave-NEMOH coupled model, (B) K_d results for NEMOH and (C) relative difference in K_d between the two models.

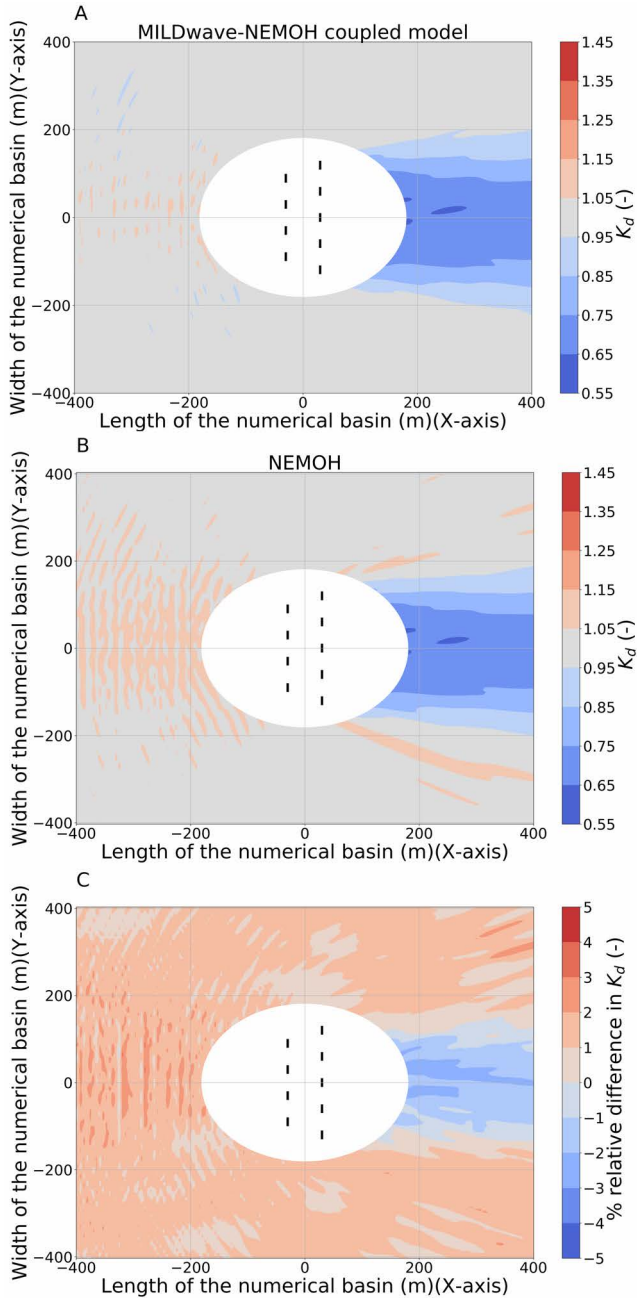


Figure B.34: Numerical validation results for Test Case 34: (A) K_d results for the MILDwave-NEMOH coupled model, (B) K_d results for NEMOH and (C) relative difference in K_d between the two models.

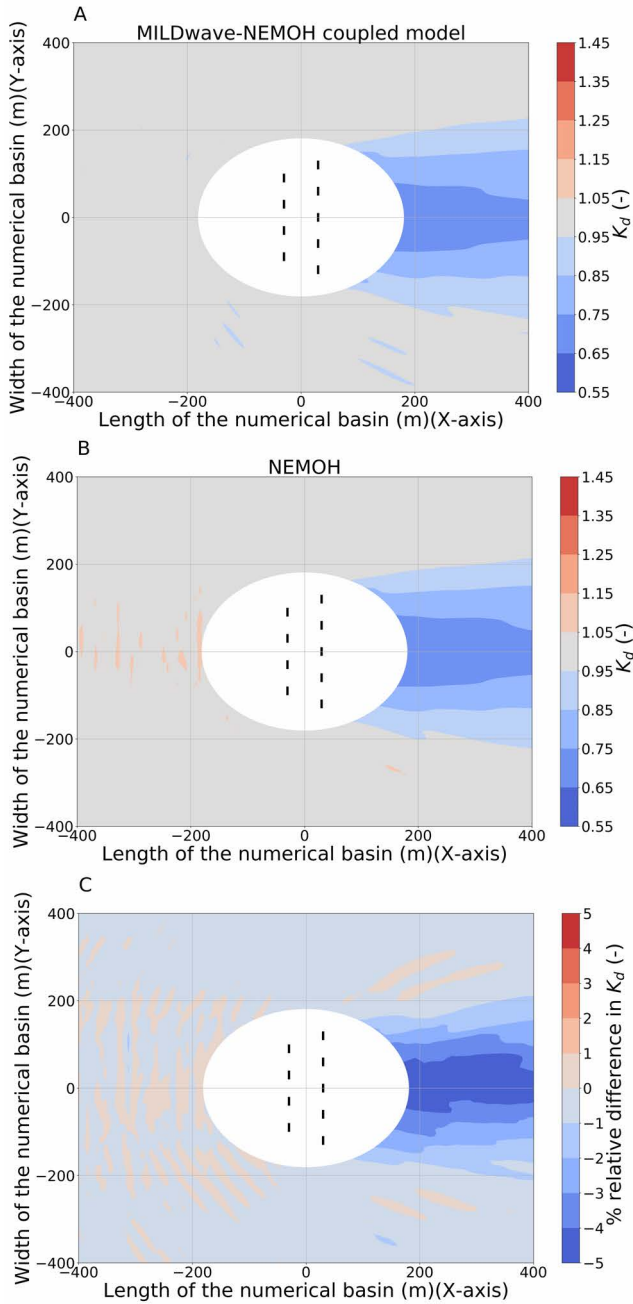


Figure B.35: Numerical validation results for Test Case 35: (A) K_d results for the MILDwave-NEMOH coupled model, (B) K_d results for NEMOH and (C) relative difference in K_d between the two models.

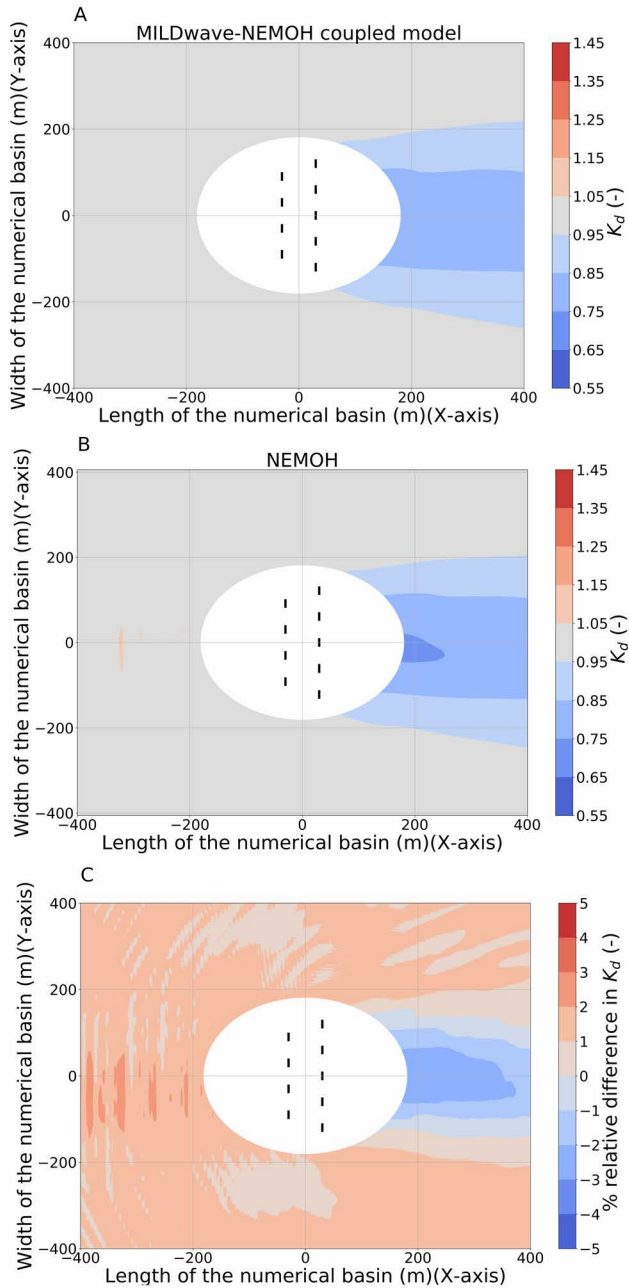


Figure B.36: Numerical validation results for Test Case 36: (A) K_d results for the MILDwave-NEMOH coupled model, (B) K_d results for NEMOH and (C) relative difference in K_d between the two models.

Appendix C

Experimental validation results

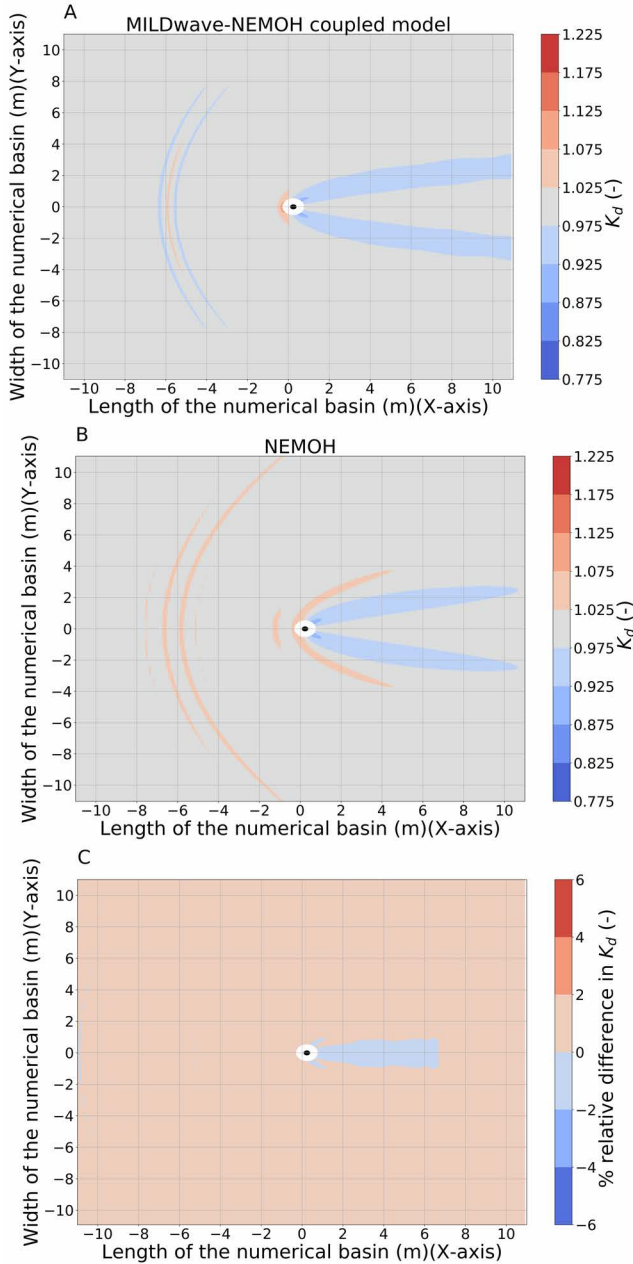


Figure C.1: Experimental validation results for Test Case 38: (A) K_d disturbance coefficient results for the MILDwave-NEMOH coupled model, (B) K_d disturbance coefficient results for NEMOH and (C) relative difference in K_d between the two models.

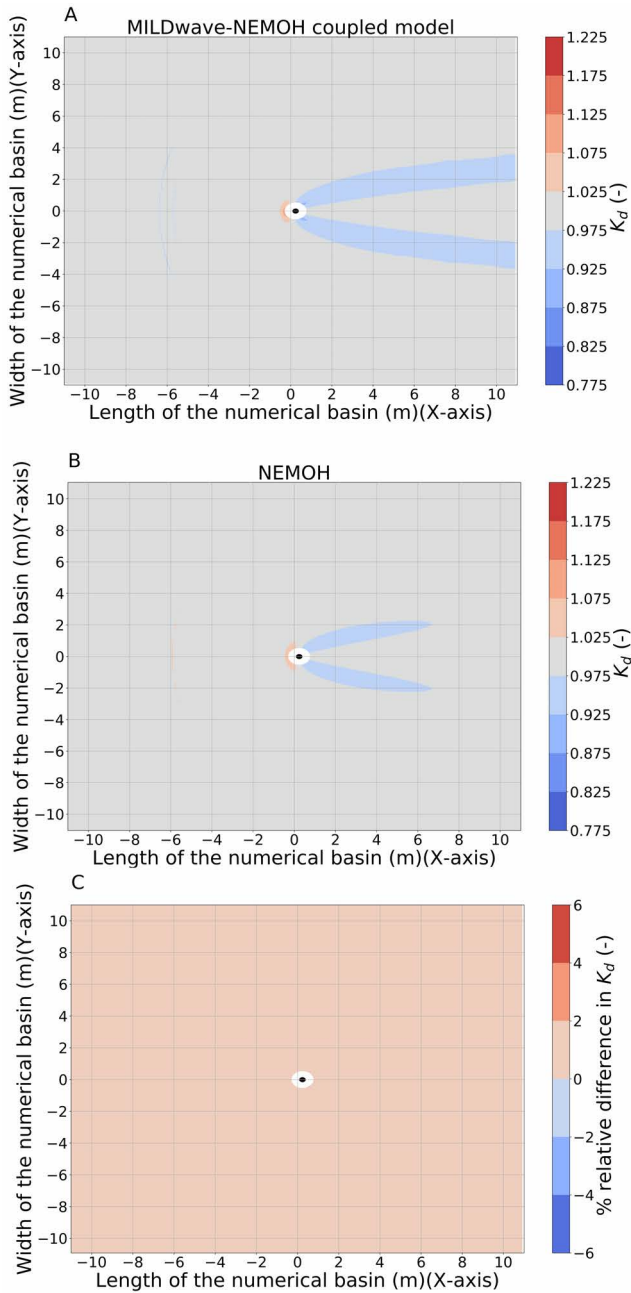


Figure C.2: Experimental validation results for Test Case 39: (A) K_d disturbance coefficient results for the MILDwave-NEMOH coupled model, (B) K_d disturbance coefficient results for NEMOH and (C) relative difference in K_d between the two models.

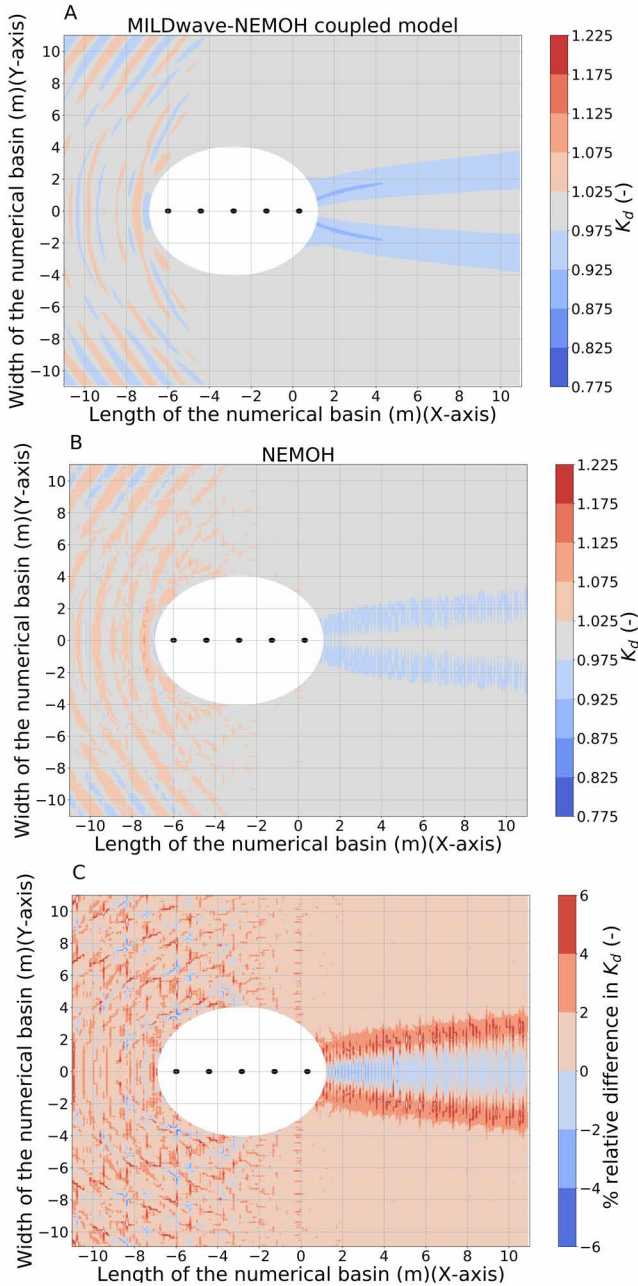


Figure C.3: Experimental validation results for Test Case 40: (A) K_d disturbance coefficient results for the MILDwave-NEMOH coupled model, (B) K_d disturbance coefficient results for NEMOH and (C) relative difference in K_d between the two models.

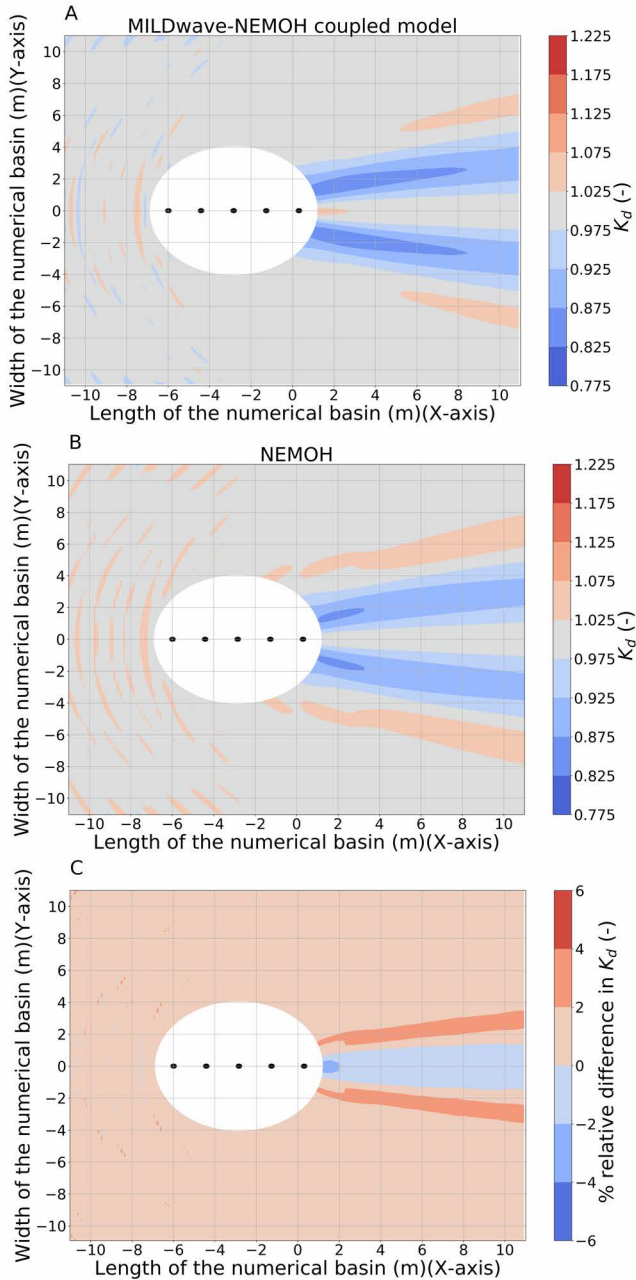


Figure C.4: Experimental validation results for Test Case 41: (A) K_d disturbance coefficient results for the MILDwave-NEMOH coupled model, (B) K_d disturbance coefficient results for NEMOH and (C) relative difference in K_d between the two models.

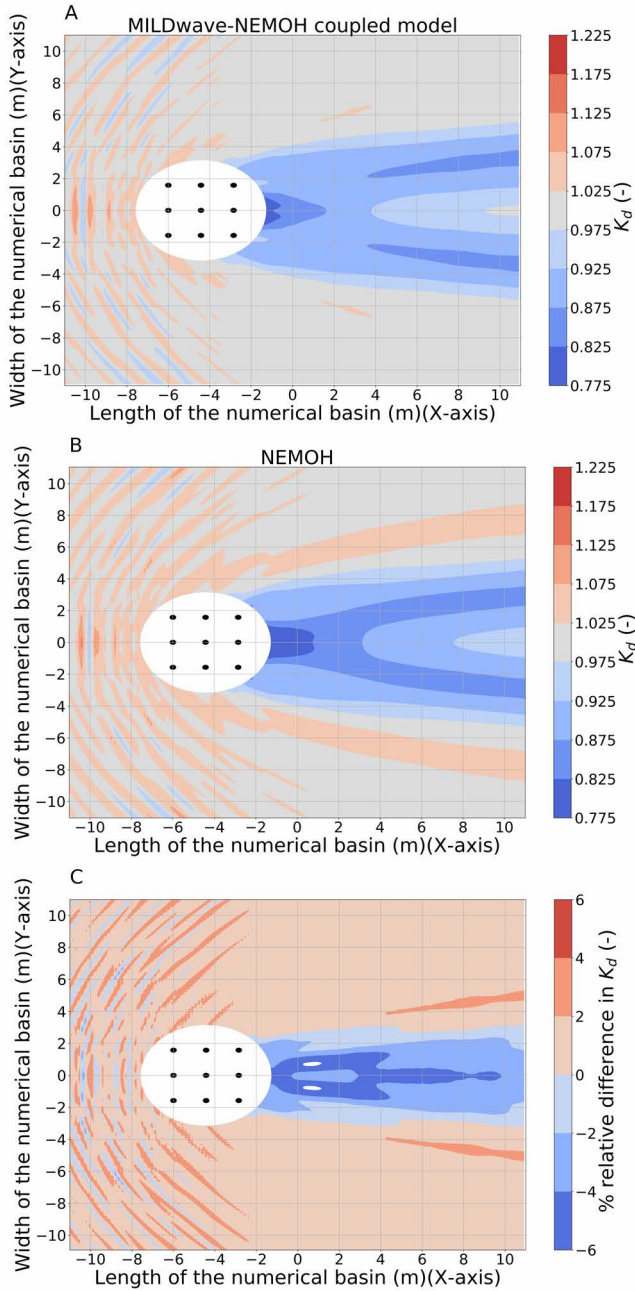


Figure C.5: Experimental validation results for Test Case 42: (A) K_d disturbance coefficient results for the MILDwave-NEMOH coupled model, (B) K_d disturbance coefficient results for NEMOH and (C) relative difference in K_d between the two models.

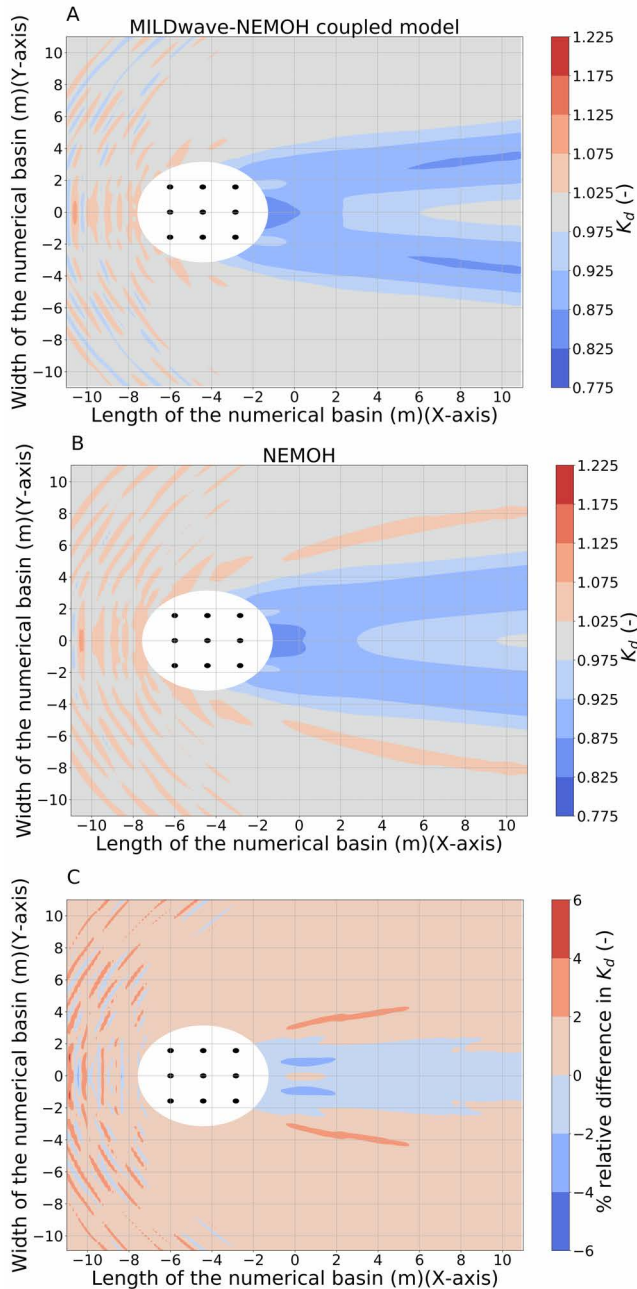


Figure C.6: Experimental validation results for Test Case 40: (A) K_d disturbance coefficient results for the MILDwave-NEMOH coupled model, (B) K_d disturbance coefficient results for NEMOH and (C) relative difference in K_d between the two models.

References

- Abanades, J., Greaves, D., and Iglesias, G. (2014). Wave farm impact on the beach profile: A case study. *Coastal Engineering*, 86:36–44.
- Agamloh, E. B., Wallace, A. K., and von Jouanne, A. (2008). Application of fluid-structure interaction simulation of an ocean wave energy extraction device. *Renewable Energy*, 33(4):748 – 757.
- Aggarwal, A. (2015). *Numerical Modelling of Irregular waves and Irregular Wave Forces with REEF3D*. PhD thesis, Norwegian University of Science and Technology.
- Alves, M. (2016a). Frequency-Domain Models. In *Numerical Modelling of Wave Energy Converters*, pages 11–30. Elsevier.
- Alves, M. (2016b). Wave Energy Converter modelling techniques based on linear hydrodynamic theory. In Folley, M., editor, *Numerical Modelling of Wave Energy Converters*, chapter 1, pages 11–65. Elsevier.
- Arean, N., Carballo, R., and Iglesias, G. (2017). An integrated approach for the installation of a wave farm. *Energy*, 138:910 – 919.
- Babarit, A. (2013). On the park effect in arrays of oscillating wave energy converters. *Renewable Energy*, 58:68–78.
- Babarit, A. and Delhommeau, G. (2015). Theoretical and numerical aspects of the open source BEM solver NEMOH. In *Proc. of the 11th European Wave and Tidal Energy Conference 6-11th Sept 2015, Nantes, France*.
- Babarit, A., Matt, F., François, C., Peyrard, C., and Benoit, M. (2013). On the modelling of WECs in wave models using far field coefficients. In *10th European Wave and Tidal Energy Conference (EWTEC2013)*, Proceedings of the 10th European Wave and Tidal Energy Conference, Aalborg, Denmark.
- Balitsky, P., Verao Fernandez, G., Stratigaki, V., and Troch, P. (2017). Coupling methodology for modelling the near-field and far-field effects of a Wave Energy Converter. In *Proceedings of the ASME 36th International Conference on Ocean, Offshore and Arctic Engineering (OMAE2017)*.

- Balitsky, P., Verao Fernandez, G., Stratigaki, V., and Troch, P. (2018). Assessment of the power output of a two-array clustered wec farm using a bem solver coupling and a wave-propagation model. *Energies*, 11(11):2907:1–2907:23.
- Beels, C. (2009). *Optimization of the lay-out of a farm of wave energy converters in the North Sea: analysis of wave power resources, wake effects, production and cost*. PhD thesis, Ghent University, Belgium.
- Beels, C., Troch, P., De Backer, G., Vantorre, M., and De Rouck, J. (2010a). Numerical implementation and sensitivity analysis of a wave energy converter in a time-dependent mild-slope equation model. *Coastal Engineering*, 57(5):471–492.
- Beels, C., Troch, P., De Backer, G., Vantorre, M., and Rouck, J. D. (2010b). Numerical implementation and sensitivity analysis of a wave energy converter in a time-dependent mild-slope equation model. *Coastal Engineering*, 57(5):471–492.
- Beels, C., Troch, P., Kofoed, J. P., Frigaard, P., Kringelum, J. V., Kromann, P. C., Donovan, M. H., De Rouck, J., and De Backer, G. (2011). A methodology for production and cost assessment of a farm of wave energy converters. *Renewable Energy*, 36:3402–3416.
- Bento, A. R., Rusu, E., Martinho, P., and Guedes Soares, C. (2014). Assessment of the changes induced by a wave energy farm in the nearshore wave conditions. *Comput. Geosci.*, 71(C):50–61.
- Borgarino, B., Babarit, A., and Ferrant, P. (2012). Impact of wave interaction effects on energy absorption in large arrays of Wave Energy Converters. *Ocean Engineering*, 41:79–88.
- Bozo, N. T., Murphy, J., Troch, P., Lewis, T., and Thomas, G. (2017). Modelling of a flap-type wave energy converter farm in a mild-slope equation model for a wake effect assessment. *IET Renewable Power Generation*, 11(9):1142 – 1152.
- Brorsen, M. and Helm-Petersen, J. (1998). On the Reflection of Short-Crested Waves in Numerical Models. In *Proc. of the 26th Int'l Conference on Coastal Engineering, Copenhagen*, pages 394–407.
- Budal, K. (1977). Theory for absorption of wave power by a system of interacting bodies. *Journal of Ship Research*.
- Carballo, R. and Iglesias, G. (2013). Wave farm impact based on realistic wave-wec interaction. *Energy*, 51:216 – 229.
- Carballo, R., Sánchez, M., Ramos, V., Fragueta, J., and Iglesias, G. (2015). The intra-annual variability in the performance of wave energy converters: A comparative study in N Galicia (Spain). *Energy*, 82:138 – 146.

- Cargo, C. J., Plummer, A. R., Hillis, A. J., and Schlotter, M. (2012). Determination of optimal parameters for a hydraulic power take-off unit of a wave energy converter in regular waves. *Proceedings of the Institution of Mechanical Engineers, Part A: Journal of Power and Energy*, 226:98–111.
- Chang, G., Ruehl, K., Jones, C., Roberts, J., and Chartrand, C. (2016). Numerical modeling of the effects of wave energy converter characteristics on nearshore wave conditions. *Renewable Energy*, 89:636 – 648.
- Charrayre, F., Peyrard, C., Benoit, M., and Babarit, A. (2014). A Coupled Methodology for Wave-Body Interactions at the Scale of a Farm of Wave Energy Converters Including Irregular Bathymetry. In *Proc. of the ASME 2014 33rd Int'l Conference on Ocean, Offshore and Arctic Engineering June 8-13, 2014, San Francisco, CA, USA*.
- Child, B. M. F. (2011). *On the configuration of arrays of floating wave energy converters*. PhD thesis, The University of Edinburgh.
- Child, B. M. F. and Venugopal, V. (2010). Optimal Configurations of wave energy devices. *Ocean Engineering*, 37:1402–1417.
- Crespo, A., Altomare, C., Domínguez, J., González-Cao, J., and Gómez-Gesteira, M. (2017). Towards simulating floating offshore oscillating water column converters with smoothed particle hydrodynamics. *Coastal Engineering*, 126:11 – 26.
- Crespo, A. J. C., Domínguez, J. M., Rogers, B. D., Gómez-Gesteira, M., Longshaw, S., Canelas, R., Vacondio, R., Barreiro, A., and García-Feal, O. (2015). DualSPHysics: Open-source parallel CFD solver based on Smoothed Particle Hydrodynamics (SPH). *Computer Physics Communications*, 187:204–216.
- Delhommeau, G. (1987). *Les problemes de diffraction-radiation et de resistance de vagues : etude theorique et resolution numerique par la methode des singularites*. PhD thesis.
- Devolder, B., Rauwoens, P., and Troch, P. (2017). Towards the numerical simulation of 5 floating point absorber wave energy converters installed in a line array using openfoam. In *Proceedings of the 12th wave and tidal energy conference*, pages 739–749.
- Devolder, B., Stratigaki, V., Troch, P., and Rauwoens, P. (2018). CFD simulations of floating point absorber wave energy converter arrays subjected to regular waves. *Energies*, 11(3):1–23.
- European Marine Energy Centre (2019). Wave Developers Database. <http://www.emec.org.uk/marine-energy/wave-developers/>. Available online: <http://www.emec.org.uk/marine-energy/wave-developers/> (accessed on Apr 10, 2019).

- European Marine Observation and Data Network (2019). EMODnet Bathymetry portal. <http://www.emodnet-bathymetry.eu>. Available online: <http://www.emodnet-bathymetry.eu> (accessed on Apr 10, 2019).
- Falnes, J. (1980). Radiation impedance matrix and optimum power absorption for interacting oscillators in surface waves. *Applied Ocean Research*, 2(2):75–80.
- Folley, M. (2016a). *Numerical Modelling of Wave Energy Converters: State-of-the-Art Techniques for Single Devices and Arrays*. Academic Press.
- Folley, M. (2016b). Phase-Averaging Wave Propagation Array Models. In *Numerical Modelling of Wave Energy Converters*, pages 221–225. Elsevier.
- Frigaard, P., Helm-Petersen, J., Klopman, G., Standsberg, C., Benoit, M., Briggs, M., Miles, M., Santas, J., Schäffer, H., and Hawkes, P. (1997). Iahr list of sea parameters: an update for multidirectional waves. In Mansard, Etienne, editor, *Proceedings of the 27th IAHR Congress, San Francisco, 10-15 August 1997*, Canada. Canadian Government Publishing. PDF for print: 11 pp.
- Garcia Rosa, P. B., Bacelli, G., and Ringwood, J. V. (2015). Control-informed optimal layout for wave farms. *IEEE Transactions on Sustainable Energy*, 6(2):575–582.
- Giorgi, G. and Ringwood, J. V. (2018). Articulating parametric nonlinearities in computationally efficient hydrodynamic models. *IFAC-PapersOnLine*, 51(29):56 – 61. 11th IFAC Conference on Control Applications in Marine Systems, Robotics, and Vehicles CAMS 2018.
- Götteman, M., McNatt, C., Giassi, M., Engström, J., and Isberg, J. (2018). Arrays of Point-Absorbing Wave Energy Converters in Short-Crested Irregular Waves. *Energies*, 11(4).
- Greaves, D. and Iglesias, G. (2018). *Wave and Tidal Energy*. John Wiley & Sons.
- Iglesias, G. and Carballo, R. (2010). Wave energy and nearshore hot spots: The case of the SE Bay of Biscay. *Renewable Energy*, 35(11):2490–2500.
- Iglesias, G. and Carballo, R. (2014). Wave farm impact: The role of farm-to-coast distance. *Renewable Energy*, 69:375–385.
- Iglesias, G., López, M., Carballo, R., Castro, A., Fraguera, J., and Frigaard, P. (2009). Wave energy potential in Galicia (NW Spain). *Renewable Energy*, 34(11):2323 – 2333.
- Lee, C. and Suh, K. D. (1998). Internal generation of waves for time-dependent mild-slope equations. *Coastal Engineering*, 34(1-2):35–57.
- Leijon, M., Bernhoff, H., Berg, M., and Ågren, O. (2003). Economical considerations of renewable electric energy production—especially development of wave energy. *Renewable Energy*, 28(8):1201 – 1209.

- McCallum, P. D. (2017). *Numerical methods for modelling the viscous effects on the interactions between multiple wave energy converters*. PhD thesis, The University of Edinburgh, United Kingdom.
- Millar, D. L., Smith, H. C. M., and Reeve, D. E. (2007). Modelling analysis of the sensitivity of shoreline change to a wave farm. *Ocean Engineering*, 34(5–6):884–901.
- Mørk, G., Barstow, S., Kabuth, A., and Teresa Pontes, M. (2010). Assessing the global wave energy potential. In *ASME 2010 29th International Conference on ocean, offshore and Arctic Engineering*.
- Onea, F. and Rusu, E. (2016). The expected efficiency and coastal impact of a hybrid energy farm operating in the portuguese nearshore. *Energy*, 97:411 – 423.
- Penalba, M., Sell, N., Hillis, A., and Ringwood, J. (2017). Validating a Wave-to-Wire Model for a Wave Energy Converter—Part I: The Hydraulic Transmission System. *Energies*, 10:977.
- Puertos del Estado (2019). Conjunto de datos: REDEXT. <http://www.puertos.es/es-es/oceanografia/Paginas/portus.aspx>. Available online: <http://www.puertos.es/es-es/oceanografia/Paginas/portus.aspx> (accessed on Apr 10, 2019).
- Python (2019). Python Language Reference, version 3.7. Available online: <http://www.python.org>. Available online: <http://www.python.org> (accessed on Apr 10, 2019).
- Radder, A. C. and Dingemans, M. W. (1985). Canonical equations for almost periodic, weakly nonlinear gravity waves. *Wave Motion*, 7(7):473–485.
- Ransley, E., Greaves, D., Raby, A., Simmonds, D., and Hann, M. (2017). Survivability of wave energy converters using CFD. *Renewable Energy*, 109:235 – 247.
- Ricci, P. (2016). Time-Domain Models. In *Numerical Modelling of Wave Energy Converters*, pages 31–66. Elsevier.
- Rijnsdorp, D. P., Hansen, J. E., and Lowe, R. J. (2018). Simulating the wave-induced response of a submerged wave-energy converter using a non-hydrostatic wave-flow model. *Coastal Engineering*, 140:189 – 204.
- Rodriguez-Delgado, C., Bergillos, R. J., Ortega-Sánchez, M., and Iglesias, G. (2018). Wave farm effects on the coast: The alongshore position. *Science of The Total Environment*, 640-641:1176 – 1186.
- Rusu, E. (2018). Study of the wave energy propagation patterns in the western Black Sea. *Applied Sciences*, 8(6).
- Rusu, E. and Diaconu, S. (2014). Costal impact of a wave dragon based energy farm operating on the near shore of the Black Sea. *Indian Journal of Marine Sciences*, 43:163–175.

- Rusu, E. and Guedes Soares, C. (2013). Coastal impact induced by a pelamis wave farm operating in the portuguese nearshore. *Renewable Energy*, 58:34–49.
- Rusu, E. and Onea, F. (2016). Study on the influence of the distance to shore for a wave energy farm operating in the central part of the portuguese nearshore. *Energy Conversion and Management*, 114:209 – 223.
- Sabatier, F. (2006). *U.S. Army Corps of Engineers, Coastal Engineering Manual (CEM), Engineer Manual 1110-2-1100*. U.S. Army Corps of Engineers, Washington, D.C.
- Sand, S. E. and Mynett, A. E. (1987). Directional wave generation and analysis. In *Proceedings of the IAHR Seminar on Wave Analysis and Generation in Laboratory Basins, Lausanne, Switzerland*, pages 363–376.
- Sheng, W. and Li, H. (2017). A method for energy and resource assessment of waves in finite water depths. *Energies*, 10(4).
- Sismani, G., Babarit, A., and Loukogeorgaki, E. (2017). Impact of Fixed Bottom Offshore Wind Farms on the Surrounding Wave Field. *International Journal of Offshore and Polar Engineering*, 27:357–365.
- Smith, H. C., Pearce, C., and Millar, D. L. (2012). Further analysis of change in nearshore wave climate due to an offshore wave farm: An enhanced case study for the wave hub site. *Renewable Energy*, 40(1):51 – 64.
- Sorensen, R. (1978). *Basic Coastal Engineering*. Ocean Engineering Series. John Wiley & Sons.
- Stokes, C. and Conley, D. C. (2018). Modelling offshore wave farms for coastal process impact assessment: Waves, beach morphology, and water users. *Energies*, 11(10).
- Stratigaki, V. (2014). *Experimental study and numerical modelling of intra-array interactions and extra-array effects of wave energy converter arrays*. PhD thesis, Ghent University, Belgium.
- Stratigaki, V., Troch, P., Stallard, T., Forehand, D., Folley, M., Kofoed, J. P., Benoit, M., Babarit, A., Vantorre, M., and Kirkegaard, J. (2015). Sea-state modification and heaving float interaction factors from physical modelling of arrays of wave energy converters. *Journal of Renewable and Sustainable Energy*, 7(7).
- Stratigaki, V., Troch, P., Stallard, T., Forehand, D., Kofoed, J. P., al. Folley, M., Benoit, M., Babarit, A., and Kirkegaard, J. (2014). Wave Basin Experiments with Large Wave Energy Converter Arrays to Study Interactions between the Converters and Effects on Other Users. *Energies*, 7:701–734.
- Stratigaki, V., Vanneste, D., Troch, P., Gysens, S., and Willems, M. (2011). Numerical modeling of wave penetration in ostend harbour. *Coastal Engineering Proceedings*, 1(32):42.

- Tay, Z. Y. and Venugopal, V. (2017). Hydrodynamic interactions of oscillating wave surge converters in an array under random sea state. *Ocean Engineering*, 145:382 – 394.
- Tomey-Bozo, N., Babarit, A., Murphy, J., Stratigaki, V., Troch, P., Lewis, T., and Thomas, G. (2018). Wake effect assessment of a flap type wave energy converter farm under realistic environmental conditions by using a numerical coupling methodology. *Coastal Engineering*.
- Troch, P. (1998). MILDwave - A Numerical Model for Propagation and Transformation of Linear Water Waves. Technical report, Department of Civil Engineering, Ghent University, Ghent. Internal Report.
- Troch, P. and Stratigaki, V. (2016). Phase-Resolving Wave Propagation Array Models. In Folley, M., editor, *Numerical Modelling of Wave Energy Converters*, chapter 10, pages 191–216. Elsevier.
- Tuba Özkan-Haller, H., Haller, M. C., Cameron McNatt, J., Porter, A., and Lenee-Bluhm, P. (2017). *Analyses of Wave Scattering and Absorption Produced by WEC Arrays: Physical/Numerical Experiments and Model Assessment*, pages 71–97. Springer International Publishing, Cham.
- Tucker, M. and Pitt, E. (2001). *Waves in Ocean Engineering, Volume 5*. Elsevier.
- Vasarmidis, P., Stratigaki, V., and Troch, P. (2019). Accurate and fast generation of irregular short crested waves by using periodic boundaries in a mild-slope wave model. *Energies*, 12(5).
- Venugopal, V. and Smith, G. (2007). Wave Climate Investigation for an Array of Wave Power Devices. In *7th European Wave and Tidal Energy Conference*, page 10, Porto, Portugal.
- Verbrugghe, T. (2018). *Coupling methodologies for numerical modelling of floating wave energy converters*. PhD thesis, Ghent University.
- Verbrugghe, T., Domínguez, J. M., Crespo, A. J., Altomare, C., Stratigaki, V., Troch, P., and Kortenhaus, A. (2018). Coupling methodology for smoothed particle hydrodynamics modelling of non-linear wave-structure interactions. *Coastal Engineering*, 138:184 – 198.
- Verbrugghe, T., Stratigaki, V., Troch, P., Rabussier, R., and Kortenhaus, A. (2017). A comparison study of a generic coupling methodology for modeling wake effects of wave energy converter arrays. *Energies*, 10(11).
- WAMIT (2006). *User Manual, Versions 6.4, 6.4 PC, 6.3, 6.3S-PC*.
- XBeach Open Source Community (2019). XBeach. Available online: <https://oss.deltares.nl/web/xbeach/> (accessed on June 6, 2019).

- Zijlema, M., Stelling, G., and Smit, P. (2011). Swash: An operational public domain code for simulating wave fields and rapidly varied flows in coastal waters. *Coastal Engineering*, 58:992–1012.

